

NOVEL INTEGRATED OPTICAL  
SENSING PLATFORMS  
FOR  
CHEMICAL AND IMMUNO-SENSING

ISBN 90-365-2117-3

Copyright © 2005 by J. van Lith, Enschede, The Netherlands

NOVEL INTEGRATED OPTICAL  
SENSING PLATFORMS  
FOR  
CHEMICAL AND IMMUNO-SENSING

PROEFSCHRIFT

Ter verkrijging van  
de graad van doctor aan de Universiteit Twente,  
op gezag van de rector magnificus,  
prof.dr. W.H.M. Zijm,  
volgens besluit van het College van Promoties  
in het openbaar te verdedigen  
op vrijdag 4 februari 2005 om 16:45 uur

door

Joris van Lith

geboren op 18 september 1976  
te 's Gravenhage, Nederland

Dit concept proefschrift is goedgekeurd door:

de promotoren: Prof. Dr. Paul Lambeck en Prof. Dr. Th.J.A. Popma

de assistent promotor: Dr. H.J.W.M. Hoekstra

# Contents

<b><u>1</u></b>	<b><u>INTRODUCTION.....</u></b>	<b><u>1</u></b>
1.1	IT STARTS .....	1
1.2	INTEGRATED OPTICAL SENSING .....	1
1.3	PROJECT AIMS.....	5
1.4	OUTLINE OF THE THESIS.....	5
1.5	REFERENCES .....	6
<b><u>2</u></b>	<b><u>THE SEGMENTED WAVEGUIDE SENSOR .....</u></b>	<b><u>7</u></b>
2.1	THE PRINCIPLE .....	7
2.2	CALCULATIONAL TOOLS .....	10
2.3	RESOLUTION ANALYSIS .....	18
2.4	THE DESIGN .....	22
2.5	REALIZATION AND STRUCTURAL CHARACTERIZATION.....	39
2.6	CHARACTERIZATION .....	43
2.7	OTHER KINDS OF SEGMENTATION .....	51
2.8	UNEXPECTED PHENOMENA .....	54
2.9	SUMMARY AND FINAL DISCUSSION .....	57
2.10	REFERENCES .....	60
<b><u>3</u></b>	<b><u>THE GAC SENSOR .....</u></b>	<b><u>62</u></b>
3.1	INTRODUCTION .....	62
3.2	THEORY .....	64
3.3	DESIGN OF THE GAC SENSOR .....	82
3.4	FABRICATION .....	91
3.5	CHARACTERIZATION OF THE GAC .....	93
3.6	SUMMARY AND DISCUSSION .....	96
3.7	REFERENCES .....	96
<b><u>4</u></b>	<b><u>NOVEL IMMUNO-SENSING PRINCIPLES.....</u></b>	<b><u>97</u></b>
4.1	INTRODUCTION .....	97
4.2	IMMUNO SENSING WITH AN SWS.....	104
4.3	IMMUNO SENSING USING MODAL ATTENUATION .....	107
4.4	IMMUNO SENSING WITH A DIRECTIONAL COUPLER .....	113
4.5	IMMUNO SENSING WITH A GAC.....	117
4.6	COMPARISON OF THE DIFFERENT IMMUNO-SENSING PRINCIPLES .....	119
4.7	REFERENCES .....	120
<b><u>5</u></b>	<b><u>THE CUT OFF SENSOR.....</u></b>	<b><u>121</u></b>
5.1	INTRODUCTION .....	121

5.2	EXPERIMENTAL .....	122
5.3	ANALYSIS.....	123
5.4	APPLICATION .....	126
5.5	FABRICATION .....	128
5.6	CONCLUSION .....	128
5.7	REFERENCES .....	129
<b>6</b>	<b><u>DISCUSSION .....</u></b>	<b><u>130</u></b>
6.1	SUMMARY .....	130
6.2	COMPARISON .....	134
6.3	EVALUATION .....	142
6.4	REFERENCES .....	143
	<b><u>SAMENVATTING .....</u></b>	<b><u>144</u></b>
	<b><u>APPENDIX A: ANALYSIS OF THE REST FIELD .....</u></b>	<b><u>147</u></b>
	<b><u>APPENDIX B: V-GROOVE DESIGN .....</u></b>	<b><u>150</u></b>
	<b><u>APPENDIX C: MIXING OF LIQUIDS WITH DIFFERENT REFRACTIVE INDEX.....</u></b>	<b><u>151</u></b>
	<b><u>APPENDIX D: THE MICROFLUIDIC SYSTEM .....</u></b>	<b><u>156</u></b>
	<b><u>APPENDIX E: CHARACTERIZATION OPTICAL TRANSDUCTION MATERIALS..</u></b>	<b><u>157</u></b>
	<b><u>APPENDIX F: INVESTIGATED TECHNOLOGICAL STEPS.....</u></b>	<b><u>159</u></b>
	<b><u>APPENDIX G: REALIZATION OF A VERTICAL TAPER.....</u></b>	<b><u>163</u></b>
	<b><u>APPENDIX H: ANALYSIS TEST STRUCTURES GAC SENSOR.....</u></b>	<b><u>164</u></b>
	<b><u>BIBLIOGRAPHY .....</u></b>	<b><u>168</u></b>
	<b><u>ACKNOWLEDGEMENTS.....</u></b>	<b><u>169</u></b>





# 1 Introduction

In the first section the start of this project will be described. The second section is intended to place the work presented in this thesis in a somewhat larger context by giving a short introduction into integrated optical sensing. In the third section the objectives of this project are presented and in the fourth section the outline of this thesis is given.

## 1.1 *It starts*

About six years ago, Dr. P.V. Lambeck and Dr. Ir. R.G. Heideman had an idea for a (and now I am quoting the title of the project application) 'Robust, highly sensitive chemo-optical integrated optical sensor based on segmented waveguides'. The segmented waveguide sensor (SWS) was expected to have low demands on the technology and on the quality of the light source, thus affording for integrated optical sensing systems which could be cheap, if compared to other integrated optical sensors. The sensor was expected to be applicable as an on/off alarm sensor or as a sensor enabling continuous measurements. The advantages and applications for this kind of sensor seemed numerous and after initial experiments looked promising, a Dutch patent application was started and a research proposal was submitted to and approved by STW (Stichting Technische Wetenschappen). The project should be carried out in the Lightwave Devices Group, some years ago renamed as the Integrated Optical Micro Systems (IOMS) group, which is one of the research groups of the MESA<sup>+</sup> institute.

The proposal foresaw in the employment of two Ph.D. students, one for two years and one for four years, and a part time technician (0.5 full time equivalent). The first Ph.D. student, ir S. Gaal, should focus on the application and if required development of the calculation methods and should provide and apply these tools for getting more insight into the operation of this sensor type. In 2002 he received his PhD degree. The other PhD student, Joris van Lith (that's me), should focus on the design and realization of this sensor. The technician, firstly ing. I. Heskamp and later on ing R. Wijn, should assist in the fabrication of the sensors.

## 1.2 *Integrated Optical sensing*

In this thesis several novel principles for chemical integrated optical (IO) sensors will be presented. It is therefore quite instructive to first explain what an integrated optical sensor is. What are the fundamental principles on which IO sensors are based? Why is integrated optical sensing interesting and what or where can it eventually be used for?

To start with answering the first question; the purpose of a chemical sensor is to measure the concentration or the change in concentration of some specific chemical compound or just merely to detect that its concentration is above some critical limit. This chemical compound, or the measurand as it will be referred to henceforth, can for example be the

concentration of CO<sub>2</sub> in air, the concentration of glucose in water or the concentration of antigens in blood plasma. In order to convert the concentration of the measurand into a physical parameter that can be directly measured, there is in general a need of a transduction layer, or sensing layer. For a sensor to be called an optical sensor, the optical properties of this transduction layer need to be dependent on the concentration of the measurand. An additional read-out system is necessary to translate the chemically induced changes of optical properties into an electrical output signal. We call a sensor 'integrated optical' if at least the sensing region consists of an integrated optical waveguiding system. Often more optical functions e.g. for conditioning the optical input and for readout, are integrated in one single monolithical integrated optical chip, but the integration can go up to a state in which the whole sensing system, including light source, sensing region, optical processing functions, optical detectors, micro-fluidics (for a controlled transport of the sample to the sensing region) and even the electronics, are configured as one single monolithical chip.

Now we know what IO sensors are, it's time to have a look on what fundamental principles they are based. As mentioned before, it is the (change in) optical properties of a specific transduction layer which need to be detected. These optical properties can be expressed by the refractive index, the absorption coefficient or the luminescent properties [1]. Although luminescent sensors generally show the highest resolution and hence are most sensitive to very low concentrations, the refractive index type sensors are attracting more and more interest. The main reason for this is that only a few materials are luminescent themselves and that in order to utilize luminescence in sensors, for each measurement, molecules provided with luminescent labels have to be added to the sample e.g. for affording a competition reaction between unlabeled and labeled molecules. Hence continuous measurements based on luminescence are often excluded. Application of optical transduction layers of which the refractive index changes (and preferably reversibly) with the measurand concentration however would allow for continuously in situ measurements. Because there is a good progress [7],[4],[9] in developing these refractive sensors to high sensitivities, they are becoming competitive to the luminescent sensors, even if very low concentrations have to be measured. These developments are based on smart application of classical optical principles, on introducing completely new sensing principles specific for integrated optics and on improvements in the micro-technologies with which the sensors are produced.

In most of the refractive IO sensors the change of the refractive index of the sensing layer is converted into a change of properties of the guided modes which are probing the sensing layer. Generally the detection is based on the change of the effective refractive index of the as a guided mode propagating light beam, a property directly related to the propagation velocity of the mode. This change of effective index is generally measured by methods based on mode coupling [6],[7],[8] or interference schemes [7],[3],[4],[5] well known from classical optics, such as Mach-Zehnder, Young or Zeeman interferometry. Interesting prospects for increasing the resolution are offered by interference based IO sensors that use resonance phenomena like the ring resonator [9],[10].

The Segmented Waveguide sensor also is a refractive index type sensor, but unlike aforementioned sensors, it exploits the change of the shape of field profile of the propagating mode to measure the refractive index of the sensing material. A sensor that also makes use of the shape of the mode profile has been investigated by G. Veldhuis [11],[12]: the bend sensor.

Using evanescent field sensing a change in refractive index, absorption or luminescence in the transduction layer applied e.g. on top of the core layer of a waveguide will be translated into a change in phase, power or wavelength of the guided mode coming out of the sensing region. Dependent on the thickness of the transduction layer the sensing method can be classified as bulk (alternatively named homogeneous) sensing or surface sensing. In bulk sensing the modal field is located completely inside the layer stack of the sensor and the propagating mode will be insensitive to optical changes outside this stack. Of course the nature of the transduction layer has to allow for in-diffusion of the measurand molecules in order for them to reach the receptor molecules, with which they have to associate, present in the layer. If this diffusion is too slow or even impossible the receptor molecules are generally immobilized in a thinner layer with the extreme of a monomolecular layer on top of the core layer and we speak about surface sensing. Such monomolecular layers are often applied in immuno-sensing. Now the evanescent tail also probes changes of the refractive index of the sample liquid above the transduction layer and reference branches may be required to compensate for this.

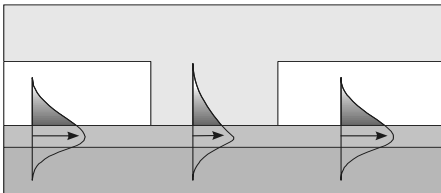


Figure 1.1. A typical bulk sensing region.

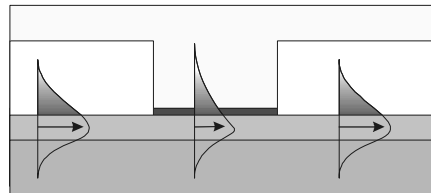


Figure 1.2. A typical surface sensing region.

Development of integrated optical sensors requires the collaboration of many different disciplines; it is a multidisciplinary activity. Firstly of course we need optics for the sensing principles applied and for the design of all required (integrated) optical components. Then we need the microtechnology for realizing the sensors. We need chemistry for developing the chemo-optical transduction layers and we also need micro-mechanics for realizing appropriate micro-fluidics systems needed for the processing and the transport of the samples and the conditioning of the sensor. Finally for the electronic processing of the data we need systems and control engineering. Depending on the type of sensor, also knowledge of thermo-dynamics, semiconductor physics, fluid mechanics and electronics is required. It is rare that one research group or company has all the required expertise at its disposal and thus cooperation is a necessity in the area of IO sensors. In this PhD project we will approach the sensor R&D from our expertise in the fields of integrated optics and micro-technology.

The first impression of IO sensors could be that they are pretty expensive to realize. Every sensor needs a light source and a separate electronic control and processing system. Advanced packaging technology is also necessary. So why would somebody

want to make IO sensors? It is probably not easy to commercialize IO sensors for purposes that are already served by existing sensors, using conventional technology, like ISFETs. Therefore we have to look to application areas where IO sensors display their strong points, like industrial applications which require EMI and explosion-free operation. Further, IO sensors offer the possibility of extreme sensitivity (note that this also implies extreme sensitivity to disturbing factors!). In health care and in environmental monitoring there is need for these extreme sensitivities and the willingness to spend on that. Because IO sensors are small, they also offer the possibility to realize multi-purpose sensor arrays and the way is open for a cheap mass production similar to the way electronic chips are produced nowadays. Additionally the R&D on IO sensors has profited and also will profit in the future from all developments of integrated optical functions for optical (tele-)communication. Therefore it is not necessary for the sensor industry to bear all the cost of the research and development of IO devices and systems by itself. So we can conclude that there are ample reasons why IO sensors should have our interest: IO sensors, to our opinion, can be expected to play a very important role in future.

I'll end this introduction to IO sensors with an overview of several types of refractive IO sensors. In Figure 1.3 they are compared to each other with respect to the smallest change in effective index that they can detect. As can be seen, both the Mach Zehnder Interferometer [4] and the Young Interferometer [7] excel in resolution, and both look to be very promising.

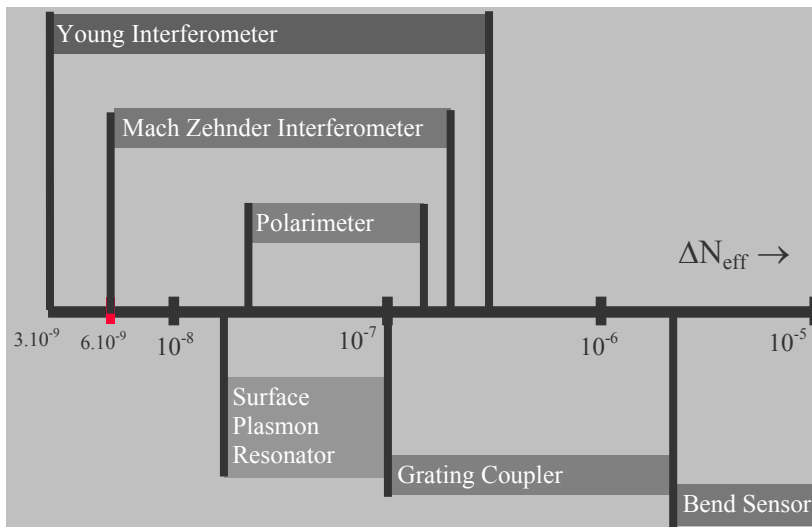


Figure 1.3. Several IO sensors compared.

### **1.3 Project aims**

The first objective of the project is to fully evaluate the principle of the segmented waveguide. In order to do this, firstly the calculational tools have to be applied and if needed to be developed in order to get a complete understanding of the principle and to determine the limits of its potential e.g. in terms of obtainable resolution. Several layouts and implementations of the sensor principle have to be conceived, investigated and evaluated. The technology for the fabrication has to be developed and a prototype sensor has to be fabricated and characterized which enables a practical proof of principle, amongst others demonstrating the correctness of our theoretical description. After that another SWS has to be realized, which will be heavily optimized with respect to its performance, mainly given in terms of attainable resolution.

The second objective is to optimize the sensor for certain applications, these applications should originate from the needs of the industry involved in the STW project.

The third objective is to use the academic freedom to investigate other interesting integrated optical sensor principles, preferably utilizing the theory and technology that has been developed for the SWS sensor.

### **1.4 Outline of the Thesis**

Beside the SWS (chapter 2), also other novel types of IO sensors have been investigated such as the co-directional Grating Assisted mode Coupling sensor (GAC, chapter 3). In chapter 4 several proposals for novel IO sensors for immuno-sensing all, just as the SWS being based on chemically induced changes of field profiles, are worked out theoretically. Chapter 5 presents a very simple type of alarming sensor based on modal cut off. The thesis will end (chapter 6) with a general discussion, some conclusions and recommendations.

## 1.5 References

- [1] P.V. Lambeck, *Integrated Optics for the Chemical Domain, ECIO 2001*, pp. 153-163
- [2] A.Ymeti, J.S.Kanger, J.Greve, P.V.Lambeck, R.Wijn and R.G.Heideman, *Realization of a multichannel integrated Young interferometer chemical sensor*, *Applied Optics*, 42, (2003), pp 5649-5660.
- [3] A.Brandenburg, *A.Differential refractometry by an integrated optical Young interferometer*, *Sensors and Actuators B38-39*, (1997), pp266-271.
- [4] R.G.Heideman and P.V.Lambeck, *Remote opto-chemical sensing with extreme sensitivity: design, fabrication and performance of a pig-tailed integrated optical phase-modulated Mach-Zehnder Interferometer system*. *Sensors and Actuators B61* (1999), pp 100-127.
- [5] P.Hua, B.Luff, G.R.Quigley, J.S.Wilkinson, K.Kawaguchi, *Integrated optical dual Mach-Zehnder interferometer sensor*, *Sensors and Actuators B87* (2002), pp 250-257.
- [6] B.J. Luff, R.D. Harris, J.S. Wilkinson, R.Wilson, D.J. Schriffrin, *Integrated-optical Directional Coupler Biosensor*, *Optics Letters Vol 21* (8) (1996), pp. 618 – 620.
- [7] T.Koster and P.V.Lambeck, *Fully integrated optical polarimeter*, *Sensors and Actuators B82*, (2002), pp213-226.
- [8] Z.Qi, K.Itoh, M.Murabayashi, H.Yanagi, *A composite optical waveguide-based polarimetric interferometer for chemical and biological sensing applications*
- [9] E.Krioukov, D.J.W.Klunder, A.Driessen, C.Otto and J.Greve, *Refractive index sensing using an integrated optical microcavity*, *Opt.Lett.* 27 (2002), pp512-514.
- [10] G.J. Bakker, MSc. Graduation report, *Microring Resonator Enhanced immunosensing*, Biophysics Group, University of Twente, March 2003.
- [11] G.J. Veldhuis, L.E.W. van der Veen, P.V. Lambeck, *Integrated Optical Refractometer based on waveguide bend loss*, *J.Lightwave Techn*, Vol. 17(5) (1999) pp. 875-864
- [12] G.J. Veldhuis, P.V. Lambeck, *Highly-sensitive passive integrated optical spiral-shaped waveguide refractometer*, *Applied-Physics-Letters*, Vol. 71(20)(1997): pp. 2895-2897

## 2 The Segmented Waveguide Sensor

In this chapter the segmented waveguide sensor (SWS) will be treated in full detail. In section 2.1 the principle of the SWS will be presented. Next (section 2.1) several methods which can be used to calculate the performances of the SW sensor will be compared. After that, in section 2.3, a theory will be presented that describes the resolution of the total sensor system, consisting of the IO-chip and all the peripheral equipment. The design of two types of SWS sensors, in which the cladding of the different segments consists of either a sensitive or a passive cladding material, will be presented (section 2.4); also integration of the IO chip with a simple micro-fluidics system has been considered. The aim of the first type of SWS was to obtain proof of principle, to try out the technology and to give an estimation of the possibilities of the SWS. The aim of the second type was to demonstrate the best obtainable resolution. The technology and the structural characterization of the SWS's will be presented in section 2.5. In section 2.6 the measured performance of the both types of SWS will be given and discussed. Two other kinds of segmentation, in which the segments differ only with respect to their geometry, will be shortly treated in section 2.7. An unexpected phenomenon occurring in the SWS sensors is discussed in section 2.8. It will be the starting point for investigations on another sensing principle, as will be described in Chapter 3. Chapter 2 ends with a summary and a discussion about the application potential of SW sensors (section 2.9).

### 2.1 *The principle*

In this section the principle of the SWS will be explained.

Segmented waveguides have raised a lot of interest due to their potential as devices for quasi-phase matching in second harmonic generation [1] or for tuning the size of the modal field [2], but up until now they never have been used for sensing purposes. A segment is defined as an in the propagation direction invariant waveguide of certain length. The principle of an SWS will be illustrated by considering a single mode waveguide channel which consists of a series of two types of segments, mutually differing with regard to their refractive index distribution in the plane perpendicular to the propagation direction. During beam propagation, at each transition between two adjacent segments, power is coupled from the guided mode of one segment into the guided mode of the next segment. The coupling efficiency is determined mainly by the degree of similarity of the mode profiles in both segments. In the SWS one of both segment types contains a material (the so-called sensing material) of which the refractive index depends on the parameter to be measured, the measurand. Hence the mode profile in these 'active' segments reflects the value of the measurand. In the other type of segments this dependency is smaller, usually being completely absent. This way the coupling efficiency and hence the modal transmission is a function of the measurand value. The two types of segments may differ from each other in a variety of ways: e.g. with respect to the cladding material only, but also with respect to the core material, or the geometry.

The sensing principle will be explained in more detail, by considering a specific SWS, implemented using SiON technology, with a segmentation based on difference in cladding material only.

In Figure 2.1 the longitudinal cross-section of a segmented ridge type waveguide is depicted. It consists of a series of two types of segments: passive segments with SiON as cladding and active segments with a sensing material as cladding. Here the sensing material is a chemically active material whose refractive index depends on the concentration,  $c$ , of a specific chemical compound, the so-called analyte. For now we will assume absence of propagation losses within an individual segment. A guided mode is launched into the first segment of the waveguide. If there would be no difference in refractive index of the SiON cladding and the sensing material, ( $\Delta n(c) \equiv n_{SiON} - n_{sens}$ ) all optical power will be transferred to the guided mode of the next segment. If however  $\Delta n(c) \neq 0$ , then due to the difference in field profiles of both types of segments not all guided mode power launched into one segment will be transferred to the guided mode of the adjacent segment. At the transition also some power will be coupled to radiation modes. The amount of power left as a guided mode is a measure for the concentration of the analyte. At low concentrations the chemically induced  $\Delta n$  generally is very small. Hence after one transition only, the loss of guided mode power would be very small too. However, with a sequence of a few thousand transitions, a quite sensitive sensor might be obtained.

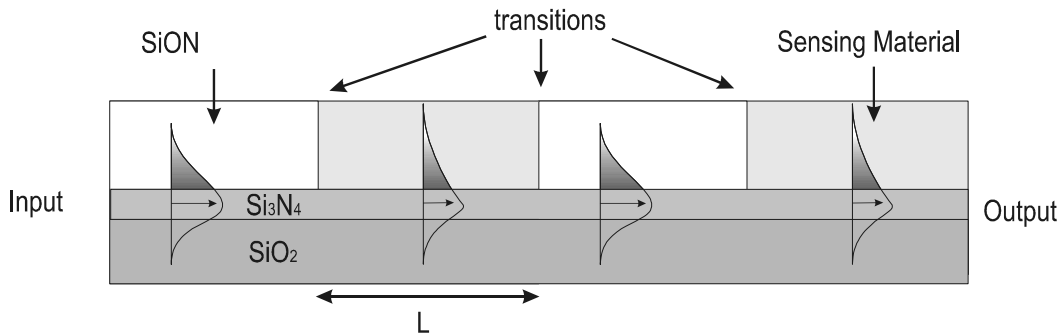


**Figure 2.1. Longitudinal cross-section of the sensor (4 segments).**

However there is a complication: part of the power radiated out at one transition will be coupled back into guided modes at next transition or even at following ones. It is the distance  $L$  between two neighboring transitions that determines both the amount and phase of the light that is coupled back into the guided mode. Depending on their phase difference, there can be constructive or destructive interference between the guided mode, which has passed the transition and the guided mode that originates from the back-coupling at that transition. Note that in the above we implicitly assumed that coupling to backward propagating modes at the transitions can be neglected; an assumption which in the regime of index differences (0-0.01) is supported by all our calculations. Note also that the principle works for any distribution of segment lengths and that the nature of the distribution itself also is a design parameter, as will be discussed further in section 2.2.4.

Although not required, for various reasons (see section 2.4.4.8) we have chosen here and in the rest of the chapter for a periodic structure.

For illustration we show in Figure 2.2 the calculated electrical field distribution resulting from launching a zeroth order guided mode into the first segment of a slab structure of the type depicted in Figure 2.1. As can be seen, radiation generated at the transitions is directed both upwards to the top of the sensor and downwards towards the substrate. It can also be observed that this radiation has a specific angular distribution. This will be discussed in more detail in Appendix A.

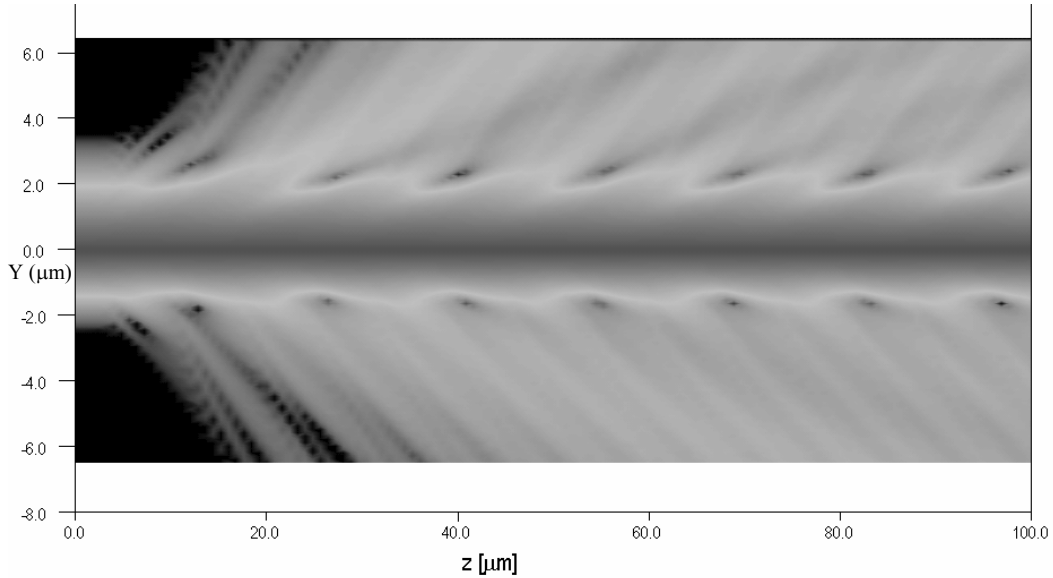


**Figure 2.2. Light propagating through a segmented waveguide structure.**

In Figure 2.3 a cross section and top view of a channel type SWS with segmentation in the cladding is depicted. The symbols used for some relevant sensor parameters are introduced.

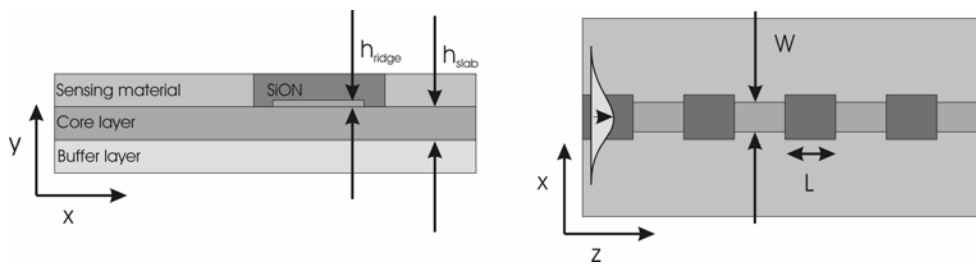


**Figure 2.3. Cross section (left) and top view (right) of an SWS with segmentation in the cladding.**

## **2.2 Calculational tools**

### **2.2.1 Introduction**

For a quantitative theoretical description of the light propagation through a Segmented Waveguide Sensor (SWS) it is necessary to have simulation tools/methods available that can handle guided and radiation modes and also their coupling very well. In this section the use of several of such methods will be briefly treated: the Finite Difference Beam Propagation Method (FD BPM) [3], the Bidirectional Eigenmode Propagation method (BEP) [3] and the Spectral Decomposition Method (SDM) [4]. It is assumed that the reader is already reasonably familiar with these simulation methods. Each method has its limitations; also it appears, that application of these methods to the SWS is not straight forward and can be very cumbersome. For each method it will be explained how it needs to be applied to the SWS in order to achieve sufficient accuracy. Applicability of the methods to the SWS will be compared, just as some results of their application to some specific SWS systems.

Unfortunately we had no 3D simulation programs available that could cope with the very thin  $\text{Si}_3\text{N}_4$  core layers commonly applied in the sensors. For this reason we had to rely on 2D methods either by using the Effective Index Method to reduce a 3D structure to a 2D structure or in specific cases by simply neglecting the lateral structuring, as is shown later on. In section 2.2.2 the amount and the angular distribution of the light coupled into radiation modes at a transition between two segments is investigated. The results will appear to justify the application of 2D calculation methods for the kind of segmented waveguide structures that will be considered in this chapter.

### **2.2.2 The radiation field**

In appendix A it is explained how the field and angular distribution of the radiation field corresponding to the radiation modes emitted at a transition can be calculated. This has been done for the typical structure of an SWS of which the design will be treated in section 2.4. In that appendix it is concluded that for this kind of structures the electrical field  $E_r$  diverges very little in the lateral direction ( $xz$ -plane, see Figure 2.3 for orientation of the axes), but considerably in the transversal direction ( $yz$ -plane). Also 3D simulations, although not very accurate, clearly show this behavior. Thus, especially for short propagation distances, the field distribution in the  $x$  direction can be approximated as being constant and therefore it is allowed to approximate the 3D SWG structure with an equivalent 2D slab structure as depicted in Figure 2.1, now being invariant in the lateral direction.

While making this approximation we have to be aware of its consequences. When the radiation generated at one transition reaches the next transition its lateral distribution has slightly changed. This may effect somewhat its back coupling into the guided modes. Also the lateral divergence will have some influence on the phase of the light that is

coupled back to guided modes. Both effects are not taken into account in the 2D approximation: the longer the propagation distance, the larger the error, with the consequence that the error is bigger the larger the segmentation lengths.

### 2.2.3 FD BPM

If the FD BPM [3] is used for this kind of calculations, there are several aspects that need attention. Firstly the influence of the grid size in transversal direction. On one hand the grid size needs to be small in comparison with the thickness of the  $\text{Si}_3\text{N}_4$  core layer (typically 50 nm), but on the other hand, the calculation window should be sufficiently large to encompass the total field profile of the guided mode (typically 5  $\mu\text{m}$ ); these two requirements together result in the necessity of a huge number of grid points, slowing down the calculation speed considerably. Using a variable grid could be a solution, but such an option is not available to us at the moment. Secondly the BPM inherently has a phase error in the propagation direction as a consequence of the grid size in the propagation direction. In the SWS, where interference effects are important, the phase error should be minimized by choosing a small grid size. Padé order approximation 4 has been used to further minimize the phase error. Transparent boundary conditions have been used to lower back reflections from the boundaries of the computational window. However, these do not work very well for the considered type of problems, in which a large number of plane waves reach the boundary. This reflection has a relatively large influence on the calculation results. In order to cancel out their effects, calculations have been performed using different window sizes and the results have been averaged. This method is known as the ‘variable-bound approach’ [5]. It can be concluded that FDBPM, enables the kind of calculations necessary to describe the light propagation through a SW sensor, but its application is quite cumbersome.

### 2.2.4 The BEP

The BEP method is based on a decomposition of the local field into the system modes of an artificial system formed by applying so-called Perfectly Matching Layers at the boundary of the computational window. Part of these system modes coincide with guided modes of the structure, the majority of them however are used to describe the radiation field. To describe the radiation field accurately, a sufficiently large number of system modes should be calculated. The PMLs are used to suppress reflection. The PML strength and thickness should be optimized for maximum suppression. Note that if the PML thickness is increased, also the number of system modes should be increased to maintain the same accuracy in the description of the radiation field. Unfortunately always a little bit of reflection by the calculation window boundary will be left, but this is in general appreciably less compared to reflection at the boundaries of the FDBPM. Propagation of a given field distribution, decomposed in system modes, through z-invariant parts of the structure can be calculated analytically. The method also takes into account reflections against the transition planes. At the transition between two different z-invariant structures the power that is coupled into the system modes of the second structure is determined

using the appropriate overlap integrals. Note that the number of necessary overlap integrals increases with the square of the number of system modes, so the processing power of the computer limits the number of system modes that can be considered. The BEP method is perfectly suited to describe segmented structures, because the system modes of two structures (both types of segments) and their overlap integrals have to be calculated only once. It is obvious that this method doesn't have problems with the small  $\text{Si}_3\text{N}_4$  core thickness. It turned out that, for calculating the light propagation through the SWS devices which we have considered, the BEP was more user-friendly and faster than the FDBPM.

## 2.2.5 The SDM

The 2D spectral decomposition method (SDM) as developed in [4] enables a semi-analytical approach, which offers directly physical insights. Here the basics of the SDM will be explained briefly in order to understand its benefits and limitations better. Analytical expressions will be derived for modal losses in a 2D SWS with an arbitrary distribution of segment length.

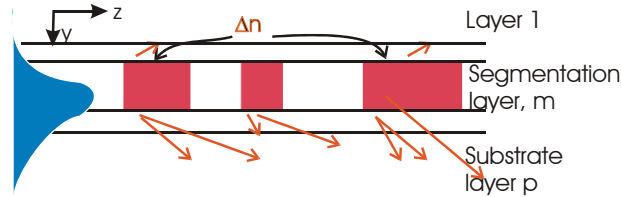


Figure 2.4. Schematic picture of the considered waveguide, with segmentation in one of the layers.

In the SDM the Helmholtz- equation for the complete segmented structure involving a  $z$ -dependent dielectric constant as depicted in Figure 2.4, is solved analytically by applying Fourier analysis. In the approximation of undepleted propagation of the guided mode (in fact limiting the use of the SDM to structures in which the power of the radiation field is much smaller than the guided mode power) the optical power  $P$  radiated into the extreme layers  $p$  and 1 of the waveguiding layer stack can be expressed approximately as:

$$P_p + P_1 = \int_{-K}^K |G_0 H_p|^2 dk_z + \int_{-K_1}^{K_1} |G_0 H_1|^2 dk_z \equiv \int_{-K}^K H |G_0|^2 dk_z \quad (2-1)$$

With  $k_z$  the component of the wave vector of the radiation mode parallel to the propagation direction,  $K_1 \equiv k_0 n_1$ ,  $K \equiv k_0 n_p$  and  $H \equiv |H_1|^2 + |H_p|^2$ .  $H_{p,l}(k_z)$  are functions which are only related to the parameters of the layer structure, i.e. the thicknesses and refractive indices of all the layers.  $G_0(k_z)$  is a function that only depends on the segmentation, the total length of the segmented structure and the effective index of the guided mode. The expressions for the functions  $H$  (expression (2-4) and (2-5)) and  $G$

(expression (2-2)) are quite complicated and therefore it is more comprehensive to graphically portray  $G$  and  $H$  as a function of  $k_z$  or alternatively as a function of  $N_{eff}$  of the radiation modes for a number of given structures. Although  $G_0$  and  $H_{p,l}$  are analytical functions, unfortunately the integrals they contain still need to be evaluated numerically. We'll now analyze the functions  $G$  and  $H$  and their dependence on the some design parameters.

The exact expression for  $G(k_z)$  is:

$$G_0(k_z) \equiv k_0^2 \Delta \varepsilon \int_0^{\infty} g(z) \exp\{i(k_z - \beta_0)z\} dz / \sqrt{2\pi} \quad (2-2)$$

where  $g(z)$  describes the segmentation. In Figure 2.5 for a periodical segmentation a typical  $G$  function is depicted. The precise values of the parameters of the SW structure that have been used for calculating this curve have been taken from Table 2.2, but at this point they are of no real interest.

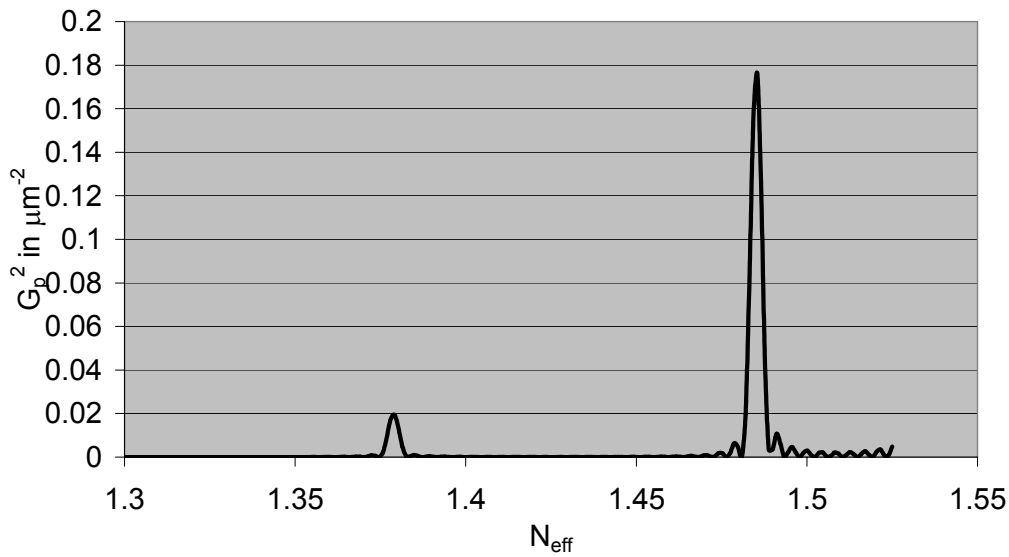


**Figure 2.5. The G function.**

For a segmentation in which all segment lengths are equal to  $L$ , the  $G$  function has peaks at:

$$N_{eff} - N_0 = m \frac{\lambda}{L} \quad (2-3)$$

where  $N_0$  is the effective index of the fundamental mode and  $m$  an integer. This expression is well known from grating literature. In Figure 2.5 the first order peak ( $m=-1$ )

is shown. The function can be seen as a delta function convoluted with a sinc-function of  $N_{eff}$ . The convolution is a consequence of the finite length of the considered segmented waveguide section. The longer the waveguide, the narrower the sinc-function until at infinite length the peak should approach a pure delta-function. The height of the peak is related to the amount of segments. By adjusting the value of  $L$ , at fixed  $N_0$  the position of the peaks can be controlled.

The  $H$  functions can be expressed as:

$$|H_1|^2 \equiv |\alpha_1| |t_{m1}(T_2 + S_2) / \{2D(k_z^2 - \beta_0^2)\}|^2 / (2k_0 Z_0) \quad (2-4)$$

$$|H_p|^2 \equiv |\alpha_p| |t_{mp}(T_1 + S_1) / \{2D(k_z^2 - \beta_0^2)\}|^2 / (2k_0 Z_0) \quad (2-5)$$

with  $\alpha_l \equiv \sqrt{k_z^2 - k_0^2 n_l^2}$ ,  $l = 1, p, m$ ,  $Z_0 \equiv \sqrt{\mu_0 / \epsilon_0}$  and  $t_{ij}$  is the transmission from layer  $i$  to layer  $j$ . The variables  $t_{mp}$ ,  $t_{m1}$ ,  $(T_2 + S_2)$  and  $(T_1 + S_1)$  are very complicated functions of the parameters of the slab structure [4] and it does not lead to more insight to mention the full expressions here.  $D$  is given by:

$$D \equiv \exp(\alpha_m d_m) - r_{m1} r_{mp} \exp(-\alpha_m d_m) \quad (2-6)$$

In Figure 2.6 a typical  $H$  function (using the structural parameters given in Table 2.2) is depicted.

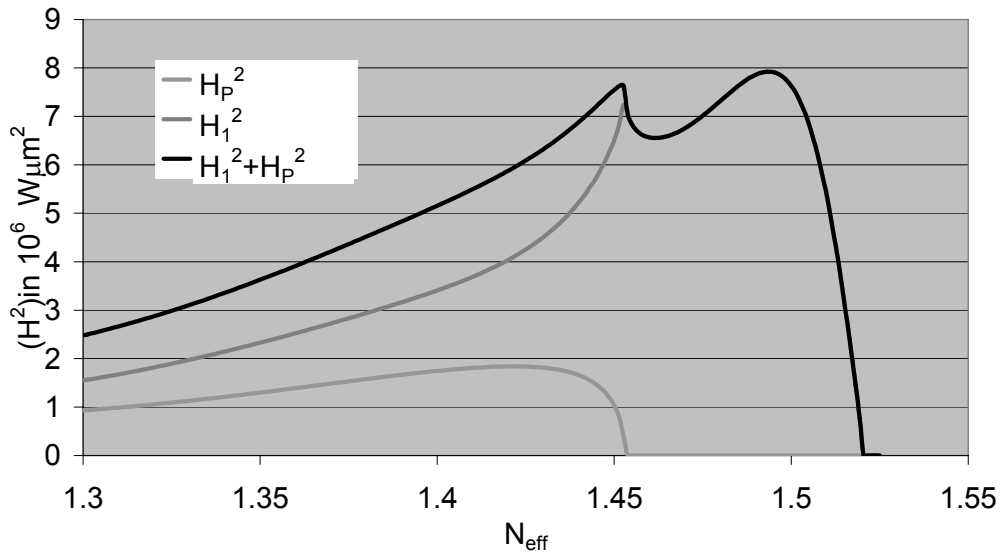


**Figure 2.6. Typical H functions.**

The  $H$  function only depends on the parameters of the slab structure. The shape of the function is related to the angular distribution of the light coupled into the radiation modes

at one transition. The cladding index is 1.52 and it can be seen that for  $N_{eff} > 1.52$  there are no radiation modes present ( $\alpha_l=0$ ). The buffer index is 1.453 and for  $N_{eff} > 1.453$  there are no radiation modes present that are directed into the buffer layer ( $\alpha_p=0$ ).

The behavior of  $t_{mp}$ ,  $t_{ml}$ ,  $(T_2 + S_2)$  and  $(T_1 + S_1)$  has been investigated, but it turned out that these functions are really complicated and we could not derive their physical links to the structural parameters of the segmented waveguide from the specific H-curves.

This leaves  $D$ ; if  $D$  approaches 0 for a specific value of  $N_{eff}$ , the  $H$  value will approach infinity. If  $D=0$ , expression (2-6) reduces to the resonance condition for guided modes. It only has solutions in the real  $N_{eff}$  domain for  $N_{eff} > n_{clad}$ . This means that the condition  $D=0$  can never be obtained within the real  $N_{eff}$  domain where  $H_{p,l}$  is non-zero. It has also been investigated whether solutions of the resonance condition in the complex domain, but located close to the real  $N_{eff}$ -axis (representing leaky modes) have an influence on the value of  $D$  on the real  $N_{eff}$ -axis. In the calculations we have performed this however was not observed.

Nevertheless there is a trick to utilize the  $D=0$  condition. When in a multimodal structure the 1<sup>st</sup> order mode is very close to cut-off, part of the corresponding peak in  $H$  will also be present at  $N_{eff} < n_{clad}$ . By positioning also the 1<sup>st</sup> order peak of  $G$  at  $N_{eff} = n_{clad}$  the overlap of expression the  $G$  and  $H$  functions near  $N_{eff} = n_{clad}$  can be made appreciably large. Also for this special case  $P_l$  appears to increase with  $z^{3/2}$  [4], [2]. This interesting case has not been investigated within this project, because of the more complex fabrication process required to fabricate the thick core layers necessary for the transversally bimodal waveguides.

## 2.2.6 Comparison of the methods

Now it's time to compare the three different methods. This will be done for a structure that is representative for the SW sensors that will be designed. The validity of the conclusions about the applicability of the calculation methods is limited to this kind of structures. But before we can come to that, we need a little bit of extra information about the SWS. Calculations [7] have shown that for this type of SWS in the approximation of low power of the radiation field (i.e.  $\Delta n < 0.002$ ), the functional loss,  $\eta$ , of the guided mode presented in dB is, proportional to the square of  $\Delta n$ . As will appear later on, the SW sensor will usually operate within this  $\Delta n$  range. The functional loss can be expressed given as:

$$\eta(\Delta n) = A \cdot L_{sensor} \cdot \Delta n^2 \quad (2-7)$$

Here  $\eta(\Delta n)$  denotes the functional loss in dB, normalized on the losses at ( $\Delta n=0$ ).  $L_{sensor}$  (in m) is the total length of the sensor.  $A$  (in dB/m) is a constant, of which the specific value depends on the optical and geometrical parameters of the SW structure. The value  $A$  is a measure for the quality of the sensing element. For the used SWS structure the SDM can only be applied for  $\Delta n < 0.0001$ . In this region expression (2-7) is valid and the

$A$  value can be calculated for various  $L$ -values. The FD BPM however gives correct results for  $\Delta n > 0.001$  only, because the FD BPM always introduces artificial propagation losses. Real propagation losses can only be distinguished from the artificial ones if they are noticeable larger. In this  $\Delta n > 0.001$  region expression (2-7) is not valid anymore and thus the FD BPM it is not capable to determine the  $A$  value. The BEP however can be used well in both domains. In order to compare the three methods, the functional loss as a function of  $L$  for  $\Delta n = -0.01$  has been calculated with the FD BPM and BEP (Figure 2.7) The  $A$  value as a function of  $L$  has been calculated with the SDM and BEP (Figure 2.8). All these calculations have been performed at  $\lambda = 850$  nm on the structure as is given in Table 2.2, i.e. the final design of the sensor. The settings of the calculation methods are given in Table 2.1. For the exact definitions of the parameters of the simulation programs, like PML strength, I refer to the manual [3].

**Table 2.1. Simulation settings of the FD BPM and BEP.**

FD BPM		BEP	
Discretization in $z$	0.1 $\mu\text{m}$	Discretization in $z$	0.1 $\mu\text{m}$
Discretization in $x$	0.005 $\mu\text{m}$	Discretization in $x$	0.005 $\mu\text{m}$
Calculation window	8 – 12 $\mu\text{m}$	PML strength	0.36
Reference index	$N_{\text{TE00}}$	PML thickness	2 $\mu\text{m}$
Pade order	4	Calculation window	8 – 12 $\mu\text{m}$
Discretization order	4	Number of 1D modes	80
Boundary conditions	transparent		

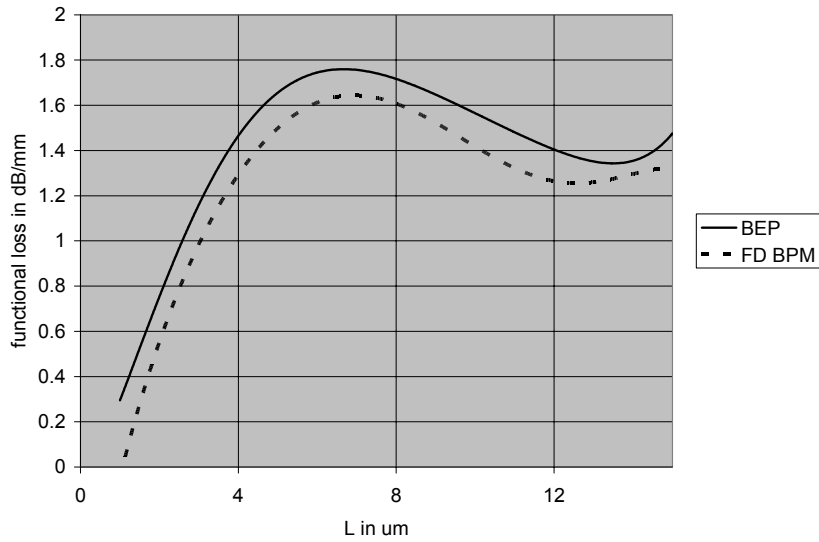


Figure 2.7. Functional loss vs  $L$  curves for  $\Delta n = -0.01$ , calculated by using BEP and FD BPM.

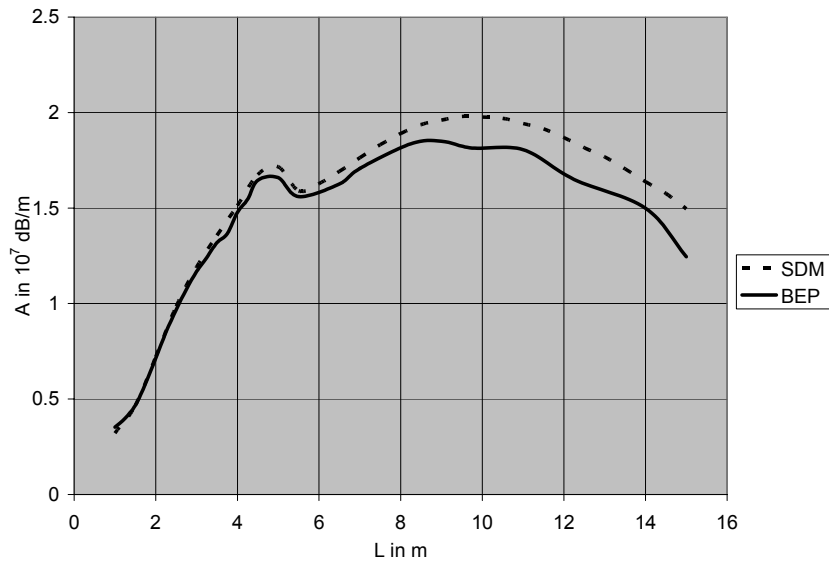


Figure 2.8.  $A(L)$  curves, calculated by using SDM and BEP.

The results of all three calculation methods appear to agree reasonably well to each other. The differences between the methods can most probably be attributed to the different type of boundary conditions at the computational window and the approximative nature of the SDM.

Of course such figures show more than just the differences between the results obtained by using different methods. They also form the basis of the design of the SWS sensor; more about this in section 2.4 where the design will be treated.

## 2.3 Resolution analysis

Every sensor application is accompanied by its own specific set of requirements to the sensor performance. Because IO-sensors are most competitive if high resolution is required [8], we will focus on this aspect and analyze the resolution prospects of the SW sensor. Resolution is defined as the smallest change in refractive index of the sensitive material that can be measured by the complete sensing system, consisting of the optical chip with the segmented structure and the peripheral equipment: the light source and the opto-electronic detection system. By this definition we have excluded the influence of the concentration-to-refractive index transduction properties of the applied chemically active material. In general high resolution is required over a small range only.

Basic behavior of this quasi-absorptive sensor can be expressed by the relation

$$P_{out} = F(\Delta n)P_{in} \quad (2-8)$$

Where  $P_{in}$  and  $P_{out}$  are the input and output power of the segmented structure, respectively and  $F(\Delta n)$  represents the transfer function of the sensor. We may assume without loss of generality that in the sensor, which will be analyzed,  $\Delta n$  is positive. Starting from relation (2-7),  $F(\Delta n)$  can be expressed as:

$$F(\Delta n) = 10^{-0.1(A\Delta n^2 + B)L_{sens}} \quad (2-9)$$

where  $L_{sens}$  is the length of the segmented structure.  $A\Delta n^2$  represents the functional losses as a consequence of the segmentation and  $B$  represents the effects of the absorption and scatter losses.  $A$  is governed by the specific design of the segmented structure,  $B$  mainly by the properties of chosen materials and technology. For the first few segments ( $\approx 5$ ) expression (2-9) is not valid yet because of starting phenomena. The light coupled into radiation modes at different transitions interferes with each other. Expression (2-9) can be applied only for the segmented part in which this interference pattern has been fully developed.

The resolution depends on the sensitivity of the sensor  $S$ :

$$S(\Delta n) = \frac{\partial(P_{out} / P_{in})}{\partial n} = \frac{\partial F(\Delta n)}{\partial n} = \frac{-\ln(10)}{10} 2A\Delta n F(\Delta n) \quad (2-10)$$

and on the accidental errors, i.e. fluctuations, in each of the three quantities given in expression (2-8). As can be seen from expression (2-10), the sensitivity is a function of  $\Delta n$ . In practice the sensor will operate in a very small domain around a fixed  $\Delta n$ , not

necessarily being  $\Delta n = 0$ . This  $\Delta n$  will be referred to as the working point and it will appear to be an important design parameter.

The accidental error in  $P_{in}$ , originates from fluctuations in the light source power and the couplings used to transport the light to the segmented structure. Generally these fluctuations can be described as a relative error  $q_1$  in the input power and as a consequence of (2-8) also as an identical relative error in the output power of the segmented structure. This output power is read out by an opto-electronic system consisting e.g. of a photodiode and electronic processing units. The accidental error related to this read out system is mostly determined by the photon noise and amplifier noise. For simplicity of the expressions we approximate this by an additional relative error in  $P_{out}$  denoted by  $q_2$ , its specific value depending on the considered power range. For this approximation to be valid of course the output power has to amply exceed the shot noise limit of the photodiode. We will assume that accidental errors in the transfer function can be neglected by appropriately conditioning the system. Influence of temperature fluctuations will be assumed to be effectively suppressed by thermostating the optical chip, while fluctuations in the concentration and hence in the refractive index of the active layer will be suppressed by an appropriate way of sample transport to the sensor.

In addition to these accidental errors, systematical errors can exist, e.g. in the transfer function, due to the tolerances of the technological processes for realizing the segmented structure. We shall assume, that their effects can be taken into account by calibration at cost however of approximately doubling the total accidental error in determining the chemically induced refractive index change.

The resolution  $\delta n$  of the sensor can be calculated from:

$$S(\Delta n)\delta n = (q_1 + q_2)P_{out} / P_{in} \quad (2-11)$$

Inserting expression (2) and (4) in (5) leads to:

$$\delta n = \frac{5}{\ln(10)} \frac{(q_1 + q_2)}{A\Delta n L_{sens}} \quad (2-12)$$

In evaluating (2-12) we have to realize, that the advantageous increase of  $\Delta n$  and/or  $L_{sens}$  also implies a decrease of  $P_{out}$ . So the lower limit of the dynamic range,  $P_{min}$  restricts the allowed  $\Delta n$ -  $L_{sens}$  combinations. We can conclude that the best resolution will be obtained if  $P_{out} = P_{min}$ . From this condition, the optimal value of  $L_{sens}$  for given  $\Delta n$  can be calculated to be:

$$L_{\max} = \frac{10 \log(P_{in} / P_{\min})}{A \Delta n_{\max}^2 + B} \quad (2-13)$$

where  $\Delta n_{\max}$  is the highest value of  $\Delta n$  for which the  $P_{out} \geq P_{\min}$ .

Substituting (2-13) into (2-12) gives:

$$\delta n = \frac{1}{\ln 10} \frac{q_1 + q_2}{\log(P_{in} / P_{\min})} \frac{A \Delta n_{\max}^2 + B}{2 \Delta n A} \quad (2-14)$$

The first factor expresses quantitatively the influence of the peripheral equipment:  $q_1$  and  $q_2$  have to be as small as possible, as could be expected and the input power as large as possible. The second factor expresses the influence of the segmented structure; its minimum value, as a function of both  $\Delta n$  and  $\Delta n_{\max}$ , is obtained if  $\Delta n = \Delta n_{\max}$  and  $\Delta n_{\max} = \sqrt{B/A}$ .

Hence the best resolution that can be obtained is equal to

$$\delta n = \frac{1}{\ln 10} \frac{q_1 + q_2}{\log(P_{in} / P_{\min})} \sqrt{B/A} \quad (2-15)$$

Note that to obtain this resolution, the length of the segmented structures should be:

$$L_{sens} = \frac{10 \log(P_{in} / P_{\min})}{2B} \quad (2-16)$$

Relation (2-15) clearly shows, that the sensitivity factor  $A$ , defined by the parameters of the segmented structure, has to be as large as possible while the scatter and absorption losses have to be as small as possible. Also it can be concluded from relation (2-15) that application of a reference branch in order to reduce the effects of the fluctuations of  $P_{in}$  is meaningful only if  $q_2 < q_1$ .

Expression (2-15) presents the best resolution, which is obtained at  $P_{out} = P_{\min}$ . If a certain minimum threshold concentration of a specific measurand needs to be measured, then the highest resolution is obtained if  $\Delta n(c=0)$  is equal to  $\Delta n_{\max}$ . Usually  $\Delta n$  values have to be measured over a certain range. Lower  $\Delta n$  values correspond to higher  $P_{out}$  values and as a consequence they will be measured with worse resolution. Assuming that the lowest  $\Delta n$  value to be measured corresponds with  $\Delta n_1$ , the worst resolution over the given range  $\Delta n_1$  to  $\Delta n_{\max}$  will be:

$$\delta n_{worst} = \frac{1}{\ln 10} \frac{q_1 + q_2}{\log(P_{in} / P_{min})} \frac{A \Delta n_{max}^2 + B}{2 \Delta n_1 A} = \frac{1}{\ln 10} \frac{q_1 + q_2}{\log(P_{in} / P_{min})} \frac{B}{A} \frac{1}{\Delta n_1} \quad (2-17)$$

Note however that generally in measuring low concentrations the  $\Delta n$  changes are small; hence the worst resolution will not differ much from the best one.

Finally, up until now it was assumed that the refractive index of the cladding layer ( $n_0$ ) can be tuned with an arbitrarily good accuracy. This is unfortunately not the case and this will limit the resolution of the sensor system. If the index of the cladding has an inaccuracy of  $\Delta n_{acc}$ , then this can be interpreted as if the  $\Delta n$  is located in an uncertainty domain  $[-\Delta n_{acc}, +\Delta n_{acc}]$ . The worst case resolution is then given by expression (2-17) with  $\Delta n_1 = 2 \cdot \Delta n_{acc}$ .

Anticipating on the design, available technology and peripheral equipment ( $q_1 + q_2 = 0.001$ ,  $B = 10^2$ ,  $A = 2 \cdot 10^7$ ,  $P_{in} / P_{min} = 1000$ ) we can estimate using expression (2-15) that a resolution of  $\delta n = 3 \cdot 10^{-7}$  should be possible.

The optimal sensor length, giving the highest resolution has to be practically realizable. Because straight channels generally are limited to lengths of around 5 cm, longer channels can be realized only by constructing them as spirals.

## 2.4 The design

In this section the design of the SWS will be treated. Firstly the design objectives and some initial conditions will be given (sections 2.4.1 and 2.4.2). Some classification of segmented structures will be treated in section 2.4.3. After that (in the sections 2.4.4.1 – 2.4.1.11) an analysis of a specific class of the segmented waveguide sensor will be given. In this sensor class the sensing section consists of two types of segments with identical geometry but differing in the chemical constitution of the cladding material, being either a sensitive material or a passive one. Here the accumulated knowledge and experience obtained from preliminary designed and realized sensing systems are utilized. For several sets of relevant design parameters the  $A$ - values, representing the sensitivity of the SWS, will be calculated using both BEP and SDM. The dependencies of  $A$  on some of the sensor parameters will be explained qualitatively. Section 2.4 ends with presenting the final design (channel structures and the lay outs) of several sensing systems which will be realized and characterized later on.

### 2.4.1 Design objectives

The SWS treated in this chapter is a bulk type integrated optical sensor. The value of a measurand is translated by an optical transduction layer into a value of the refractive index of that transduction layer. Naturally we would like the sensor to be as sensitive to the specific measurand as possible. Since here we focus on the design of an optical sensing platform, rather than a specific sensor, we would like that this platform shows a refractive index resolution as high as possible. Also compactness of the IO structure is desired. A strong point of the SWS is that the technology for the realization is expected to be relatively simple in comparison with that of other integrated optical sensors. To exploit this strong point low cost has been defined as another design objective.

Primary design objectives:

- High resolution
- Low cost

In section 2.3 it was derived (expression (2-15)) that to obtain optimum resolution the sensitivity  $A$  of the segmented waveguide region need to be maximized and the propagation loss  $B$  needs to be minimized. Further it was implicitly assumed in chapter 2.3 that the only losses in the system were the propagation losses and the functional losses of the segmented section. However there are additional losses in the system, caused by the incorporation of other functions into the IO circuitry such as fiber-to chip coupling functions, bends and splitters. These losses will also limit the quotient  $P_{in}/P_{min}$  as mentioned in expression (2-15) and part of the generated scatter light may reach the output fiber. The functional losses of these components need to be minimized by an appropriate design and this will limit the freedom of design of the segmented sensing section.

Another aspect that influences the attainable resolution is the noise generated in the system. The noise is caused by fluctuations in the output power of the light source, fluctuations in the polarization of the light source, changes in temperature, temperature gradients on the chip, shot noise, temperature dependence of the dark current of the detector, amplifier noise, etc. This noise needs to be minimized.

Secondary design objectives to achieve high resolution:

- High sensitivity of the segmented waveguide region ( $A$ )
- Low channel propagation losses ( $B$ )
- Low functional losses of other components
- Low sensitivity to disturbances
- Good control of technology in order to really produce the designed systems

To achieve low cost it is necessary that the individual steps of the fabrication process are simple and reproducible and that the sensor system is tolerant to fabrication errors. Further the peripheral equipment like light source, fiber-to chip coupling and optical detection system have to be cheap.

Secondary design objectives to achieve low cost:

- Simple fabrication process
- Compactness of the IO circuitry
- High tolerance to fabrication errors
- Cheap peripheral equipment

Conflicts arising from trying to obey both the cost objectives and the performance objectives are expected. Sometimes this will lead to some compromise but also more often, since this project is performed in a scientific light, priority is given to the performance objectives.

## 2.4.2 Boundary conditions

1. The most important boundary condition is set by the prerequisite that the SiON technology as available in the clean room laboratory of the MESA<sup>+</sup> institute should be applied. So the material class has been defined in advance and the tolerances related to already developed technologies had to be a starting point. For example: the best accuracy with which the refractive index of the top cladding can be controlled is 0.0005, the smallest dimension of lateral structures that can be realized is 2  $\mu\text{m}$ . There is a multitude of such boundary conditions and they will be mentioned there where needed. However if relevant to the development of the sensors, new technological steps could be developed or existing steps improved.
2. The available peripheral equipment is another limiting factor. It determines e.g. the  $P_{in}$ ,  $P_{min}$ ,  $P_{out}$  and the available wavelengths.
3. In case of analyzing chemical concentrations in solutions a well controlled transport of liquid samples to the sensing section is required. A simple micro fluidics system has to be integrated on the IO chip.

4. The optical transduction layer needs to be applied in the last technological step in order to avoid that its performance will be degraded by following processing steps.

### 2.4.3 Classification of SW structures

The SWS principle can be applied in any kind of segmentation where the mode profiles of the different types of segments respond differently to  $\Delta n$ . Even the smallest difference in refractive index distribution of both types of segments lets the system function as an SWS. However we are interested in the kind of segmentation that meets the design objectives mostly and that satisfies all boundary conditions. The many kinds of segmentation, one can imagine can be divided into three classes:

1. The different types of segments have an identical geometry, but they are different with respect to materials chosen. For example one segment type contains the active sensing material, while in the other segment type the corresponding volume is taken in by a passive material (e.g. a SiON material). The refractive index of the latter controls the state in which the transmission is at maximum. An example of such a segmentation is given in Figure 2.3. This type of segmentation generally is highly tolerant to fabrication errors in waveguide geometry, but its tolerance to the value of the refractive index of the passive material is low.
2. The different types of segments have a different geometry, but identical materials are used for corresponding parts of the segments. Hence both segment types contain the sensitive material e.g. as a cladding material. As a result of the different geometry the mode profiles of both segments will respond differently to a change of the refractive index of the sensitive material. The state of maximum transmission is mainly defined by the waveguide geometry. This type of segmentation generally is highly tolerant to fabrication errors in the value of the refractive indices, but its tolerance to the waveguide geometry is low.
3. The different types of segments show both a different geometry and a difference in their materials constitution.

Each of this trio of classes can be subdivided in several groups depending on the specific nature of the differences in geometry or refractive index.

From a preliminary theoretical exploration of many of these segmented structures at least three types of segmentation types have been defined which were estimated to deserve further analysis and possibly even realization (Section 2.7). However this does not exclude that in other classes or groups also relevant structures may be found. Here it has to be noted that, due to a lack of useful 3D simulation methods, segmented structures of which the dimensions of the segments differ in all directions, the transversal, the lateral and the longitudinal ones, either invariant or not invariant along the propagation direction, could not be analyzed well and are not considered.

Out of these three types of segmentation we shall mainly pay attention to the one which belongs to class 1 and of which segments differ only in the cladding material being either sensitive or not. Analysis, realization and characterization of this type of segmented structure will be described in section 2.4.4.

### 2.4.4 Optimization class 1 SWS

The principal structure of the segmented sensing component is given in Figure 2.9.

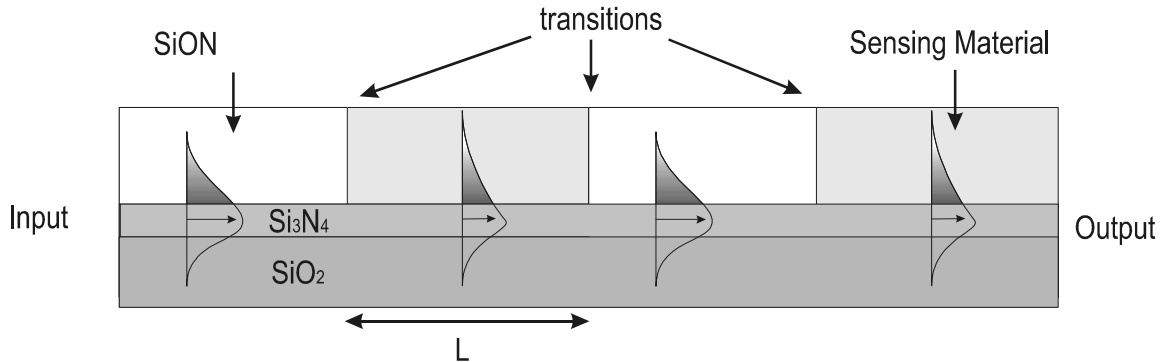


Figure 2.9. Longitudinal cross-section of the sensor (4 segments).

Optimization of the SW sensing section to high sensitivity and resolution implies (see expression (2-15)) a maximization of the parameter  $A$ , and a minimization of the parameter  $B$ . For this optimization many parameters have to be taken into account: the nature of the waveguide materials (defined by their refractive indices  $n_i$ ), the cross-sectional geometry of the segments (defined by the thickness of the layers, the width  $W$  and the ridge height  $h_r$  of the waveguiding channel) and the length of the segments. Also the wavelength (distribution) of the launched light is at choice. However not only the requirements on the segmented structure itself are relevant, but also requirements arising from an efficient functioning of other IO components in the system. The freedom of choice will also be limited by the desire to arrive at a compact system and at relatively cheap technology.

Two simple layouts of the complete IO system are given in figure 2.10 and figure 2.11.

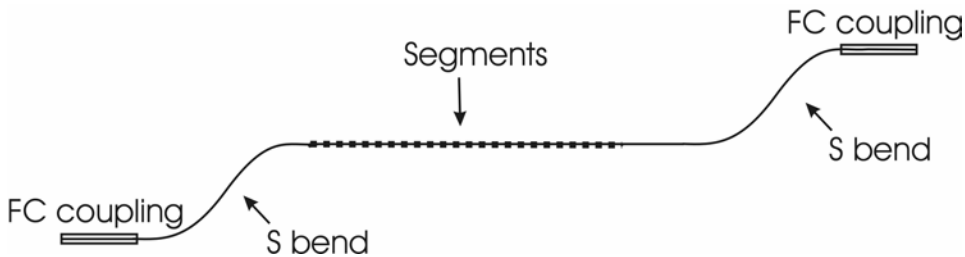
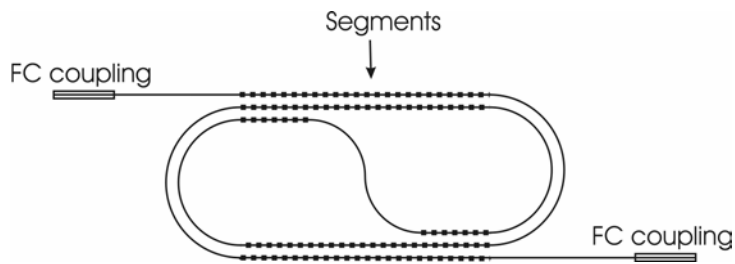


figure 2.10. Layout of an SWS: a straight SW section with S-bends.



**figure 2.11. Layout of an SWS: a spiral configuration.**

The first system contains a linear segmented waveguide, but for decreasing the amount of stray light at the output S-bends have been introduced. In the second system the segmented section is folded like a spiral for lowering the needed chip area. The introduction of bends however creates other boundary conditions: because a low  $B$  value is required the waveguiding channels have to be structured in such a way that the bend losses should be low. Fiber to chip coupling sections needed for an efficient transfer of the light to and from the chip are also indicated.

We now discuss various aspects for arriving at a system close to the optimal one. In this discussion we have confined ourselves to transversally monomodal channel waveguides of the ridge type and to segments which are invariant along the propagation direction.

#### **2.4.4.1 The wavelength**

The dimensions of all optical components on the chip with the same functionality scale approximately linearly with the wavelength. In order to minimize the dimensions of the optical chip and to minimize the required thickness of the layer stack needed for optical confinement, the wavelength should be as small as possible. Note however that absolute technological tolerances will get relatively larger for smaller wavelengths. Scatter losses, mainly due to roughness of the interfaces of the different optical layers, also increase strongly with smaller wavelengths. At 850 nm wavelength there are cheap commercial VCSELs (Vertical Cavity Surface Emitting Laser) available. At 632.8 however the characterization of the sensor is easier, because this wavelength is in the visible domain. Designs have been made for both wavelengths.

#### **2.4.4.2 The layer structure**

A high refractive index of the core layer affords for a high sensitivity of both  $N_{eff}$  and the modal field profile to changes of the refractive index of the cladding material [9]. Hence, taking into account the boundary condition of using SiON technology, the core layer will consist of  $\text{Si}_3\text{N}_4$ . There are several reasons to choose for the buffer layer, the layer in between the core layer and the Si wafer, the material with the lowest refractive index available. Firstly, at the lowest index the fraction of power propagating through this layer is minimal, promoting a larger power fraction in the cladding layer, which will increase

more, the larger the difference,  $n_{cl}-n_{buffer}$ , between the index of the cladding and buffer layer. Secondly, leakage of light into the Si wafer can be reduced to below a preset limit using a thinner buffer layer. Thirdly, for the realization of such a layer a simple and very well controlled technology is available: thermal oxidation of the Si wafer, leading to  $n_{SiO_2} = 1.452$  at  $\lambda = 850$  nm. The refractive index of the passive cladding layer is completely defined by the refractive index range of the sensitive material and the intended working point. If the application should allow for that, it is advantageous to take the refractive index of the cladding layer much larger than that of the buffer layer, in that way offering an appreciable enlargement of the power fraction propagating through the cladding layer and hence of the sensitivity. Anticipating on later sections the cladding refractive index will be taken 1.50 or 1.52.

#### **2.4.4.3 Monomodality, polarization and the thicknesses of the layers**

For simplicity and on base of some preliminary simulations on multimodal waveguides we have chosen to limit ourselves to monomodal waveguides. The performance of the sensor depends on the polarization of the guided mode. The operation of the sensor should be independent of the polarization of the light at the input. Therefore (assuming in first instance infinitely thick outer layers) a waveguide in which the  $TE_{00}$  mode will be used and where no TM modi can be guided is designed. For this purpose the thickness of the core layer has to be chosen between 80 nm (cut-off thickness  $TM_{00}$  mode) and 44 nm (cut-off thickness  $TE_{00}$  mode). A buffer layer thickness of 2.5  $\mu\text{m}$  is sufficient to reduce propagation losses due to leakage of light into the Si-wafer to below 0.01 dB/cm for all the considered core layer thicknesses. Similarly also the cladding layer has to have such a thickness, that also at the cladding side the modal field is well confined within the layer stack. In that way the modal field in the passive segments will be insensitive to changes in the environment and in addition one gets rid of scattering caused by the roughness of the upper surface. Limiting the thickness of the entire layer stack to a technologically acceptable (related to tension in the layers and fabrication time) value of 5  $\mu\text{m}$ , this confinement asks for a core layer thickness of 60 nm at minimum.

#### **2.4.4.4 Losses**

All losses not arising from the segmentation itself have to be as low as possible in order to minimize the parameter  $B$ . Propagation losses are mostly a matter of technology, although at a given technology the losses also can be influenced somewhat by the specific nature of the channel structures. The propagation loss of previously fabricated waveguides of the kind which we will apply in this type of SWS structure was measured to be  $0.5 \pm 0.3$  dB/cm. They are attributed to scattering. Propagation losses can be somewhat different for each batch of sensors, but for now this value will be used in the design.

Also functional losses arising from other components in the system have to be as small as possible. These functional losses can be due to imperfect fiber to chip coupling, bends

(bend losses) and if applied also to Y- junctions. Not only do these losses lower the output power, but also because they generate scatter light, some part of this scatter light may be captured by the output fiber, thus degrading the performance of the sensor.

### 2.4.4.5 Bends

In both systems, presented in figure 2.10 and figure 2.11, bends have been applied. In order to increase compactness, small bending radii with acceptable bending losses ( $<0.1$  dB/cm) are desired. At given bending radius the bending losses become smaller with increasing lateral refractive index contrast. The lateral contract is the highest at a rib type waveguide channel, but technological limitations require a remaining thickness of the slab adjacent to the channel of about 5 nm. Bend loss calculations for a structure having a channel height of 60 nm, a channel width of 7  $\mu\text{m}$  and a ridge height of 55 nm (the final design) have been performed, using the c2v bend solver [3] to determine the minimum acceptable bending radius of the designed channel structure. The results are shown in Figure 2.12.

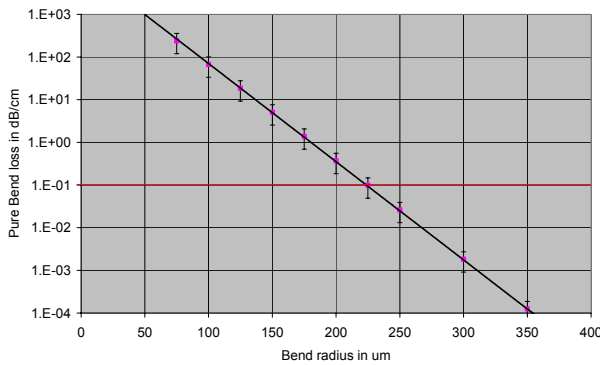


**Figure 2.12. Bend loss calculations.**

From Figure 2.12 it can be concluded that a minimum bending radius of 300  $\mu\text{m}$  is acceptable. Note that at the transition between a bend and a straight waveguide there are losses due to the difference in mode profile of the guided modes. By shifting the position of the centers of both waveguides relative to each other this type of transition loss can be reduced. By a tiny reduction of the width of the straight waveguide, the matching of the modal fields at the transition can be improved even more and calculations show that in this way this type of transition losses can be made negligible. Both methods have been applied.

### 2.4.4.6 Fiber to chip coupling

For having an efficient fiber to chip coupling, the modal fields of the single mode input fiber (mode field diameter 4.6  $\mu\text{m}$  for  $\lambda=632.8$  nm and 6.0  $\mu\text{m}$  for  $\lambda=850$  nm) and the channel waveguide have to be as similar as possible (large overlap integral). Using structures as given above, the optimum values of the overlap integral are found at a

channel width around 7  $\mu\text{m}$ . Such a waveguide channel does not guide TM polarized modes. However the waveguide is multimodal in the lateral direction. Overlap integral calculations show that the power coupled from the fiber to the higher order modes is negligible even when taking into account the small practical deviations from optimal fiber alignment. In fact using a lateral taper the width of the channel can be gradually reduced from 7  $\mu\text{m}$  at the input to the desired value at the sensing section, however at cost of increasing the sensor length. We did not apply these tapers. A multi mode output fiber was used to collect maximally the output power of the guided mode, at the cost of also capturing more stray light. For having a rigid connection between fiber and optical chip the fibers will be mounted into V-grooves made in the Si-wafer [10].

#### 2.4.4.7 Y-junction

In later sections it will appear that under certain conditions it is useful to introduce into the IO system also a 3dB Y-junction splitter. We now already discuss its design. In such a 3 dB Y-splitter one waveguide has to be split into two waveguides, which both are tilted under an angle  $\pm\beta$ . If  $\beta$  is too large, the splitter is not adiabatic and functional losses can be appreciable. If  $\beta$  is too small, the splitter takes up too much space on the chip. The optimum  $\beta$  (functional loss =0.1 dB) has been designed to be  $0.23^\circ$ . With this angle both channels will be separated 10  $\mu\text{m}$  after about 1 mm. Notice that due to the limited resolution of the lithographical process there will always be a blunt separation between the channels and the splitter will never be really adiabatic.

#### 2.4.4.8 SW sensing section

In fact, as a result of the previous discussion, nearly all parameters have been defined. Remaining parameters to discuss are the precise height of the core ( $h$ ) within the range 50-80 nm and the segmentation. Both have to be chosen in such a way that the parameter  $A$  is maximized. There are several aspects that determine the value of  $A$ :

1. Related to the overlap of field profiles of the guided modes at both sides of a transition:
  - The amount of light that is coupled into radiation modes at one transition ( $h$ )
  - The angular distribution of the light coupled into radiation modes ( $h$ )
2. Related to back coupling of radiation modes at transitions:
  - The amount of light in radiation modes that is coupled back into the guided mode at the next transition ( $h$ , segmentation)
  - The phase of the light in radiation modes that is coupled back into the guided mode at the next transition ( $h$ , segmentation)
3. Related to the total length of the sensor  $L_{\text{sensor}}$ 
  - The amount of transitions

The aspects of group 1 are mostly determined by the value of  $h$ , the other ones mainly by the segmentation but also somewhat by  $h$ .

We can describe the influence of the segmentation as follows: usually part of the light coupled into radiation modes will couple back into the guided mode at the next transition. The phase difference between the guided mode beam passing the transition and the guided mode which is generated by back coupling from the radiation modes depends on both the segment length and the angular distribution of the radiation modes. As extremes there can be completely constructive or completely destructive interference. The longer the segment length, the larger the phase difference, but also (as a result of the divergence of the radiated light) the smaller the fraction of the radiative power that can couple back; however a longer segment length also implies a smaller number of transitions per unit length of the segmented structure. Hence it is expected that there is one specific segment length which is optimal. If each segment has this length, the SWS will function with optimum sensitivity. So in fact we arrive at a periodic structure, a grating, as being optimal. We have to realize however, that periodicity is not a requirement for the operation of the sensor. In non-periodic structures or when using a very broad band light source, there will be a more random distribution of the phase differences but nevertheless the SW sensor will still function. The same holds in case of high attenuation of the radiation modes. In such types of structures the sensitivity of the sensor is reduced with a factor 2 at maximum in comparison with a (hypothetical) system with complete de-constructive interference of all radiation power. In this project we have confined ourselves to periodic distributions to demonstrate optimum sensitivity. Note that such grating structures also will reflect a part of the guided mode power at those values of the refractive index of the sensitive material at which the so-called resonance condition is obeyed. We have calculated that, in all structures we have investigated, these higher order Bragg reflections can be neglected (reflected power is less than 0.1% of the launched power).

The easiest way to optimize this type of segmented structure is to calculate the  $A$  value (using the BEP) for different values of  $h$  and  $L$  and to look for the maximum  $A$  value. This has been done and the results are given in Figure 2.13. More detailed calculations also showed that, for the type of waveguides we have investigated here, the value of  $A$  is nearly independent on the waveguide width and the ridge height; this justifies our decision to use these parameters to optimize the other IO-functions needed for the complete sensing system, i.e. the bends and the fiber to chip coupling units. This indeed leaves the exact thickness of the core layer ( $h$ ) and the segmentation length ( $L$ ) as the two most important parameters to optimize  $A$ .

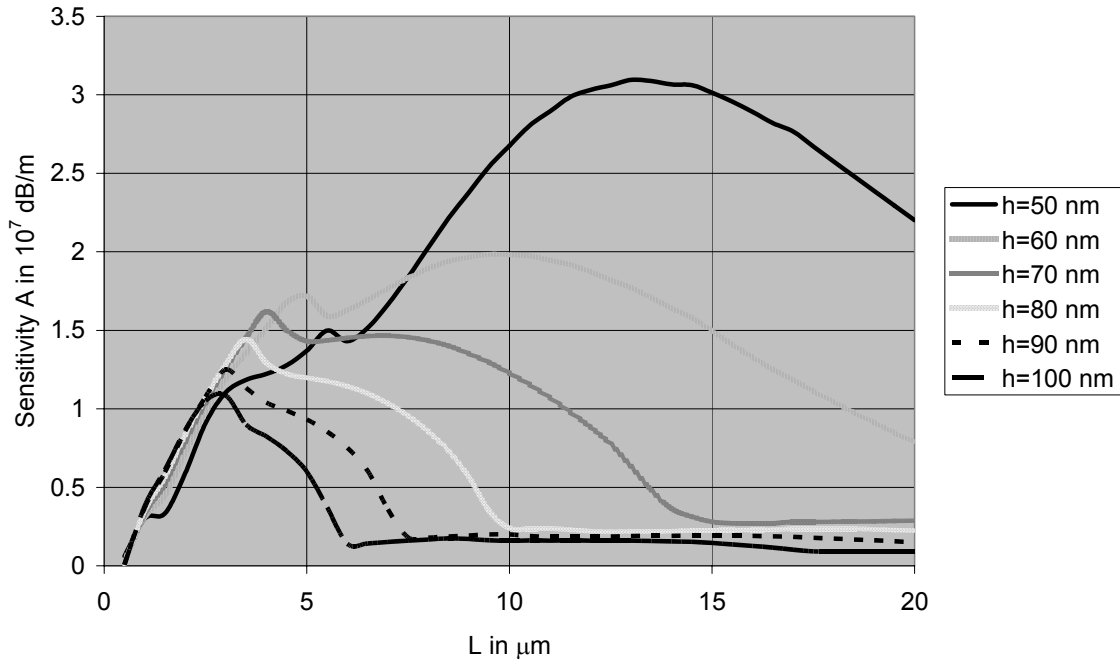


**Figure 2.13. Comparison sensitivity SW sensors with different core thickness.**

The curves clearly show that the thinner the core layer the larger the  $A$  value. This is related to the larger power fraction in the cladding, which causes a larger difference between the field profiles of both types of segments for a given  $\Delta n$ .

Also the angular distribution of the radiation is a function of the core height. Therefore each characteristic is different for different values of  $h$ . The interplay between the effects of “as many transitions as possible” and “deconstructive interference of radiation modes and guided mode at the transitions” leads to the optimal segment length being different for different core thicknesses. From Figure 2.13 it follows that the optimum value for  $h$  that still obeys the boundary conditions is 60 nm. The corresponding optimum value for  $L$  is found to be 10  $\mu\text{m}$ .

For explaining other features of these graphs we have to rely on the SDM method, which indeed will appear to enable to get more physical insight in the phenomena. For this purpose we consider how, using the SDM, the power that for a given length is lost to the radiation modes can be maximized. For this we apply expression (2-1). We start from an SWS structure as shown in Figure 2.1 and we insert all the parameters of the designed SW section as given in Table 2.2 and we look how to manipulate with the two remaining unknown parameters: the core thickness ( $h_{\text{core}}$ ) and the segment length  $L$  in order to obtain maximum sensitivity. Because the function  $G$  is nearly independent from  $h_{\text{core}}$  and the  $H$  function is independent on  $L$ , both functions can be tailored independently to maximize expression (2-1). In Figure 2.14  $H$  as a function of the effective index of the radiation modes is depicted for various values of the core thickness. In Figure 2.15  $G$  as a

function of the effective index of the radiation modes has been presented for various values of  $L$ .

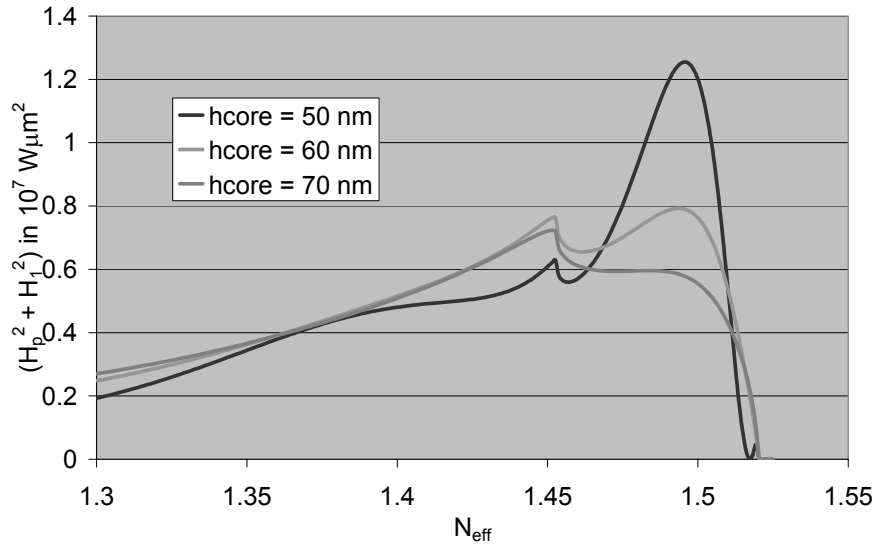


Figure 2.14.  $H$  as a function of  $N_{eff}$  for different values of core thickness.

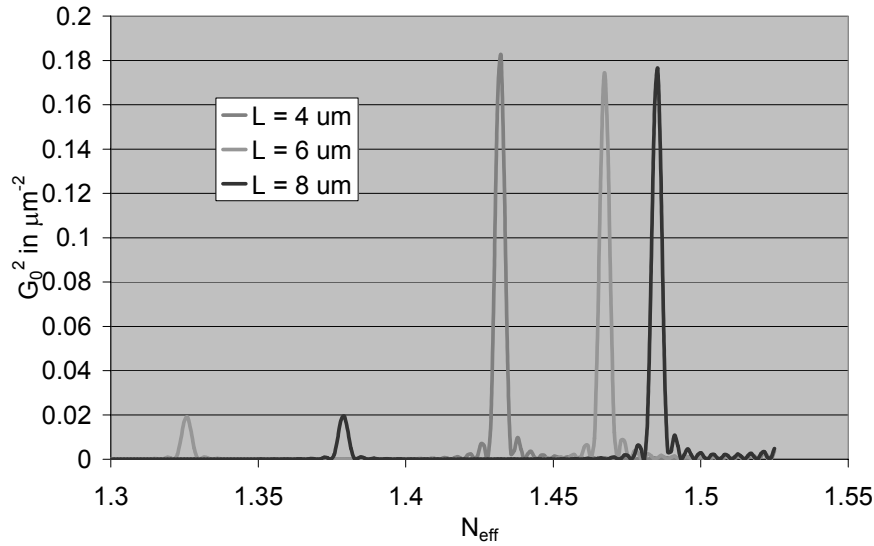


Figure 2.15.  $G$  as a function of  $N_{eff}$  for different values of  $L$ .

In Figure 2.14 it can be seen that the maximum value of  $H$  is a function of  $h_{core}$ . As can be seen in Figure 2.15, the position of the maximum of  $G$  is a function of  $L$ . If we now choose such a value of  $L$  that the  $G$ -maximum occurs at that value of  $N_{eff}$ , where also the  $H$ -function is at maximum (hence choosing that value of  $h_{core}$  that yields the highest peak) of  $H$ , then the integral given in expression (2-1) is (close to) maximum. We arrive at exactly the same optimized SW structure as the BEP presented:  $h = 60$  nm and  $L = 10$   $\mu$ m.

The SDM offers more than an optimization; it also enables to explain most features of Figure 2.13. From comparing Figure 2.14 with Figure 2.13, it can be concluded that the origin of the two local maxima in fig 2.14 is in the  $H$ -function. So the angular distribution of the light coupled into radiation modes at one transition is at the basis of these two maxima and not the interference between non guided light generated at different transitions. It can also be concluded that for small  $L$ -values ( $G$ -is at maximum at small  $N_{eff}$  values) the  $A$ -values reduce almost to 0; this is because the  $H$ -value is decreasing for smaller  $N_{eff}$  values. Also for some specific high  $L$ -values there is a sudden drop in  $A$ . This can be explained by the fact that  $H=0$  for  $N_{eff} > n_{clad}$ . So for values of  $L$  where the peak is located at  $N_{eff} > n_{clad}$  we expect the  $A$ -value to be nearly 0 dB/m.

The only parameter left to define is the optimum length of the segmented section,  $L_{sensor}$ . This length can be calculated using expression (2-16). Entering representative values for  $q_1+q_2$  ( $=0.002$ ) and  $B$  ( $=100$  dB/m) yields an optimum length of 15 cm. So indeed a spiral shaped segmented section will be necessary. Using expression (2-15) the resolution of this SW sensor is calculated to be  $\delta n = 6.10^{-7}$ .

#### 2.4.4.9 Perturbing factors

Up to now we have considered the resolution taking into account the power fluctuations of the light source and the noise of the detector system only. In expression (2-15) they are represented by the  $(q_1+q_2)$  factor. In practice there are in the complete sensing system more disturbing factors which are threatening to degrade the resolution. They are given in Figure 2.16 and related with the site where they are interfering with the primary sensing action.

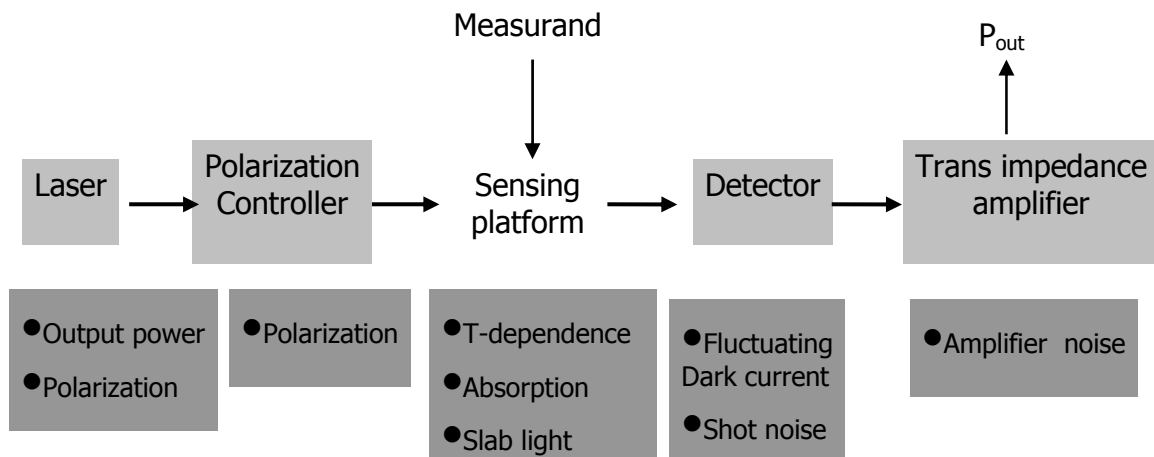


Figure 2.16. A simple optical detection system, with identified noise sources

- The output power and the polarization state of the laser fluctuate; this disturbance is represented by the  $q_1$  factor.

- In spite of the insertion of a polarization controller in the fiber the polarization at the input of the sensing platform will fluctuate. This is caused by the mechanical relaxation and the temperature depended behavior of the input fiber. Because the waveguide channel only guides modes of TE polarization, such a fluctuation in polarization manifests itself as an additional fluctuation in output power at the optical detector.
- The performance of all optical components on the sensing platform is somewhat temperature dependent.
- The stray light generated at various functions and mainly propagating as slab modes can couple back partly into the output waveguide. This might be especially disturbing, because in this SW sensing system, the output power of the guided mode may be several orders of magnitude smaller than the power of the generated slab light.
- It is not excluded, that not only the real refractive index of the transduction material changes with time or temperature, but also its absorption coefficient.
- The dark current of the optical detector varies with temperature. Of course shot noise is always present.
- The amplifier adds noise.

There are various ways to decrease (the effects) of these noise sources:

- The influence of fluctuations of the input power can be strongly reduced by introducing a reference branch. This can be accomplished by inserting after the input section a Y-junction, which divides the power over the sensing branch and the reference branch. Effects of the fluctuations in input power are suppressed if the ratio of the output powers of both channels is measured.
- Temperature dependent dark current can be compensated for by using matched detectors for measuring both output powers.
- The amplifier noise can be reduced by integrating a pre-amplifier with the detectors.
- Both options, matched detectors and the aforementioned integration, are provided by the 'Nirvana auto-balanced receiver' which we shall apply for this type of measurements. The receiver also contains processing electronics which deliver directly the ratio of the optical power falling on both detectors.
- For reducing fluctuations in temperature, the system can be thermostated, but this will increase the costs of the total system.
- By replacing the reference channel by an identical sensor, which is subjected to a controlled environment, the influence of various disturbances can be reduced simultaneously; amongst them the temperature dependence of the optical components and the time and temperature dependence of the absorption of the transduction material
- To reduce the disturbing effects of the slab light, S-bends have been implemented into the waveguide channel before and after the sensing section (Figure 2.20). Also the in and output channels on the chip are never in one line. Black tape is attached above the waveguide channels to absorb the slab light.

After all these improvements as proposed above have been implemented, the optical detection system will look as illustrated in Figure 2.21. Leaving the temperature gradient on the chip and shot noise as the main sources of noise. The level of reduction of effects is difficult to be predicted theoretically. Experiments on real sensing systems are needed for that.

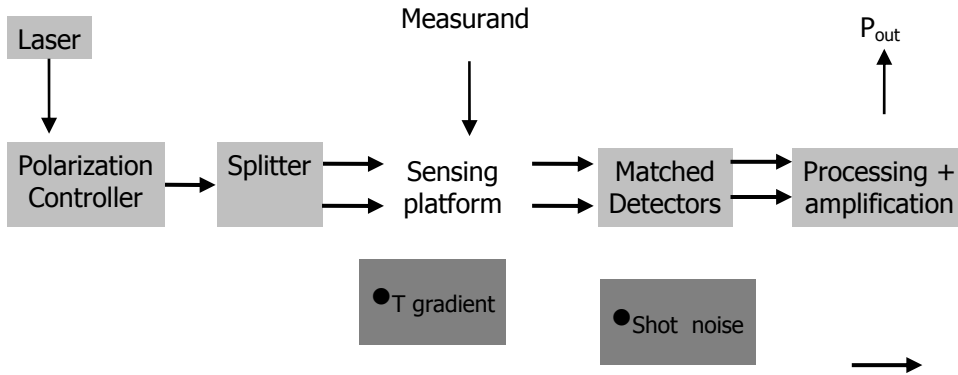
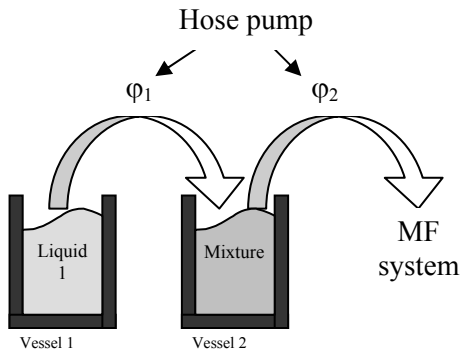


Figure 2.17. An advanced optical detection system.

#### 2.4.4.10 Miscellaneous aspects related to the sensor characterization

For verification of the predicted performance of the sensing systems and for determining the performance aspects, that could not be predicted theoretically some sensing systems have to be produced and their performance has to be determined. Essentially this implies the determination of the  $P_{out}/P_{in}$  ratio of the sensor as a function of the refractive index of the sensitive material. Best characterization will be obtained if this refractive index could be varied continuously in a very well controlled way. The best option to do this is by transporting a liquid to the sensing section of which the constitution can be varied continuously.

For having such a liquid with continuously varying index available we developed a system as shown in Figure 2.18, in which two liquid chemical compounds can be mixed in a very controlled way. We derived a formula for the refractive index of the output liquid as a function of time and verified this formula experimentally (Figure 2.19).



**Figure 2.18. Liquid mixing system.**

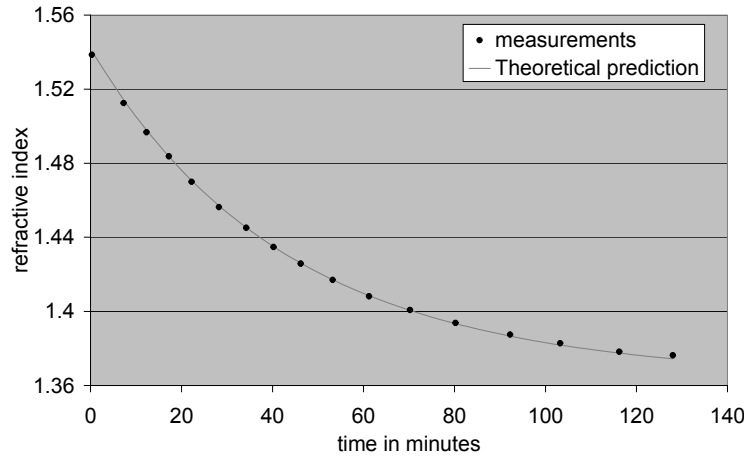


**Figure 2.19. Refractive index control using the mixing system of Figure 2.18.**

Details of the system, the derivation of the formula and the experimental verification of this formula are given in Appendix C.

The liquid has to be fed to the sensing section in a well controlled way, avoiding any influence of dead volumes. For this accurate control a micro fluidics (MF) system is necessary. The main advantages of the use of such a micro-fluidics system over a bulk cuvette are the absence of dead volumes and the very small amounts of sample liquid which are necessary. The MF channels will be defined in thin glass plate, followed by gluing of this MF chip on top of the IO-chip. Details of this MF system are given in Appendix D.

In principle mixtures of many liquids can be chosen. However we intended to use the originally fabricated sensor for measuring relative humidity (RH) using gelatin and polysiloxane. The refractive index of the gelatin interface layer varies from 1.545 to 1.49 in the 0-100% R.H range. The refractive index of the polysiloxane used [10] varies in the same RH range from 1.50 to 1.45. The refractive index of the cladding material was chosen 1.52 for the gelatin interface and 1.50 for the polysiloxane interface. To characterize SWS sensors with such a high cladding index, the well mixable couple of liquids ethanol ( $n = 1.3612$  at  $20\text{ }^{\circ}\text{C}$ ) and benzyl alcohol ( $n = 1.5424$  at  $20\text{ }^{\circ}\text{C}$ ) has been chosen. The refractive index and thickness changes of gelatin as a function of the RH have been carefully analyzed using ellipsometry (see Appendix E). The mixing properties of both fluids have been treated in detail in Appendix C.

### 2.4.4.11 The final designs

We have designed two types of sensing systems. One was designed for 850 nm wavelength with a relatively short length of the segmented structure (5 mm), called type one. This type was designed in order to demonstrate the principle itself (see figure 2.10). The second type (type two) was designed for a wavelength of 632.8 nm (visible light, thus easier for the characterization) and had much longer (up to 30 cm!) spiral shaped segmented structures (see figure 2.11). The sensors of type two were designed for demonstrating the high resolution that can be obtained. Note however that on each wafer many sensing structures with identical channel cross sections have been produced, but differing in the lay out, different segment period  $L$ , different sensor length  $L_{sensor}$ , with or without reference branches etc.. Also a multitude of test structures such as straight waveguides and bends have been implemented on each wafer. We shall report on some representative examples of these sensors only.

The cross sectional parameters of both types of structures are given in Table 2.2. The layout of a spiral SWS with a simple reference channel is depicted in Figure 2.20. In Figure 2.21 the layout of the most complicated SWS with integrated reference sensor is shown. Also the geometry of the micro fluidic system is depicted.

**Table 2.2. Designs of both SWS's.**

Parameter/Property	Designed value type 1	Designed value type 2
Wavelength	850 nm	632.8
Buffer layer index	1.453	1.458
Core layer index	1.99	1.99
Cladding layer index	1.52 (1.50)	1.473
Buffer layer thickness	>2.5 $\mu\text{m}$	> 2 $\mu\text{m}$
Cladding layer thickness	2.0 $\mu\text{m}$	2.0 $\mu\text{m}$
Waveguide width	7.0 $\mu\text{m}$	2.0 $\mu\text{m}$
Core thickness	60 nm	30 nm
slab height	$\approx$ 5 nm	$\approx$ 5 nm
segment length	Range 3-15 $\mu\text{m}$	8.4 $\mu\text{m}$
$L_{sensor}$	5 mm	Range 37-559 mm
A-value	$2 \cdot 10^7$ dB/m	$6 \cdot 10^7$ dB/m

Note that the A-value for the type 2 sensor is about three times larger than the A-value of the type 1 sensor. This means that at identical values of the propagation losses the best attainable resolution of this sensor could in principle be better (see expression (2-15)). This larger A-value might be partly due to the smaller wavelength.

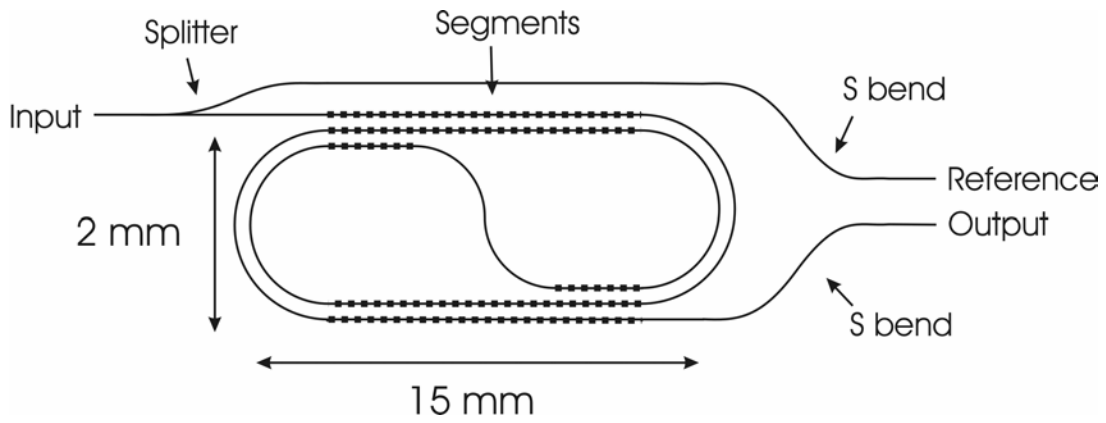


**Figure 2.20. Layout of an SWS with a simple reference channel.**

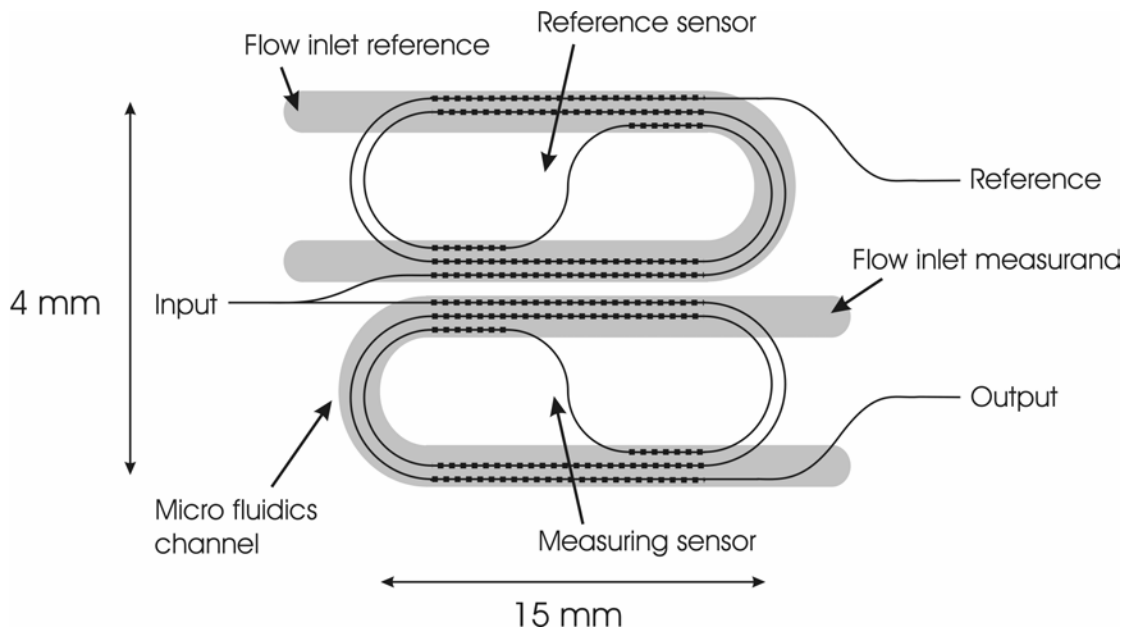


**Figure 2.21. Layout of an SWS with a reference sensor and micro fluidic system.**

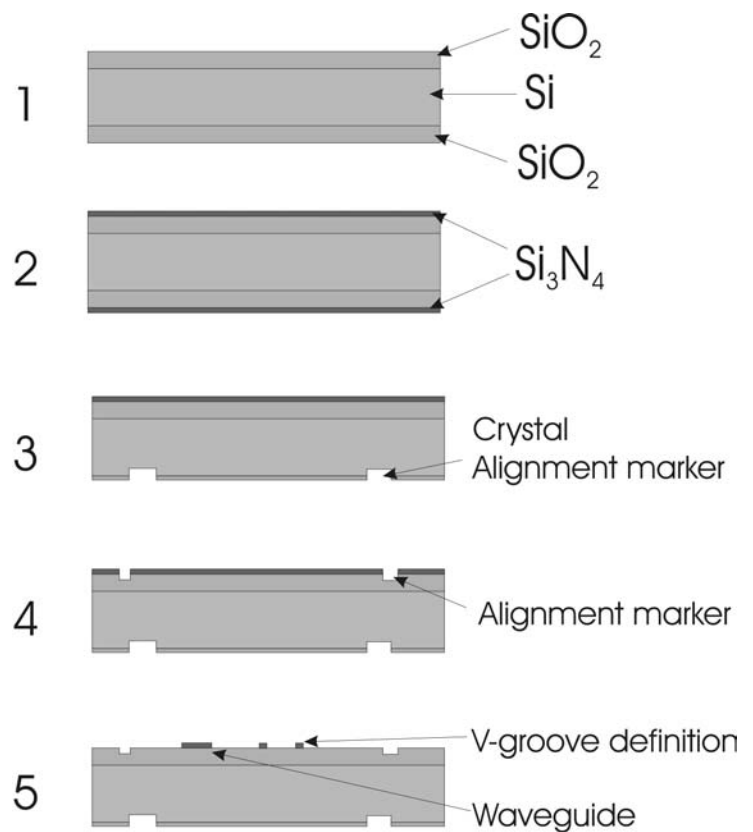
## 2.5 Realization and structural characterization

### 2.5.1 The fabrication process

In this chapter the fabrication process will be treated. First the design of the process will be given, some non standard technological steps had to be developed and these developments are discussed in appendix F. The systems have been produced and the constitutional parameters of the obtained systems are presented.

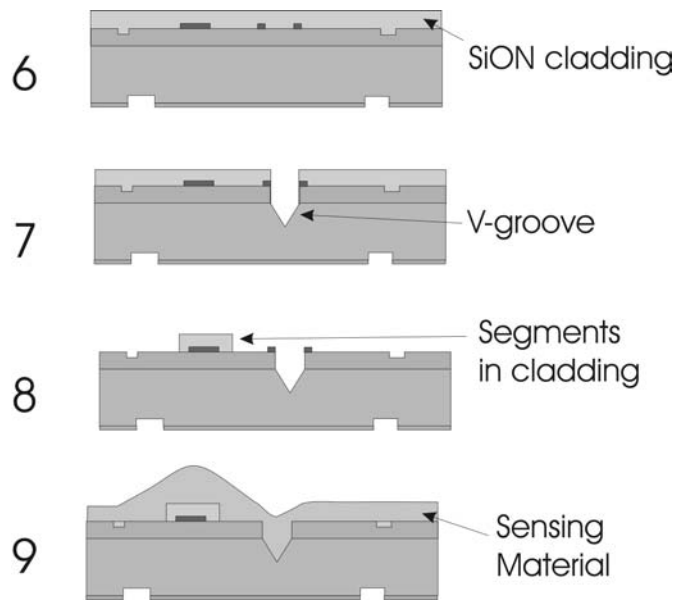
Figure 2.22. The fabrication process.

1. On a standard 4" (100) wafer a  $\text{SiO}_2$  buffer layer is grown using wet thermal oxidation.
2. A  $\text{Si}_3\text{N}_4$  core layer of optical quality is deposited using LPCVD [14]. The  $\text{Si}_3\text{N}_4$  and part of the  $\text{SiO}_2$  layers at the back side are etched off using BHF and the structures needed for determining the crystal orientation are implemented in the back side of the Si-wafer using RIE followed by KOH etch. Notice that at the front side the layer stack had no contact with the KOH (protected by photoresist) preventing any KOH induced roughening of the surface.
3. Next the markers for the mask alignment, matched to the crystal axis orientation are etched on top of the wafer using RIE.
4. The positions of the waveguide channels and the V-grooves are defined simultaneously in one photolithographic step [15] and the ridges and openings for the V-grooves are realized by locally etching the  $\text{Si}_3\text{N}_4$  layer using RIE followed by a short wet etching step to reduce the surface roughness.



5. A SiON layer with a refractive index matched to the specific sensing material (in our case  $n=1.500, 1.520$  or  $1.473$ ) is deposited using PECVD [11], [12].

6. The V-grooves are realized, for this first the cladding and residual core layer above the V-groove will be removed using RIE. The buffer layer is then removed using wet chemical BHF etching. Because of the high selectivity of the BHF etch, the position of the V-groove defined by the core layer is maintained. After that an anisotropic KOH- etch step is applied to obtain the V-groove shape.



7. The sensing windows are etched in the SiON layer, using a two step process. Firstly the main part of the SiON layer is locally etched using RIE, giving the desired perpendicular sidewalls. Secondly the last part is etched off using BHF, offering a smoother end face and a better control of the etching speed than RIE. On top of the waveguide, pillars of SiON will remain. Everywhere else the SiON will be removed. This type of cladding structure has two advantages compared to the structure in which the only windows are etched away: the uniformity in etch rate will be larger, both for RIE and BHF-etching, and also the wetting properties of the sensing materials (spun on top of the chip in step 9) will be better.

8. The end plane of the V-groove near the IO channel is realized by sawing [16]. After that the wafer will be diced.

9. Finally the sensing material will be spun top of the wafer. With a last local BHF dip the V-grooves will be cleared of the sensing material and the IO chip is ready.

After every process step the fabricated structure is characterized. For this purpose often preruns or dummy wafers, which follow the same process steps as the original wafers, have been used. Also some test areas on the wafer have been made available for ellipsometric characterization of a layers by locally etching off the already applied layer(s) before depositing that specific layer. Surface profile scans are used to determine step heights and AFM is used for determining surface roughness. SEM pictures are made to determine the geometry, amongst others the lateral dimensions of the realized structures.

Originally it was intended to implement also detectors in the Si wafer. Many options to do so have been investigated (see appendix F), but finally we decided to refrain from integrating these detectors.

## 2.5.2 Structural characterization

All relevant structural parameters have been characterized either in intermediate steps in the technological process or at the final structure. The result for the sensors of type 1 are depicted in Table 2.3 and the results of type 2 (the second spiral shaped SWS) in Table 2.4. A SEM photo of the realized structure (type 1) is shown in Figure 2.23 and Figure 2.24.

**Table 2.3. Parameters of the realized SWS of type 1.**

Parameter	Intended Value	Realized value and measurement accuracy
Wavelength	850 nm	
Thickness Si <sub>3</sub> N <sub>4</sub> core layer	60 nm	58 ± 0.1 nm
Channel width	7.0 μm	6.9 ± 0.1 μm
Thickness SiON cladding layer	2.0 μm	2.00 ± 0.02 μm
Index SiON	1.520	1.520 ± 0.001
Thickness SiO <sub>2</sub> buffer layer	>2.5 μm	2.8 ± 0.1 μm
Under-etch SiON		0.5 ± 0.1 μm
Angle wall SiON		53 +/- 5 degrees
Propagation loss (dB)		0.5 ± 0.3 dB/cm

From the table data it can be concluded, that the structural parameters of the realized structure are very close to their intended values. With one exception however: the side walls are not perpendicular to the layer boundaries but show an angle of about 53 degrees. Calculations on segmented structures with various side wall angles show, that an angle of about 50 degrees reduces the A-value with about 10%.

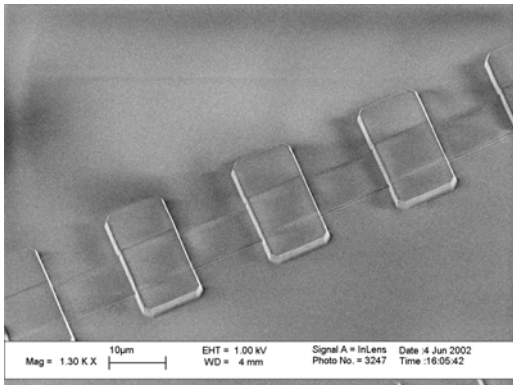


**Figure 2.23. SEM photo of realized SWS**

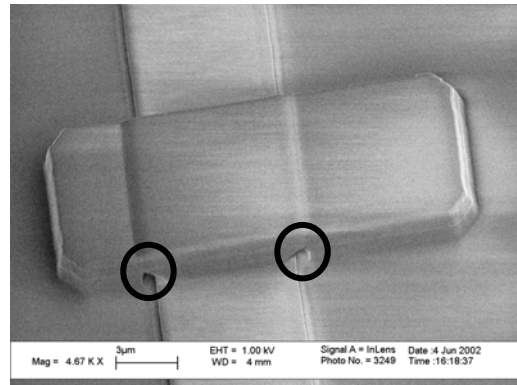


**Figure 2.24. Close up of the realized SWS**

According to Figure 2.23 the SWS seems to be perfect, but in the close-up, shown in Figure 2.24, it can be seen that there are cave like holes (voids) in the SiON near the ridges on both sides of the waveguide. This is caused by the well known overgrowth effect [12], which occurs when SiON is grown over step like structures. After the SiON deposition these voids are small, but during BHF etching, these voids fill up with the BHF, the walls of the voids are etched too and even after the wafer is removed from the BHF, this etching continues. Fortunately these voids are expected not to hamper the operation of the SWS sensor. Because the mode profile is mostly confined to the inside of the channel these voids do not cause significant propagation losses. At the straight-to-bend interfaces however the field profile matching is more disturbed and here the voids may result into significant scatter losses. It has to be noted that in the IOMS group research is going on with P and B doped SiON materials. Due to the doping the melting point of the material is strongly lowered and at annealing at temperatures close to this melting point reflow will occur and the voids will disappear.

For the sensors of type 2 the comparison between intended and realized structural parameter values is given in Table 2.4.

**Table 2.4. Parameters of the SWS sensors of type 2.**

Parameter	Intended Value	Realized value
Wavelength	632.8 nm	
Thickness Si <sub>3</sub> N <sub>4</sub> core layer	30 nm	30 ± 0.1 nm
Refractive index Si <sub>3</sub> N <sub>4</sub> core layer	1.99	1.96 ± 0.01
Thickness SiO <sub>2</sub> cladding layer	2.0 μm	2.1 ± 0.1 μm
Refractive index SiO <sub>2</sub> cladding	1.473	1.470 ± 0.004
Thickness SiO <sub>2</sub> buffer layer	> 2 μm	2.84 ± 0.04 μm
Refractive index SiO <sub>2</sub> buffer layer	1.458	1.45 ± 0.01 μm
Slab height	> 5 nm	
Segment length	8.4 μm	8.2 and 8.6 μm
Under-etch	0 μm	0.2 μm
Channel width	2.0 μm	
Average propagation loss (B)	0.5 dB/cm	13 ± 3 dB/round 4 ± 0.8 dB/cm
A-value	6.10 <sup>7</sup> dB/m	(3 ± 0.5).10 <sup>8</sup> dB/m

Also here the parameter values of the realized structure are very close to the intended ones, with one exception: the average refractive index of the core layer is slightly smaller than expected. It is supposed that the first few nanometers of the LPCVD nitride have a slightly lower refractive index due to start up phenomena, thus lowering the average refractive index of the total layer.

## 2.6 Characterization

In this chapter first the measurement setup will be presented. After that the results of the SWS, which has been characterized using liquids with variable refractive index, will be compared to the theory (sections 2.6.2 and 2.6.3). Then the SWS's covered with sensing materials will be treated. During the characterization an unexpected phenomenon was observed. This phenomenon could be explained (section 2.8) and served as the basis for the second IO sensor that will be treated in this thesis: the GAC sensor. This will be treated in chapter 3.

### 2.6.1 The measurement setup

In Figure 2.25 the measurement setup is depicted schematically. The light source consists of a 850 nm solid state laser [ $P_{out}=3mW$ ] or a 632.8 HeNe [Melles Griot,  $P_{out}=1mW$ ] laser, both lasers being pig tailed with a single mode fiber (mode field diameter  $4.6 \mu m$  for  $\lambda=632.8$  nm and  $6.0 \mu m$  for  $\lambda=850$  nm). The input fiber contains a polarization controller and after mounting the fiber into the V-grooves, the fiber light is eventually coupled into the sensing platform. A single mode fiber is used here to obtain efficient fiber to chip coupling. At the output of the chip a multimode fiber is used to couple the light out of the chip. The output power is determined using a Nirvana auto-balanced photodetector [New Focus, model 2007]. The value of  $(q_1 + q_2)$  of the complete sensor system was about 0.002, which was determined from direct noise measurements.  $P_{in}$  was about 1 mW and  $P_{min}$  amounted to an equivalent of about  $1 \mu W$ .

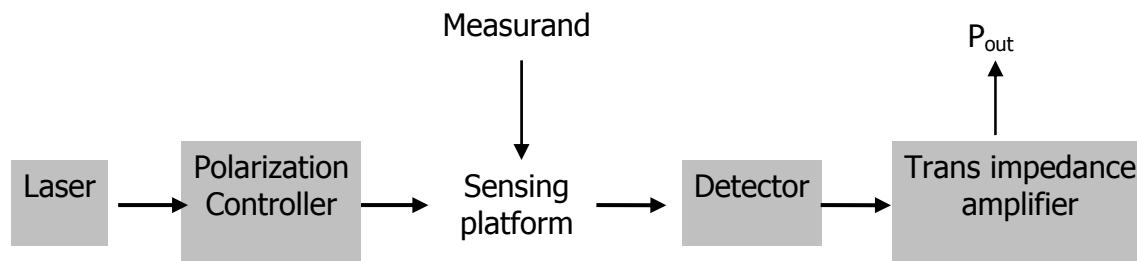


Figure 2.25. The measurement setup.

The performance of two types of sensors has been determined experimentally: sensors where the segmented section was in direct contact with a liquid and sensors where a solid interface, sensitive to relative humidity ( $RH$ ) or  $CO_2$  had been applied on top of the segments. For the characterizing of type 1 a cuvette was applied on top of the segmented structure and this cuvette was successively filled with liquid mixtures of various compositions. Refractive indices of these mixtures have been measured using an Abbe refractometer in that way however introducing an error of about 0.001 in the value of this refractive index. This error partly originates from the inaccuracy of the Abbe refractometer itself, partly from the dispersion of the refractive index: the Abbe refractometer uses white light and our measurements have been done with

monochromatic light with a wavelength of 850 nm. For characterizing the spiraled structures we used a simple microfluidic system that is glued on top of the segmented structure. A liquid with continuously varying value of the refractive index is flowing through this MF system. This has been described already in section 2.4.4.10 and in Appendix C.

For measuring the second type of sensors a gas atmosphere with well controlled *RH* or CO<sub>2</sub> concentration had to be generated around the sensor. For this purpose we used a miniaturized climate chamber as is depicted in Figure 2.26. The chip is placed in this chamber, which can be covered with a lid. Nitrogen gas with a specific value of the relative humidity or the CO<sub>2</sub> concentration is fed into the chamber. The gas leaves the chamber through small holes divided equally over the sides of the chamber. The *RH* or the concentration CO<sub>2</sub> is controlled using flow controllers. Three different gas mixtures (100 % N<sub>2</sub>, 5 % CO<sub>2</sub> + 95% N<sub>2</sub> and N<sub>2</sub> with a *RH* of 100 %) can be mixed in arbitrary ratios, where the accuracy of the flow controllers (1% of full scale systematic error) eventually determines the accuracy of the concentration (accuracy: 2-3%).

The whole setup is automated. A Labview program has been written to perform automated measurements. The flow rates of the gasses are controlled using a computer. The output power and temperature are automatically read out.

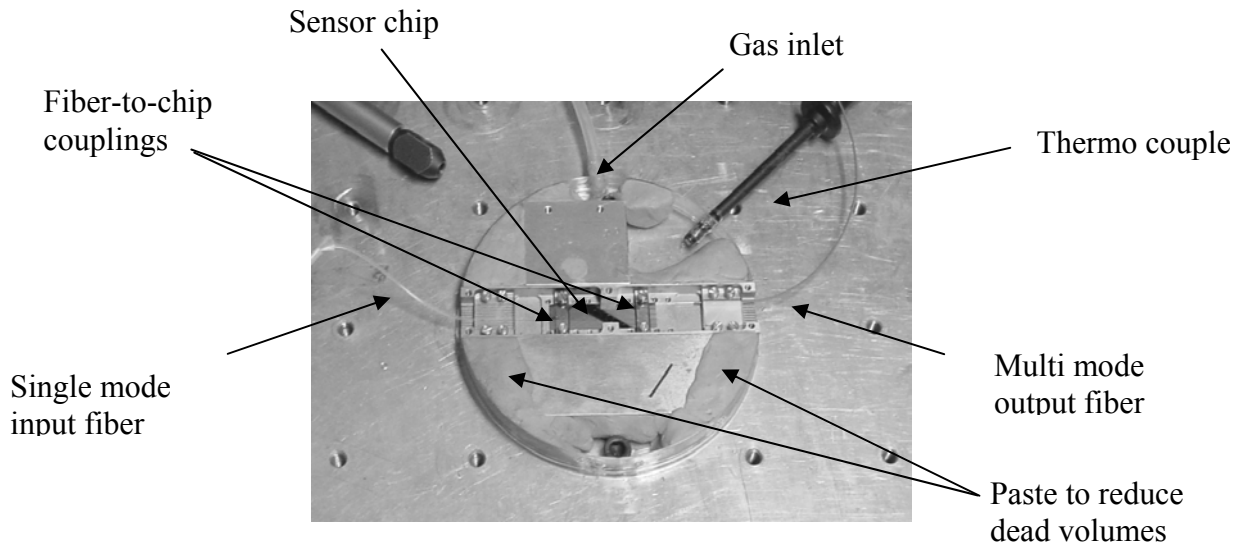


Figure 2.26. A small climate chamber.

## 2.6.2 Characterization type 1 SWS using liquids

A type 1 sensor with a sensing section length of 0.5 cm has been characterized. The output power was measured as a function of  $\Delta n$ , the difference between the actual refractive index and the refractive index at maximum transmission. A typical result is shown in Figure 2.27, where the functional loss per millimeter is given as a function of  $\Delta n$ . Also the theoretically calculated relation is depicted.

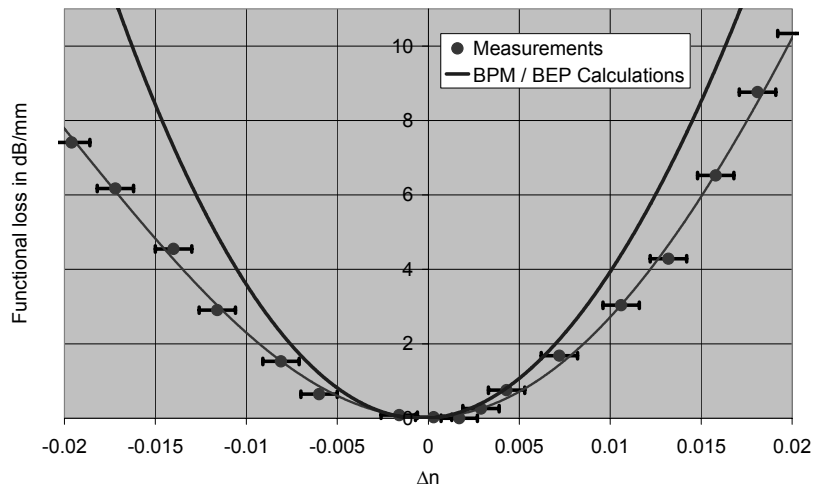


Figure 2.27. SWS characteristic for  $L = 9 \mu\text{m}$ , measurements (points) and simulations (line).

Because the absolute refractive index of such a mixture could not be determined exactly, the whole characteristic has been shifted along the  $\Delta n$ -axis to put the minimum in functional loss at  $\Delta n=0$ . This shift was within the accuracy of the refractive index measurements.

In Figure 2.28 and Figure 2.29 both the experimentally obtained and theoretically calculated dependences of the functional losses of the segmented structure as a function of the segment length  $L$  are presented for  $\Delta n = \pm 0.01$ . The calculations in this case were performed for the realized structure, which was, due to technological inaccuracies, slightly different from the designed structure. The uncertainties in the value of  $\Delta n$  are the main contribution to the error bars in the figures. The error in the determination of the functional loss itself is negligible.

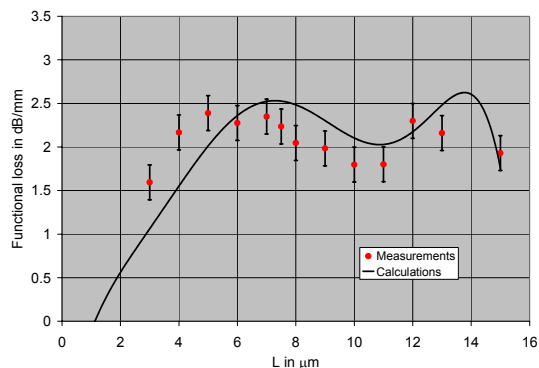


Figure 2.28. SWS characteristic  $\Delta n = -0.01$ .

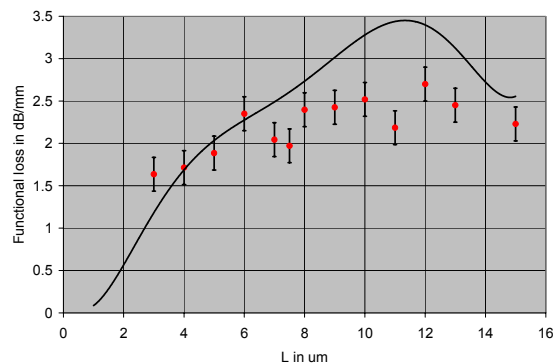


Figure 2.29. SWS characteristic  $\Delta n = +0.01$ .

As can be seen, the experimental points agree reasonably well with the theory. We attribute the difference between theory and experiments to the fact that all the

calculations were done in 2D and not in 3D. Further it can be seen that the highest sensitivities are obtained for  $L > 5 \mu\text{m}$ . In this region the dependency of the sensitivity on  $L$  is small. From the characteristic in Figure 2.27 the  $A$  value can be determined by curve fitting around  $\Delta n=0$ . The maximum  $A$ -value of the sensors characterized is  $2,7 \cdot 10^7$  dB/m, agreeing very well with the  $2,0 \cdot 10^7$  dB/m as has been designed in section 2.4. The  $B$  value is estimated to be about 50 dB/m.

### 2.6.3 Characterization type 2 SWS using liquids.

The previous section dealt with an SWS with a short sensing length (only 5 mm) and the aim was to investigate the behavior of the sensor, compare the calculations with the experiments and to obtain proof of principle. In order to obtain high resolution however, the sensor length needs to be much longer. The optimum sensor length is given by expression (2-16). The sensors with spiral geometry (type 2), are designed to demonstrate the high resolution which can be obtained. In Table 2.4 the intended and realized values of the cross sectional channel parameters have been given.

Many spiral shaped sensors have been put into the measurement set up. Losses at maximum transmission ( $\Delta n = 0$ ) appeared to be much larger than expected. The propagation loss has been estimated from the maximum output powers of two spiral SW sensors with different length and amounted to about 13 dB/round trip and 4 dB/cm. This unexpected high propagation loss is probably due to the increased absorption and scattering of 632.8 nm light in comparison with the 850 nm light.

Performance characteristics of two SWS spiral sensors with different length are given in Figure 2.30 (for a spiral, containing  $1\frac{1}{2}$  rounds and having a total length of the segmented sections of 3.7 cm) and Figure 2.31 (for a spiral containing  $5\frac{1}{2}$  rounds, corresponding with a total length of the segmented sections of 14.1 cm).

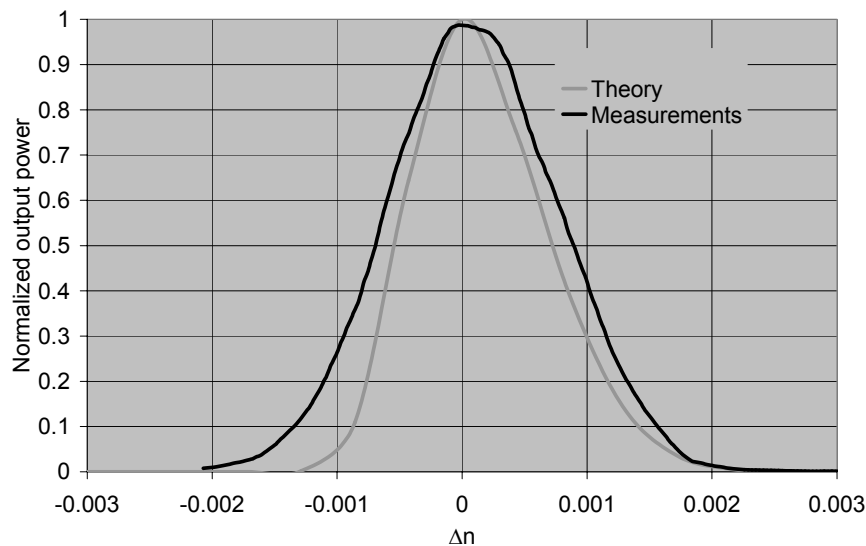


**Figure 2.30. Characteristic spiral SWS, 1½ rounds.**

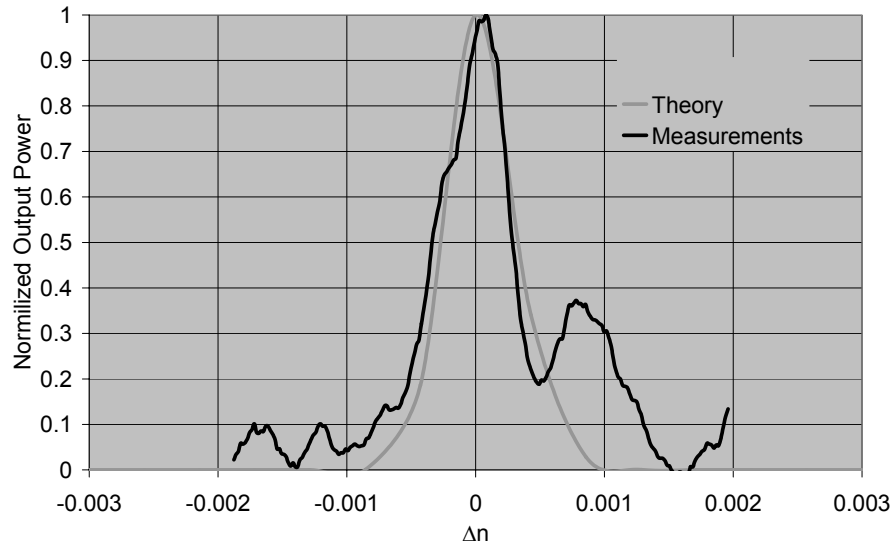


**Figure 2.31. Characteristic spiral SWS, 5½ rounds.**

The measurements fit the theory reasonably well. The sensitivity of the measured sensor is slightly lower than calculated. For this there are two explanations, which can be clarified with Figure 2.32, which shows a SEM picture of a waveguide channel (horizontal stripe) with a segment on top (vertical stripes). Clearly it can be seen that the sidewall of the segment is slightly slanted. The angle of the sidewall of the segment was measured to be  $75 \pm 5^\circ$ . Closer inspection shows that the duty cycle of the realized sensor is 0.48. Both effects reduce the sensitivity of the realized spiral SWS slightly with respect to the calculations, which have been performed with a duty cycle of 0.5 and angle  $\alpha = 90^\circ$ .

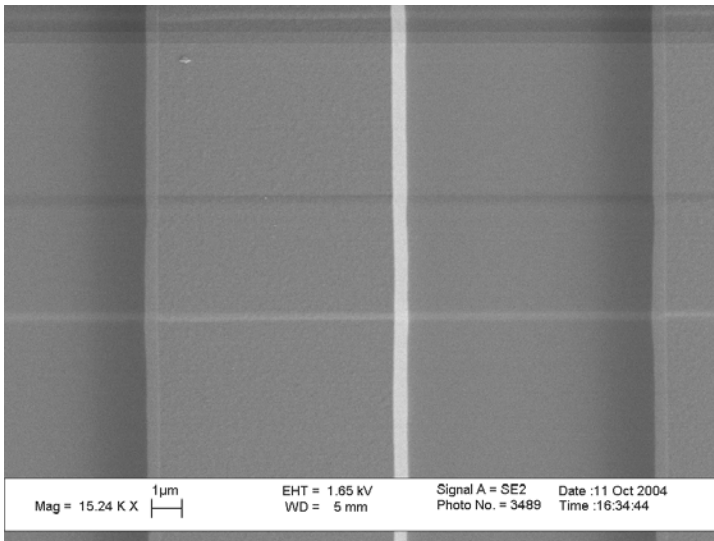


**Figure 2.32. SEM photo of a segment on top of a channel.**

The characteristic given in Figure 2.31 was obtained while measuring very low output powers. We attribute the side peaks to slab light coupled into the output fiber. The reproducibility of the width and position of the central peak has been established. Unfortunately during a second measurement, due to a sudden deterioration of fiber to chip coupling, the output power related to the side peaks reduced to below the detection limit of the detector, thus the reproducibility of the side peaks could not be confirmed.

Note that the transmission peaks are very narrow (a 3dB width of  $\Delta n = 0.002$  only) and that without a micro fluidic system and without a method to accurately and continuously vary the refractive index of the liquid it would have become very difficult, if not impossible to detect the presence of such very narrow peaks!

### 2.6.4 Characterization SWS with chemo-optical transduction layers

Two sensors of type 1 with channel cross sectional parameters as have been given in Table 2.3 have been characterized. One was provided with a gelatin layer and one with a polysiloxane layer. The refractive index of the passive SiON cladding is matched to the index range of the polysiloxane;  $n_{\text{SiON}} = 1.50$ . The sensor with gelatin had a segment length  $L = 20 \mu\text{m}$ , for the sensor with polysiloxane  $L$  was equal to  $12 \mu\text{m}$ . Because, as is discussed in appendix E, the polysiloxane appeared to be insensitive to changes of the  $\text{CO}_2$  pressure, but did show some dependence on the Relative Humidity  $RH$  too, both sensors have been characterized by varying the  $RH$  of the surrounding atmosphere.

Output power has been measured as a function of  $RH$  and the results are depicted in Figure 2.33 and Figure 2.34.

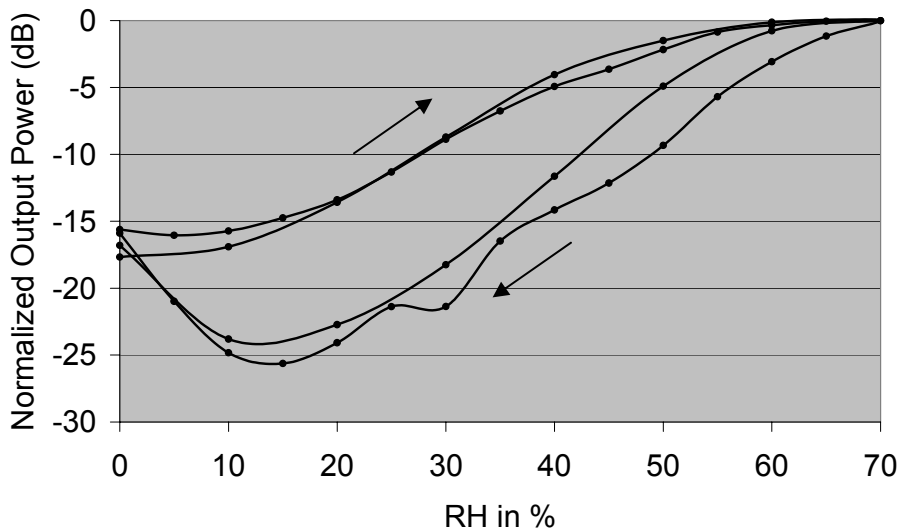


Figure 2.33. Characteristic of SWS with polysiloxane for  $L = 12 \mu\text{m}$ .

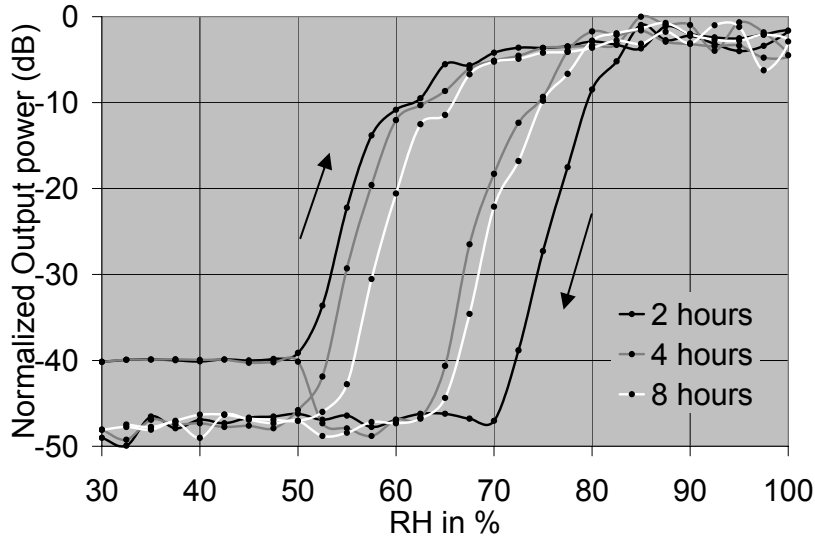


Figure 2.34 Characteristic of SWS with gelatin for  $L = 20 \mu\text{m}$ .

For the characterization of the polysiloxane containing sensor we started from 0 %  $RH$  and the  $RH$  has been increased in steps of 5 % to its maximum value 70 % in 4 hours and back again. This has been done twice to check reproducibility. The time between two measurement points was taken to be 9 minutes, which was sufficient for obtaining the corresponding equilibrium state of the transduction layer, i.e. constant output power. For the gelatin containing sensor we started from 30 %  $RH$  and the  $RH$  has been increased in steps of 2.5 % to 100% and back in respectively 2, 4 and 8 hours. This variation in duration has been introduced to check that equilibrium states have been reached. We expected identical performance curves. However, it can be seen that the sensor behavior is completely different from what had been expected: both curves shows a very big hysteresis and bad reproducibility.

Note that this hysteresis had not been observed in characterizing plane gelatin and polysiloxane layers. Note also that the ellipsometric characterization of a plane gelatin layer occurred in exactly the same climate chamber as this sensor, so any difference in behavior of gelatin has to be attributed to the fact that the gelatin is now deposited inside a segmented waveguide structure. Also such a hysteresis phenomenon was absent when the polysiloxane was characterized using a Mach Zehnder interferometer [13].

The large hysteresis, the non-reproducibility of the measurements and the memory effects (the latter explaining the minimum in the polysiloxane sensor characteristic) all hint at irreversible changes in the internal structure of the transduction layers caused by an external change in relative humidity. We attribute these phenomena to mechanical effects; while equilibrating with the offered relative humidity next to the refractive index change of the sensing layer also its thickness will tend to change. Due to the adhesion of the sensing material to the SiON at the transitions at low changes clamping effects will degrade the intended effects, while at higher changes the materials will be deformed irreversibly. Note that these disturbing effects did not manifest themselves in the flat

gelatin layers, which have been applied in an evanescent field type Mach Zehnder Interferometers before.

Despite the hysteresis and non reproducibility we can recognize some expected features: the position of maximum transmission is as could be expected from the refractive index of the passive cladding material and the *RH* sensitivities of the materials: for polysiloxane around 70% *RH* and for gelatin around 90 % *RH*. From these observations we can conclude that both polysiloxane and gelatin inside an SWS sensor don't behave like a reversible sensing material. We have to conclude that the SW sensors are not applicable for these chemo-optical transduction layers, probably related to irreversible mechanical effects caused by the swelling of these materials at increasing *RH*.

## 2.7 Other kinds of segmentation

Up to now we have focused on a special type of segmentation belonging to the class of segments with identical geometry but containing different materials. We now will have a closer look to sensor type from class 2: the segments contain the same materials but have a different geometry. We first consider the structure given in Figure 2.35.

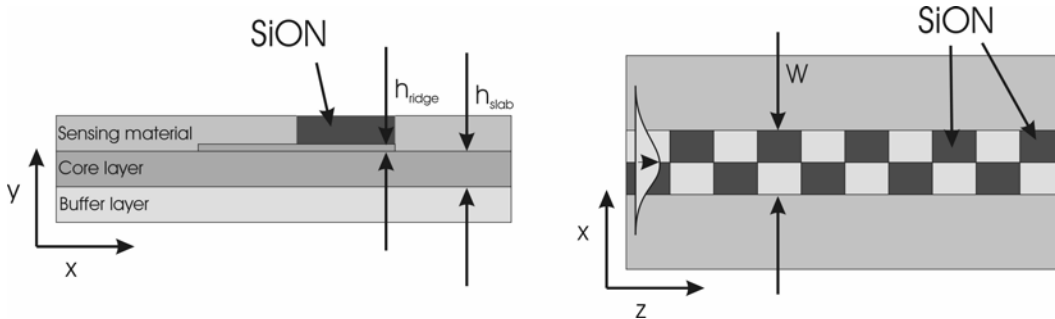


**Figure 2.35.** SW structure of class 2; cross section (left) and longitudinal top view (right).

In this type of segmented structure the guided mode is loosely guided by the thin ridge. A small increase in the  $n_{\text{sens}}$  will pull the guided mode in all segments inside the region with the sensing material. As a result the modal field profiles in two adjacent segments will be pulled in opposite directions and a large change of the value of the overlap integral can be expected. This behavior can be efficiently described in terms of the “rest field generated at a transition”, the field that is the direct source of the radiation modes, as has been treated in detail in Appendix A. In fact, while thinking over segmented waveguides in terms of these rest fields we realized the relevancy of this type of segmented structures. First let’s see how we would like that our ‘rest field’ looks like:

1. For a given  $\Delta n$ , the ‘rest field’ should be as large as possible: the more power is coupled into radiation modes, the larger the maximum theoretical sensitivity of the SWS.
2. If focusing on having small interference effects at the transitions, the radiation field has to show a large divergence: the angle between the propagation direction of the radiation modes and the axis of the waveguiding channel should be as large as possible. Of course if the back coupled radiation should interfere destructively with the guided mode, this would increase the desired effects at the transitions. However for small angles, these radiation modes need to travel a long way before a phase difference of  $\pi$  with the guided mode is built up and the number of transitions per unit length would be low. So in general large angles are preferred. Large angles can be associated with small distances between adjacent zero-lines of the ‘rest’ field.

Large rest fields can be expected if the field profiles of the modes in different types of segments should shift laterally in opposite direction but the distances between zero-lines cannot be predicted from qualitative reasoning.

In Figure 2.36 and Figure 2.37 the rest-field (confined within the slab structure) and the angular distribution of the radiation in the  $xz$  plane are depicted for a structure with  $W=4\mu\text{m}$ ,  $h_{\text{ridge}}=1\text{ nm}$ ,  $n_{\text{slab}}=1.5$  and  $h_{\text{slab}}=59\text{ nm}$ ,  $\Delta n=0.001$  at  $\lambda=850\text{ nm}$  (a structure with low lateral contrast) implemented in the standard  $\text{SiO}_2/\text{Si}_3\text{N}_4/\text{SiON}$  layer structure.

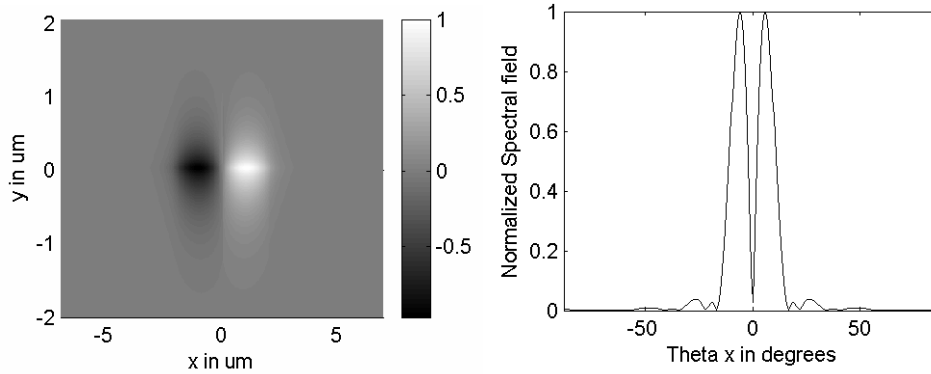


Figure 2.36. (left) The normalized ‘rest field’ distribution.

Figure 2.37. (right) The normalize angular distribution of the ‘rest field’ in the  $xz$  plane.

Compared to the type 1 SW structure that is designed and realized in section 2.4, the magnitude of the ‘rest field’ appears to be increased with a factor of about 150. This hints at the possibility that this kind of SWS could have a better resolution. However the divergence of the radiation is pretty small compared to that of the SWS structure of section 2.4 (see Appendix A). This implies large segment lengths, which will reduce the sensitivity. Further calculations showed that the larger the channel width  $W$ , the larger also the ‘rest fields’, but the smaller the exit angles. A reasonable trade off has been found in  $W=4\mu\text{m}$ . Using the BEP for this structure the A factor has been calculated for different segment lengths. Because of the high reflection at the calculation boundaries, related to the small angles of the radiation, the maximum segment length that could be considered was  $100\mu\text{m}$ . The results have been depicted in Figure 2.38.

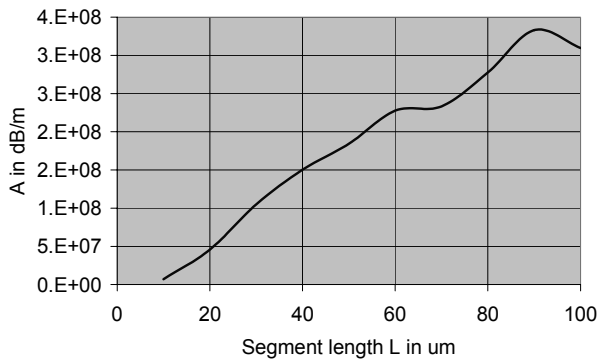
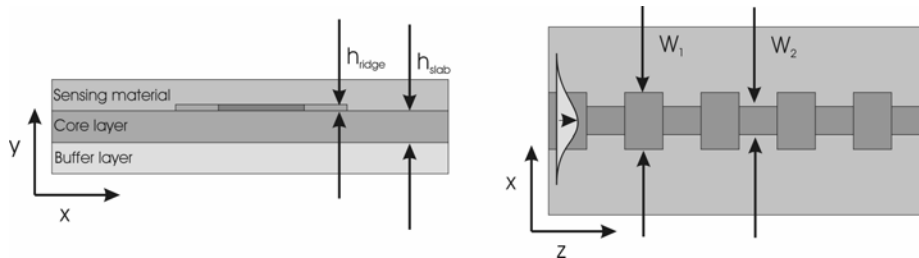


Figure 2.38. A factor for different segment lengths.

As expected, large segment lengths are needed to get appreciable effects; the  $A$  parameter continuously increases over a large  $L$ -range up to a value of  $3.5 \cdot 10^8$  dB/m at a segment length of  $90 \mu\text{m}$ . The  $A$  factor of the type 1 SWS that has been realized in section 2.4 was determined to be  $2 \cdot 10^7$  dB/m. Thus despite the larger segment length this kind of segmentation offers roughly a factor 4 improvement in resolution. Note also that, as a result of the small ridge height, propagation losses can be expected to be smaller than those of the SWS designed in section 2.4.

A second structure belonging to class 2 has been depicted in Figure 2.39.



**Figure 2.39.** SW structure of class 3; cross section (left) and longitudinal top view (right).

Because the width of the field profiles of the zeroth order mode as a function of the channel width shows a minimum, for a range of segment widths, there will be complementary segments showing the same confinement, but another value of the channel width [17]. Close to such a complementary couple, width combinations are expected where the overlap integral of the field profiles of modes propagating through the corresponding segments shows a (local) maximum. If the refractive index of the cladding material changes the mode profile of one of the segment types will expand laterally, while that of the other segment will shrink. Thus relative large changes of the overlap integral can be expected. We have explored this type of systems theoretically, but the simulations showed, that the maximum guided mode transmission through a single transition was quite low, which led to relatively large  $B$ -values, making this kind of sensor uninteresting for attaining high resolutions.

## 2.8 Unexpected phenomena

During the characterization of the performance of the sensor of type 1 using liquids with continuously monotonously varying refractive index, at low values of  $n_{liquid}$  additional ‘dips’ were observed in the normalized output power versus  $n_{liquid}$  curves. In Figure 2.40 such a dip is shown.

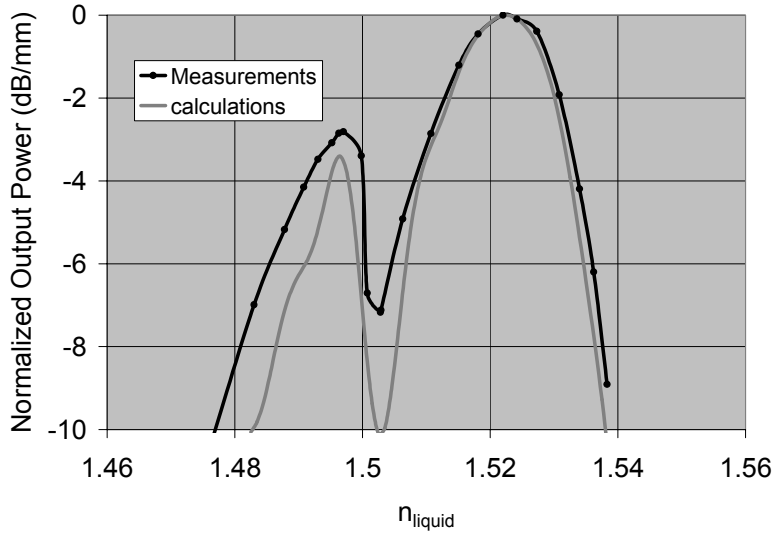
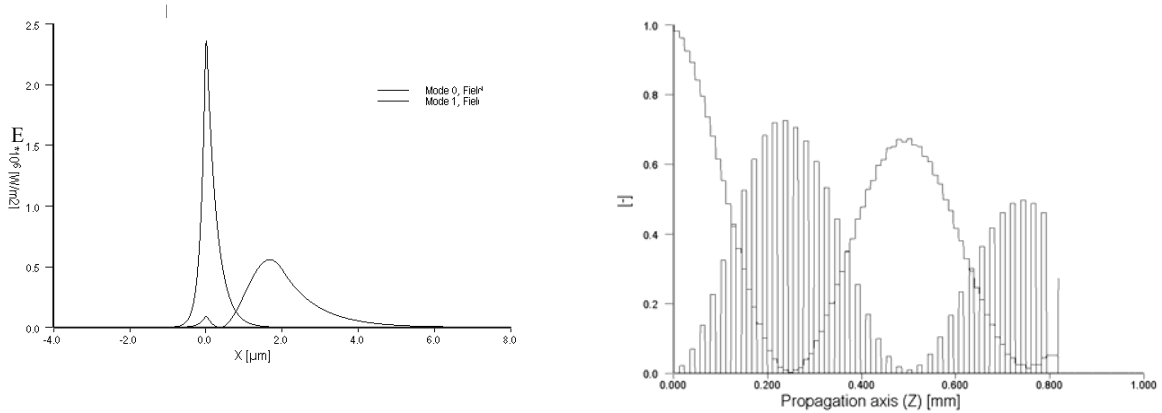


Figure 2.40. ‘Dip’ in SWS characteristic with  $L = 12 \mu\text{m}$ .

Around  $n_{liquid} = 1.52$  the SWS behaves as expected, showing maximum transmission at  $n_{liquid} = n_{SiON}$ . Using the BEP method, the behavior of the SWS over the whole  $n_{liquid}$  range has been calculated and indeed the calculations confirm the existence of the dip and even predict its position very accurately.

For the explanation of this phenomenon we have to take a closer look at the SW structure. One of the segment types is covered with a liquid with a varying refractive index. For the whole range of liquid refractive indices considered, the waveguide in this segment type is strictly mono-mode. The other segment type is covered with SiON with a refractive index of 1.52 and a layer thickness of  $2.0 \mu\text{m}$ . One would expect this waveguide to be mono-mode also. It is however important to realize that on top of this SiON layer there is also liquid present. For  $n_{liquid}$  values smaller than  $n_{SiON}$  the  $\text{Si}_3\text{N}_4$  and SiON layer together act as one large core layer, with the result that the system is bimodal for  $n_{liquid} < 1.515$ . In Figure 2.41 the mode profiles of the fundamental and 1<sup>st</sup> order mode supported by such a segment are depicted. The  $\text{Si}_3\text{N}_4$  layer is only 60 nm thick and located at  $x=0 \mu\text{m}$ . As can be seen, most of the field of the 1<sup>st</sup> order mode is propagating through the SiON layer.



**Figure 2.41. (left): modal profiles of 0<sup>th</sup> (black) and 1<sup>st</sup> order mode (grey).**

**Figure 2.42. (right): mode coupling between 0<sup>th</sup> (black) and 1<sup>st</sup> mode (grey).**

Now imagine light propagating as the 1<sup>st</sup> order mode in the “passive” segments. At the transition to the next segment, all the power in the guided mode will be converted to radiation modes. Over the small length of the next segment the shape of the field profile of the radiation will however be similar to that of the guided mode. The radiation will diverge somewhat, but still a substantial part of the radiative power will couple back into the 1<sup>st</sup> order guided mode at the next transition. Effectively the 1<sup>st</sup> order mode will propagate like a normal guided mode, however with additional propagation losses.

The SWS consists of segments with a fixed length. Although the principle of operation doesn’t depend on this, effectively the SWS resembles a grating. Grating assisted coupling between the two guided modes will occur if the period of this grating and the effective indices of the guided modes satisfy the corresponding resonance condition, BEP calculations of the propagation of the field inside a ‘dip’ show that this is indeed the case. To illustrate this, the modal powers of the 0<sup>th</sup> and 1<sup>st</sup> order modes are depicted as a function of propagation distance for the system with  $L = 12 \mu\text{m}$  and  $n_{\text{liquid}} = 1.502$  (just at the minimum of the ‘dip’) in Figure 2.42. Also it has been verified that the dips observed indeed correspond to situations where this resonance condition is met.

If coupling to the first order mode occurs, extra losses are induced by the radiation losses of the quasi guided 1<sup>st</sup> order mode. Because the effective indices of both modes change as a function of  $n_{\text{liquid}}$ , (note that the change of  $N_{\text{eff}}$  of the first order mode is strongly dominant) the resonance condition is only satisfied for a very small range of  $n_{\text{liquid}}$  values, resulting in a very narrow ‘dip’ in the SWS characteristic. The ‘dip’ inside the SWS characteristic does locally increase the sensitivity of the sensor and this phenomenon might therefore be used to improve the resolution of the SWS.

Imagine now that the width and the depth of the dip are such that in this region just the shape of the dip determines the sensitivity of the sensor. Then the segmented waveguide principle hardly contributes to the sensitivity anymore, but the change of transmission is nearly completely determined by the grating assisted mode coupling and the first order

mode losses. It is therefore not necessary to implement the mode coupling principle in an SWS, but probably a better resolution can be obtained when this phenomenon is isolated and optimized in a separate sensor. This is what has been done in the Grating Assisted mode Coupling sensor (GAC) and it will be treated in detail in the next chapter.

## **2.9 Summary and final discussion**

In this section the results presented in this chapter 2 will be summarized and discussed. After that the applicability of SWS sensors will be considered. The section ends with recommendations for further development.

In section 2.1 the principle of the SWS was explained. It became clear that, in order to describe the behavior of the SWS correctly, simulation/calculation methods are necessary that could handle the radiation field very well. In section 2.2 the application of three calculation methods, the Finite Difference Beam Propagation Method (FD BPM), the Bidirectional Eigenmode Propagation method (BEP) and the Spectral Decomposition Method (SDM,) to the SWS structure has been explained and the methods have been compared. It was concluded that the BEP would be the preferred method for the calculations but that the SDM would offer the most insight in the operation of the sensor.

Next, in section 2.3, a model was developed to determine the attainable resolution. In the final expression (expression (2-15)) the resolution was given as the product of two factors a factor representing the characteristics of the peripheral equipment and a factor originating from the sensing section and containing relevant sensor parameters.

In section 2.4 several SWS sensing structures (consisting of sensing sections and necessary auxiliary IO components) have been analyzed and some structures which would be realized indeed, have been designed. It has been shown that the segmented structures can be classified according to the nature of the difference between the segments. Main focus has been on an SWS of the so-called first class, characterized by the fact that the segments differed in constitution of the cladding only: either a sensitive or a passive material. A sensor system with a short sensing section has been designed to demonstrate the principle and to evaluate the technologies applied. Sensor systems containing elongated sensing sections, structured as spirals, were designed to investigate the resolution potential of SW sensors.

Section 2.5 has shown that a relatively simple SiON based technology enables the production of these SW sensors. From characterization of all structural parameters it has been shown that there is a really good correspondence between intended parameter values and the realized ones.

In section 2.6 the sensors have been characterized and discussed. For the characterization of the sensor, fluids with different refractive index have been fed to the sensing section. A fluidic system has been developed which enables a continuous transport of a liquid with a continuously monotonously varying refractive index to a small microfluidic system, glued on top of the sensing section. Experimental results did show a very good correspondence with the theoretical expectations. The differences between theory and experiment have been attributed to the fact that all the calculations were done in 2D and not in 3D.

For the first type of sensors an A-value (most relevant measure for the sensitivity of the sensor) of  $2 \cdot 10^7$  dB/m has been obtained, while for the spiralized sensors (type 2) the A-value appeared to be an order of magnitude larger:  $3 \cdot 10^8$  dB/m. For the short sensors (type 1) the losses were as expected, about 0.5 dB/cm. The losses of the spirallized sensors appeared to be much larger, about 4 dB/cm. These high losses degrade the resolution. Taking into account the properties of the available peripheral equipment, resolutions in the refractive index of  $6 \cdot 10^{-7}$  (type 1) and  $3 \cdot 10^{-7}$  (type 2) have been obtained.

Performance of the SW sensors provided with gelatin or polysiloxane interfaces (both being sensitive to relative humidity, *RH*) appeared to be bad: a clear hysteresis and bad reproducibility has been observed. Because both sensitive materials deposited as a smooth layer showed no hysteresis and a good reproducibility, the behavior observed with the SWS has to be ascribed to the segmentation. Because in addition to the *RH* induced change of refractive index of both materials also their dimensions are changing (swelling at higher *RH* values), we attribute the unexpected effects to mechanical effects related to the clamping and/of detachment of the interfaces by/from the segmented structure. Hence the SW sensors are not suitable for applications in which swelling interface layers have to be utilized.

In section 2.7 two other types of segmented structures in which all segments contain the sensitive material, but in which the geometry of the segment types is different, have been analyzed theoretically. One of them shows to be very promising, but due to a lack of time this structure has not been realized.

During the characterization several mysterious ‘dips’ were discovered in the SW characteristics. The existence of these ‘dips’ was explained (section 2.8) and this sparked the idea for a novel sensor principle which will be treated in chapter 3.

Now that we know most of the possibilities and limitations of the SWS it’s time to say something about the applicability of this sensor. In the introduction it was already mentioned that IO sensors are inherently expensive because of the high cost of the IO chip, light source, processing electronics and packaging. In exchange they offer high resolution and EMI- and explosion- free operation. Therefore main application areas have been defined [8] as being health care, ecology and some industrial processes.

In comparison with other IO sensors the strong point of the SWS is the cost. The technology is very simple and there are relatively low requirements on the light source. On the other hand, the best resolution that could be achieved (up to  $\delta n = 3 \cdot 10^{-7}$  for now is not as high as that of the Mach Zehnder interferometer (MZI) [10] with  $\delta n = 2 \cdot 10^{-8}$  [10] or the Young interferometer [7] with  $\delta n = 5 \cdot 10^{-9}$ .

The SWS can be used in various ways. Firstly it can be used to measure the refractive index of liquids in for example the chemical industry. The sensor is extraordinary suitable for this because of the high resolution, explosion free operation, inertness and low cost. Secondly it can be used with chemo-optical transduction materials provided that the

change of refractive index is not accompanied by considerable swelling. We believe that it might be possible to reduce the stresses inside the transduction material considerably, by appropriately adjusting the geometry of the SW structure, but no attention has been paid to that in this project. A restriction is that the working point of the sensor is controlled by the refractive index of the cladding. This implies that the refractive index of the passive SiON layer has to be matched to the relevant range of values of the refractive index of the chemo-optical transduction layer. Hence each batch of sensors needs to be customized for their application. A third application area might be immuno-sensing often characterized by a very thin often monomolecular chemo-optical transduction layer. The small thickness of the transduction layer opens new perspectives, not only for immuno-sensing but also for other applications for which the necessary transduction layers can be applied only as 4-10 nm thick layers. So these methods might be also promising for measuring RH, using now ultra thin gelatin layers. These methods will be worked out in Chapter 4. Note that the uncertainties of the technological processes require calibration of the (individual) sensors (as is the case for most IO sensors).

Notice, that not all types of segmented sensing structures have been investigated yet. In section 2.7 it was made clear that the SW principle can be applied to SW structures with widely varying geometries of which most have not been analyzed yet. We expect that this large uncharted territory still hides some structures which will offer a much higher resolution than the options which have been investigated in this chapter.

Further developments on the technological level to reduce the cost of packaging and peripheral equipment will be advantageous. One option might be to integrate both the light source and optical detector in the sensor chip. Hence both on the theoretical as well as on the experimental side a lot of research still has to be done on SW sensors.

## 2.10 References

- [1] J. Webjorn, F. Laurell, G. Arvidsson, *Fabrication of periodically domain-inverted channel waveguides in lithium niobate for second harmonic generation*, J. Lightw. Technol. 7 (1989), 1597-1600
- [2] Z. Weissman, I. Hendel, *Analysis of periodically segmented waveguide mode expanders*, J. Lightw. Technol., Vol. 13(10) (1995), pp 2053-2081
- [3] OlympIOs; *C2V software*, version 5.1.12
- [4] H.J.W.M. Hoekstra, J. van Lith, S. Gaál, P.V. Lambeck, *The Spectral Decomposition Method: a Transparent Theory for Losses in Segmented Waveguides*, proceedings ECIO 2003, pp. 339-342
- [5] T.Tamir, *Topics in Applied Physics volume 7*, Springer-Verlag Berlin Heidelberg New York, 2<sup>nd</sup> edn. 1979
- [6] G.H. Brooke and M.M.Z. Kharadly, “*Scattering by abrupt Discontinuities on Planar Dielectric Waveguides.*”IEEE Trans. Microwave Theory Tech., vol. MTT-30, no.5 (1982) pp.760-770
- [7] S. Gaál, doctoral thesis, *Novel Methods to calculate guided and radiation modes in slab and channel waveguides*, Lightwave Devices Group, University of Twente, dec. 2002
- [8] P.V. Lambeck, *Integrated Optics for the Chemical Domain*, ECIO 2001, pp. 153-163
- [9] O.Parriaux and G.J.Veldhuis, *Normalized analysis for the sensitivity optimization of integrated optical evanescent wave sensors*, J. Lightw. Technol. 16 (1998), pp 573-582
- [10] R.G. Heideman, P.V. Lambeck, *Remote opto-chemical sensing with extreme sensitivity: design, fabrication and performance of a pigtailed integrated optical phase-modulated Mach-Zehnder interferometer system*, Sensors-and-Actuators-B-Chemical. Vol. B61(1-3) (1999), pp 100-27
- [11] K. Wörhoff, P.V. Lambeck, A. Driessen, *Design, tolerance analysis, and fabrication of silicon oxynitride based planar optical waveguides for communication devices*, J. Lightw. Technol., Vol. 17 (8) (1999) pp. 1401-1407
- [12] K.Wörhoff, L.T.H.Hilderink, A.Driessen and P.V.Lambeck, *Silicon Oxynitride, a versatile material for integrated optics applications*, J.Electrochem. Soc 149 (2002), pp F85-F91
- [13] P.Tabbers, MSc. Graduation report, *Design, Realisation and Characterization of a Mode-mismatch sensor with thermo-optical feedback and a AEO/PTMS polysiloxane cladding*, Lightwave Devices Group, University of Twente, June 2001
- [14] K.Worhoff, P.V.Lambeck, H.Albers, O.J.F.Noordam, N.F. van Hulst and T.J.A.Popma, *Optimization of LPCVD Silicon Oxynitride growth to large refractive index homogeneity and layer thickness uniformity*, SPIE vol 3099 (1997) pp257-268

- [15] T. Koster, doctoral thesis, *TE/TM based integrated optical sensing platforms*, Lightwave Devices Group, University of Twente, dec. 2000
- [16] R.G.Heideman, G.J.Veldhuis, E.W.H.Jager and P.V.Lambeck, *Fabrications and packaging of integrated optical sensors*, Sensors and Actuators B 35-36, (1996), pp 234-240
- [17] Integrated Optics ed. T.Tamir, second edition 1979 Springer Verlag, Berlin ISBN 0-387-09673-6, p 28
- [18] A.Ymeti, J.S.Kanger, J.Greve, P.V.Lambeck, R.Wijn and R.G.Heideman, *Realization of a multichannel integrated Young interferometer chemical sensor*, Applied Optics, 42, (2003), pp 5649-5660

## 3 The GAC sensor

### 3.1 Introduction

Triggered by the observation made in chapter 2.8, we decided to explore the potential of a Grating Assisted Coupler for use as a chemical sensor. In literature [1] a lot of attention has been paid to Bragg grating based sensors implemented in both fibers and integrated optics. In these sensors the so called contra-directional mode coupling, implying coupling from a forwards propagating guided mode to a backwards propagating one, is exploited. We however are more interested in GAC's based on co-directional coupling, meaning coupling from a forward propagating guided mode to another forward propagating mode, as is the origin of the phenomenon observed in Chapter 2.8.

The basic idea behind this co directional GAC sensor can be given in a qualitative way. Consider a bimodal ridge-type waveguide of which the upper cladding consists of a chemo-optical sensing material. The effective indices of both modes ( $N_0, N_1$ ) depend on the index of the sensing material ( $n_{sens}$ ). The zeroth order mode is launched with power  $P_{in}$ . At and closely around the so-called coupling condition (which will be treated in section 3.2. in more detail) modal power of the launched zeroth order mode is, while propagating through the grating, gradually coupled to the first order mode. The amount of coupled power depends on the difference between the effective refractive indices of both modes,  $\Delta N \equiv N_0 - N_1$ , and hence on the refractive index of the cladding  $n_{sens}$ . Thus both the power fraction in the zeroth order mode,  $P_0/P_{in}$ , and the power fraction in the first order mode,  $P_1/P_{in}$ , are a measure for  $n_{sens}$ . In principle both power fractions can be measured individually by separating the modes spatially from each others by means of a mode splitter (see Figure 3.1). Mode splitters however generally show an appreciable cross talk degrading the resolution of the sensor. Also the type of waveguide channels that will be presented in this chapter will be bimodal in transversal direction and making a mode splitter for these types of modes requires a complicated technology. A better option might be to remove the power of the first order mode completely from the channel, e.g. by vertically tapering the channel to a monomodal one or by applying bends that attenuate specifically the first order mode. Of course now only the modal power  $P_0$  can be determined. Such a removal of the second mode is exactly what happened inside a 'dip' in the SWS response (section 2.8).

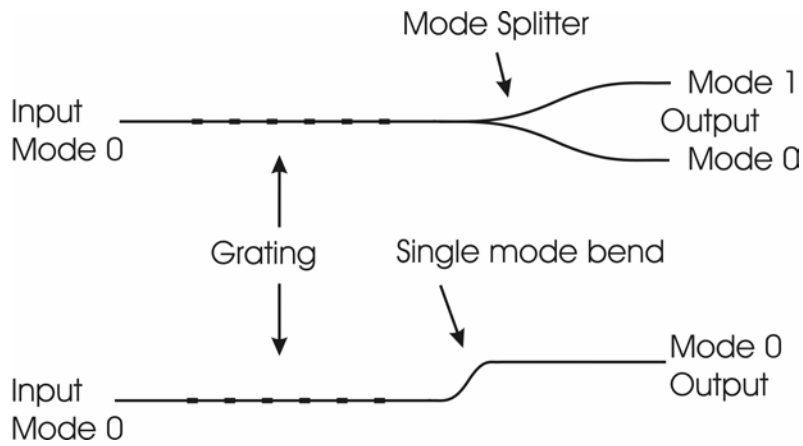


**Figure 3.1. Possible 3.1. layouts of a GAC sensor.**

This chapter is structured as follows: In section 3.2 the basic theory describing the behaviour of this type of sensors will be presented. After that, in section 3.3, a theory will be presented to evaluate the resolution of the total sensor system, consisting of the IO-chip and all the peripheral equipment. Some designs of GAC sensors are treated in section 3.4. The fabrication process is given in section 3.5, just as the characterization of the realized structures. Sensor performance is measured and discussed in section 3.6 and the main results have been summarized in section 3.7.

## 3.2 Theory

In this section some theoretical aspects necessary for the design of the GAC sensor will be treated.

### 3.2.1 The basics

We start from a bimodal waveguide in which locally over a length  $L$  a grating has been implemented (Figure 3.2).

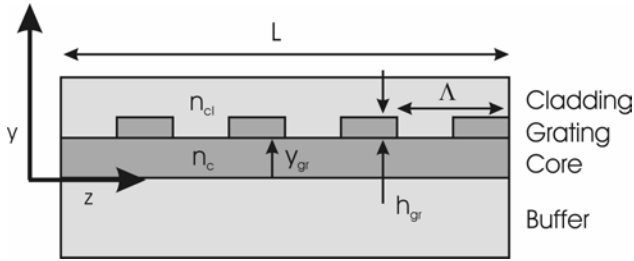


Figure 3.2. An indentation grating on top of a waveguide.

The coupling from the launched zeroth order mode to the first order mode is maximal when:

$$N_0 - N_1 = \Delta N_{res} = m \frac{\lambda_0}{\Lambda} \quad (3-1)$$

Here  $N_i$  is the effective index of mode  $i$ ,  $\lambda_0$  the vacuum wavelength and  $\Lambda$  the grating period.  $m$  is an integer. Expression (3-1) is also known as the resonance, phase matching or coupling condition.

Both forward and backward coupling can be described with the so-called Coupled Mode Theory, valid only if the value of the so-called coupling strength's  $k_{10}$  and  $k_{01}$  are low and if coupling to other modes can be neglected. In CMT a parameter  $s$  is introduced defined as:

$$s = \sqrt{k_{01}k_{10} + \left(\frac{k_0 \delta N}{2}\right)^2} \quad (3-2)$$

in which  $\delta N$  denotes the detuning from the resonance condition ( $\delta N \equiv \Delta N - \Delta N_{res}$ ) and  $k_0 \equiv 2\pi/\lambda_0$ . Limited to TE-modes, a perfect rectangular grating and an  $m$ -value equal to 1, the coupling constants  $k_{10}$  and  $k_{01}$  are identical and are given by the expression [2],[4]:

$$k_{01} = \frac{S_{m,rel}\omega}{2c\sqrt{N_{eff,0}N_{eff,1}}} \frac{\iint E_0(x,y)n(x,y)\Delta n_{gr}E_1(x,y)dx dy}{\sqrt{\iint E_0(x,y)^2 dx dy} \iint E_1(x,y)^2 dx dy} \quad (3-3)$$

Here  $E_i$  is the electrical field profile of TE-mode  $i$ ;  $x$  and  $y$  are the coordinates in lateral and transversal direction respectively;  $x=0$  corresponds to the middle of the waveguide, while  $y=0$  corresponds to the buffer-core layer interface.  $\Delta n_{gr}$  is the grating contrast  $n_c - n_{cl}$  and  $S_{l,rel}$  is the amplitude of the  $m^{\text{th}}$  spatial harmonic of a rectangular grating structure [4], relative to first spatial harmonic of a perfect sinusoidal grating:

$$S_{m,rel} = \frac{4}{m\pi} \sin(m\pi F) \quad (3-4)$$

$F$  denotes the duty cycle of the grating ( $F=0.5$  for a symmetrical grating).

For calculating the coupling constant we have used 2D mode profiles. Since there are no programs available that give the full 2D solution of the modal fields in a form that can be use to evaluate expression (3-3), the effective index method (EIM) is used instead, being a very good approximation for the ridge type waveguide we will utilize later on. The EIM uses the following approximation for the modal field in ridge waveguides:

$$E(x,y) = E(x).E(y) \quad (3-5)$$

Assuming a grating depth very small compared to half width of the transversal mode profiles it is a good approximation to keep the  $E(y)$  constant within the grating region and equal to  $E(y_{gr})$ . Here  $y_{gr}$  denotes the transversal position of the grating. This allows for approximating the expression for the coupling factor as:

$$k_{kl} = \frac{S_{m,rel}\omega n_c \Delta n_{gr}}{2c\sqrt{N_{eff,0}N_{eff,1}}} \frac{E_k(y_{gr})E_l(y_{gr})h_{gr} \int E_k(x)E_l(x)dx}{\sqrt{\int E_k^2(x)dx} \int E_k^2(y)dy \int E_l^2(x)dx \int E_l^2(y)dy} \quad (3-6)$$

Close to phase matching ( $\Delta N \approx \Delta N_{res}$ ), neglecting coupling to other guided or radiation modes and assuming no propagation losses for the co-directional coupling of TE modes, we can derive:

$$P_{1,out} = P_{0,in} k_{01}^2 \left( \frac{\sin(s.z)}{s} \right)^2 \quad (3-7)$$

Where  $z$  is the coordinate along the propagation direction and  $z=0$  defines the beginning and  $z=L$  the end of the grating section.

A useful quantity at forward coupling is the coupling length  $L_{cij}$ , which gives the  $z$ -value at which all modal power is coupled from mode  $i$  to mode  $j$  in case the resonance condition is satisfied:

$$L_{c01} = \frac{\pi}{2k_{01}} \tag{3-8}$$

Note that after  $z = L_{c01}$ , power starts to couple back again from the first order to the zeroth order mode. From expression (3-8) and (3-6) it can be seen that  $L_{c01}$  is approximately inversely proportional to  $\Delta n_{gr}$  and the grating depth  $h_{gr}$ .

### 3.2.2 Comparison co and contra directional GAC

For the contra-directional coupling between the forward propagating fundamental mode to the backward propagating one, the power coupled to the reflected mode for a grating length  $L_{gr}$  can be derived [2] to be:

$$P_1 = P_0 k_{01}^2 \frac{\sinh^2(s.L_{gr})}{s^2 \cosh^2(s.L_{gr}) + \left(\frac{k_0 \delta N}{2}\right)^2 \sinh^2(s.L_{gr})} \quad (3-9)$$

Here  $P_1$  denotes the power which is coupled from the forward propagating fundamental mode to the backward propagating one. The power transmitted by the grating,  $P_{out}$ , is given as

$$P_{out} = P_0 - P_1 \quad (3-10)$$

Both for co and contra-directional coupling, the coupled power at the end of the grating depends on the input power  $P_0$ , the coupling constant  $k_{01}$ , the grating length  $L$  and the difference between  $\Delta N$  and  $\Delta N_{res}$  ( $\delta N$ ). However their dependence on  $L$  is completely different. While for co-directional coupling, during the propagation through the grating, the power is continuously exchanged by both modes, for contra-directional coupling an increase of the grating length only results in a gradual decrease of the transmitted power. This has been illustrated in Figure 3.3, where the output power is given as a function of  $\delta N$  for co-directional and contra-directional coupling within gratings with an identical coupling length ( $L_c=146 \mu\text{m}$ ) and grating length ( $L= 13.L_c$ ). Just the period of both gratings is different, being adapted to the appropriate coupling condition.

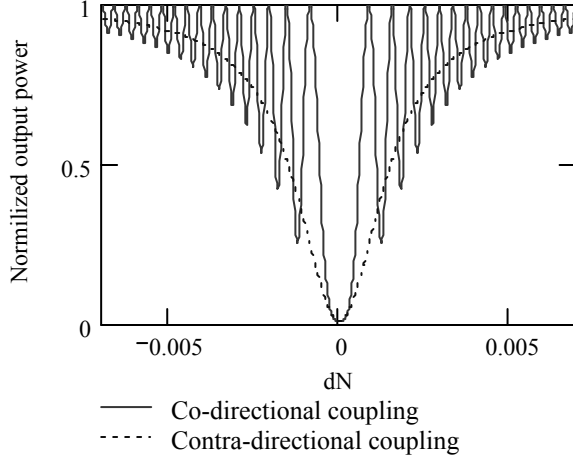


**Figure 3.3. Comparison co and contra directional coupling.**

It can be seen that in the same  $\delta N$  range the out put power of the transmitted zeroth order power shows one broad minimum for contra-directional coupling, while for co-directional coupling the power strongly oscillates. This implies that the sensitivity  $\partial P_{out}/\partial \delta N$  for co-directional coupling can be locally much larger than for contra-directional coupling and just this prospect on a much higher sensitivity makes the co-directional GAC sensors interesting. The value of  $\delta N$  which corresponds to the first  $P_{out} = 1$  peak in Figure 3.3 can easily be derived from expression (3-7):

$$\delta N_{first\_peak} = \frac{1}{k_0} \sqrt{\frac{2k_{01}\pi}{L} + \frac{\pi^2}{L^2}} \quad (3-11)$$

It can be seen that the peaks (or dips) get closer with increasing  $L$  and decreasing  $k_{01}$ . Also, using expression (3-7), the half-width of the envelope of the curve can be expressed as:

$$\delta N_{half\_width} = 2 \frac{k_{01}}{k_0} \quad (3-12)$$

For co-directional coupling the  $P_{out}$  versus  $\delta N$  curves have been calculated for  $L = L_c$ ,  $L = 5/4 L_c$  and  $L = 6/4 L_c$  (see Figure 3.7). This corresponds with gratings of a constant length with increasing coupling strength. The curves clearly show that the larger the deviation from  $L = L_c$ , the smaller the amount of coupled power, becoming zero even for  $L = 2 L_c$ . Hence we can conclude that at given length of the grating for co-directional coupling the shape of the  $P_{out}$  versus  $\delta N$  curves strongly depend on the value of the coupling constant.

Hence the sensitivity will be larger, the smaller the coupling strength and the larger the length of the grating, provided that the length just corresponds with an odd integer times

the coupling length, where higher values of this integer favor the sensitivity. A very good control of the coupling length might be necessary to fulfill the last condition and this will be investigated in section 3.2.3.

It is interesting to compare the prospect of the co-directional GAC sensors qualitatively with those of the Bragg sensors. In foregoing we have shown that in certain  $\delta N$  ranges the sensitivity  $\partial P_{out}/\partial \delta N$  of the co-directional GAC sensors is expected to be much larger than that of the Bragg sensors. However the sensitivity  $\partial \Delta N / \partial n_{sens}$  of the Bragg sensors is at least twice that of the co-directional GAC sensor, because in the Bragg sensor  $\Delta N = 2N_0$ , while in the co-directional GAC  $\Delta N = N_I - N_0$ .

We have seen, that in the co-directional GAC sensors the sensitivity is strongly dependent of the ratio of the grating length to the coupling length, being at maximum if the ratio is an odd integer and being minimal if the ratio is an even integer, Hence for obtaining good sensitivity a good control of the coupling strength is required. In the Bragg sensor this ratio is far from critical, good effects are obtained if  $L \gg L_c$ .

It has to be noted that the co-directional GAC sensors are vulnerable to losses to radiation modes, meaning that the launched mode suffers also to grating assisted coupling to radiation modes. Such a coupling is not possible in Bragg sensors. For the gratings that we have designed, these radiation losses are very modest and they are smaller than 0.25 dB/mm.

With respect to technology, the co-directional GAC's being bimodal in the transverse direction will require much thicker core layers than the monomodal Bragg sensors. However the Bragg sensors require relatively small grating periods (around 400 nm) which cannot be obtained with the photolithography as available in MESA<sup>+</sup> clean room lab. Required grating period in the co-directional GAC's are about one order of magnitude larger.

So in general: in theory, for perfect technology, the GAC sensors can show much larger sensitivities, the length of the grating expressed as its ratio to the coupling length being a very critical parameter. The GAC sensor at first sight is much more demanding on the control of technology. Hence it is clear that a tolerance analysis of the co-directional GAC sensor is required.

### 3.2.3 Influence of limitations of technology and equipment

In order to obtain a high sensitivity the  $\Delta N$  value has to be close to  $\Delta N = \lambda_0/\Lambda$  (i.e.  $\delta N = 0$ ). In addition, the sensor length has to be an odd multiple of the coupling length. So both  $\Delta N$  and the coupling strength  $k_{01}$  have to be controlled very well.

#### 3.2.3.1 Uncertainty of the coupling strength

There is no practical way to actively compensate for an error in  $k_{01}$  after the sensor has been fabricated. Therefore during the fabrication process good control over the coupling strength is necessary to satisfy the requirement  $L = (1+2i)L_c$ . In this section we'll investigate the influence of uncertainties in different device parameters on the uncertainty of  $k_{01}$ .

From expression (3-6) we can derive that:

$$\frac{\Delta k_{01}}{k_{01}} = \frac{\Delta h_{gr}}{h_{gr}} \quad \text{and} \quad \frac{\Delta k_{01}}{k_{01}} \approx \frac{\Delta \Delta n_{gr}}{\Delta n_{gr}}$$

Here  $\Delta$  denotes the uncertainty in the parameter. Relative errors in grating depth and grating contrast translate directly into relative errors in  $L_c$ .

Applying the sensitive material directly on top of a surface grating etched in the core layer would have the consequence that  $\Delta n_{gr}$  would vary with the measurand value too. A better option is to have on top of this grating a very thin planarized passive layer, e.g.  $\text{SiO}_2$ , leaving  $\Delta n_{gr}$  constant. Only small  $\Delta n_{sens}$  induced changes of field profile would influence the coupling strength. The uncertainty in  $\Delta n_{gr}$  is mainly determined by the uncertainties in the refractive indices of core and cladding layer and can be estimated to be 0.1 % only.

The uncertainty in the grating depth is very influential. In order to have a small coupling strength,  $h_{gr}$  has to be small: in the  $\text{SiO}_2/\text{Si}_3\text{N}_4/\text{SiON}$  layer stacks we will apply,  $h_{gr}$  will be about 1 nm only. In order to have a relative error in  $k_{01}$  of 1% only, the grating depth should have to be controlled with an accuracy of  $10^{-2}$  nm!! This requires a material with very good run-to-run reproducibility properties and a very good control of the etching parameters. It is well known, that an 0.5-1.0 nm thick surface layer of the  $\text{Si}_3\text{N}_4$  layer is partly oxidized, the degree of oxidation being dependent on the cooling process. Hence it is advised to remove this layer before implementing the grating. Also it is clear, that the etching process has to be very slow using diluted etching solutions under well controlled conditions of concentrations and temperature. Careful experiments have to be performed in order to determine the remaining uncertainty. For the coming analysis we will estimate this relative inaccuracy to be 3%.

Also other factors influence the accuracy of the coupling strength: for example the uncertainties in the channel structure parameters, which will influence the field at the position of the grating. Another factor is a small uncertainty in the grating duty cycle as a consequence of some under-etch during definition of the grating.

Although no data exist on these factors we will estimate them to be equivalent to a contribution to the uncertainty in  $k_{01}$  of about 2 %. Summing up all uncertainties we arrive at an accidental error of about 6% in the coupling constant.

From expression (3.7) it can be easily calculated that in case  $L=L_c$ , a 6% deviation corresponds with a minimum power being -20 dB of the input power. Also in practice, often it has been found that minimum power, for various reasons, can not be reduced below that level.

### 3.2.3.2 Uncertainties in $\Delta N$

The GAC sensor requires a bimodal waveguide. This waveguide can be bimodal either in lateral or transversal direction. Simulations show that the uncertainty in  $\delta N$  ( $\Delta \delta N$ ) is mainly determined respectively by the uncertainty in the waveguide width ( $\Delta W$ ) or the core thickness ( $\Delta h_c$ ). Since with our technology the relative accuracy of  $h_c$  is much better than the relative accuracy of  $W$ , a bimodal waveguide in transversal direction is preferred. The influence of  $\Delta h_c$  on  $\Delta \delta N$  can be expressed by the partial derivative

$$\Delta \delta N_{hc} = \frac{\partial \delta N}{\partial \Delta h_c} \Delta h_c \quad (3-13)$$

The high uncertainty in  $\delta N$  requires a way to tune  $\delta N$  to an optimum value. For just obtaining “proof of principle” we can change  $n_{sens}$  to shift  $\delta N$ . The range over which the  $\delta N$  can be shifted is determined by the available range in  $n_{sens}$  ( $\Delta n_{sens}$ ) and should be sufficiently high to compensate for both  $\Delta \delta N_{hc}$  and the effects of the uncertainty in  $k_{01}$  (expression (3-14)).

$$\Delta \delta N_{nsens} = \frac{\partial \delta N}{\partial n_{sens}} \Delta n_{sens} \quad (3-14)$$

In practical applications however the  $n_{sens}$  is determined by the measurand and the sensor should operate at optimum resolution at a fixed  $n_{sens}$  in the middle of its variation range. Another way of tuning  $\delta N$  is needed which provides sufficient tuning range to compensate  $\Delta \delta N_{hc}$  and the  $\Delta k_{01}$  effects and in addition provides sufficient tuning accuracy to set the working point with the required accuracy.

Several options have been considered: electro-optical, thermo-optical, mechano-optical and wavelength tuning. Electro-optical tuning has the disadvantage of relative small tuning ranges and of a complicated technology to implement. Thermo-optical tuning will deliver a larger tuning range, but can influence the interaction between the measurand and receptor layer in unforeseen, thus unwanted ways. Mechano-optical tuning by bending the optical chip changes both the grating period and the refractive indices of the layers. Its implementation might be complicated and preliminary calculations show that the tuning range in  $\delta N$  is too small to be useful.

Wavelength tuning has the big advantage that it can be applied externally, thus not complicating the fabrication process of the sensor chip itself. The obvious disadvantage is of course that an external tunable light source adds to the cost of the complete sensing system. The wavelength tuning range of the used tunable laser together with the channel structure determine the  $\delta N$  tuning range and its wavelength resolution the precision of the  $\delta N$  tuning. Calculations show that both the range ( $\Delta\lambda_{tun}$ ) and resolution ( $\Delta\lambda_{res}$ ) of the tunable laser we intend to use are sufficient (section 3.3.8). The tuning range in  $\delta N$  can be calculated using the following partial derivative:

$$\Delta\delta N_{\lambda} = \frac{\partial\delta N}{\partial\lambda} \Delta\lambda_{tun} \quad (3-15)$$

Note that  $\Delta\delta N_{hc}$ ,  $\Delta\delta N_{nsens}$  and  $\Delta\delta N_{\lambda}$  are mutually connected. It is not possible to change one and not change the two others. This has to be taken into account with the design process.

### 3.2.3.3 Propagation loss and losses due to coupling to radiation modes

In the grating two types of losses can be observed: the usual propagation losses, due to scattering on inhomogeneities and absorption (being around 0.5 dB/cm) and losses due to power transfer to radiation modes. No analytical formulas are available which quantitatively describe the latter type of losses. We have to rely on BPM and BEP calculations for calculating them. For all structures we have designed in later sections of this chapter these losses appeared to be lower than 2.5 dB/cm. Taking into account these losses results into the appearance of an additional factor in expression for the coupled power [2]:

$$P_1 = P_0 k_{01}^2 \left( \frac{\sin(s.z)}{s} \right)^2 e^{-(\alpha_0 + \alpha_1)z} \quad (3-16)$$

In which  $\alpha_i$  is the imaginary part of the propagating constant of mode i. In later sections we shall assume  $\alpha_0 = \alpha_1$ .

Experimentally the effects of the losses inside the grating and in other channel sections of the IO circuitry can (nearly) be eliminated by introducing an additional experimental step: before transporting the sample liquid to the sensing section, the sensor should be supplied by a liquid with a refractive index corresponding with a  $\delta N$  far from the resonance condition. The output power measured in this state then takes over the role of  $P_{in}$ . Notice that here we have assumed that the losses due to coupling to radiation modes do not depend on the refractive index of the liquid on top of the sensing section.

### 3.2.4 Resolution

Up to now we have focused on the sensitivity of the sensor, but our main interest is to investigate what the best resolution is that can be obtained. In case of bulk sensing (also called homogeneous sensing) the resolution is defined as the minimum change in refractive index of the sensing layer ( $n_{sens}$ ) that can still be detected ( $\delta n$ ). For surface sensing, as is used in immuno-sensing applications, the resolution is defined as the minimum change in effective thickness  $h_i$  of the sensing layer that can still be detected ( $\delta h_i$ ). Since the operation of the sensor is functionally identical for both bulk and surface sensing, from now on the theory will be confined to bulk sensing only. Just as in case of the SWS the resolution will depend on both the peripheral equipment and the structure of the optical part of the sensor; the analysis of the best attainable resolution will proceed along similar lines as we did for the SWS.

We shall start from the assumption that the only losses that occur are those related to removing the power of mode 1 from the IO system. Propagation losses and losses due to coupling to radiation modes can be taken into account in the way we described in previous section. Hence all optical power at the beginning of the sensor is assumed to be coupled into the fundamental mode of the bimodal waveguide, so  $P_{0,in} = P_{in}$ . At the output of the GAC sensor the remaining power in the fundamental mode should be given as  $P_{out} = P_{in} - P_{1,out}$ , where  $P_{1,out}$  represents the power coupled to the first order mode which has been removed out of the output channel in one of the ways described earlier. The error in the output power is given by  $(q_1 + q_2)(P_{in} - P_{1,out})$ , where just as in the SWS  $q_1$  and  $q_2$  denote the relative accidental errors in respectively the input power  $P_{in}$  and read out system.  $P_{min}$  stands for the lower limit of the dynamic range of the detector. The resolution  $\delta n$  can now be expressed as:

$$\delta n = \frac{(q_1 + q_2)(P_{in} - P_{1,out})}{\frac{\partial P_1}{\partial s} \frac{\partial s}{\partial \delta N_{res}} \frac{\partial \delta N}{\partial n_{sens}}} \quad (3-17)$$

By inserting

$$\frac{\partial P_{1,out}}{\partial s} = 2P_{1,out} \left( \frac{\cos(sz)}{\sin(sz)} z - \frac{1}{s} \right) \quad (3-18)$$

and

$$\frac{\partial s}{\partial \delta N} = \frac{k_0^2 \delta N}{4s} \quad (3-19)$$

in expression (3-17), we arrive at:

$$\delta n = \left| \frac{(q_1 + q_2) (s^2 - k_{01}^2 \sin^2 sL) \frac{2s^2}{\frac{\partial \delta N_{res}}{\delta n_{sens}} (k_{01}^2 \sin^2 sL) k_0^2 \Delta N_{res} (sL \frac{\cos(sL)}{\sin(sL)} - 1)}}{\frac{\partial \delta N_{res}}{\delta n_{sens}} (k_{01}^2 \sin^2 sL) k_0^2 \Delta N_{res} (sL \frac{\cos(sL)}{\sin(sL)} - 1)} \right| \quad (3-20)$$

Taking into account expression (3-2) we can conclude that the resolution depends on three design parameters only:  $L$ ,  $k_{01}$  and  $\delta N$ . However expression (3-20) does not open a way for optimizing the resolution in an analytical way. Numerical evaluations are required.

Nevertheless it can be seen that for systems wherein  $L=\pi/2k_{01}$  and  $\delta N \rightarrow 0$  (i.e. the resonance condition is approached), expression (3-20) predicts that the resolution  $\delta n$  approaches zero. For this situation however also  $P_{out}$  drops below  $P_{min}$ , violating the condition that  $P_{out} > P_{min}$ .

Both practical experience with coupling based devices and the tolerance analysis given in section 3.2.3 show that it is very hard to get a difference between maximum and minimum output power which is larger than 20 dB. Notice that also the capture of stray light at the chip output can contribute to this limitation. To make the model more realistic this should be introduced in expression (3-20), which can be done relatively easy by modifying expression (3-7) into:

$$P_{1,out} = (1 - 10^{\frac{g}{10}}) P_{0,in} k_{01}^2 \left( \frac{\sin(s.z)}{s} \right)^2 \quad (3-21)$$

(with  $g = -20$  dB) and following exactly the same procedure as mentioned above. Note that by using expression (3.16) automatically the condition  $P_{out} > P_{min}$  ( $= 0.01 P_{in}$ ) will be satisfied.

### 3.2.5 Investigation of the resolution

In order to get some idea of the influence of the design parameters and to look for possible trends we have calculated  $P_{out}$  and  $\delta n$  as functions of  $\delta N$  (which can be tuned in practice, see section 3.2.3.2) for different values of  $k_{01}$  and  $L$ . From all calculations we did, we will present here only a few. Generally the trends we will deduce from them are confirmed by more calculations, which are not presented here. For the calculations presented here the following parameter values have been taken:  $(q_1 + q_2) = 0.002$ ,  $\partial N / \partial n_{sens} = 0.1$ ,  $\lambda = 634$  nm,  $P_{in} = 1$  mW,  $P_{min} = 1 \mu\text{W}$  (too optimistic) and  $L_c = 1$  cm. Note that these values differ from those of the sensor which is eventually designed as discussed in section 3.3.

In Figure 3.4, with  $L=L_c=1$  cm, a typical GAC characteristic is shown.

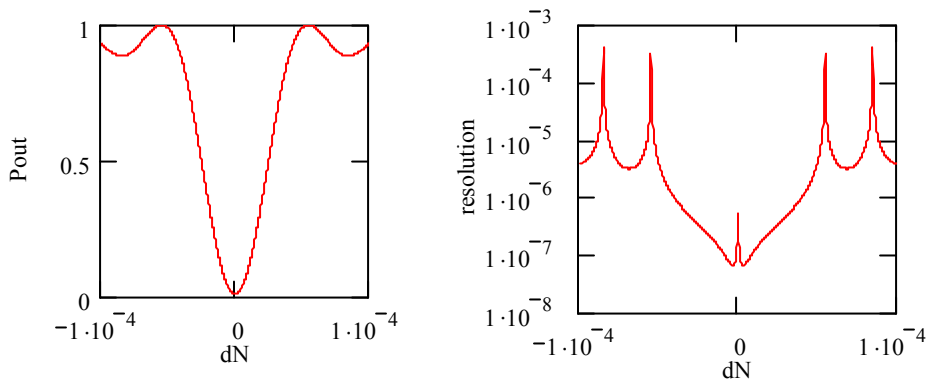


**Figure 3.4. Typical  $P_{out}$  and  $\delta n$  characteristic for  $k_{01}=\pi/2L$  and  $L=L_c$ .**

From this characteristic we can conclude:

- If  $\partial P / \partial N = 0$  there is a peak in the resolution, meaning a bad resolution.
- The resolution is good when  $P_{out}$  is small and  $\partial P / \partial N$  is large.
- Best resolution is not obtained at  $\delta N = 0$  but at  $\delta N$  values close to  $\delta N = 0$  (related to the  $g$  value).

In Figure 3.5  $L$  is increased to  $3L_c$  with  $L_c$  staying fixed to 1 cm.

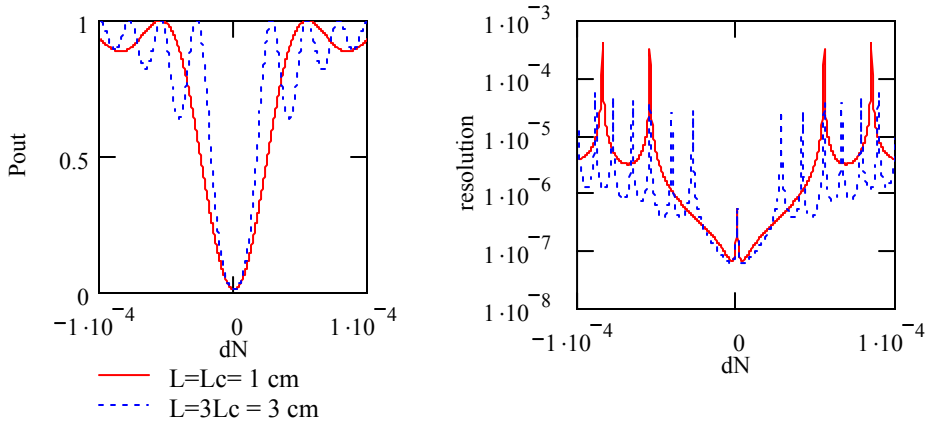


**Figure 3.5.  $P_{out}$  and  $\delta n$  characteristics for  $L_i L_c =$  and different grating lengths  $L$ .**

It can be concluded that by increasing of the integer  $i$ , while  $L = (2i+1)L_c$  and  $L_c$  is kept constant:

- The best resolution is somewhat improved.
- At the local minima of  $\delta n$  the resolution is improved.

In next figure the sensor length  $L$  is fixed to a value of 1 cm, but the curves related to two values of  $L_c$  are compared:  $L_c = L$  and  $L_c = 1/3 L$ .

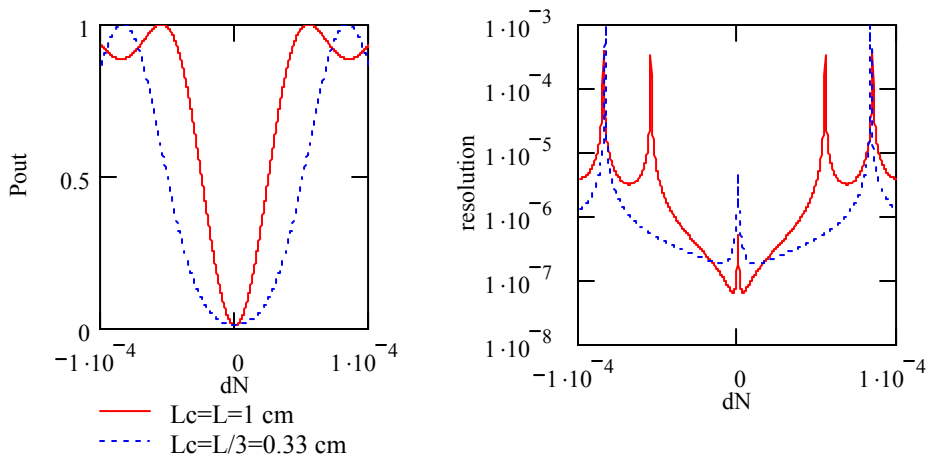


**Figure 3.6.  $P_{out}$  and  $\delta n$  characteristics for  $L=1$  cm and two values of  $L_c$ .**

From the curves it can be concluded, that by an increase of the integer  $i$  while  $L = (2i+1)L_c$  and  $L$  is kept constant:

- The  $P_{out}$  versus  $\delta N$  curves expands laterally.
- The best resolution is degraded.
- The resolution at the local minima in  $\delta n$  is degraded.

In the next system we illustrate the influence of  $L$  being unequal to  $(1+2i)L_c$  by varying at a fixed value of  $L=1$  cm, the coupling length from  $L_c = L$  ( $i=0$ ) to  $L_c = 5/4L$  and  $L_c = 6/4L$ . The corresponding curves are given in Figure 3.7.

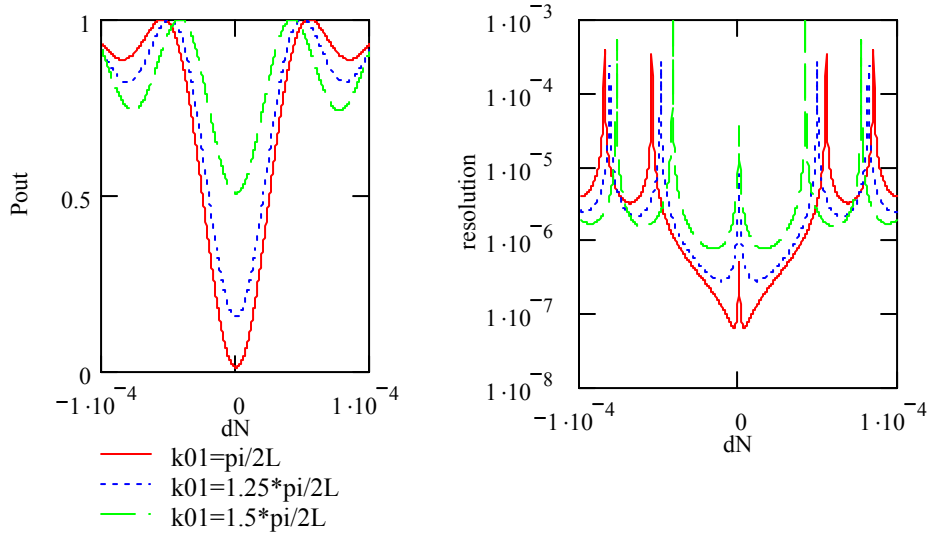


**Figure 3.7.  $P_{out}$  characteristics for fixed  $L$  and different values of  $L_c \neq L/(2i+1)$ .**

From Figure 3.7 it can be concluded that the more the condition  $L = (2i+1)L_c$  is violated

- The more the  $P_{out}$  versus  $\delta N$  curves contract in vertical direction.
- The more the best resolution degrades.
- The more the resolution at the local minima improves.

From all the obtained results we can derive criteria for optimizing  $k_{01}$  and  $L$  for obtaining the best values of the resolution:

- A small value of the coupling strength
- A grating length  $L$  equal to  $L = (2i+1)L_c$ , where  $i$  is an integer.
- Taking a high value of  $i$ .

In Figure 3.4 it is seen that a resolution better than  $\delta n = 10^{-7}$  is attainable. This looks very promising. However one has to realize that in order to obtain this resolution it has been assumed that  $k_{01}$  and  $\delta N$  can be controlled perfectly. Hence here we have required a perfect match between the grating length and the coupling length, a requirement that can not be met in practice. Starting from an uncertainty in the coupling length of 6 % it is clear that at a sensor length of e.g. 13 times the coupling length, the difference between the intended  $L = 13 L_c$  and the real relationship can be in the order of  $0.7 L_c$ , deteriorating strongly the sensitivity and the resolution. Note also that in practice the sensor length is limited. However we can propose a way to escape on most of these limitations. For that we have to modify the structure (Figure 3.8).

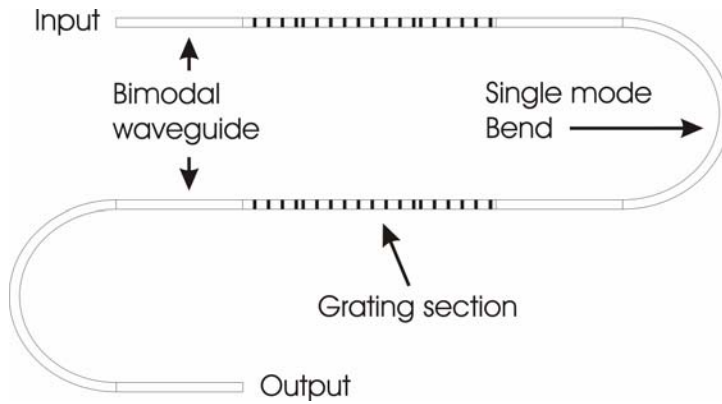


**Figure 3.8. Possible implementation of a GAC sensor.**

We make an IO circuit consisting of several  $L=L_c$  gratings in series, inserting in between each couple of adjacent gratings a function that removes all first order power exiting the previous grating, e.g. a bend, a tapered monomodal section or a combination of both. In that way each grating starts with the exit zeroth order mode power of the previous grating only. Also the total length of all gratings can be e.g.  $13 L_c$  without any summation of the inaccuracy of the coupling length. The structure in Figure 3.8 could also be implemented in a spiral configuration, thus affording for a larger accumulated grating length than possible with the configurations shown in Figure 3.1.

### 3.2.6 Operation of the GAC sensor

In this section two possible methods of operation (way of measurement and calibration) of the GAC sensor are treated. In both methods the option of (static and dynamic) tuning of the wavelength of the laser source is essential.

For both methods we assume, that within the tuning range of the light source a wavelength  $\lambda_0$  can be found at which at a measurand value zero, the sensor state will correspond to a sensitive point on the  $P_{out}$  versus  $\delta N$  curves, as are given in Figure 3.4. This working point will be given by the parameter values  $\lambda_0, n_{sens,0}$  and  $P_{out,0}$ . Differences between the actual parameter values and those of the working point are referred to by  $\Delta\lambda$ ,  $\Delta n_{sens}$  and  $\Delta P_{out}$  respectively. It is supposed that these differences are so small that linearization, as will be described later on, is allowed. For measurements where high resolutions within small ranges are required, this approximation is generally valid. The dispersion of the relevant materials is ignored.

In the first method the value of  $P_{out}(\delta N(n_{sens}, \lambda))$  is measured at a given wavelength, both at the actual and the zero value of the measurand. From these data  $\Delta n_{sens}$  will be determined using the relationship

$$\Delta n_{sens} = \int_{P_{out,0}}^{P_{out}} \left. \frac{\partial n_{sens}}{\partial P_{out}} \right|_{\lambda} dP_{out} = \int_{P_{out,0}}^{P_{out} + \Delta P_{out}} \left. \frac{\partial \lambda}{\partial P_{out}} \right|_{n_{sens}} A(\lambda, n_{sens}) dP_{out} \quad (3-22)$$

The  $P_{out}/\partial\lambda$  can be measured continuously by modulating the wavelength of the tunable laser and  $A(\lambda, n_{sens})$  is a parameter that needs to be determined in a calibration step:

$$A(\lambda, n_{sens}) = \left. \frac{\partial n_{sens}}{\partial \lambda} \right|_{\delta N} = - \frac{\left. \frac{\partial \delta N}{\partial \lambda} \right|_{n_{sens}}}{\left. \frac{\partial \delta N}{\partial n_{sens}} \right|_{\lambda}} \quad (3-23)$$

We will suppose that the difference between the actual states and the working point is so small, that it is allowed to approximate  $A(\lambda, n_{sens})$  by  $A(\lambda_0, n_{sens,0})$ . For these small changes around the working point, expression (3-22) can then be approximated by:

$$\Delta n_{sens} = A(\lambda_0, n_{sens,0}) \frac{\Delta P_{out}}{\left. \frac{\partial P_{out}}{\partial \lambda} \right|_{n_{sens,0}}} \quad (3-24)$$

For utilizing this relationship,  $A(\lambda_0, n_{sens,0})$  has to be determined (only once) by calibration. For determining the  $A$ -value, we offer a known value of  $n_{sens}$  and determine the wavelength difference  $\Delta\lambda$  required to equalize  $P_{out}$  to the value  $P_{out,0}$ . Then  $A(\lambda_0, n_{sens,0})$  can be calculated from expression (3-23).

If desired a more accurate  $A$ -value can be determined by ending the Taylor series for  $A(\lambda, n_{sens})$  not directly after the constant term, but after the linear terms:

$$A(\lambda, n_{sens}) = A_0 + a.\Delta\lambda + b.\Delta n_{sens} \quad (3-25)$$

Here the constants  $a$  and  $b$  can be found by determining the  $A$ -value at two additional intervals within the  $(\lambda, n_{sens})$  domain.

The resolution as given in expression (3-26) has to be optimized by varying  $\lambda$ .

$$\delta n = A(\lambda_0, n_{sens,0}) \frac{(q_1 + q_2)(P_{out})}{\frac{\partial P_{out}}{\partial \lambda}} \quad (3-26)$$

Note that the resolution depends on  $n_{sens}$  via  $P_{out}$  and  $\partial P_{out}/\partial \lambda$ . This resolution is guaranteed for a small  $n_{sens}$  range only.

In the second method of operation, the output power is kept constant at  $P_{out,0}$  by adjusting the wavelength. The change in wavelength  $\Delta\lambda$  required for this is a measure for  $\Delta n_{sens}$ :

$$\Delta n_{sens} = \int_{\lambda_0}^{\lambda_0 + \Delta\lambda} A(\lambda, n_{sens}) d\lambda \quad (3-27)$$

In this method both  $P_{out}$  and consequently approximately  $\partial P_{out}/\partial \lambda$  are being kept constant and thus continuous operation at constant resolution is guaranteed.

For more accurate measurements expression (3.25) can be applied, resulting into the following relation between  $\Delta n_{sens}$  and  $\Delta\lambda$ .

$$\Delta n_{sens} = \frac{A_0.\Delta\lambda + \frac{1}{2}a.\Delta\lambda^2}{(1 - b.\Delta\lambda)} \quad (3-28)$$

Thus, in order to perform a measurement, the following procedure has to be performed:

1. Determine  $A_0$  and if required  $a$  and  $b$ . Most probably this calibration step has to be performed only once for each (batch of) sensor(s).
2. By wavelength tuning, the resolution as expressed in (3-26) has to be optimized.
3. Measure  $\Delta n_{sens}$  at/around this optimum wavelength by either operating the sensor according the constant output power or the constant wavelength method.

### **3.3 Design of the GAC sensor**

#### **3.3.1 Introduction**

The design process of the co-directional GAC sensor is very similar to that of the SWS. In fact it has been evolved according the same lines and all aspects taken into account in the SWS design are relevant to the GAC sensor too. However there are two main differences. At first a substantial one: for the GAC a bimodal waveguide channel is required in which the mode coupling from the launched zeroth order mode to the first order mode will occur, while in addition some monomodal sections are needed for removing the power of the first order mode from the channel structure. Secondly a design objective had to be added originating from boundary conditions as to time and funding (clean room lab activities are very expensive!) available for realization of these sensors: one batch of sensors only should be realized, while there would be very limited opportunities to develop new process steps. So we focused on a “safe” design, which should enable (at preference even should guarantee the possibility) to show that the ideas about the GAC sensor were correct (proof of the principle) even if it should be at cost of our second aim to determine the limits of the resolution potential of these sensors. The designed sensor should show a high tolerance of its operation to fabrication errors. We shall limit ourselves to bulk (or homogeneous) sensing. For surface sensing a similar even nearly identical approach will be required.

Because of the large similarity in both the design approach and design aspects of SWS and GAC sensors we shall not treat the design of the GAC sensor in as much detail as has been done for the SWS sensor. We shall assume that the reader is familiar with chapter 2 and often we shall refer to discussions and reasoning given there. The focus will be on the design aspects which are novel and which originate from the specific requirements of the GAC sensor. Of course all technological boundary conditions mentioned in chapter 2 section 2.4.2 are valid here too.

#### **3.3.2 Wavelength**

The operating wavelength is chosen to be around 632.8 nm, not only for the reasons mentioned in section 2.4.4.1, but also because it turned out to be the lowest wavelength around which tunable lasers were commercially available. In addition larger wavelengths would require a larger  $\text{Si}_3\text{N}_4$  thickness, which causes problems with the fabrication (maximum core thickness is 600 nm).

### 3.3.3 Nature of bimodality and layer stack

We have chosen for an in transversal direction bimodal waveguide structure for two reasons. Firstly, because in ridge type channel guides with a perfect lateral symmetry and gratings produced by etching segments over whole the channel width, symmetry forbids any coupling between the zeroth and the first order mode. Breaking the symmetry of the channels or the gratings should introduce novel technological uncertainties degrading the control of the coupling strength even more. Hence lateral coupling would require at least a three modal channel, introducing new complications. Secondly we have concluded (section 3.2.3) that control of the resonance condition is much easier in transverse bimodal structures. However the choice for transversal bimodal structures requires a very thick core layer, while also the introduction of monomodal sections will require extra technological steps.

Using SiON technology several types of transversally bimodal layer stack structures can be realized. In section 2.9 a structure with a 60 nm thick  $\text{Si}_3\text{N}_4$  core layer and a 2  $\mu\text{m}$  thick  $\text{SiO}_2$  core layer showed an interesting bimodality, provided that the layer on top of the  $\text{SiO}_2$  layer should have a refractive index lower than that of the cladding material: a zeroth order mode, well confined in the structure and a first order mode propagating mainly through the cladding (see Figure 2.41). As a consequence  $\Delta n_{sens}$  induced  $\Delta(N_1 - N_0)$  values are nearly equal to  $\Delta N_1$ , resulting into a relatively high  $\partial\Delta(N_1 - N_0)/\partial\Delta n_{sens}$  sensitivity. However we have chosen for a more conventional transversally bimodal  $\text{SiO}_2/\text{Si}_3\text{N}_4/\text{SiON}$  structure in which both modal field profiles are mainly located in the  $\text{Si}_3\text{N}_4$  core layer, not being aware of the technological problems we would meet with that type of structures.

For the three layer stack with semi-infinite outer layers, we calculated for a wavelength of 632 nm,  $n_{\text{SiON}} = 1.47$  and  $n_{\text{Si}_3\text{N}_4} = 2.01$  a cut off thickness of the first order TE modes of 300 nm. Hence in the bimodal section the core layer thickness has to exceed this value. Such a  $\text{Si}_3\text{N}_4$  layer cannot be made by our current LPCVD technology, because as a result of stresses the maximum thickness that can be realized without cracking is 170 nm only. So we have to rely on PECVD made  $\text{Si}_3\text{N}_4$  layers. Preliminary ellipsometric experiments showed that if these layers are applied on top of a thermally grown  $\text{SiO}_2$  layer they show some initial layer, which can be modeled by a 3 nm thick layer with a refractive index 1.70. The refractive index at 632 nm wavelength of the remaining part of the PECVD layer has been measured to be 1.92. The cut off thickness of the zeroth, first and second order TE modes are calculated to be 15 nm, 272 nm and 529 nm respectively. Hence  $h_c$  has to be larger than 15 nm. Other factors are codetermining the  $h_c$ -value. Firstly the value of  $(\partial\delta N/\partial n_{sens})$  is determined by  $h_c$ : the smaller  $h_c$ , the larger  $(\partial\delta N/\partial n_{sens})$ . However, the required grating period is decreasing with  $h_c$ , thus the minimum allowed grating period of 4  $\mu\text{m}$  determines the minimum  $h_c$ , which is  $h_c = 540$  nm. So finally we have chosen  $h_c$  to be 540 nm in the bimodal section.

The  $\text{Si}_3\text{N}_4$  layer thickness in the monomodal sections should be in between 15 nm and 272 nm, being the cut off thickness of the zeroth and first order modes respectively. For removing the small amount of TM light that might be coupled into the chip it is advantageous that the channel cannot support any TM mode, meaning that  $h_c$  has to be lower than cut off thickness of the  $\text{TM}_0$ -mode, 26 nm. Later on, after definition of the core ridge height,  $h_{\text{ridge}} = 20$  nm, and the channel width  $W = 2.4\mu\text{m}$ , we have calculated that efficient fiber to chip coupling requires  $h_c = 20\text{-}30$  nm. From the desire to have a total thickness of the layer stack of  $5\mu\text{m}$  at maximum and the requirement to have a Si induced modal attenuation of the zeroth order mode smaller than 0.01 dB/cm, it can be derived that  $h_c$  has to be larger than 40 nm. For having a simpler technology we decide to have one  $h_c$  value for both the monomodal and the fiber-to-chip sections, being 40 nm.

At first sight it may look as if we have now sacrificed our desire to remove all TM light. By adjusting the thickness of the  $\text{SiO}_2$  buffer layer to  $2.5\mu\text{m}$ , however, a  $\text{TM}_0$  slab mode attenuation caused by power leakage into the Si wafer of 13 dB/cm has been calculated, while the corresponding  $\text{TE}_0$  mode attenuation is below 0.01 dB/cm.

### 3.3.4 Tapers

The sections with different core thickness have to be interconnected using vertical adiabatical tapers from 45 nm to 540 nm. For the waveguide channel structures as will be finally defined (see Table 3.1) the functional taper loss has been calculated for various taper angles using FDBPM [3]. For a taper angle of  $0.1^\circ$  this amounted to a loss of 0.04 dB/taper, which can almost be considered adiabatic propagation, contrary to a  $3^\circ$  taper angle resulting in a loss of 0.6 dB/taper. A small part of this loss appeared to be caused by coupling from the  $\text{TE}_{00}$  mode to the  $\text{TE}_{10}$  mode. This is really unwanted, because the GAC section will be designed for  $\text{TE}_{00}$  mode input power only. The latter is the main reason for requiring adiabatic tapers with a taper angle  $< 0.1^\circ$ .

The conventional IOMS-fabrication process of vertical tapers yields minimum taper angles of  $3^\circ$ , therefore it was necessary to develop a new process to fabricate better tapers. This novel process will be described in Appendix G and it results into vertical tapers with a taper angle of about  $0.015^\circ$  and a taper length of about 2 mm, having a functional loss of 0.02 dB/taper.

Another source of mode conversion would be an abrupt transition at the end of a sensing window, where the cladding index changes from 1.472 to the refractive index of the liquid that is being characterized. To prevent this, also the transition to the sensing window has been tapered vertically.

### 3.3.5 The channel structure

We intend to design ridge type channels being monomodal in the lateral direction and bimodal in the transverse direction showing cross-sectional dimensions with somewhat relaxed influence of technological uncertainties on the relevant grating properties. We have already defined the thickness of the core layer in the bimodal and monomodal sections. Left are the definition of the ridge height and the width of the channels in both sections.

Here we meet some limitations arising from the technology. The maximum allowed ridge height is 20 nm. Any larger ridge height is expected to result in the formation of voids in the subsequently deposited PECVD SiO<sub>2</sub> cladding layer (see section 2.5.2). Such ridges are preferably realized using wet chemical etching. The under-etch which accompanies this process causes the side-walls of the waveguide channel to be somewhat slanted. From SEM pictures it has been determined that at  $h_{\text{ridge}} = 20 \text{ nm}$  these sidewalls have an angle with the wafer surface of  $17 \pm 2^\circ$ . This under-etch has to be taken into account when calculating effective indices, overlap integrals and especially bending losses.

Due to the technology we are using, the channel width is 2  $\mu\text{m}$  at minimum. To allow for some unexpected technological errors, we will use in practice a minimum width of 2.4  $\mu\text{m}$ . For technological simplicity we shall use identical ridge heights in both the thin and the thick core sections. In order to be able to reduce bending radii we have chosen the maximum ridge height, 20 nm, and for suppressing higher order lateral modes in the sensing section we have chosen the minimal channel width, 2.4  $\mu\text{m}$ .

Unfortunately in the straight channel waveguide with the thin core still two lateral modes, both the TE<sub>00</sub> and TE<sub>01</sub>, are guided. With perfect fiber to chip coupling alignment no light will be coupled into the TE<sub>01</sub> mode for symmetry reasons. Of course we cannot expect perfect alignment. Bends are needed to attenuate the TE<sub>01</sub> mode further. In the monomodal section the bend losses of the TE<sub>01</sub> mode in a bend with radius 1 mm and the aforementioned channel cross section are 25 dB/cm versus 10<sup>-3</sup> dB/cm for the TE<sub>00</sub> mode. Hence the TE<sub>01</sub> power can be very effectively removed from the channel. The same bend gives TM modes an additional attenuation. The cross sections of both channel types are depicted in Figure 3.9.

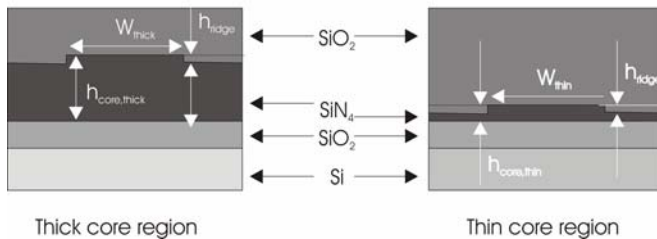


Figure 3.9. Channel cross sections of the transversally mono- and bi-modal sections.

At the fiber to chip coupling, the waveguide width is matched to optimum coupling efficiency (5.8  $\mu\text{m}$ ) giving a coupling efficiency of 40 %. At this width however also the  $\text{TE}_{02}$ ,  $\text{TE}_{03}$  and  $\text{TE}_{04}$  modes exist. After tapering the channel width to 2.4  $\mu\text{m}$  and after a bend, the light coupled into these modes at the FC coupling will have disappeared from the channel. V-grooves will be applied for aligning the fibers. It has been calculated that for the given channel structure the optimal position of the fiber is 0.15  $\mu\text{m}$  above the top of the buffer layer. Following Appendix B, we arrive at a V-groove width of 142,5  $\mu\text{m}$ .

### 3.3.6 Bends

Bends will be inserted on the chip for two purposes. Firstly the bends are helpful to get rid of light coupled into undesired guided modes. Secondly the S-type bends are used to shift the lateral position of the in and outputs of the sensor with respect to each other, to prevent light propagating as slab modes or radiation modes, generated at the FC coupling and inside the sensing region, from reaching the output fibers. At the grating section light from the  $\text{TE}_{01}$  is coupled to the  $\text{TE}_{01}$  mode. The main contribution to this stray light arises from the light in the  $\text{TE}_{01}$  mode which is converted to radiation modes at and after the vertical taper which connects the thick to the thin core section. We have observed in simulations that light in radiation modes, contrary to common assumption, does follow bends, be it with high bend losses. The bending radius should be sufficiently small to remove this stray light from the channel structure, yet large enough not to lose the light in the guided fundamental mode (low bending losses). Other parameters governing the bend loss are the thickness of the core layer and the ridge height and the width of the waveguide channel.

It has been observed experimentally in previous test S-bends with constant bend radius that at its inflexion point, in spite of applying the appropriate lateral off-sets and contrary to theoretical calculations, strong scattering is generated. This phenomenon is probably related to the specific geometrical structure of the realized waveguide channels. To eliminate this problem special S-bends have been used, where the inflexion point is removed. The radius of the curvature of these S-bends varies as a cosine function of the propagation distance along the channel. At the beginning of the S-bend the radius is maximal, in the middle the radius is zero. One of such S-bends is depicted in Figure 3.10. Using these special S-bends it is expected that this scattering will not occur.

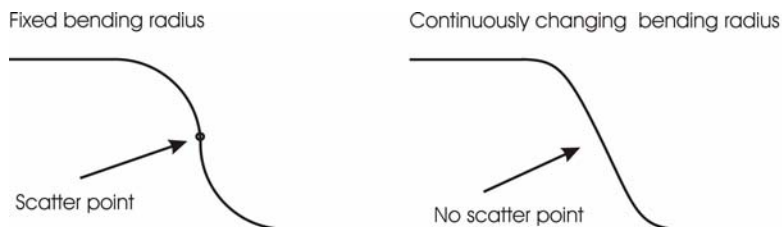


**Figure 3.10. Two different S-bends.**

The minimum bending radius of the special S-bend is chosen to be 1 mm. The maximum bending losses have been calculated, using an FD generic bend solver [3] to be  $5 \cdot 10^{-3}$  dB/cm. The straight-to-bend overlap loss is 3% per interface. By giving the straight channels a small offset with respect to the bends, this overlap loss can in theory be reduced to almost 0%. In practice it was however observed that large scatter points are generated at these transitions. This is probably due to the limited resolution of the lithography. Therefore we decided not to implement such offsets in the S-bends.

### 3.3.7 Functional Design and Implementation

So we arrive at a layout of the GAC sensor as is schematically depicted in Figure 3.11. The dimensions are not on scale, but characteristic dimensions have been indicated.

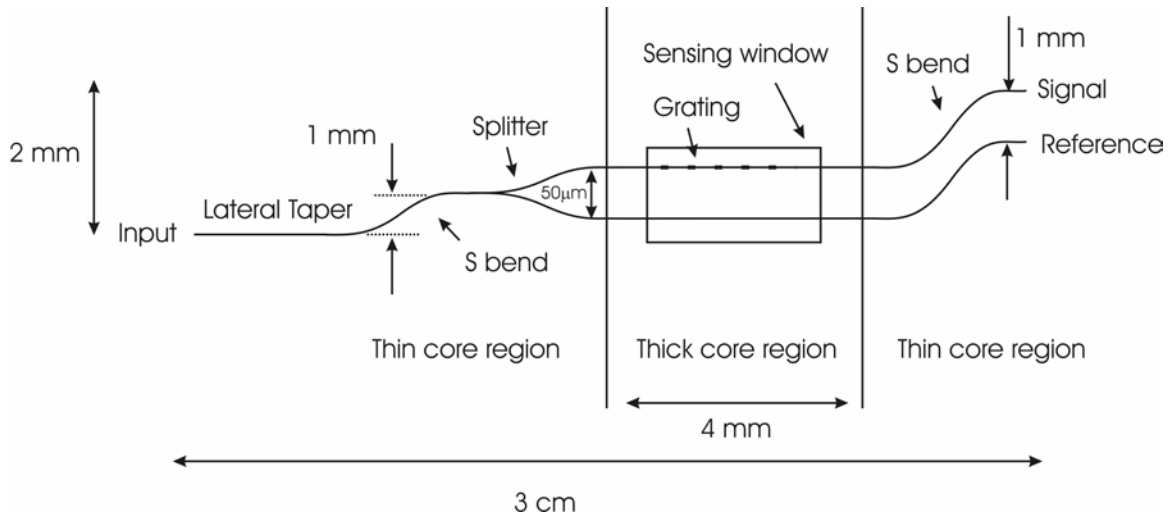


Figure 3.11. Layout of GAC sensor with reference channel.

On top of the grating section a simple microfluidic system will be positioned as is described already in section 2.4. Only the design of the grating parameters is left.

### 3.3.8 Design of the grating

In previous sections the refractive index distribution of the channel in which the grating function has to be implemented has been defined already; partly from the requirement of transversal bimodality, as is needed for the grating function itself, partly from requirements originating from other IO components, partly from (the desire to have a simple) technology. In this section the remaining grating parameters, the period  $A$ , the grating length  $L$  and the grating depth  $h_{gr}$  will be optimized. It also has to be verified whether this channel structure is not conflicting with requirements from optimal operation of the grating.

At a given channel structure and at a given wavelength,  $h_{gr}$  is the only parameter left to define the coupling strength  $k_{0l}$  at resonance condition. We have concluded earlier that resolution will be larger, the more the resonance condition is approached (appropriate value of  $\Delta$ ), the smaller the coupling strength  $k_{0l}$  (hence the smaller  $h_{gr}$ ), while  $L$  should be as large as possible and an odd multiple of the coupling length  $L_c$ ;  $L = (2i+1) L_c$ .

From the cross sectional data of the bimodal channel it has been calculated that in the middle of the range of available refractive indices of the liquid above the grating (1.36-1.54), the period  $\Lambda$  has to be equal to 3.91  $\mu\text{m}$ . This period can easily be obtained with our technology.

The smaller the  $h_{gr}$  values, the larger the uncertainty in the value of the coupling strength (see section 3.2.3). Taking into account the relatively high rms surface roughness of the upper plane of the PECVD  $\text{Si}_3\text{N}_4$  layer, about 3 nm, we decided that choosing  $h_{gr} = 1$  nm would be too risky. For better control of the coupling strength we have chosen a  $h_{gr}$  value of about 6 nm. Assuming a grating contrast being equal to  $n_{\text{Si}_3\text{N}_4} - n_{\text{SiON}} = 1,92-1,47$  we have calculated a coupling length of 146  $\mu\text{m}$ .

The longer the grating, the larger the effects of the local variation of the resonance condition. Limiting this value to 3 mm should imply that the maximum integer  $i$  is 9. Thus we arrive at an intended grating structure as has been given in Table 3.1. In addition we have given all other relevant intended data of the complete sensing system.

For the intended structure both the  $P_{out}-\delta N$  and  $\delta n-\delta N$  curves have been calculated and they are given in Figure 3.12 (the  $\delta N$  range displayed here corresponds with the available  $n_{sens}$  range).

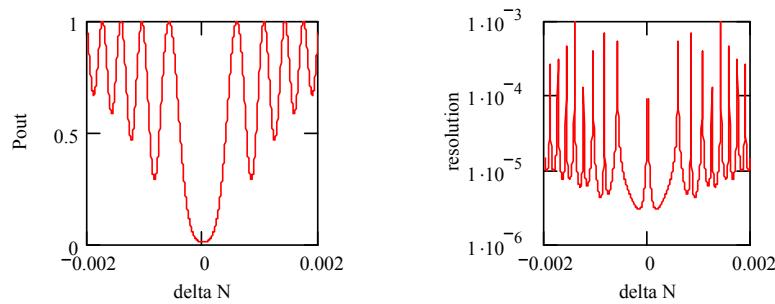


**Figure 3.12.**  $P_{out}$  and the resolution as a function of  $\delta N$  for  $L=19 L_c$ .

**Table 3.1. Properties and designed parameters of the GAC sensor.**

<b>Properties of the layer structure</b>	Symbol	Requirement/value
Core layer thickness thin region		40 nm
Average core layer index thin region	$n_c$	1.87
Average Core layer index thick region	$n_c$	1.92
Accuracy core thickness at 540 nm		5 nm
uniformity core thickness at 540 nm		$\pm 4$ nm
Surface roughness core layer at 540 nm		3 nm
Buffer layer thickness		$> 2.5$ $\mu\text{m}$
Cladding layer thickness		2-3 $\mu\text{m}$
<b>Geometrical parameters of the waveguide structure</b>		
Waveguide width	$W$	$> 2$ $\mu\text{m}$
Accuracy waveguide width	$\Delta W$	0.15 $\mu\text{m}$
Ridge height	$h_r$	20 nm
Accuracy Ridge height		1 nm
Sidewall steepness	$\alpha$	17 $\pm$ 2 degrees
Core thickness	$h_c$	40 / 540 nm
<b>Properties/parameters of the grating structure</b>		
Grating period	$\Lambda$	3.91 $\mu\text{m}$
Grating depth	$h_{gr}$	6 nm
Core thickness thick region	$h_c$	540 nm
Grating length	$L$	2.76 mm
$\Delta N$		0.162
Coupling constant	$k_{01}$	1.07 $\cdot 10^{-2}$ $\mu\text{m}^{-1}$
Coupling length	$L_c$	146 $\mu\text{m}$
$\partial \delta N / \partial n_{\text{sens}}$		0.05
$\partial \delta N / \partial h_c$		$5 \cdot 10^{-4}$ $\text{nm}^{-1}$
$\partial \delta N / \partial \lambda$		$1.2 \cdot 10^{-4}$ $\text{nm}^{-1}$
Resolution	$\delta n$	$5 \cdot 10^{-6}$
<b>Properties of the peripheral equipment</b>		
Operating wavelength	$\lambda$	635 nm
Wavelength tuning range	$\Delta \lambda_{\text{tun}}$	6 nm
Wavelength tuning accuracy	$\Delta \lambda_{\text{acc}}$	0.09 nm
Sensing material index	$n_{\text{sens}}$	1.36-1.52
Laser output power		1 mW
Effective detection limit	$P_{\text{min}}$	1 $\mu\text{W}$

The precise values of the grating period, the coupling constant and the grating length will be calculated after the core layer and waveguide channels have been fabricated and characterized, this to minimize the influence of uncertainty in waveguide dimensions on  $\delta N$  and  $k_{01}$ .

We now shall compare the  $\delta N$  tuning range (wavelength tuning and tuning by varying the refractive index of the liquid on top of the grating) with the technological uncertainty of  $\delta N$ . The wavelength can be varied over 6 nm and this corresponds for the intended structure with a  $\delta N$  range  $\pm 5 \cdot 10^{-4}$ . The refractive index  $n_{sens}$  can be varied in the range corresponding to a  $\delta N$  tuning range of  $\pm 4 \cdot 10^{-3}$ . Comparing these tuning ranges to the  $\delta N$  difference between two adjacent local minima in resolution it is guaranteed that wavelength tuning offers the possibility to tune to one of these minima for every value of  $n_{sens}$ .

**Table 3.2. Influence fabrication errors on uncertainty in  $\Delta N_{res}$ .**

Parameter	Uncertainty	Uncertainty in $\delta N$
Core thickness ( $h_c$ )	$\pm 7$ nm ( $\pm 1\%$ )	$\pm 3 \cdot 10^{-3}$
Initial undefined PECVD layer	3 nm thick, index = 1.7	$+2 \cdot 10^{-3}$
Core index ( $n_c$ )	$\pm 0.01$	$\pm 3 \cdot 10^{-4}$
Waveguide width ( $W$ )	$\pm 0.3$ $\mu$ m	$\pm 2 \cdot 10^{-4}$
Ridge height ( $h_r$ )	$\pm 1.6$ nm	$\pm 10^{-4}$

From the data in Table 3.2 it can be concluded that the worst case uncertainty in  $\delta N$  is  $6 \cdot 10^{-3}$  while the total tuning range is only  $\pm 4.5 \cdot 10^{-3}$ . So it is unclear whether the  $\delta N$  value corresponding to the best resolution can be obtained in practice. To cope with the uncertainty in  $\delta N$ , various gratings with small differences in the period will be realized.

Besides  $\delta N$  also  $k_{0I}(L_c)$  needs to be controlled. In section 3.2.3 we have estimated the inaccuracy in  $L_c$  at 6 %. This implies that at an intended total grating length of  $19 L_c$  the deviation in length may be more than 100% of  $L_c$ . In order to cope with this uncertainty, several gratings with different grating lengths will be implemented on the chip in such a way that at least one sensor will be able to operate with the optimum resolution around  $\delta N = 0$ . So by realizing a manifold of GAC systems differing in grating period and grating length, we expect that one of them will be in a state in which the resolution will be close to that of the intended structure, thus providing proof of principle.

### 3.4 Fabrication

In this section the fabrication process and the structural characterization of the fabricated structure will be treated.

For clarity the main structure of the GAC sensor is recapitulated. At the sensing region the waveguide should be bimodal in transversal direction, thus a ridge type waveguide channel is defined in a relatively thick (540 nm) PECVD  $\text{Si}_3\text{N}_4$  layer. An indentation grating with a specific length, pitch and depth is etched on top of this channel and above the grating a sensing window should be defined in which a thin smooth layer of  $\text{SiO}_2$  is left on top of the grating. The bimodal grating section is on both sides via transversal adiabatic tapers connected to monomodal sections with a core layer thickness of 40 nm. In these sections also bends will be implemented. V-grooves are applied for aligning the in and output fibers to the chip.

#### 3.4.1 The fabrication process

The fabrication process of the GAC sensor is illustrated in Figure 3.13. In Table 3.3 the relevant structural parameters of the designed structure are given.

We start with a thermally oxidized silicon wafer. Crystal orientation is determined and alignment markers matched to this orientation are applied. Some areas are etched free of  $\text{SiO}_2$  for on wafer characterization of layers, which will be deposited later on. Subsequently a 540 nm thick PECVD  $\text{Si}_3\text{N}_4$  layer is deposited (1). Another PECVD  $\text{Si}_3\text{N}_4$  layer of identical thickness is deposited on the back side of the wafer (not shown in Figure 3.13) to prevent the wafer from bending, which would reduce the quality of the lithography.

Using the process described in appendix G, the vertical tapers will be fabricated (2). Next the waveguide channels and the openings for the V-grooves will be etched using wet chemical BHF etching. After that the grating is etched (3). Because of the very small grating depth and the high accuracy required, a highly diluted HF solution is used for this in order to enable good control of the etching time.

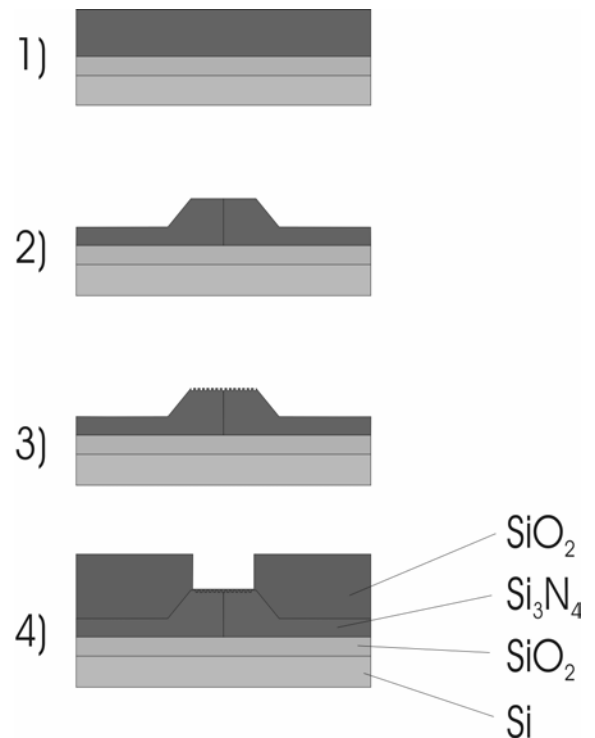


Figure 3.13. Fabrication process GAC sensor.

A PECVD SiO<sub>2</sub> cladding is deposited, and the V-grooves are opened. The V-grooves are produced using KOH etching and a trench is milled at the channel end of the V-grooves to produce a flat FC coupling area. Finally the sensing windows are etched, using wet chemical BHF etching (4). Not all SiO<sub>2</sub> will be etched off; inside the window a ca 30 nm thick SiO<sub>2</sub> layer will be left. The chips will be diced and fitted with fibers.

### 3.4.2 Structural characterization

All relevant structural parameters have been measured either as an intermediate step or after complete realization of the sensing system. In table 3.3 both the intended and the realized values are given.

**Table 3.3. Parameters of the realized GAC sensor.**

Parameter	Designed value with allowed tolerances	Realized value with measurement accuracy
<b>Si<sub>3</sub>N<sub>4</sub> thickness bimodal section</b>	<b>540 ± 7 nm</b>	<b>546 ± 1 nm</b>
<b>Si<sub>3</sub>N<sub>4</sub> refractive index bimodal sect</b>	<b>1.92 ± 0.01</b>	<b>1.919 ± 0.002</b>
<b>Grating period</b>	<b>3.91 μm</b>	<b>4 ± 0.4 μm</b>
<b>Grating depth</b>	<b>6 ± 0.6 nm</b>	<b>6.8 ± 1 nm</b>
<b>Grating duty cycle</b>	<b>0.5</b>	<b>0.6 ± 0.05</b>
<b>Si<sub>3</sub>N<sub>4</sub> thickness monomodal section</b>	<b>40 ± 2 nm</b>	<b>40.9 ± 0.5 nm</b>
<b>Si<sub>3</sub>N<sub>4</sub> refractive index monomodal s</b>	<b>1.92</b>	<b>1.90 ± 0.02</b>
<b>Thickness SiO<sub>2</sub> cladding</b>	<b>2 μm</b>	<b>2.00 ± 0.05 μm</b>
<b>Refractive index SiO<sub>2</sub> cladding</b>	<b>1.472</b>	<b>1.47 ± 0.02</b>
<b>Thickness SiO<sub>2</sub> buffer layer</b>	<b>&gt;2.5 μm</b>	<b>3.43 ± 0.02 μm</b>
<b>Refractive index SiO<sub>2</sub> buffer layer</b>	<b>1.453</b>	<b>1.459 ± 0.001</b>
<b>Ridge height</b>	<b>20 ± 5 nm</b>	<b>25 ± 2 nm</b>
<b>Channel width</b>	<b>2.4 μm</b>	<b>?</b>
<b>Residual SiO<sub>2</sub> in sensing window</b>	<b>30 nm</b>	<b>100 ± 50 nm</b>

Clearly all structural parameters have been realized within the tolerances required.

## 3.5 Characterization of the GAC

In this section the performance of one of the realized GAC sensors has been determined experimentally; results are discussed.

### 3.5.1 Measurement setup

The measurement setup was almost identical to that used for characterizing the SWS. However we applied another light source, a He/Ne laser operating at a wavelength of 632.8. Unfortunately, the tunable laser (622-628 nm) which we intended to use did not operate as expected; the output power was strongly oscillating as a function of the wavelength. In our setup we can continuously vary the refractive index of the liquid inside the sensing window from 1.36 to 1.54 using the micro fluidic system which has been described in Appendix D. Because in preliminary experiments stray light was suspected to be captured by the multimodal output fiber in a not negligible amount we have used monomodal fibers at both the input and the output.

### 3.5.2 Experimental results

It was very disappointing to observe that the input sections of nearly all sensors showed such a low quality that nearly no light could be coupled in. We attribute this to the brittleness of the PECVD  $\text{Si}_3\text{N}_4$ , which is the origin of the fact that while milling the trench at the channel end of the V-groove, the channel is strongly damaged.

Because of the bad FC coupling efficiency, a lot of sensors were characterized using a multi modal output fiber. Due to the bad FC coupling, there was also a lot of slab light present in the system. In order to reduce the slab light, black paint has been applied on top of the slab structure. This reduced the slab light captured by the output fiber considerably. The output power of the sensors that were characterized with the multi mode output fiber however showed no significant dependence on  $n_{\text{sens}}$ .

In order to reduce the influence of the slab light, one sensor has been fitted with two single mode fibers. With careful aligning and fixing the fibers with glue, we managed to get just enough light out of the sensor to characterize it.

The response of this GAC sensor as is calculated by inserting the realized values of the parameters into the CMT theory is shown in Figure 3.14. As a result of the technological uncertainties the exact value of  $n_{\text{sens}}$  at  $\delta N = 0$  cannot be given, but taking all the tolerances into account, it has been calculated that for this sensor the  $\delta N = 0$  state should be located within the available  $n_{\text{sens}}$  range (1.36 - 1.54).

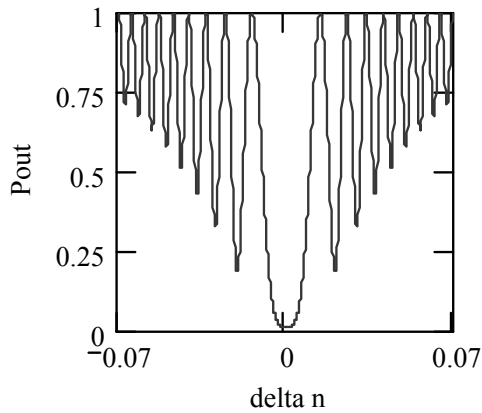


**Figure 3.14. Expected response GAC sensor.**

In Figure 3.15 the response as is determined in two successive measurements is depicted.

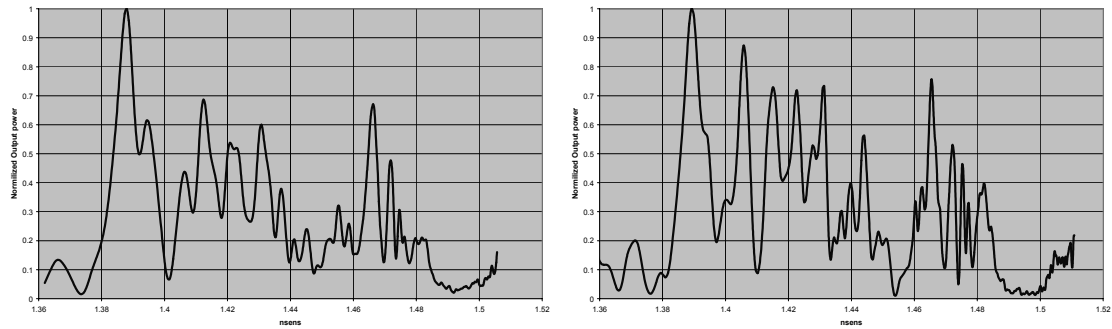


**Figure 3.15. Measured responses GAC sensor with  $\Lambda = 3.90 \mu\text{m}$ .**

It can be seen that the response from the sensor is quite different from the theoretically expected one. The position from the peaks is reproducible except for a small shift due to some uncertainty in the value of the refractive index. The height of the peaks differs and these differences in average about 15% of the maximum transmitted power.

Successive measurements on a similar waveguide channel (without grating) showed that the coupling efficiency can vary  $\pm 20\%$  over the course of 2 hours. These power fluctuations decreased with time and after about 12 hours after applying the fibers they appeared to be reduced to  $\pm 5\%$ . We attribute this to some relaxation process related to drying of the index matching gel / glue, which has been applied in between the fiber end and the beginning of the waveguide channel. Unfortunately, due to a lack of time, we were not able to pay more experimental attention to the cause of this non-reproducibility.

### 3.5.3 Analysis

Clearly the response of the GAC sensor is not as expected. This can have different origins.

First we shall discuss the possibility that that our modeling using CMT is not sufficiently sophisticated to predict the performance correctly. Theory predicts that at one single value of  $n_{sens}$  the normalized output power should be zero; the experiments however show that zero values are obtained at various values of  $n_{sens}$  and this may point to some interference effects. And indeed there is a coupling that is not taken into account in the CMT: the coupling to higher order radiation modes. Additional calculations have been performed using BPM and BEP. The resulting  $P_{out}$  versus  $\delta N$  curves are nearly identical to the curve in Figure 3.17. They also show that only a very small amount of power (<0.25 dB/mm over about 3 mm) will be coupled to radiation modes. This means that if the coupling to radiation modes would show some dependence on  $n_{sens}$ , it could only cause a ripple smaller than -0.75 dB of the output signal.

Also notice that the positions of the dips, due to grating assisted mode coupling, for the SWS (section 2.8) have been predicted very accurately using the BEP, showing that our simulation tools can handle these kind of systems very well. In short, we are sure that the model is good enough to describe the behavior sensor with the intended structure.

A second origin of the unexpected performance may be noise. It can be that we're not measuring the response of the sensor, but noise only. Figure 3.15 shows that the position of the peaks is reproducible; hence the presence of non-systematic noise is excluded. Values of  $P_{out}$  at the maxima of the peaks show a non-reproducibility of about 15% average. For explaining this accidental difference we have investigated various potential sources of noise in more detail. The noise in laser output power in the frequency range above 0.5 Hz is determined to be about -15 dB. Using Fourier analysis or a similar method this noise can be filtered out completely. The drift in laser output power was determined to be about 4 % of the output power. This drift cannot be distinguished from the response. The drift in polarization at the input of the chip is estimated to cause a drift in output power of also a few percent. Noise originating from both these sources however is far too small to mask the sensor response. Probably instability of the fiber to chip connection related to changing properties of the matching gel might explain the non-reproducibility of the magnitude of the peaks. However, more experiments would be needed to actually proof this. In principle we cannot exclude the possibility that we're actually measuring the power of stray light entering the output fiber, instead of guided mode power. However also at the output a single mode fiber has been used, so this possibility is highly unlikely.

A third explanation for the unexpected response could be the presence of a Fabry Perot cavity somewhere inside the integrated sensor system. This FP cavity should be in contact with the liquid in order to show the specific  $n_{sens}$  dependence. We have

investigated this possibility, but no cavity could be discovered with the right geometrical parameters to explain the characteristics in Figure 3.15.

At last we shall discuss the possibility that this unexpected behavior is due to unexpected technological inaccuracies. Having an inaccuracy in  $L_c$  of about 6% it is not excluded that the real sensor is close to a state in which  $L_{sens} = 2i.L_c$  and in this state the grating effects would not be visible in the output power. However the output power is far from being constant so we can rule out this uncertainty as the origin of the unexpected performance. From Table 3.3 it can be seen that the values of nearly all structural parameters differ only a little from the intended ones only, thus we don't think that technological inaccuracies can explain the measured sensor characteristics.

We have to conclude that at this moment no solid explanation for the unexpected response of the GAC sensor can be given.

### **3.6 Summary and discussion**

In this chapter the potential of co-directional grating assisted mode coupling based IO sensors has been investigated. A model has been developed to describe the behavior of the sensor. Designs of the IO channel structures have been made with the aim to prove the correctness of our analysis and directed to demonstrate the resolution that might be obtained. A batch of GAC sensors has been realized and the realized values of the structural parameters are very close to the intended ones. Although many sensors, differing in grating period and grating length have been produced, as a result of the low quality of the FC coupling, only a single one could be characterized. The performance of this sensor was not as theoretically expected and until now we cannot offer a well proven explanation for this.

### **3.7 References**

- [1] G.J. Veldhuis, J.H. Berends, R.G. Heideman, P.V. Lambeck, *An integrated optical Bragg-reflector used as a chemo-optical sensor*, Pure and Applied Optics Vol. 7, (1998), pp 23-26.
- [2] J.H. Berends, doctoral thesis, *Integrated optical Bragg Reflectors as Narrowband Wavelength Filters*, Lightwave Devices Group, University of Twente, jan. 1997, chapter 3.
- [3] OlympIOs; *C2V software*, version 5.1.12
- [4] F. Horst, doctoral thesis, *Soliton switching in an integrated optical nonlinear Bragg reflector*, Lightwave Devices Group, university of Twente, june 1997.

## 4 Novel immuno-sensing principles

In this chapter four different novel principles for IO immuno-sensors are proposed, analyzed and compared to each other.

### 4.1 Introduction

The highest resolution can be obtained by applying luminescence based methods. Here often competition methods are used e.g. by adding antigens labeled with luminophoric groups to the sample. Because of the cost of the labeled measurand particles and the relative complexity and limitations of the measuring process, there is a general desire to substitute these luminescence methods by label free detection methods with similar resolution. Also the label free methods offer the possibility of continuous in situ measurements as is very advantageous e.g. in alarming systems.

In section 4.1.1 it will be explained how the evanescent field is used to perform immuno-sensing. Three out of the four new immuno-sensing principles are based on the change in the modal field. The basic waveguiding structure is the same for all these sensors and the characteristics and fabrication of this structure will be explained in section 4.1.2. Finally in section 4.1.3 the general design aims and boundary conditions will be given.

#### 4.1.1 Immuno-sensing using the evanescent field

With immuno-sensing the detection of antigens (e.g. viruses) with its conjugated type of antibodies is meant. Usually a monomolecular receptor layer is bonded covalently to the surface of the core layer of a waveguide and measurand induced changes in this layer are probed by the evanescent field of a mode, as illustrated in Figure 4.1. When the measurand molecules such as antigens associate with the receptors, as a primary effect the thickness and as a secondary effect also the refractive index of the receptor layer change, thus changing the properties ( $N_{eff}$ ,  $E(x,y)$ ) of the guided mode.

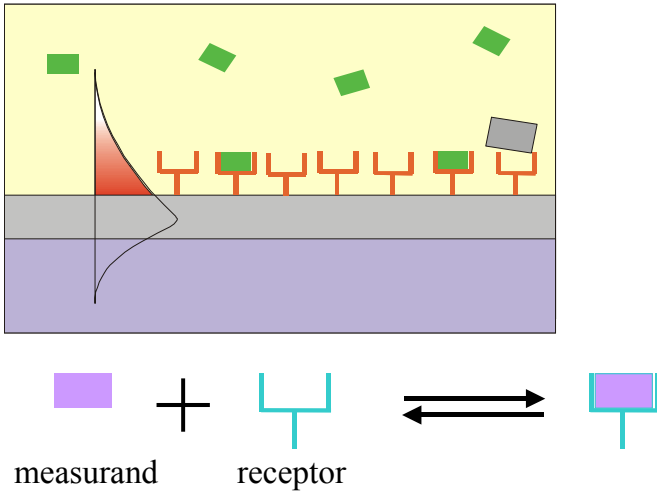


**Figure 4.1. Schematic representation receptor layer on top of a waveguide.**

The association reaction of the antibodies and antigens is a reversible one and is characterized by an association constant  $K_{ass}$ , defined as:

$$K_{ass} = \frac{[empty\_antibodies][antigens]}{[filled\_antibodies]} \quad (4-1)$$

and as a consequence the fraction of the antibodies that is associated  $F$  can be expressed as:

$$F = \frac{K_{ass}c}{1 + K_{ass}c} \quad (4-2)$$

where  $c$  denotes the concentration of the measurand (antigens). Hence, for measuring low concentrations, on the one hand  $K_{ass}$  has to be large, which is a task for the chemists, and on the other hand small  $F$  values need to be detected, which is where IO sensors step in.

A monomolecular antibody layer is typically 4 nm high and has a refractive index of about 1.5. Such a layer, partially filled with e.g. antigens will not have a uniform thickness, but since the dimensions of the antigen are small compared to the wavelength and the distances between the different bounded antigens are also small, the guided mode will experience the presence of the antigens as a small uniform increase of the layer thickness. In this chapter we have taken an example system where complete coverage with antigens corresponds with an increase in effective layer thickness ( $h_i$ ) from 4 to 5 nm. However in practice the filled fraction of the antibody layers  $F$  is much smaller than 1: hence the change in effective thickness ( $\Delta h_i$ ) is really very small and generally a resolution better than  $10^{-3}$  nm is necessary [1].

### 4.1.2 The Basic structure

Existing label-free evanescent field type IO immuno sensors like the Young Interferometer [2], the Mach Zehnder Interferometer [3] and the Surface Plasmon Resonance based ones [1] determine  $\Delta h_i$  by measuring the change in  $N_{eff}$ . In contrast to these existing IO sensing principles, the novel sensing principle treated in this chapter use the change in the modal field profile  $E(x,y)$  to determine  $\Delta h_i$ .

In the first three principles in the sensing region, single mode, strip loaded channel waveguides are utilized, wherein the strip consists of antibodies only, as is depicted in Figure 4.2.

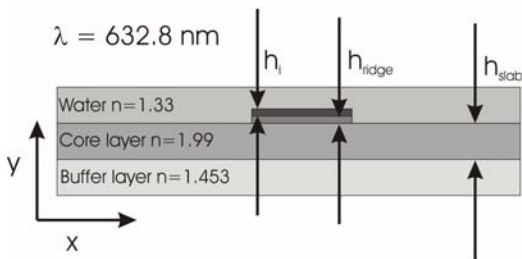


Figure 4.2. Basic immuno-sensing waveguiding structure.

In these waveguides the TM mode is weakly guided in the lateral direction by the thin immuno sensing layer and the mode effectively is close to cut off. Because of this the lateral shape of the mode profile is strongly dependent on  $\Delta h_i$  as is illustrated in Figure 4.3, while the field profile in transversal direction hardly changes. These kinds of structures can be described very well using the EIM.

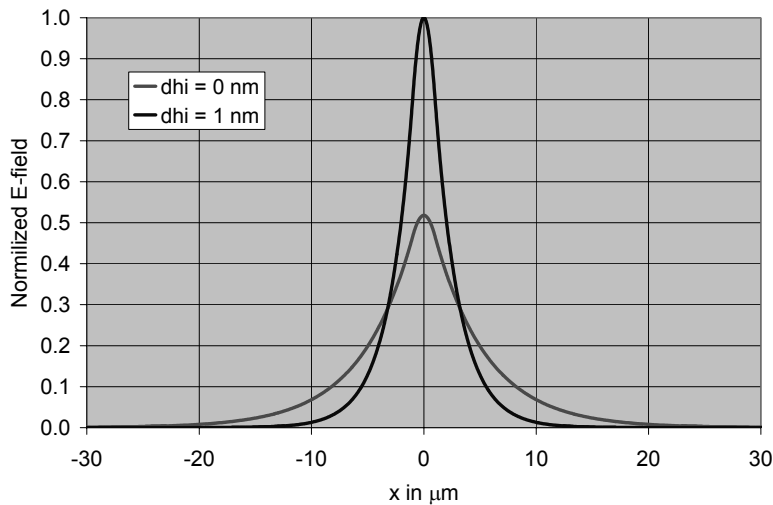


Figure 4.3. Lateral field profile of the waveguide structure in Figure 4.2 for different thicknesses of the antibody layer.

Theoretically the lateral extension of the modal field and hence also the  $\Delta h_i$  induced changes of their lateral shape can be increased even further by applying the receptor layer inside a small trench, this however does not necessarily have to result in an improved resolution. The lateral extension is also larger the narrower the waveguide therefore the by photolithography limited minimum waveguide width of 2  $\mu\text{m}$  will be taken. It is also important that the output power of the sensor has a small sensitivity to changes in the refractive index of the solvent ( $n_{solv}$ ). Because the solvent is present as well on top of the strip as well as on top of the neighboring slab regions while the transversal mode profiles above the ridge and slab are almost identical, the shape of the mode profile will be very insensitive to changes in  $n_{solv}$ . However in analyzing the different sensing principles not only the resolution in  $\Delta h_i$  will be considered, but also the equivalent value of  $\delta n_{solv}$  will be given. In addition changes of temperature will influence the sensor output, but they cannot be calculated theoretically easily and experiments have to show their influence.

In the first sensing principle, called immuno segmented waveguide sensing (iSWS), the change of modal field is converted into a change of the attenuation of the propagating light by using a segmented structure in which one type of segments contains the antibody layer (the strip load) while in the other type this layer is absent. In the second principle called modal attenuation sensing (MAS) the waveguide is invariant along the propagation direction and the change in modal field profile is monitored by applying absorptive regions on a certain distance of the channel. The change of field profile manifests itself as a change of the modal attenuation. In the third principle, called the immuno-sensing directional coupler sensing (iDC), the change of modal field results into a change of the coupling constant of a directional coupler built from the described type of strip loaded channel waveguides and the change is monitored as a change of the powers of both coupler outputs.

Although the sensing structures themselves are very simple, the coupling of light into these structures is not that simple. Due to the large lateral extension of the modal field of the waveguide, the efficiency of a direct fiber to sensing waveguide coupling would be extremely low. This efficiency can be strongly increased by inserting in between the fiber and the sensing waveguide a tapered waveguide, where the taper is defined by a gradual change of the height of a ridge applied below the antibody layer strip. At the chip edge the taper height should show a value appropriate for a lateral modal confinement similar to that of the fiber mode.

As an alternative to FC coupling, grating coupling might be used. However because of the low lateral contrast the effective refractive index of the channel is very close to that of the surrounding slab and hence apart from coupling into the channel, also a lot of light will be coupled into the slab modes of the layer stack. Note that when using grating couplers the system can be used as a disposable, which could be mounted in hardware similar to that what has been developed for the pointer sensor by Kunz [4].

All the sensor principles treated here measure the intensity in the output channel. In most cases there is a large amount of slab light present in the system, be it because of the bad

coupling to the guided mode or because of the nature of the operating principle of the sensor. It is important that as little slab light as possible couples into the output fiber. This could be achieved by using S-bends, but due to the weak lateral confinement of the guided mode however only bends with a very large bending radius can be realized. In Figure 4.4 spatial separation of slab light from the guided mode is demonstrated using an S-bend (foot print: 1.5 mm x 40  $\mu\text{m}$ ) for the waveguide structure of Figure 4.2 with  $h_{\text{ridge}} = 0$  nm. In this figure a Gaussian start field much wider than the field of the guided mode is launched. Part of the Gaussian beam is coupled to the guided mode, but a large part is also coupled to slab modes. The small peak in normalized power density at the end of the S-bend corresponds to the field of the guided mode. Clearly it can be seen that a relatively small S-bend already does a very good job to separate spatially the slab modes from the guided mode.

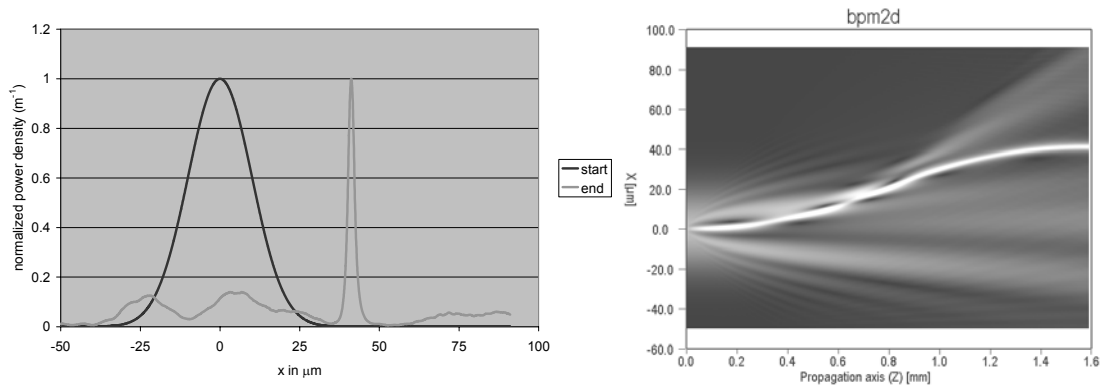


**Figure 4.4. Slab light reduction.**

By implementing some kind of structures in the  $\text{Si}_3\text{N}_4$  slab which reflect or absorb the slab light, the influence of the slab light could be reduced even further.

The fabrication of the basic structure (with  $h_{\text{ridge}} = 0$  nm) is very simple. A slab structure as depicted in Figure 4.2 can be realized by wet oxidization of a Si wafer followed by LPCVD deposition of  $\text{Si}_3\text{N}_4$ . After that the receptor layer has to be deposited and patterned for defining the lateral structure of the strip loaded channel waveguide. In case of grating coupling before applying the antibody layer an input and if desired output grating has to be defined within the  $\text{Si}_3\text{N}_4$  layer, while the S-bend can be introduced in the mask for patterning the antibody layer.

In case of fiber coupling after depositing the  $\text{Si}_3\text{N}_4$ , the tapered ridges have to be applied. In principle this can be done by sputtering a thin  $\text{SiO}_2$  layer using a sputter mask, delivering the desired vertical taper structure, comparable with the ZnO deposition as done in [3]. After having protected the area above the channel with photo resist, dry etching will be applied in order to define the tapered ridge. The thickness of the  $\text{SiO}_2$  layer at the chip edges has to be close to zero while its (maximum) thickness at the sensing region can be derived from the intended (maximum) value of the ridge height at the chip edge and the rate of the etching processes in both  $\text{SiO}_2$  and  $\text{Si}_3\text{N}_4$ . If desired in the same steps using a more complicated sputter mask also the ridges and related tapers

for S-bends can be applied. Note that in case ridges have been defined the antibody layer patterning will be somewhat inaccurate. In case the fibers have to be aligned by V-grooves some well known additional technological steps have to be introduced. Clearly, from a technological point of view, grating coupling is the preferred method.

Finally a microfluidic system, similar to that mentioned in chapter 2 and 3, will be attached on top of the chip. For the structures we are considering here, this gives some complications because there is no protecting cladding layer on top of which the microfluidic system can be mounted. By mounting the microfluidic system directly on top of the Si<sub>3</sub>N<sub>4</sub>, the light will be unguided in lateral direction for a short distance while passing the contact regions and the field profile will expand in lateral direction. This is not a big problem since the width of the waveguide after the contact region can be adjusted to compensate for this and minimize the losses.

### 4.1.3 Design aims and boundary conditions

It is the very large resolution, which can be obtained by integrated optical sensors, which make them so interesting for immuno sensing applications. Therefore with the analysis of the different sensing principles in this chapter most of the attention is paid to the resolution that can be obtained using in all systems the same peripheral equipment as in chapter 2 and 3. The resolution  $\delta h_i$  can be calculated with expression (4-3).

$$\delta h_i = \frac{(q_1 + q_2)P_{out}}{\frac{\partial P_{out}}{\partial h_i}} \quad (4-3)$$

Generally the resolution of an IO sensor improves proportional to the length of the sensing section ( $L_{sens}$ ). In the design process we shall limit  $L_{sens}$  to 1 cm; in the systems we are considering here it is not possible to increase  $L_{sens}$  using a spiral configuration due to the weak lateral modal confinement, which makes it impossible to realize bends with a small bending radius ( $< 0.5$  mm) with acceptable bending losses. In order to be able to detect the output signal it is required that  $P_{out} > P_{min}$ , the latter being minimum output power at which the detection system can still operate with an accuracy  $q_2$ . If this requirement is not met for  $L_{sens} = 1$  cm, for the calculation of the best resolution the total length of the sensor is chosen such that  $P_{out} = P_{min}$ .

For most IO sensors the highest attainable resolution improves with decreasing wavelength. At lower wavelengths however scatter losses are increasing. So we have chosen to analyze all the sensing principles at a wavelength of 632.8 nm, which in addition is the lowest wavelength for which there is still a sufficient supply of commercially available cheap light sources and optical components like single mode fibers and 3dB splitters.

Further the sensor should have a low sensitivity to the refractive index of the liquid which contains the antigens ( $n_{sol}$ ). Before a measurement the sensor is flushed with a reference liquid without antigens. When the real liquid with antigens is inserted two things change at the same time: both  $n_{sol}$  and [antigens]. It is important that a change in  $n_{sol}$ , which could be caused by a change in pressure or temperature, is not interpreted as a change in [antigens]. Because  $n_{sol}$  changes suddenly and the change of  $\Delta h_i$  shows some (specific) time dependence in principle both effects can be discriminated by a careful analysis of the time dependence of the change of attenuation.

Apart from the resolution  $\delta h_i$ , we will also present a value  $\delta n_{sol}$ , being the change in  $n_{sol}$  giving the same change of output power as a change in  $\Delta h_i$  equal to  $\delta h_i$ . Hence for utilizing the best resolution the change of  $n_{sol}$  has to be smaller than  $\delta n_{sol}$ , the larger  $\delta n_{sol}$  the better. If  $\delta n_{sol}$  would be too small, a reference channel is necessary.

The theoretical analysis given in this chapter has the character of a feasibility study. No extended optimizations have been carried out for finding the best structure, but we have tried to find structures with attractive properties leaving some room for improvement. We have not considered some other relevant aspects such as the fabrication tolerances (especially the thickness uniformity and refractive index homogeneity of the  $\text{Si}_3\text{N}_4$  layer) and the cost of fabrication. As a result of the technological tolerances, individual calibration of each sensor is expected to be required. Due to a lack of time, which is limited in a PhD project, the proposed sensor systems have not been realized and characterized.

## 4.2 Immuno sensing with an SWS

Until now the SW principle has only been applied to bulk sensing (see chapter 2). There are however possibilities to apply this principle to immuno-sensing too. In this chapter the principle, analysis and the design of a from a technological point of view very attractive immuno-sensing SWS (iSWS) will be treated.

### 4.2.1 The principle

The following simple sensing section of an iSWS is proposed:

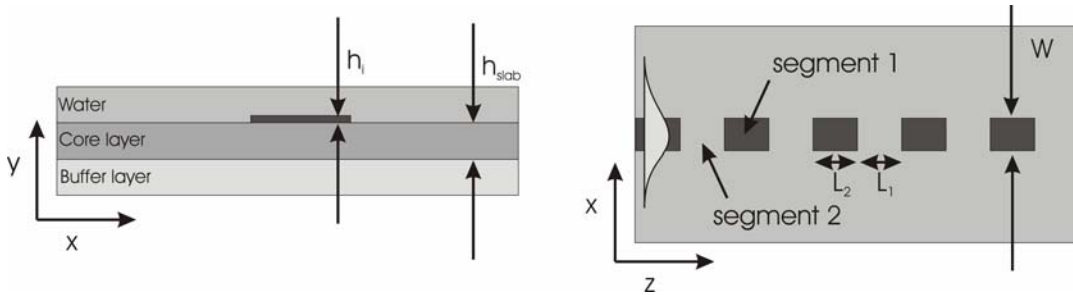


Figure 4.5. Free space iSWS structure; cross section (left) and longitudinal top view (right).

The strip loaded waveguide channel is defined by a strip of an antibody layer. The SW region consists of segments where this layer is present and segments where it is absent. In the guided mode segments (e.g. segment 1 of Figure 4.5) the mode is weakly guided in the lateral direction by the thin antibody layer. In the unguided segments (e.g. segment 2) the incoming guided field will start diverging laterally similar to that of a Gaussian beam, as shown in Figure 4.6. The angle of the divergence depends on the width of the mode-profile and thus on  $\Delta h_i$ . At a next segment a fraction of the power of all unguided modes will couple back into the guided mode. Here also the phases of these modes play an important role, just like with the bulk SWS.



Figure 4.6. Light propagation through the iSWS (window: 3mm x 120 $\mu$ m).

## 4.2.2 Analysis

The optical properties of the layer stack are defined by the standard technology, hence only the spatial dimensional parameters can be used for optimization of the resolution of the sensor:  $L_1$ ,  $L_2$ ,  $h_{slab}$ ,  $h_{ridge}$  and  $W$ . Here  $h_{slab}$ ,  $h_{ridge}$  and  $W$  determine how the width of the mode profile depends on  $\Delta h_i$ .  $L_1$  and  $L_2$  determine the amount and phase of the radiation modes that couple back into the guided mode. They also determine the number of transitions per cm. For simplicity a periodical segmentation has been chosen. A perfect technology has been assumed.

## 4.2.3 Design

In Table 4.1 the parameters of an iSWS structure showing a high resolution are given and in Figure 4.7 the output power characteristic is shown.

**Table 4.1. Design of the free space iSWS.**

Parameter/property	Value
$h_{slab}$	60 nm
$W$	2 $\mu\text{m}$
$L_1, L_2$	166 $\mu\text{m}$
$L_{sens}$	1 cm
$\delta h_i$	$7 \cdot 10^{-4}$ nm
$\delta n_{solv}$	$10^{-5}$

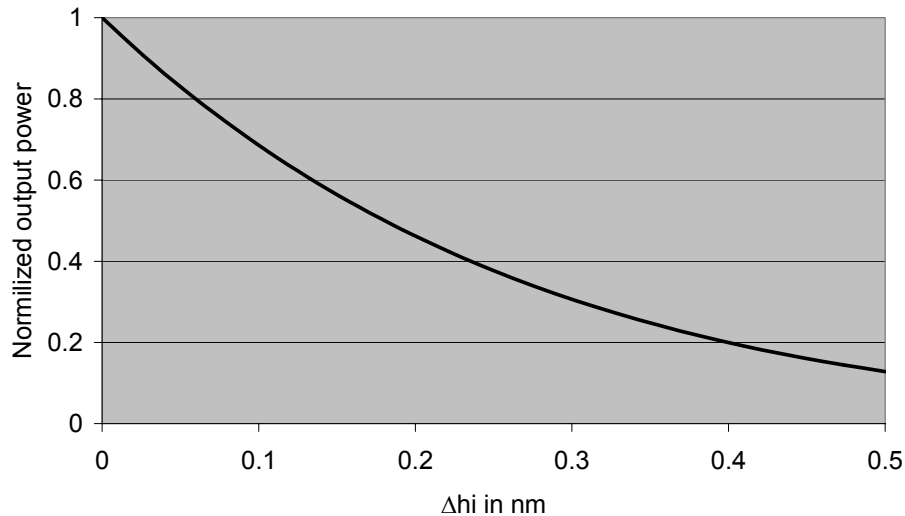


**Figure 4.7. Output power characteristic of a 'free space' iSWS.**

A very acceptable resolution of  $7 \cdot 10^{-4}$  nm can be achieved, while  $\delta n_{\text{sol}}$  is equal to  $10^{-5}$ , leading e.g. to the requirement that the temperature needs to be stabilized within 0,1 °C. It has to be noted that by depositing the sensing layer inside a trench (Figure 4.2,  $h_{\text{ridge}} < 0$  nm) to reduce the lateral contrast does not have a significant influence on the resolution, since then the  $L_{\text{sens}}$  needs to be decreased to continue satisfying the condition  $P_{\text{out}} > P_{\text{min}}$ . The fabrication of this iSWS is very simple and has been discussed already in section 4.1.2.

### 4.3 Immuno sensing using modal attenuation

#### 4.3.1 The principle

The structure of the modal attenuation sensor (MAS) [8] is presented in Figure 4.8.

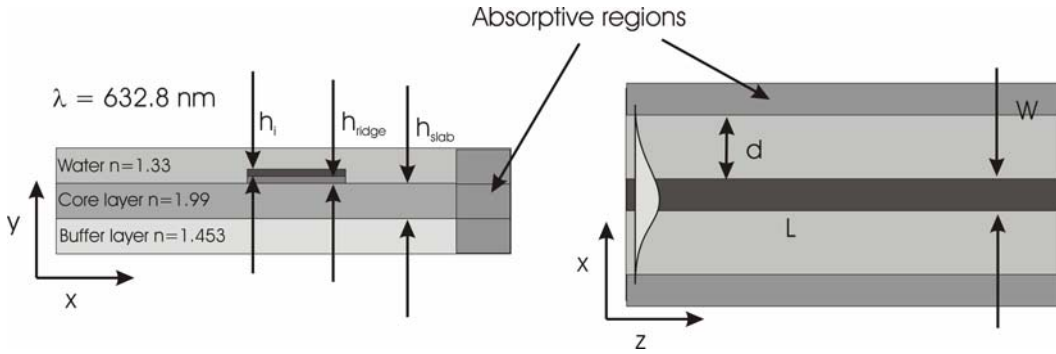


Figure 4.8. Modal attenuation sensor: channel cross section (left) and longitudinal top view (right).

Also here the sensing structure consists of a monomodal strip loaded type channel waveguide in which the strip is formed by a monomolecular antibody layer. But in addition at both sides of the channel, starting at a distance  $d$  from the strip walls, the slab layer is made absorptive. A change of the field profile now results into a change of the fraction of the modal power,  $P_{frac}$ , which propagates through the absorptive regions. As a consequence the modal attenuation will become dependent on the mode profile and hence a measure of  $h_i$ . Thus in this structure changes in  $h_i$  are measured as changes of the modal attenuation.

#### 4.3.2 Analysis

For the development of a model of this sensor the EIM has been applied. In Figure 4.9 the EIM has been schematically depicted together with the relevant symbols.

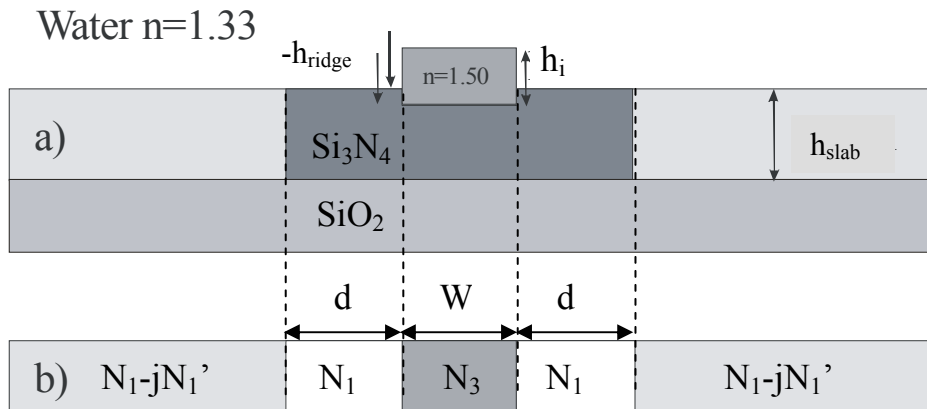


Figure 4.9. A cross section and the equivalent slab structure obtained by applying the EIM.

The relation between the input power  $P_{in}$  and the output power  $P_{out}$  of the sensing region can be described approximately by:

$$P_{out} = P_{in} \exp - \left( a + P_{frac} N_1' k_0 \right) L \quad (4-4)$$

where  $k_0$  is the vacuum wave vector of the used monochromatic light.  $a$  represents the channel losses for  $N_1' = 0$ , i.e. the normal channel losses mainly caused by scattering. The second term in the exponent expresses the modal attenuation due to absorption in the absorptive regions. Here  $L$  is the total sensor length. Starting from general expressions for the magnetic field of the  $TM_0$  mode in a three-layer slab structure [5] and making some small approximations based on the very small differences between the (effective) refractive indices involved one can derive:

$$P_{frac} = 2 \frac{(N_3^2 - N_{eff}^2)}{(N_3^2 - N_1^2) \left( w k_0 \sqrt{N_{eff}^2 - N_1^2} + 2 \right)} \exp \left( - 2 k_0 d \sqrt{N_{eff}^2 - N_1^2} \right) \quad (4-5)$$

where  $N_{eff}$  is the real part of the effective index of the channel mode.

Notice that for simplicity of the expressions we have assumed that the effective index of the slab ( $N_l$ ) is equal to the effective index of the absorptive regions. The modal attenuation can be expressed as the imaginary part of the effective index of the channel mode,  $N_{eff}$ , and is given by:

$$N_{eff}' \cong P_{frac} N_1' \quad (4-6)$$

For the small changes of  $h_i$  that we are interested in, the relationship between  $P_{frac}$  and  $h_i$  can be approximated as being linear. Thus we can rewrite expression (4-4) to:

$$P_{out} = P_{in} \exp - \left[ a + N_1' k_0 \left\{ P_{frac}(c=0) + \frac{\partial P_{frac}}{\partial h_i} \Delta h_i \right\} \right] L \quad (4-7)$$

The resolution  $\delta h_i$  can be calculated from:

$$\delta h_i = \frac{(q_1 + q_2) P_{out}}{\frac{\partial P_{out}}{\partial h_i}} = \frac{(q_1 + q_2)}{k_0 N_1' \frac{\partial P_{frac}}{\partial N_3} \frac{\partial N_3}{\partial h_i} L} \quad (4-8)$$

The larger  $L$ , the better the resolution. But also here the  $L$  value will be limited by the condition that  $P_{out} > P_{min}$ . This condition can be worked out with (4-7) and as a result we obtain:

$$L_{\max} = \frac{\ln\left(\frac{P_{in}}{P_{min}}\right)}{a + k_0 N_1' P_{frac}} \quad (h_i = 4nm) \quad (4-9)$$

Substitution of (4-9) in (4-8) gives:

$$\delta h_{i,\min} = \frac{(q_1 + q_2)}{\ln(P_{in} / P_{min})} \frac{1}{\left| \frac{\partial P_{frac}}{\partial N_3} \frac{\partial N_3}{\partial h_i} \right|} \left( \frac{a}{k_0 N_1'} + P_{frac} \right) \quad (4-10)$$

The resolution can be described as the product of two factors, the first one reflecting the quality of the peripheral equipment, the second one the quality of the IO-channel structure itself. As expected the equation expresses that the resolution improves for smaller  $a$ , larger  $\partial N_3 / \partial h_i$  and larger  $N_1'$ . In addition the equation shows that under the condition that  $a \ll k_0 N_1' P_{frac}$ , a small ratio  $P_{frac} / (\partial P_{frac} / \partial N_3)$  is required, while the dependence on  $N_1'$  is in good approximation removed.

### 4.3.3 Design

In this section a design of a MAS optimized for high resolution, will be presented. In Figure 4.10 the design process is depicted. To obtain high resolution several quantities, following from expression (4-10), have to be optimized using the four relevant sensor parameters, which are  $W$ ,  $h_{slab}$ ,  $h_{ridge}$  and  $d$ , while still taking into account the boundary conditions regarding the available technology and peripheral equipment.

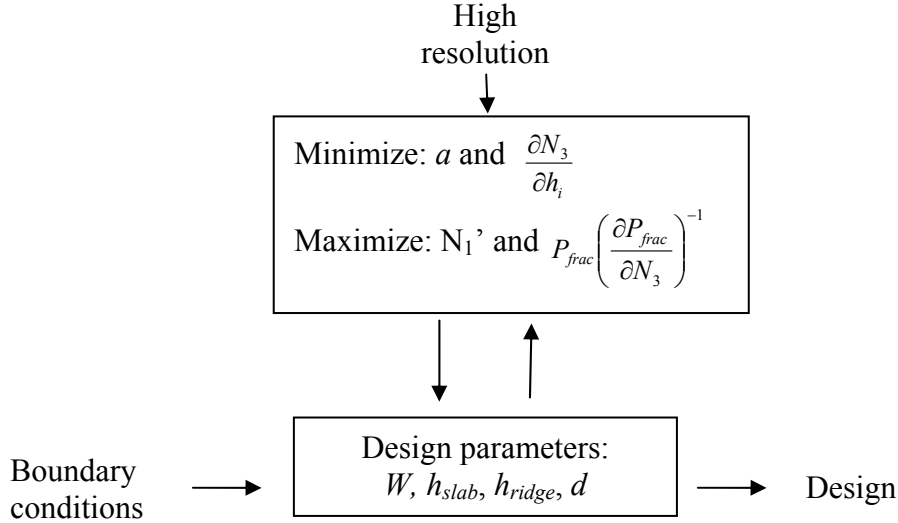


**Figure 4.10. Design scheme MAS.**

The propagation loss for  $N_1' = 0$ , characterized by  $a$ , is determined by the available technology: A typical propagation loss of 1 dB/cm translates into  $a = 0.25 \text{ cm}^{-1}$ .

The factor  $\partial N_3 / \partial h_i$  is mainly determined by  $h_{slab}$ . Because we have an asymmetric layer system, with a layer with the lower refractive index on top, there is an optimum value for  $h_{slab}$  that optimizes  $\partial N_3 / \partial h_i$ :  $h_{slab} = 70 \text{ nm}$  corresponding to  $\partial N_3 / \partial h_i = 0.00055 \text{ nm}^{-1}$ . This value is in approximation constant for the whole range of  $h_{ridge}$  and  $h_i$  values that we'll consider later.

$N_1'$  characterizes the absorption of the absorbing regions. This absorption can be realized in several ways and it can be made almost arbitrarily large. When  $N_1'$  is chosen such that  $a \ll k_0 N_1' P_{frac}$  its influence on the resolution is, according to expression (4-10), negligible.

Finally  $P_{frac} / (\partial P_{frac} / \partial N_3)$  needs to be minimized. Intuitively one would say that  $P_{frac}$  can be decreased by increasing  $d$ , this however at the cost of making the other factor smaller too. The factor  $\partial P_{frac} / \partial N_3$  can be increased by increasing the  $\Delta h_i$  induced changes of the modal field, which can be realized by reducing both the lateral refractive index contrast and the width of the channel waveguide. Indeed the simulations we performed confirmed

this expectation. Hence an attractive and technologically simple waveguiding structure will consist of a strip-loaded channel, in which the lateral structure of the channel is defined by a thin chemically active layer only ( $h_{ridge} = 0$  nm). Lateral extension of the modal field can be improved even more, by applying the active layer on top of a small trench etched in the core layer ( $h_{ridge} < 0$  nm) and minimizing  $W$  to the technological limit of  $2 \mu\text{m}$ .

In Figure 4.11 the ratio  $P_{frac}/(\partial P_{frac}/\partial N_3)$  is given as a function of  $N_3$  for different values of  $d$ , the distance between the strip and the absorptive region. Here  $N_3$  serves as a measure for  $h_{ridge}$  which is used to control the lateral contrast.

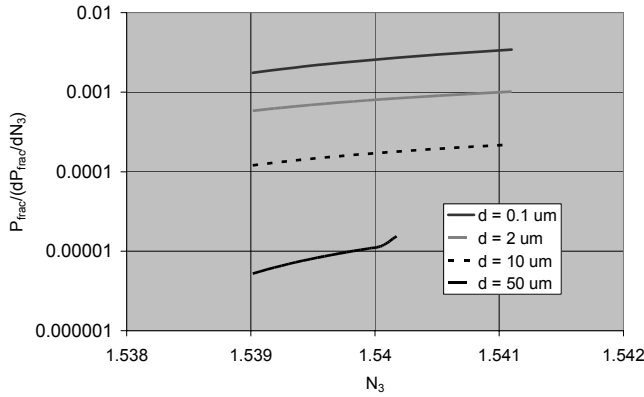


**Figure 4.11.** The ratio  $P_{frac}/(\partial P_{frac}/\partial N_3)$  as a function of  $N_3$  for different values of  $d$ .

Note that the effective index of the slab  $N_1$  is 1.5380.  $N_3 = 1.5389$  corresponds to  $h_{ridge} = -0.75$  nm. The technologically more attractive variant with  $h_{ridge} = 0$  nm corresponds with  $N_3 = 1.5393$ . According to Figure 4.11 indeed the ratio decreases with decreasing  $N_3$  and increasing  $d$ .

From Figure 4.11 one would conclude that the ratio can be made arbitrarily small by increasing the distance  $d$ . One has to realize however that the optimum value for  $L$ , with fixed  $N_1$  as given in expression (4-9) increases with increasing  $d$ . In practical applications the length of the sensing channel is limited to about 1 cm. On the other hand, the optimum value for  $L$  can be reduced by increasing  $N_1'$  until we arrive at a modal field with a very small evanescent tail in a highly absorbing slab region. The maximum values for  $d$  and  $N_1'$  will be limited by technology, for example by variations in  $N_1$ ,  $h_{slab}$ , maximum dopant levels, etc.. It is very hard to give an accurate estimation for the expected maximum values. Therefore for the calculation of the resolution in our opinion reasonable estimates for both the  $d$  and  $N_1'$  have been made.

Taking  $P_{in} = 1$  mW,  $P_{min} = 1 \mu\text{W}$ ,  $(q_1 + q_2) = 0.002$ ,  $a = 0.25 \text{ cm}^{-1}$ ,  $h_{slab} = 70$  nm,  $W = 2 \mu\text{m}$ ,  $h_{ridge} = -0.75$  nm,  $N_1' = 2.10^{-3}$  and  $d = 50 \mu\text{m}$  we arrive at an attainable resolution  $\delta h_i = 5.10^{-6}$  nm with a sensor length of about 13 mm. The technologically more attractive variant with  $h_{ridge} = 0$  nm and  $d \approx 40 \mu\text{m}$  will increase the attainable resolution roughly with a factor two.

As with all the immuno-sensors the  $\delta n_{sol}$  should be small.  $P_{frac}$  as given in expression (4-5) is a complicated function of  $N_1$ ,  $N_3$  and  $N_{eff}$  which are all dependent on  $n_{sol}$ . Numerical evaluation gives for  $n_{sol} = 1.33$  a value of  $(\partial P_{frac} / \partial n_{sol}) = 0.75$ . Using expression (4-8) and the values for the sensor parameters mentioned above, we arrive at  $\delta n_{sol} = 2.2 \cdot 10^{-5}$ .

$$\delta n_{sol} = \frac{(q_1 + q_2) P_{out}}{\frac{\partial P_{out}}{\partial n_{sol}}} = \frac{(q_1 + q_2)}{k_0 N_1' \frac{\partial P_{frac}}{\partial n_{sol}}} L \quad (4-11)$$

The fabrication of the sensing system has been treated already in section 4.2.1, except for the application of absorptive regions immediately after the  $Si_3N_4$  deposition. This can be done by deposition of a thin metal film or in-diffusion of absorbent ions from e.g. the first transition series. Note that this will most probably influence  $N_1$  and this has to be taken into account with the design, e.g. if  $N_1$  has to remain constant an appropriate change of the thickness of the  $Si_3N_4$  layer in the absorptive region should be required. Also the precise value of  $N_1'$  defines the length of the sensing section.

According to this analysis it is possible assuming perfect technology to realize an MAS with the very good resolution of  $10^{-5}$  nm. Also here the sensitivity to  $n_{sol}$  requires a stabilization of the temperature better than  $0.2$  °C.

## 4.4 Immuno sensing with a directional coupler

In this section the attainable resolution and application of a directional coupler for immuno-sensing (iDC) will be investigated.

### 4.4.1 Principle

A structure consisting of two monomodal strip loaded waveguide channels in a directional coupling (dc) configuration is considered (Figure 4.12).

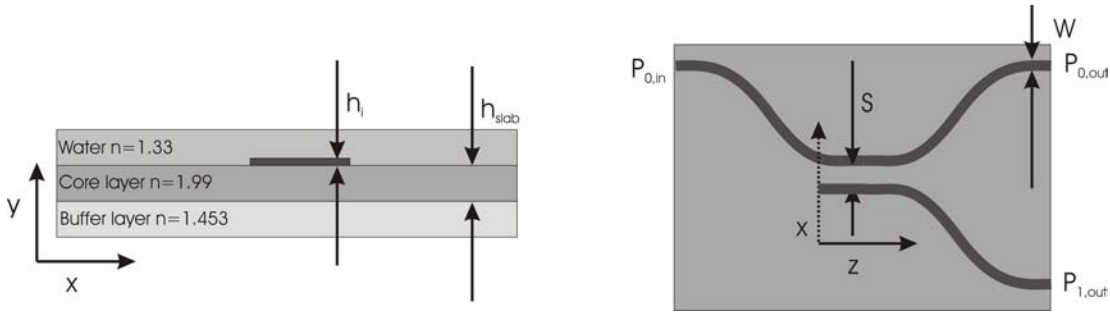


Figure 4.12. The DC immuno-sensor; channel cross section (left) and longitudinal top view (right).

When light is launched into the upper channel, in the dc region light will be coupled into the lower channel. When this coupling is weak, the coupled mode theory can be applied and the coupling strength ( $k_{01}$ ) depends linearly on the overlap integral of the two channel modes over the area of one of the channels. Because the waveguide modes are so weakly guided by the immuno-layer ridge, a small change in immuno-layer thickness will result in a relatively big change in the mode profile, thus the coupling strength is heavily influenced by  $h_i$ . The change in coupling strength can be determined by measuring the modal power in one of the two output waveguides. We'll assume that  $P_{1,out}$  is measured.

### 4.4.2 Analysis

Now a simple model will be presented to estimate the attainable resolution. The output power in the lower channel ( $P_{1,out}$ ) can be approximated using:

$$P_{1,out} = P_{0,in} \sin^2(k_{01}L_{dc}) \quad (4-12)$$

with  $L_{dc}$  the total (effective) length of the coupling section. The  $k_{01}$  can be calculated from the effective indices of the system modes of the dc region:

$$k_{01} = \pi \frac{\Delta N_{sys}}{\lambda} \quad (4-13)$$

here  $\Delta N_{sys}$  is the difference in effective index between the symmetric and anti-symmetric system mode. Expression (4-12) is only exactly valid in the absence of slab light and only if a channel mode decomposes equally into the symmetric and anti symmetric system mode and. The latter is only the case for very weak coupling. It will appear that for this kind of sensor, strong coupling is preferred, in which case the minimum in normalized output power is not 0 but  $g$ , where the  $g$  value represents the effects of slab light and coupling to the symmetric and asymmetric system mode. We can modify expression (4-12) to take into account a non-zero  $g$  value:

$$P_{1,out} = P_{0,in} ((1 - g) \sin^2(k_{01}z) + g) \quad (4-14)$$

giving a sensitivity:

$$\frac{\partial P_{1,out}}{\partial h_i} = P_{0,in} (1 - g) (k_0 L_{dc}) \frac{\partial \Delta N_{sys}}{\partial h_i} \sin(k_{01} L_{dc}) \cos(k_{01} L_{dc}) \quad (4-15)$$

The resolution can be calculated using:

$$\delta h_i = \frac{(q_1 + q_2) P_{1,out}}{\frac{\partial P_{1,out}}{\partial h_i}} = (q_1 + q_2) \left( \tan(k_{01} L_{dc}) + \frac{g}{(1 - g) \sin(k_{01} L_{dc}) \cos(k_{01} L_{dc})} \right) \frac{1}{(k_0 L_{dc}) \frac{\partial \Delta N_{sys}}{\partial h_i}} \quad (4-16)$$

here again the first factor describes the influence of the quality of the peripheral equipment. The middle term needs to be minimized by determining the optimum value for  $k_{01} L_{dc}$ . In the case of weak coupling and no slab light ( $g=0$ ) this would amount to the requirement of  $k_{01} L_{dc} \rightarrow n \cdot \pi$  with  $n$  an integer. A larger  $g$  value directly increases the value of the middle term. The third term shows that both  $L_{dc}$  and  $\partial \Delta N_{sys} / \partial h_i$  need to be maximized.

The factor  $\partial \Delta N_{sys} / \partial h_i$  and the  $g$  value both depend on the separation  $S$ ,  $h_{slab}$  and  $W$ , so this is the parameter space in which the resolution has to be optimized. For all the sensor parameters individually there is a trade off between a large factor  $\partial \Delta N_{sys} / \partial h_i$  (strong coupling) and a small  $g$  value (weak coupling).

It is interesting to compare the proposed sensing structure with a dc sensor where the two branches of the dc are situated on top of each other; the receptor layer is in this case placed on top of the top channel. This kind of geometry has been investigated before [6], [9], but here the effect relies on the measurand induced change of the effective refractive index of the upper channel. However expression (4-16) can also be used for describing the layer stacked dc coupler system. In this option as well as in the one with horizontal coupling the effective refractive index of both the system modes increases with increasing  $h_i$  and we expect that the resolution of both systems will be similar. The

largest difference comes from the technology, the technology for the layer stacked dc being more complicated. However if in the dc structure proposed by us the IO chip has been permanently bonded to a microfluidic system, substitution of a degenerated antibody structure by a fresh one is nearly impossible because of the need for patterning the antibody layer.

Note that with the Mach Zehnder Interferometer (MZI) only the effective index of the sensing branch ( $N_0$ ) depends on  $h_i$  and the index of the reference branch ( $N_1$ ) doesn't. From this it follows that  $\partial(N_0-N_1)/\partial h_i > \partial\Delta N_{sys}/\partial h_i$ , which gives the MZI an inherent advantage with respect to performance on the directional coupler configurations.

### 4.4.3 Design

A design has been made using an approach as depicted in Figure 4.13. The parameters and properties of the designed iDC are given in Table 4.2.

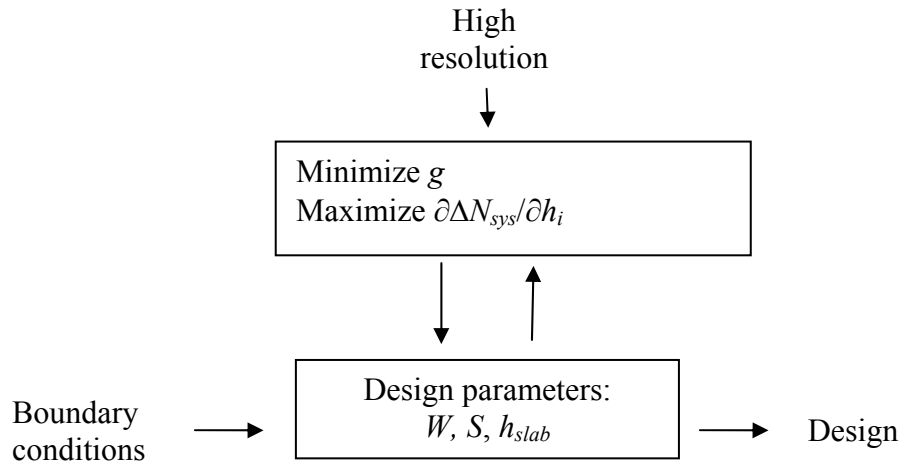


Figure 4.13. Design scheme iDC.

Table 4.2. Design of the iDC.

Parameter/property	Value
$h_{slab}$	100 nm
$W$	4 $\mu\text{m}$
$S$	4 $\mu\text{m}$
$g$	0.06
$L_{dc}$	$\approx 1$ cm
$\delta h_i$	$4 \cdot 10^{-4}$ nm
$\delta n_{solv}$	$4 \cdot 10^{-5}$

The fabrication of this sensor is very simple and similar to that of the iSWS. The technology has already been treated in section 4.2.1. To minimize the second factor in expression (4-16) good control over the coupling strength is required. From practical experience it is known that the coupling strength (mostly determined by  $S$ ) is hard to predict theoretically and thus multiple sensors with different  $S$  need to be fabricated after which the optimum  $S$  can be determined. However, with constant technology, this optimum  $S$  can be used for all the sensors that are fabricated afterwards.

Using very simple technology the iDC offers the possibility of a resolution of  $4 \cdot 10^{-4}$  nm. Notice how much the technology and the attainable resolution of the iDC and the iSWS look alike.

## 4.5 Immuno sensing with a GAC

In this section the application of the GAC sensor for immuno-sensing purposes will be investigated. In principle exactly the same boundary conditions apply as for the bulk GAC sensor. For this design however we suppose that it is possible to fabricate gratings with a grating depth  $h_{gr} = 1$  nm and we will limit the grating length to 1 cm.

The design procedure differs from that of the bulk GAC only in two minor ways: firstly the refractive index of the cladding layer is now taken to be 1.33 (water) and secondly the factor  $\partial\delta N/\partial\Delta h_i$  is now maximized in stead of  $\partial\delta N/\partial\Delta n_{sens}$ . We refer to chapter 3, section 3.2.1 for the rather complicated definition of  $\delta N$ .

Following the design procedure as given in section 3.3 we arrive at an optimal structure of which the parameters are given in Table 4.3 and the  $P_{out}$  and  $\delta h_i$  characteristics are given in Figure 4.14.

**Table 4.3. Designed iGAC sensor.**

Parameter/property	symbol	Value
Core layer height	$h_r$	550 nm
Grating depth	$h_{gr}$	1 nm
Grating period	$\Lambda$	3.91 $\mu\text{m}$
Coupling length	$L_c$	0.70 mm
$\partial\delta N/\partial\Delta h_i$		$1 \cdot 10^{-4} \text{ nm}^{-1}$
Resolution	$\delta h_i$	$10^{-5} \text{ nm}$
	$\delta n_{solv}$	$3 \cdot 10^{-8}$

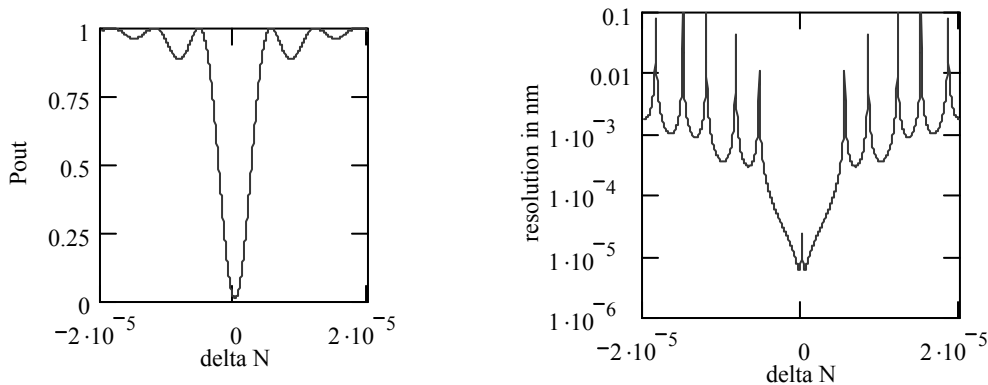


**Figure 4.14. Output power and  $\delta N$  characteristic iGAC sensor.**

As can be concluded from Figure 4.14 the GAC sensor has theoretically the potential to operate with the high resolution of  $10^{-5}$  nm. For this however it is necessary that  $\delta N$  is tuned very precisely to the optimal working point. The available tuning range in  $\delta N$ , using just wavelength tuning with the currently available tunable laser (range 632-638 nm), is about  $\pm 2 \cdot 10^{-4}$ . With the current technology however there is an uncertainty in  $\delta N$  of  $\pm 4 \cdot 10^{-3}$  and it is clear that just wavelength tuning cannot compensate for this.

There are however commercially available tunable lasers with larger tuning ranges. Also on the side of the technology there is room for improvement. The inaccuracy of the core thickness, which has the largest contribution to the uncertainty in  $\delta N$ , can be decreased by improving the etching process used to control the core thickness. It is also possible first to characterize the waveguide channel and then to determine the grating period, in which case the uncertainty of  $\delta N$  is determined by the accuracy of the characterization method and not by the accuracy of the technology.

The GAC is extremely sensitive to changes in  $n_{solv}$ , which is not so unexpected, since nearly the same design of the GAC is used for bulk sensing. This implies that the use of a reference sensor, covered with an immuno-layer which is desensitized, is mandatory.

There are still some unsolved issues (section 3.6) and in fact more research is required for answering the question how far one can proceed on the way to realize GAC sensors that operate indeed with the very high resolution of  $10^{-5}$  nm.

## 4.6 Comparison of the different immuno-sensing principles

The three different sensor types, the iSWS, MAS and iDC, all exploit a measurand induced change in the modal field to measure the effective increase of the thickness of the monomolecular antibody layer,  $\Delta h_i$ . In all three sensors the waveguiding channels are defined as strip loaded ones, of which the strip is formed by patterning the antibody layer. In all sensors theoretically high resolutions can be achieved (see table 4.4) The shape of the modal field depends very little on  $n_{solv}$  and therefore these three sensor principles have a relatively low sensitivity to changes in  $n_{solv}$ . The fourth sensor, the GAC, however is utilizing a change in effective refractive index of a guided mode in a grating waveguiding system to determine  $\Delta h_i$ . Because a GAC can be used both for bulk and immuno sensing (like the MZI ), and the optimal designs for both applications do not differ so much ,the sensitivity of the GAC to changes in  $n_{solv}$  is very high and a reference sensor is definitely necessary.

In Table 4.4 the different immuno-sensing principles are listed, together with the theoretically attainable resolution. Also an assessment has been made to the complexity of the required technology to fabricate the sensors using those principles.

**Table 4.4. Overview of the different immuno-sensing principles.**

Sensor method	Key word	Resolution	Technology	$\delta n_{solv}$
iSWS	Segmented waveguide	$7 \cdot 10^{-4}$ nm	++	$10^{-5}$
iDC	Directional coupler	$4 \cdot 10^{-4}$ nm	+	$4 \cdot 10^{-5}$
MAS	Modal attenuation	$10^{-5}$ nm	+/-	$2 \cdot 10^{-5}$
iGAC	Grating assisted mode coupling	$10^{-5}$ nm	-	$3 \cdot 10^{-8}$

If very high sensitivity is required, the MAS seems to be the most interesting option, because of the simple technology. The GAC sensor looks to be the least promising because of the small  $\delta n_{solv}$  and its complicated technology. The sensor which is easiest to fabricate is by far the iSWS.

Notice the trade off between the difficulty of the technology and the attainable resolution.

Finally it is relevant to compare the theoretical resolution of the new sensor types with experimentally proven resolutions of well known sensor systems like the Mach Zehnder Interferometer [3], the Young Interferometer [7] and the Surface Plasmon Resonance based sensors:  $2 \cdot 10^{-5}$  nm,  $10^{-3}$  nm and  $5 \cdot 10^{-4}$  nm respectively. Taking into account the considerably simpler technology of the sensors proposed in this chapter, it is valuable to continue investigating the potential of these sensors in practice.

## 4.7 References

- [1] www.Biacore.com
- [2] A.Ymeti, J.S.Kanger, J.Greve, P.V.Lambeck, R.Wijn and R.G.Heideman, *Realization of a multichannel integrated Young interferometer chemical sensor*, Applied Optics, 42 (2003), pp 5649-5660.
- [3] R.G.Heideman and P.V.Lambeck, *Remote opto-chemical sensing with extreme sensitivity: design, fabrication and performance of a pig-tailed integrated optical phase-modulated Mach-Zehnder Interferometer system*, Sensors and Actuators B61 (1999), pp 100-127.
- [4] Integrated Optical circuits and components; design and applications, ed. E.J.Murphy, Marcel Dekker inc., Chapter 10: Integrated optics in sensors: *advances toward miniaturized systems for chemical biochemical sensing*, pp. 335-380, author R.E. Kunz.
- [5] *Integrated optics*, T.Tamir ed. Springer Verlag Berlin 1979, ISBN 3-387-09673-6, pp 45-53.
- [6] Luff BJ, Harris RD, Wilkinson JS, Wilson R, Schiffrin DJ, *Integrated-optical directional coupler biosensor*, optics letters 21(8) (1996), pp 618-620.
- [7] A.Ymeti, J.S.Kanger, J.Greve, P.V.Lambeck, R.Wijn and R.G.Heideman, *Realization of a multichannel integrated Young interferometer chemical sensor*, Applied Optics, 42, (2003), pp 5649-5660.
- [8] Paul V.Lambeck, Hugo J.W.M.Hoekstra, Joris van Lith and Gijs van Elzakker, *Two novel Integrated Optical sensor types for measuring chemical concentrations, based on chemically induced changes of modal field profiles*, J. of Nonlinear Optics, to be published 7/2007
- [9] H. Kreuwel, doctoral thesis, *Planar waveguide sensors for the chemical domain*, Lightwave Devices Group, University of Twente.

## 5 The cut off sensor

### 5.1 Introduction

During the research on the chip fabricated for the characterization of the GAC sensor (see chapter 3) some unexpected response of a reference channel was encountered: when the refractive index of the liquid ( $n_{sens}$ ) was increased, the output power suddenly dropped very steeply. Closer examination showed that this drop occurred around the  $n_{sens}$  value corresponding with the cut off of the guided mode in part of this reference channel, meaning that at higher  $n_{sens}$  values no guided mode can be supported by this channel structure anymore.

By mounting the microfluidic system on top of the reference channel in fact we had made a segmented waveguide with only two transitions, as is schematically depicted in Figure 5.1. The structure contains essentially two types of segments: one segment of the first type, in which the core layer is covered with a SiON cladding layer ( $n= 1.472$ ) with a thickness of  $2\ \mu\text{m}$ , on top of which the liquid with variable value of the refractive index had been applied. This segment is connected to two segments of the second type: sections in which the liquid is replaced by the walls of the microfluidic system and these walls are schematically represented in Figure 5.1 as semi-infinite  $\text{SiO}_2$  layers. In a non-guiding state of the central section, all power of the guided mode at the first transition would be transferred to radiation modes and will radiate away. A fraction will be recaptured as guided mode power at the second transition. Note that in the system  $L \approx 15\ \text{mm}$ .

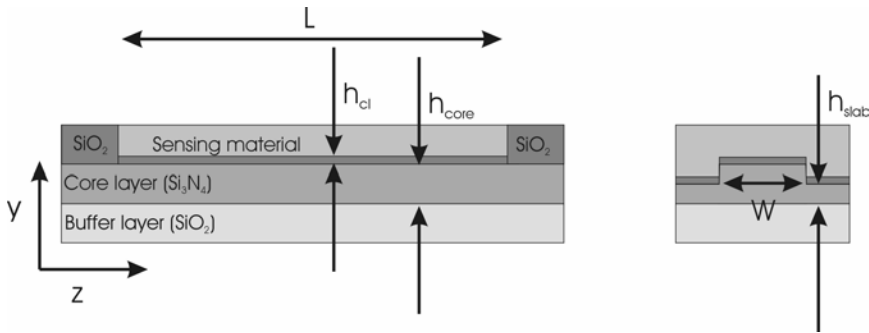


Figure 5.1. Longitudinal (left) and transverse (right) cross section cut off sensor.

So, just as with the immuno-sensors treated in chapter 4, we are exploiting the large change of the extension of the field profiles close to cut off, but now along the transversal and not the lateral direction. In addition in this sensor we are even passing the cut off condition on varying  $n_{sens}$ .

In this chapter we first treat the experimental results obtained on the reference channel of the GAC treated in chapter 3. After that the system is analyzed on the basis of a 2D model, and it will be explained why the drop in output power is so steep. Then we'll discuss how this new phenomenon can be applied to make cheap and sensitive IO sensors. The chapter ends with a conclusion.

## 5.2 Experimental

The longitudinal cross section of the waveguiding system on which the experiment has been performed is depicted in Figure 5.1. The system has been realized using the fabrication process of the GAC (section 3.4.1.); hence its layer stack contains a SiO<sub>2</sub> buffer layer (n= 1,452), a Si<sub>3</sub>N<sub>4</sub> core layer (n= 1.92) and a SiON cladding layer (n= 1.472). The waveguide has been structured as a ridge type channel waveguide with  $h_{cl} = 2 \mu\text{m}$ ,  $h_{core} = 40 \text{ nm}$ ,  $h_{slab} = 20 \text{ nm}$ ,  $W = 2.4 \mu\text{m}$  and  $L = 1.5 \text{ cm}$ . Its sensing performance will be characterized by  $P_{out}/P_{out,max}$  versus  $n_{sens}$  curves, measured with the measurement setup as described in section (2.6.1) at a wavelength of 632.8 nm. The measured characteristics have been depicted in Figure 5.2.

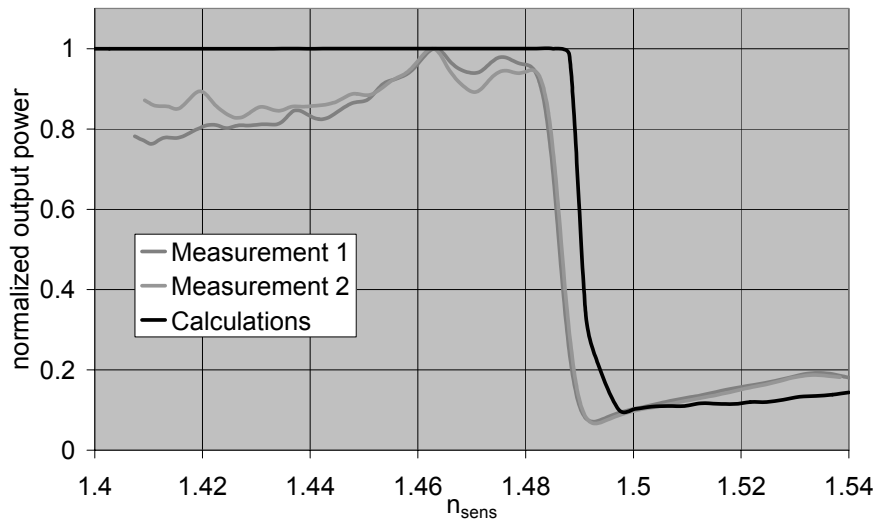


Figure 5.2. Measured  $P_{out}$  versus  $n_{sens}$  characteristic.

From comparing both experimental curves it can be concluded that the measurements are well reproducible. The most noticeable fact however is that the normalized output power,  $P_{out}$ , drops from 0.8 to 0.2 within a very small  $n_{sens}$  range.

### 5.3 Analysis

We also calculated the  $P_{out}$  versus  $n_{sens}$  curves for the given structure using the BEP method. Because we are able to perform BEP calculations on 2D structures only, we approximated the 3D structure by a 2D slab structure of the type as depicted in figure 5.1. However we have reduced the value for  $h_{core}$  to 38 nm so that the cut off value for  $n_{sens}$  is identical for both the 3D and equivalent 2D structure. As can be seen from Figure 5.2, the calculations match the measurements reasonably well. The difference in the position of the drop between the 2D BEP calculations and the measurements are attributed mainly to the inaccuracy in determining  $n_{sens}$  and to the uncertainty in the effective index of the guided mode at the in and output sections.

We have called the structure in Figure 5.1 a cut off sensor. We will call the region between the points  $n_{sens} = n_{SiON}$  (corresponding with  $P_{out} = 1$ ) and the cut off value of  $n_{sens}$  (corresponding with the lowest value of  $n_{sens}$  for which the centre section does not support a guided mode, hence  $P_{out} = 0$ ) the transition region. Within this region for increasing  $n_{sens}$  the mode profile strongly widens, becoming infinitely wide at the cut off value.

The precise effects within this transition region will depend on the structural parameters of the waveguiding structure. While investigating the influence of the structural parameters, we have limited ourselves to the aforementioned materials and so in our approximate 2D structure as variable parameters only  $h_{core}$ ,  $h_{cl}$  and  $L$  are left. At first we will have a look at the effect of varying  $h_{cl}$  with  $h_{core} = 40$  nm (Figure 5.3).

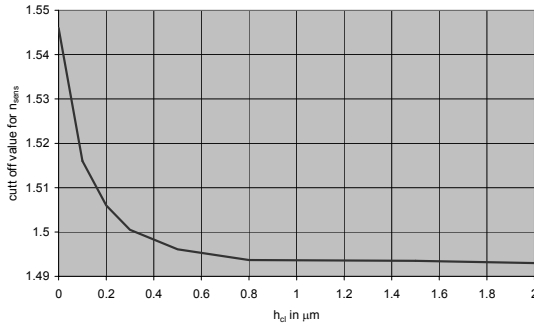


**Figure 5.3.** Cut off value of  $n_{sens}$  for different  $h_{cl}$

The cut off value of  $n_{sens}$  decreases from 1.545 (at  $h_{cl} = 0$ ) to 1.492 (at  $h_{cl} = 2.0 \mu\text{m}$ ). Thus the transition region increases for smaller  $h_{cl}$  values. And hence for smaller  $h_{cl}$  values a more gradual change of the overlap integral as a function of  $n_{sens}$  at the first transition can be expected. Using the BEP, also the  $P_{out}$  versus  $n_{sens}$  curves have been calculated for various  $h_{cl}$  values, as is shown in Figure 5.4 and Figure 5.5.

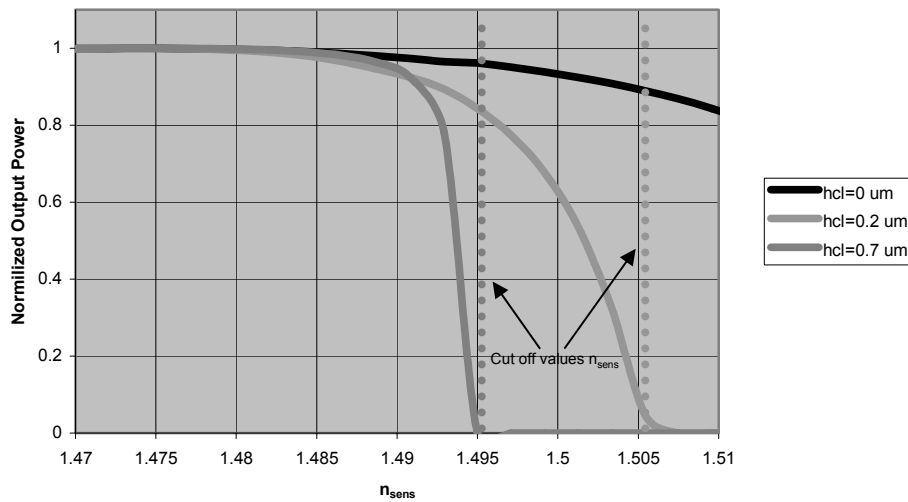


Figure 5.4.  $P_{out}$  versus  $n_{sens}$  curves for different  $h_{cl}$  ( $h_{core} = 40$  nm,  $L = 2$  cm).

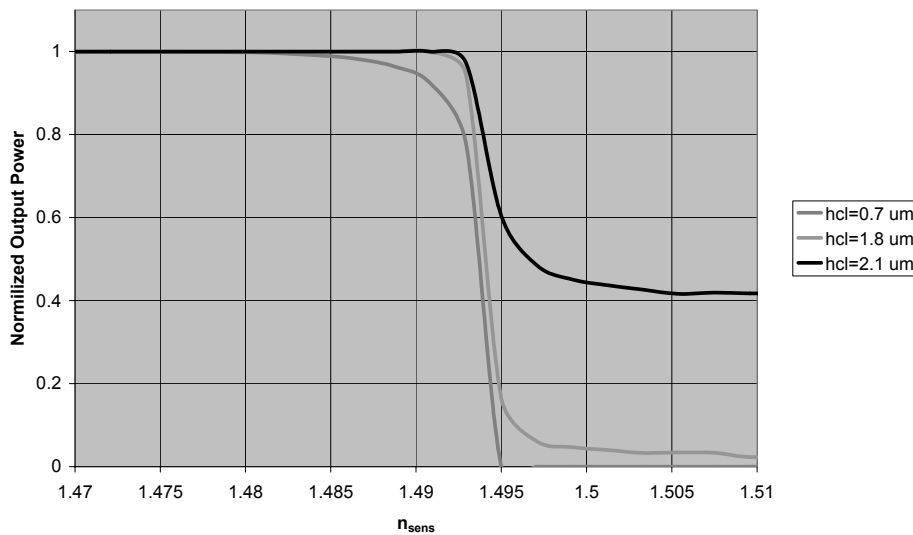


Figure 5.5.  $P_{out}$  versus  $n_{sens}$  curves for different  $h_{cl}$  ( $h_{core} = 40$  nm,  $L = 2$  cm).

Note that the onset of the transition region is determined by the refractive index of the cladding material (1.472); when  $n_{sens} = n_{SiON}$  the overlap at the transition between the sensing region and the in/output regions is 1 and thus  $P_{out} = 1$ . The end of the transition region is defined by the cut off value of  $n_{sens}$ , where  $P_{out} = 0$ . The steepness of the transition region is related to the difference between  $n_{SiON}$  and  $n_{cutoff}$ .

One should expect that continuously increasing  $h_{cl}$ , hence continuously decreasing the width of the transition region, steepness should increase continuously too. However for  $h_{cl} > 0.7$   $\mu\text{m}$  a deviating performance is calculated.

The unexpected behavior for  $h_{cl} > 0.7 \mu\text{m}$  originates from the behavior of the radiation modes, i.e. the amount and phase of the light coupled from radiation modes to the guided mode at the second transition. When we analyze the  $h_{cl} > 0.7 \mu\text{m}$  systems further we find that here the radiation modes propagate in the form of a leaky mode. For these systems the field profile of the leaky mode is very similar to that of the guided mode in the in/output sections and at the first transition a major fraction of the guided mode power is transferred to this leaky mode in the second section. The field profile of the leaky mode is similar to that of the guided mode; only part of the field is now present inside the high index sensing material, causing the mode to leak power into the sensing material. This explanation is confirmed by the fact that by calculating the  $L$  dependence of  $P_{out}$  versus  $n_{sens}$  curves for the  $h_{cl} > 0.7 \mu\text{m}$  systems, using a leaky wave model as given by [1] and [2], results have been obtained which perfectly agree with those of the BEP calculations.

For the configuration ( $h_{cl} = 0.7 \mu\text{m}$  and  $n_{sens} = 1.4935 < n_{cutoff}$ ) the length dependency of  $P_{out}$  has been calculated and is depicted in Figure 5.6.

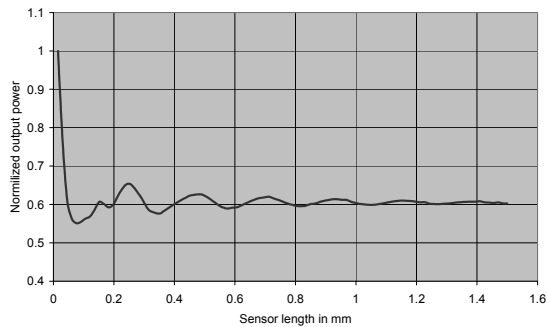


**Figure 5.6. Length dependence  $P_{out}$ .**

It can be seen that for small  $L$  values, almost all the radiation is captured again at the second transition. For large  $L$ , no radiation couples back into the output section. In between there are some interference effects between the radiation modes and the guided mode. These effects could in principle be used to increase the sensitivity, but the improvement is marginal. It can also be observed that in this case a sensing length of only 1 mm is already sufficient to prevent all the radiation from coupling into the guided mode of the output section.

For illustration it is shown in Figure 5.7 how a guided mode launched from the input section propagates through a sensing section.

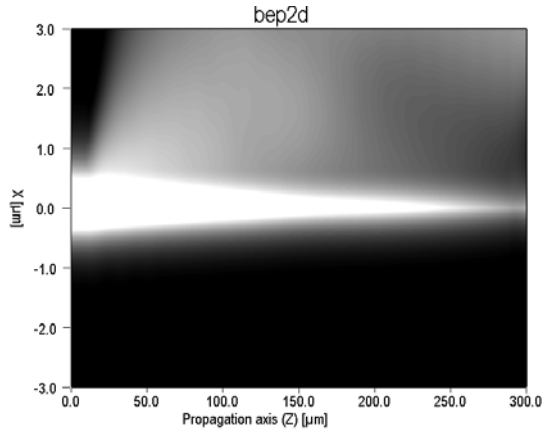


Figure 5.7. BEP calculation cut off sensor for  $h_{core} = 40$  nm,  $n_{sens} = 1.4935$  and  $h_{cl} = 0.7$ .

## 5.4 Application

The typical  $P_{out}$  versus  $n_{sens}$  characteristic of the cut off sensor makes it ideal for operation as an alarm sensor. The device can be designed such that the throughput jumps from 1 to 0 after passing a very narrow  $n_{sens}$  band around a certain threshold value of  $n_{sens}$ . The threshold value can be easily adapted to requirements of a specific application by varying the core thickness ( $h_{core}$ ), as is illustrated in Figure 5.5.8.

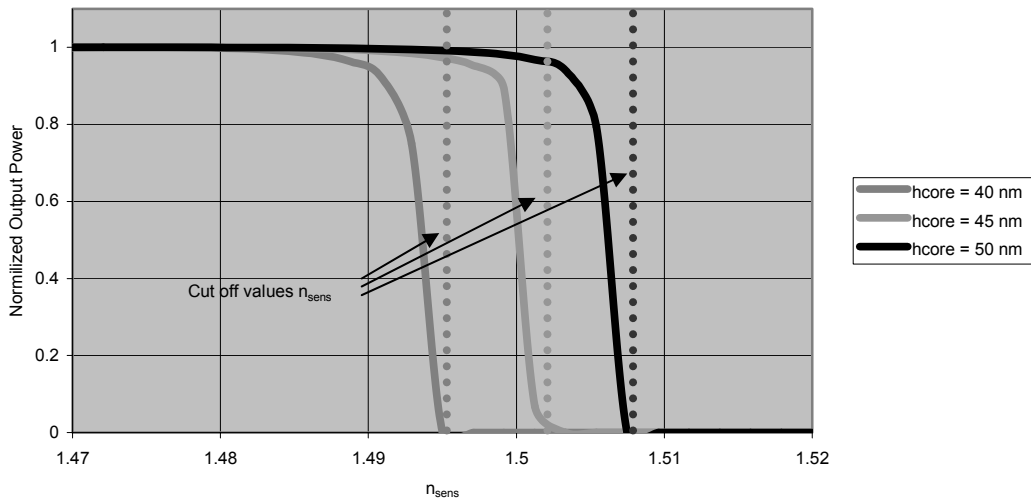


Figure 5.5.8. Setting the threshold value by varying  $h_{core}$  ( $h_{cl} = 0.7$   $\mu\text{m}$ ,  $L = 1$  mm).

Notice that the slope of the characteristic is almost constant implying a nearly linear behavior of the sensor over this small range. One could also think of a sensor which is designed to operate in a certain range of  $n_{sens}$  values. The upper limit of this range can be

controlled using  $h_{core}$ . The lower limit of the  $n_{sens}$  range can be controlled by the refractive index of the cladding layer, which could be varied using our SiON technology.

The resolution of the sensor ( $\delta n$ ), taking into account light source power fluctuations and noise in the detectors and processing electronics only, can be calculated using expression (5-1).

$$\delta n = \frac{(q_1 + q_2)P_{out}}{\left(\frac{\partial P_{out}}{\partial n_{sens}}\right)} \quad (5-1)$$

So in approximation the resolution is inversely proportional to the range of  $n_{sens}$  values.

In Chapter 2 we showed already our interest in measuring Relative Humidity (RH) using gelatin as a chemo-optical transduction layer. We observed a large hysteresis and a bad reproducibility of SW sensors fitted with a gelatin sensing layer, which we attributed to the swelling of the gelatin. Let's assume that the gelatin follows in the cut off sensor its RH characteristics as given in Appendix E and that the swelling of the gelatin doesn't degrade the intended behavior. Then an interesting structure would be the following one:  $n_{SiON} = 1.472$ ,  $h_{core} = 50$  nm,  $h_{cl} = 0.7$   $\mu$ m and  $L = 1$  mm. The  $n_{sens}$  range of this sensor is  $3.10^{-3}$ . Setting  $(q_1 + q_2) = 0.002$ , the resolution in the middle of the sensing domain ( $P_{out} = 0.5$ ) is calculated to be  $3.10^{-6}$ . If a thick gelatin layer is applied, the  $P_{out}$  versus RH curve can be calculated and is given in Figure 5.9.

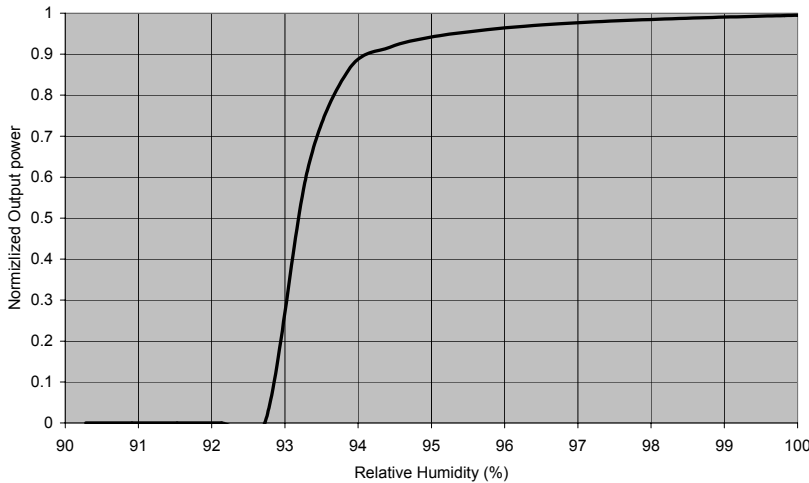


**Figure 5.9. Cut off sensor applied to measuring relative humidity.**

As can be seen the  $P_{out}$  jumps from 0 to 0.9 within just 1 % change in the RH. The value of  $h_{core}$  can be tailored ( $h_{core} = 37$  nm) to have the jump around RH= 99.5 % and this sensor could provide a low cost solution for mist detection.

## 5.5 Fabrication

The simple technological process needed for the fabrication of the cut off sensor is perhaps one of its strongest points. A technologically very interesting option is presented by a disposable chip consisting only of a slab structure to confine the light in transversal direction and fitted with gratings (2x2 mm) for the coupling of light into and out of the IO chip. The principle allows for a slab structure without any channel definition because the sensing segment length  $L$  can be small. The slab mode will only diverge a little in the lateral direction, causing some additional insertion loss. We expect that the sensor chip can be very small, having a foot print of less than 10 mm<sup>2</sup> per sensor. Of course free space beam optics is necessary for this, the same optics as has been discussed already in section 4.1.2.

The sensor structure of the type as depicted in Figure 5.1 can be realized by thermal oxidation of a silicon wafer, followed by LPCVD deposition of the Si<sub>3</sub>N<sub>4</sub> core layer (Notice that it is not necessary to use PECVD Si<sub>3</sub>N<sub>4</sub> like with the GAC sensor). After that the gratings will be defined in the core layer. Next a PECVD SiO<sub>2</sub> cladding layer is deposited and sensing windows need to be defined using the RIE/BHF etching procedure which has been described in Appendix F. Finally the sensing layer can be applied, for example by spinning.

The only critical parameter that needs to be controlled in the whole process is the thickness of the core layer, which determines the threshold value of  $n_{sens}$ . The required accuracy for this is of course application dependent. For example, assuming an accuracy in core thickness of 1%, the threshold value of the RH sensor related to Figure 5.9 can be controlled with an accuracy of 0.3 % RH.

## 5.6 Conclusion

An unexpected steep drop in  $P_{out}$  versus  $n_{sens}$  curves measured at a reference channel in a GAC sensor triggered the investigation of its origin and from that the cut off sensor had been proposed. The sensor can be considered as belonging to the class of segmented waveguide sensors, where this modification contains only three segments. It was discovered that the response of the cut off sensor could be dramatically improved by optimizing the thickness of a thin cladding layer deposited on top of the core layer in the middle segment.

The sensor principle can be applied for continuous sensing; a typical resolution  $\delta n$  was calculated to be  $3 \cdot 10^{-6}$  with an operating range of  $3 \cdot 10^{-3}$ . The center of the range can be adjusted to the application requirements by adjusting the thickness of the core layer or/and the refractive index of the SiON cladding layer.

Very low demands are put on both the detector and light source. The fabrication of this kind of sensors is very simple and if grating coupling is used, a disposable sensor with a very small foot print (about 10 mm<sup>2</sup>) can be obtained; thus cheap mass production should be possible.

To our opinion this kind of sensor would be excellent for use as an alarm sensor and especially if they are needed in large quantities. So we calculated, that such as sensor fitted with a gelatin layer can indicate the passing of 99.5 % relative humidity with an accuracy of the set point of 0.3 %. Even though this kind of sensors is probably exceptionally cheap for an IO sensor, for all applications its performance/price ratio has to be carefully compared to that of other types of sensors.

## **5.7 References**

- [1] G van Elzaker, MSc. Graduation report, *Design of a Integrated optical evanescent field based read-out system for a MEMS gyroscope*, Lightwave Devices Group, University of Twente, December 2003.
- [2] G. Altena, thesis, IOMS, University of Twente, to be published.

## **6 Discussion**

In this chapter firstly a summary of the thesis will be given. Then the concepts for IO sensors as treated in this thesis will be compared to a few existing IO sensors. Eventually the results of this project will be evaluated.

### **6.1 Summary**

#### **6.1.1 General introduction**

Main objective of this PhD research project has been to explore the potential of Segmented Waveguide Sensors (SWS) for application in the chemical domain. And indeed large attention has been paid to this SW -principle both for bulk sensing (Chapter 2, design, realization and characterization of a SW sensing system) and for surface sensing (section 4.2, theoretical analysis of an SWS for immuno-sensing). However both the theoretical analysis of, and the experimental results obtained at SW sensors led to ideas about various novel refractive sensing principles. One of them the co-directional Grating Assisted Coupling sensor has been worked out very thoroughly both theoretically and experimentally (Chapter 3), while various other principles have been worked out theoretically only. Here we mention the principles tailored for surface sensing, which have been described in Chapter 4 and which just as the SWS are based on chemically induced changes of modal field profiles. Another sensor, which we have called the Cut Off sensor, is based on a chemically induced passing of the cut off condition of a guided mode (Chapter 5).

This PhD project has especially exploited/ utilized expertise in the fields of integrated optics and microtechnology. For developing a complete sensing system based on an IO sensing principle however expertise on other disciplines has to be involved too, e.g. in the fields of electronics (for control and processing purposes), micromechanics (a microfluidic system for processing the sample liquid and accomplishing a well controlled transport of liquids to the sensing region) and chemistry, the latter for offering or developing the optical transduction materials.

### 6.1.2 The segmented waveguide sensor (SWS)

The SWS-principle is based on the fact that at a transition between two waveguide channels only a part of the modal power of the incoming guided mode is transferred to the power of the guided mode propagating at the other side of the transition. This fraction depends on the difference of the cross sectional index distributions at both sides of the transition and this difference can be influenced by the measurand, the concentration of a certain analyte e.g. by having incorporated an appropriate chemo-optical transduction material inside the relevant refractive index distribution of one of the wave guides. By having a series of these transitions, hence making a segmented structure as presented in Figure 2.1, the effect can be enhanced.

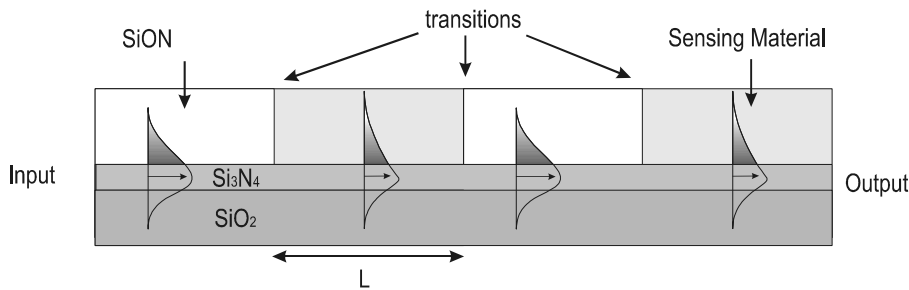
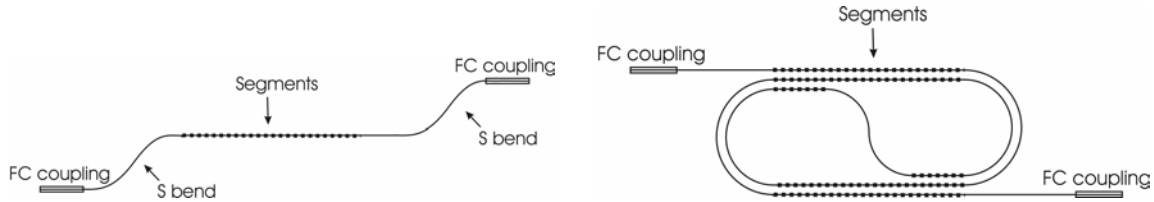


Figure 6.1. Longitudinal cross-section of the SWS (4 segments).

Starting from this principle the behavior of SWS sensors has been investigated theoretically. Soon it became clear, that part of the power “lost” at a transition to radiation modes could couple back to the guided mode at next transitions. Hence it had to be concluded that, in order to describe the behavior of the segmented sensing section correctly, simulation/calculation methods were necessary that could handle the radiation field very well. Three methods, the FD Beam Propagation Method, the Bidirectional Eigenmode Propagation method and a Spectral Decomposition Method, have been considered. It was concluded that the BEP method had to be preferred for accurate calculations, but that the SDM offered the most insight in the operation of the sensor. In SDM the response could be described as a product of two factors, one of them being dependent on the channel structure and the other on the segmentation. The model enables to determine how both factors have to be matched to each other in order to get large sensing effects.

A theory has been developed which enables to determine the attainable resolution. The resolution could be expressed as the product of two factors, one containing the characteristics of the peripheral equipment the other containing the sensor parameters only. A manifold of segmented structures, being either multimodal or monomodal with segments differing in geometry, material composition or both, can be considered. It was decided to focus on a simple type of segmentation, in which two types of segments are present only mutually differing with respect to the constitution of the cladding, being either a sensitive or a passive material. An SWS of this type has been designed taking

into account not only the requirement of the sensing section but also those of other IO functions which had to be implemented into the circuitry such as fiber to chip coupling functions, bends and Y splitters. A top view of such an IO circuit has been given in Figure 6.2 (left).



**Figure 6.2.** Two possible layouts of the SWS.

Next to straight sensing sections also spiral shaped sensing functions with a total segmented length up to 15 cm as shown in Figure 6.2 (right) has been designed. A manifold of SW sensors with identical channel structures but mutually differing in segmentation and length of the sensing section have been realized using SiON technology. Although the fabrication process is in principle simple, there were however several non-standard steps in the fabrication process that proved to be more challenging than expected. All structural parameters (refractive indices and geometrical parameters) of the realized sensor have been determined and they appeared to be close to the intended values.

The performance of many of these sensors has been determined by replacing the sensitive cladding material by liquids of which the refractive index could be controlled very precisely. For this a mixing system was developed which offers at its output a binary liquid mixture of which the refractive index continuously increased with time. This fluid was transported to a microfluidic system attached on top of the sensing section. The experimental results agreed reasonably well with the theory. Their difference was attributed to the fact that in all calculations the systems had to be approximated as 2D systems while in reality they are of course 3D. Using properties of currently available “standard” peripheral equipment, an attainable resolution  $\delta n \approx 3 \cdot 10^{-7}$  was estimated.

Also some practical chemo-optical transduction materials have been applied to the sensors: gelatin and polysiloxane both being sensitive to relative humidity (RH) and reacting to a change of the RH by a change of their refractive index as well of their volume. In their  $P_{out}/P_{in}$  versus  $n_{sens}$  characteristics they showed a very large hysteresis and irreproducible behavior. This has been attributed to the adhesion of the transduction materials to the SiON cladding at the transitions. At small expansion of the materials clamping effects will degrade the intended effects, while at larger expansion the materials will be deformed irreversibly. So we had to conclude that the SW sensors are not applicable for chemo-optical transduction layers, in which refractive index changes are accompanied by considerable swelling.

A second segmented structure consisting of segments, which differed in the lateral compositions of the passive cladding material has been identified as being very promising, showing theoretically a resolution being a factor 4 higher than that of the

realized simple segmented structures described earlier. During the characterization several unexpected ‘dips’ were discovered in the SW characteristics. The existence of these ‘dips’ was explained and this sparked the idea for the Grating Assisted mode Coupling sensor (GAC).

### 6.1.3 The grating assisted mode coupling sensor (GAC)

The potential of the grating assisted mode coupling principle for IO sensing has been analyzed in a way similar to the SW sensor. A model has been developed to describe the behavior of the sensor and a design for obtaining a “proof of principle” has been made. Two batches of GAC sensors have been fabricated. The first batch didn’t work because of technological problems. These problems were all solved in the second batch. Structural parameters have been measured either as an intermediate step during the production or at the final system and all parameter values appeared to be close to the intended ones. However the response of the realized sensor was not as expected and up to now we do not have a solid explanation for the behavior of the sensor. Notice e.g., that in section 2.8 experiment and theory about such a GAC sensor did correspond well!!

During the characterization of the sensor however an unexpectedly steep drop in output power was observed starting at a specific refractive index of the liquid used for characterization. This observation led to the investigation of the cut off sensor.

### 6.1.4 Various novel immuno- sensing principles

Several novel immuno-sensing principles all based on concentration induced changes of modal field profiles have been conceived and investigated theoretically: a special type of segmented waveguide sensor suitable for immuno-sensing (iSWS), a modal attenuation sensor (MAS) in which changes of the lateral modal field profile influence the portion of the modal field inside an absorptive region, and the directional coupler (iDC) in which the changes of the lateral modal field profile influence the coupling strength. In all sensors the waveguiding channels are defined by or provided with a patterned cladding layer consisting of a one molecule thick anti-body layer immobilized on top of the core layer. The iSWS, MAS and iDC all exploit the corresponding change in the lateral modal field to measure the change of the effective sensing layer thickness ( $\Delta h_i$ ). A high resolution is achieved as a result of the large dependency of the width of the modal field on  $\Delta h_i$  in case the waveguide is close to the lateral cut off condition. In all three sensors the lateral contrast of the strip loaded waveguide depends very little on the refractive index of the solvent ( $n_{solv}$ ) and therefore they have a relatively low sensitivity to changes in  $n_{solv}$ .

A fourth sensor presented also in this chapter (the iGAC) is exploiting the change in effective refractive index to determine  $\Delta h_i$ . Because an identical GAC could be used both for bulk and immuno sensing the sensitivity to changes in  $n_{solv}$  is very high and for this sensor a reference branch is indispensable.

The MAS combines a good (calculated) value of the resolution ( $\approx 10^{-5}$  nm) with a simple fabrication process. It has to be noted however that no profound analysis of influences of the technological tolerances has been performed. Of the four sensors considered, the sensor by far the easiest to fabricate is the iSWS, which is still able to attain a reasonable resolution of  $\delta h_i \approx 7 \cdot 10^{-4}$  nm. With a resolution of  $4 \cdot 10^{-4}$  nm and a more complicated fabrication process, the iDC seems to be clearly inferior to both previous sensors. The GAC sensor can obtain a resolution similar to the MAS ( $\Delta h_i \approx 10^{-5}$  nm), however it is very sensitive to  $n_{solv}$  and the fabrication process is the most complicated one, therefore to our opinion it is the least promising option.

### 6.1.5 The Cut off sensor (COS)

An unexpected steep drop in output power as a function of  $n_{sens}$  triggered the investigation of the cut off sensor. Closer examination showed that when  $n_{sens}$  is higher than a certain value, no guided mode is supported by the waveguiding structure and a large part of the modal power radiates away. It was discovered that the response of the cut off sensor could be dramatically improved by optimizing the thickness of a thin cladding layer deposited on top of the core layer.

The sensor principle can be applied for continuous sensing; a typical resolution was calculated to be  $3 \cdot 10^{-6}$  with an operating range of  $3 \cdot 10^{-3}$ . Because of the characteristic response of the sensor however, a really interesting application would be as an alarm sensor. Very low demands are put on both the detector and light source. The fabrication of this kind of sensors is very simple and the sensor chip itself has a very small foot print, thus cheap mass production should be possible. We think that this kind of sensors would be excellent for alarm type sensors, which need to be produced in large quantities.

## 6.2 Comparison

To place the results of this project in a somewhat larger context, a comparison is necessary between the IO sensor principles worked out in this PhD thesis and other already existing IO sensors. There is however a huge amount of different IO sensors, each with their own advantages and disadvantages. A complete overview is therefore not feasible. In the comparison we will confine ourselves to two other IO principles, the Surface Plasmon Resonance (SPR) as is commercialized e.g. by the company Biacore and the Mach Zehnder Interferometer (MZI) as has been developed in the IOMS group at the end of the nineties [4].

It has to be noted that sensing systems realized in academic research in general can function as demonstrators only; they can present a “proof of principle” showing the correctness of the ideas and the way they have been worked out theoretically taking into account the primary effect as well as all factors which can degrade the information content of the obtained signals. Generally a large trajectory of development is needed to

transform this demonstrator into a prototype of a product that can be produced industrially for a (certain class of) applications.

## 6.2.1 Surface Plasmon Resonance (SPR)

There is a huge amount of literature about SPR for sensing purposes and fortunately in 2000 a paper was published [2] which gave a very good overview. The basic principle implies the monitoring of a concentration induced change of the resonance condition for coupling power from a collimated beam or from a guided mode to a surface plasmon (SP) mode. Many methods requiring different system configurations can be used for monitoring this condition. An extremely large part of the field profile of the surface plasmon mode propagates through the dielectric medium on top of the surface plasmon supporting metal layer and hence the sensitivity  $\partial N_{\text{eff}} / \partial n_{\text{diel}}$  is rather high compared to that of the common modes propagating through e.g. a SiON waveguide being about 1.3 and 0.2 respectively. The surface plasmon however is strongly attenuated (it shows a propagation length of some tens of micrometers only) and hence the resonance peak is broad and its shift can be determined with a limited accuracy only. The attainable resolution ( $\delta n$ ) at bulk sensing is about  $10^{-7}$ , while for surface sensing, using a monomolecular anti-body layer, a  $\Delta h_i$  resolution of about  $5 \cdot 10^{-4}$  nm can be obtained. The SPR principle affords for simple 2D sensor arrays: spots of different chemo-optical transducer materials can be applied close to each other on a single thin metal layer, each spot representing an individual sensing region, and all sensing regions can be interrogated simultaneously by applying a wide collimated free space beam for the SP-excitation. The amount of coupling is manifesting itself in the power of the reflected beams. Here the short propagation length shows to be an advantage: with mutual distances of 50 – 10  $\mu\text{m}$  any interdependence of the behavior of the individual sensor is excluded.

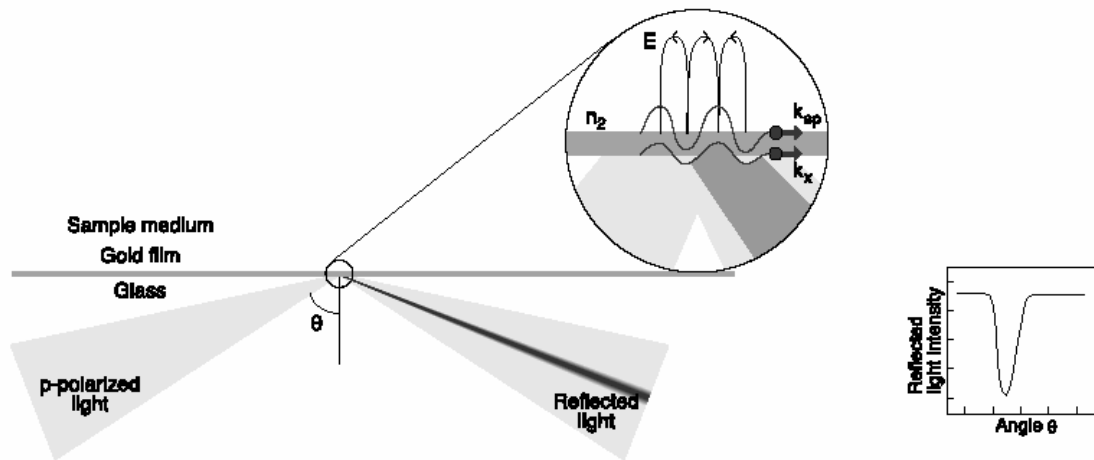


Figure 6.3. SPR principle.

The Biacore's SPR technology [2] consists of a surface plasmon resonance detection system, a microfluidic system and a sensor chip, consisting of a gold surface with sensing

layer. The chip is the only disposable part of the system. Biacore developed a technology to fabricate a thick very porous layer of a hydrogel. At the inside of these pores the receptor molecules (antibodies ) are immobilized. This kind of layer allows for an improvement of the sensitivity to concentration changes in the resolution in terms of minimum concentration. This type of transduction layer can also be applied to most types of IO sensors, thus it will not be taken into account when comparing IO sensors.

## 6.2.2 MZI

The layout of a MZI with very good resolution [4] has been depicted in Figure 6.4.

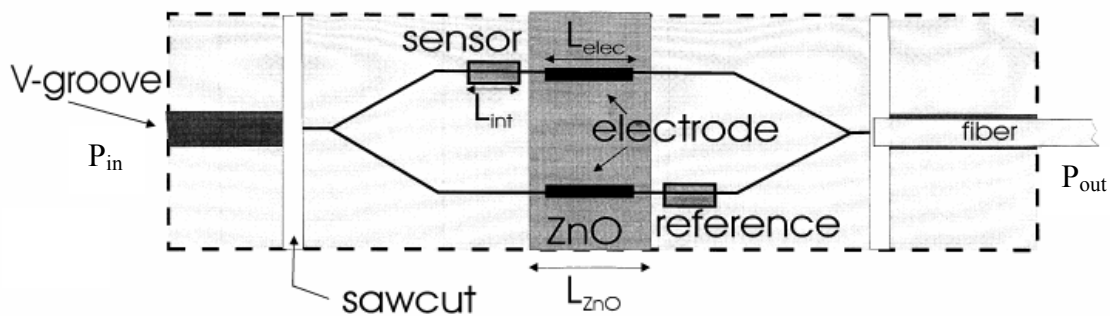


Figure 6.4. The MZI

Light is coupled into the chip (containing a MZI circuitry built from monomodal waveguiding channels) from a fiber positioned within a V-groove and then the modal power is equally divided at the first Y-junction between two channels. The upper branch contains a sensing window, suitable for both bulk and surface sensing, in which the chemo-optical transduction material is applied. The lower branch contains an identical reference sensing window, but this window is supplied with an insensitive layer of identical refractive index and thickness as the sensitive layer inside the upper window. At the second Y-junction the light from both branches is recombined. Depending on the phase difference  $\Delta\phi$  between both modes incoming at the second Y-junction their interference can vary from completely constructive ( $P_{out} = P_{in}$ ) to completely destructive ( $P_{out} = 0$ ). The phase velocity of the mode propagating along the sensing window will depend on the refractive index of the sensitive layer. Effects of the dependencies of the phase velocities on the sample liquid index (in case of surface sensing) are cancelled as a consequence of the intrinsic balance of this symmetrical MZI. Apart from this feature the strength of this system is the insertion of identical electro-optical phase modulators in both branches controlled by triangular ac voltage put in anti-phase on the modulators. This serrrodyne type modulation is tuned in such a way, that due to these modulators the  $\Delta\phi$  gets an additional component continuously varying in between zero and  $2\pi$ . The final effect will be that the information about the  $\Delta\phi$  change as a result of a concentration change is given by the change of the time difference in between the zero-points of the modulation voltage and the zero points of the ac component of the output power of the

MZI. As one of the consequences the information is nearly independent on fluctuation of  $P_{in}$ . Using this sensor with individually optimized IO components, a  $\delta n$  resolution  $2 \cdot 10^{-8}$  has been attained. Production of those MZI sensors requires a complicated technology consisting of a manifold of technological steps.

### 6.2.3 Comparison

The ideal IO sensor should have an incredible high resolution, an unlimited range and an infinitely short response time; it should be able to be combined with all kinds of sensing layers, for any sensing domain; it does not require any calibration, is stable under all conditions, has an infinite life time and ..... costs nothing. But alas, the world is imperfect and in practice for each sensor, performance and price have to be matched to the requirements and willingness to pay a certain price and hence the performance/price ratio will be very relevant.

Performance and cost will be treated in separate sections. Each type of sensor will be evaluated on the same set of aspects. Only if a sensor type should show a specific strong or weak point, that point will be mentioned.

#### 6.2.3.1 Performance

In this PhD thesis the potential of the sensor has been mainly expressed in terms of the attainable *resolution* and the *complexity of the technology* needed for realizing the sensors. Although in practice for concentration measurements the resolution is defined in terms of concentration (e.g. the resolutions as the minimal concentration change of a given analyte which can be detected), we always present resolution in terms of minimal refractive index change (bulk sensing) or minimal change in effective height (surface sensing) of a transduction layer, which can be measured. So we have left the transduction layer with all kinds of properties which have to be optimized to the chemists and we have limited ourselves to presenting properties of an IO sensing platform.

The attainable *resolution* strongly depends on the properties of the IO sensing platform: the sensitivity e.g. for bulk sensing defined as the relative change of the output signal per change in refractive index of the chemically sensitive material to be probed, and the way the platform can cope with disturbing effects, both factors depending on the design of the IO circuitry and the quality of the technology. But there are other factors which co-determine the resolution: the quality of the peripheral equipment (e.g. stability of the light source, noise of the electronic processing system) and the conditions of the measurement (e.g. temperature fluctuations, aggressiveness of samples). In general we have chosen for peripheral equipment of moderate quality and measurements that are performed under laboratory conditions. For most of the sensors which we have treated in this PhD thesis the data given for the resolution are mainly based on theoretical calculations in which some experimental data have been incorporated.

It has to be noted here that there is a certain trade off between the attainable *resolution* (performance) and the *complexity of the technology* (cost). Usually the *resolution* can be

improved by complicating the technology. For example the resolution of most sensor principles is greatly enhanced by adding a reference branch.

This especially holds for sensing systems suited for both bulk and surface sensing, such as the MZI, the GAC and the SPR: if applied for surface sensing the system will be automatically be sensitive for changes in the refractive index of the solvent. This dependency can be compensated for by insertion of a reference sensor covered with a desensitized sensing layer, at the cost of complicating the fabrication process. Notice that referencing can also compensate for other disturbing factors. For nearly all sensors referencing implies that in addition to the output from the sensing branch also an output of the reference branch has to be realized, making the IO platform more complicated. The MZI is the exception: here there is an internal referencing based on the interference of sensing and reference beams.

*Range* is defined as the difference between maximum and minimum value of  $n_{sens}$  which can be measured. It is not such an important characteristic since in general when high resolution is asked for, the effects are small. For some sensors (like the GAC and SWS) the range is centered on a specific  $n_{sens}$  value arising from the needs of a specific application. A new design has to be made for each new application. Other sensors (like the MZI) can operate in a very large range and the center of the range does not have to be considered with the design. Thus the MZI is more *versatile*.

*Reliability* strongly depends on the measuring problem (specifications) and the measurement conditions and this aspect has not been considered. *Response time* is completely determined by the properties of the sample and the transduction layer hence we have not considered here this in practice relevant aspect. *Stability* is strongly dependent on the conditions of the measurement and these have not been discussed here.

### 6.2.3.2 Cost

After having developed a prototype of the sensor suitable for production (costs of R&D) the remaining costs can be divided into several categories:

1. Cost of production of the IO chips, costs of peripheral equipment, cost of assembling and packaging. All these types of cost are relevant for the price of purchase of the complete sensing system. All these costs are not only dependent on the substantial nature of the sensing system, but also on the amount of sensors to be produced. For the latter the versatility for functioning as a sensor platform for many types of sensors is a very relevant aspect.
2. Costs of use: is skilled personal necessary, costs of calibration, life time of the sensor chip (reuse of the sensor) etc..
3. Marketing costs

Both latter types of costs depend very much on specific states of application and commercialization and cannot be taken into account here. The first type of costs will be considered only, not taking into account their dependence on the turn over.

Aspects influencing the complexity of the technology are the number of technological steps, the costs of an individual technological step (price of equipment, room and installation) and the price of use itself. For example we shall associate wet etching with a '+' versus dry etching with a '-'. Other aspects are the required fabrication tolerances, the need to insert special materials. All sensors (except the SPR sensors) which we will compare in this section have been designed to be realized using the SiON technology as available in the clean room lab of the MESA+ institute, a technology that is also used by the IO foundry Lionix BV.

All described IO sensing circuits not only contain a sensing section but also other optical components such as fiber-to-chip coupling functions, bends and Y-splitters. The MZI also contains modulators built from an electro-optical material and hence the technology for these IO circuits is much more complicated. The fabrication process of the GAC is very complicated, while the fabrication of the sensor chips for the SPR, the iSWS and iDC on the other hand is very simple.

Aspects influencing the cost of peripheral equipment are the requirements of the light source (e.g. narrow (-) versus wideband (+), coherency of the light, stability of emitted power, polarization and wavelength etc.), the necessity of using free space beam components (-), the need of controlling one of the IO functions (e.g. the modulators in the MZI, (-)) and the complexity of the detection and the processing of the detected signals.

For most sensor types the peripheral equipment has to process two output powers (reference and signal). For the MZI the electronics is more complicated: also electronic functions for controlling the modulators are required while the processing of the time dependent output power is also more demanding. For nearly all sensor principles power fluctuations of the light source are manifesting themselves directly in the obtainable resolution. However in the MZI their influence is strongly reduced but here the demand on the stability of the wavelength much more severe. The GAC sensor requires a tunable laser and electronics to process the wavelength modulated signal. The peripheral equipment for the SPR is very expensive.

Cost of assembling and *packaging* depend partly on the lay out of the optical chip but also on the requirements of the specific application. It has not been considered here. It is also not possible in this stage to say how far the *chip area* can be reduced, since this is something that has to be considered during the development of the sensor.

The MZI is the most *versatile* of all sensors: any kind of sensor layer, be it for bulk or surface sensing, can be applied on a single platform structure. The iSWS, iDC (and possibly the SPR) work for most immuno-sensing layers. The SWS, (i)GAC, COS and iMAS chips need to be customized for the specific application. Note that the SWS of the type described in chapter 2 only operates well under certain conditions: the transduction layer is not allowed to expand or shrink as a result of changes of the value of the measurand and in addition when applying SiON technology the refractive index of this layer has to be larger than 1.47. Also the COS only operates well if the refractive index of

the transduction layer exceeds this value (1.47). Extension to sensing arrays is estimated to be feasible for all sensor types.

Two other properties that are important are the *ease of use* and the *speed of a single measurement*. The ease of use is determined by the level of training that is required for the operator. Generally calibration of individual sensors will be required, decreasing the *ease of use*. The speed of a single measurement is especially an important factor e.g. for the detection of bio-terrorist threats. Both these properties are very application dependent and as such we cannot say much about them here.

#### **6.2.4 General comparison**

Data about the nature of the sensors and their relevant properties are given in Table 6.1. Here ‘++’ means very strong point, and ‘--’ means very weak point. A ‘0’ is used when the sensor doesn’t perform particularly good or bad and NR means ‘not relevant’. Since not all sensor principles have been worked out in similar detail, it has to be noted that an evaluation based on comparison of these data is incomplete. Also there is a certain subjective component to the evaluation and comparison. Hence this evaluation should be interpreted more as a gauging of the potential of an IO sensing principle than as offering absolute and final statements.

**Table 6.1 Comparison different IO sensing principles.**

Aspect	SWS	iSWS	GAC	iMAS	iDC	COS	MZI	SPR
General								
-Bulk sensing/Surface sensing /both	bulk	surface	both	surface	surface	bulk	both	surface
-Principle ( $\Delta N_{eff} / \Delta E$ )	$\Delta E$	$\Delta E$	$\Delta N_{eff}$	$\Delta E$	$\Delta E$	$\Delta N_{eff}$	$\Delta N_{eff}$	$\Delta N_{eff}$
Performance								
-(Theoretical) resolution bulk $\delta n$	+	NR	++	NR	NR	0	+	+
-(Theoretical) resolution surface $\delta h_i$	NR	+	++	++	+	NR	++	0
-Range	-	0	-	0	0	+	++	0
-Reliability				Application				
-Response time				Area				
-stability				Dependent				
Cost								
-Complexity fabrication	+	++	--	0	++	++	--	+
-Tolerance to fabrication errors	0	+	--	0	-	++	+	+/0
-Chip area	0	0	-	+	0	+	-	++
-Peripheral equipment	0	0	-	0	0	0	-	--
-Versatility	--	0	-	-	0	-	++	+
-Ease of use	?	?	-	?	?	+	?	++
-Packaging				Not considered				
-Time of a single measurement				Not considered				

From Table 6.1 we have drawn the following conclusions:

- In the bulk sensing mode none of the proposed novel sensing systems can beat the MZI with respect to the resolution.
- For attaining high resolution for surface sensing the iSWS, iMAS and iDC offer interesting (calculated) values of the resolution  $\delta h_i$  being  $7 \cdot 10^{-4}$ ,  $10^{-5}$  and  $4 \cdot 10^{-4}$  nm respectively. They compare well to the resolution of the MZI, being  $2 \cdot 10^{-5}$  nm. Especially because of their large  $\delta n_{solv}$  values, these sensor types deserve further investigation,.
- The GAC shows the best theoretical resolution. Unfortunately the realized GACs do not show the theoretically predicted performance Also the complicated fabrication process and the expensive peripheral equipment pose a problem.
- The application of the SWS as has been investigated in full detail in section 2.4 shows a resolution of  $3 \cdot 10^{-7}$ . It can be well used for measuring refractive index changes of fluids. Notice however that another very promising modification (Figure 2.35) has been proposed, but it has not been investigated in more detail. The SWS for immuno-sensing as treated in chapter 4 shows a resolution of  $7 \cdot 10^{-4}$  nm and deserves further investigation.

- The SWS and COS look interesting for application as cheap alarming sensors. Notice that the iSWS can also be applied for measuring RH using very thin sensitive layers.
- Notice that improvement of the quality of the SiON technology, such as reduced insertion and propagation losses, will be very beneficial for the ultimate performance of IO sensors.

### **6.3 Evaluation**

In the introduction (chapter 1) the three objectives for this project were presented. In this section we'll evaluate in how far these objectives have been achieved.

The first objective was to fully evaluate the principle of the segmented waveguide. In this project the SWS principle has been analyzed theoretically leading to a good understanding of the phenomena occurring in this type of sensors and how to manipulate them. SWS structures of a special type (two types of segments differing in constitution of the cladding only, being either a passive or a sensitive material) have been designed, aimed at obtaining the best resolution. Many sensors of this type have been realized and have been characterized both with respect to their structural parameters and their performance. Experimentally obtained results match well the theoretical predictions. Two other SWS modifications have been proposed and worked out theoretically both giving a clear prospect of improved performance. In spite of all this research, research on SWS sensors is far from being exhausted. A manifold of other configurations, especially those in which the segments show differences in all three dimensions is open yet for investigations in future. We can conclude that the first objective has been achieved.

The second objective was to optimize the sensor for some given applications, which originate from the needs of the industry: the determination of relative humidity and immuno-sensing. Unfortunately, due to both a lack of suitable optical transduction materials and a lack of time and funding (clean room hours are very expensive) this could not be done.

The final objective was to use the academic freedom to investigate new ideas about other interesting integrated optical sensor principles, which were generated by our research on SWS sensors, preferably using theory and technology that have been developed for the SWS sensor. A phenomenon observed during the characterization of the SWS sensor sparked the idea for the GAC sensor. For design and fabrication, both the theory and technology developed for the SWS were used. A phenomenon observed during the characterization of the GAC sensor sparked the idea for a cut off sensor, which subsequently has been worked out theoretically. Beside this, the wide selection of new immuno sensing principles, all just as the SWS being based on the influence of the measurand on the shape of the modal field, have been worked out. Especially the iSWS and the iMAS look promising enough to warrant further investigation. We can conclude that the research on the SWS generated really interesting ideas and principles suitable for application.

Thus, two out of three objectives have been realized and besides by thoroughly evaluating both the SWS and GAC, several interesting sensor principles were discovered which are worth further investigation: The iSWS, the iMAS and the COS.

## **6.4 References**

- [1] R.G.Heideman and P.V.Lambeck, *Remote opto-chemical sensing with extreme sensitivity: design, fabrication and performance of a pig-tailed integrated optical phase-modulated Mach-Zehnder Interferometer system*. Sensors and Actuators B61 (1999), pp 100-127.
- [2] J. Homola, S.S. Yee, G. Gauqlitz, *Surface plasmon resonance sensors review*, Sensors and Actuators B54 (1999), pp 3-15.
- [3] [www.Biacore.com](http://www.Biacore.com)

# Samenvatting

## Algemene introductie

Het hoofddoel van dit promotieonderzoek is het onderzoeken van de mogelijkheden die een sensor gebaseerd op een gesegmenteerde golfgeleiderstructuur (SWS) heeft voor toepassing in het chemische domein. Er veel aandacht besteed aan het SWS principe, zowel voor bulk (hoofdstuk 2) als voor oppervlakte toepassingen (sectie 4.2). Zowel de theoretische analyse als de experimentele resultaten van de SWS leidde naar ideeën over verschillende nieuwe brekingsindex sensor principes. Eén van deze, de codirectionele traliegekoppelde mode sensor (GAC), is diepgaand uitgewerkt, zowel theoretisch als experimenteel (hoofdstuk 3). Andere principes voor immuno-sensors gebaseerd op een veldverandering, zoals behandeld in hoofdstuk 4, zijn alleen in theorie uitgewerkt. In hoofdstuk 5 is een sensor gebaseerd op overkoppeling van een geleide naar een lekkende mode behandeld.

## De segmented waveguide sensor (SWS)

Het SWS principe is gebaseerd op het feit dat op een overgang tussen twee golfgeleiderkanalen slechts een gedeelte van het modale vermogen van de inkomende geleide mode wordt overgekoppeld naar de geleide mode aan de andere kant van de overgang. Dit gedeelte hangt af van het verschil in dwarsdoorsnede van de brekingsindexverdeling aan beide kanten van de overgang. Dit verschil kan worden beïnvloed door de te meten grootte o.a. via een optisch transductie materiaal dat in de brekingsindexverdeling van een segment is ingebracht. Door meerdere overgangen achter elkaar te zetten (segmentatie van de golfgeleider) kan het effect worden versterkt.

Uitgaande van dit principe is de SW sensor theoretisch onderzocht. Het werd snel duidelijk dat een gedeelte van het op de overgang verloren gegaande vermogen weer kan terugkoppelen in de geleide mode op volgende overgangen. Om het gedrag van de SWS goed te kunnen beschrijven zijn dus simulatie methodes noodzakelijk, die het stralingsveld goed aankunnen.

Hiervoor zijn drie methodes, de Finite Difference Beam Propagation method (FDBPM), de Bidirectional Eigenmode Propagation method (BEP) en de Spectral Decomposition Method (SDM) zijn onderzocht. Het bleek dat voor nauwkeurige berekeningen de BEP de voorkeur kreeg, terwijl de SDM het meeste inzicht opleverde. Bij de SDM is de reactie van de sensor beschreven als het product van twee factoren waarbij de één afhangt van de kanaalgeometrie en de ander van de segmentatie. Het model laat zien hoe beide factoren op elkaar afgestemd moeten worden om grote effecten te verkrijgen.

Een theorie is ontwikkeld om de haalbare resolutie te beschrijven. Het bleek dat de resolutie kon worden uitgedrukt als het product van twee factoren waarvan er één alleen de karakteristieken van de randapparatuur bevatte, terwijl de ander alleen de

eigenschappen van de geïntegreerde sensor bevatte. Er bestaat een grote verscheidenheid aan gesegmenteerde structuren. We hebben besloten om ons te richten op een simpel type segmentatie waarbij beide segmenten slechts verschillen in de samenstelling van de toplaag. Deze toplaag bestaat uit ofwel een gevoelig transductiemateriaal ofwel een passief materiaal. Een SWS van dit type is ontworpen.

Een ruime verscheidenheid aan SW sensoren, die verschillen in segmentatie, totale lengte en geometrie, is gerealiseerd met behulp van onze SiON technologie. Hoewel het fabricage proces in principe simpel is, bleek ontwikkeling van een aantal niet standaard processtappen ingewikkelder dan aanvankelijk was aangenomen. Alle structuurparameters van de gerealiseerde sensor (brekingsindices en geometrische parameters) zijn gekarakteriseerd en zij bleken zeer dicht bij de ontworpen waardes te liggen.

De prestaties van vele van deze sensoren zijn bepaald door het optische transductie materiaal te vervangen door een vloeistof waarvan de brekingsindex zeer precies kon worden gevarieerd. De experimentele resultaten stemmen redelijk overeen met de theorie. Het verschil wordt toegeschreven aan het feit dat alle berekeningen zijn gedaan aan 2D systemen, terwijl in werkelijkheid deze systemen 3D zijn. Bij gebruik van standaard beschikbaar randapparatuur was een behaalbare resolutie van  $\delta n \approx 3 \cdot 10^{-7}$  geschat.

Ook enige praktische chemo-optische transductie materialen zijn toegepast op de sensoren: gelatine en polysiloxaan, beide gevoelig voor relatieve luchtvochtigheid (RH). De materialen reageren op een verandering van RH zowel met een verandering van brekingsindex als met een verandering van volume. In hun  $P_{out}/P_{in}$  versus  $n_{sens}$  karakteristieken lieten zij een grote hysteresis en niet-reproduceerbaar gedrag zien. Dit hebben wij toegeschreven aan de adhesie van de transductiematerialen aan de SiON toplaag en aan de overgangen. We moesten concluderen dat SW sensoren niet toegepast kunnen worden bij materialen waar brekingsindexveranderingen gepaard gaan met een grote uitzetting.

Een tweede gesegmenteerde structuur, bestaande uit segmenten die verschillen in de laterale compositie van de passieve toplaag, ziet er veelbelovend uit. Berekeningen laten een theoretisch behaalbare resolutie zien die een factor 4 hoger is dan de resolutie van de gerealiseerde structuren.

Tijdens de karakterisatie van de SWS werd verscheidene keren een onverwachte afname in het uitgangsvermogen waargenomen. Nadere beschouwing hiervan leidde tot het idee van de traliegekoppelde mode sensor.

## **De grating assisted mode coupling sensor (GAC)**

Het potentieel van het GAC principe voor sensortoepassingen is geanalyseerd op een zelfde manier als het SWS principe. Een model is ontwikkeld om het gedrag te beschrijven en een ontwerp is gemaakt om bewijs van het principe te verkrijgen. Er zijn twee lichtingen GAC sensoren gefabriceerd. De eerste werkte niet vanwege technologische problemen. Deze problemen zijn opgelost bij de tweede lichting.

Structuur parameters zijn gemeten ofwel als tussenstap tijdens de productie, ofwel aan de uiteindelijk gerealiseerde structuur. De gerealiseerde parameters lagen dicht bij de ontwerpparameters. Het gedrag van de sensor was echter niet als verwacht en we hebben hier nog steeds geen aannemelijke verklaring voor. Merk op dat in sectie 2.8 de experimenten en de theorie aan een soortgelijke GAC sensor wel goed overeenkwamen.

+

Tijdens de karakterisatie werd, bij een heel specifieke waarde van de brekingsindex, een onverwacht sterke afname in het uitgangsvermogen waargenomen. Deze observatie leidde tot het onderzoeken van de cut off sensor (COS).

## **Een aantal nieuwe sensor principes**

Er zijn vier nieuwe immuno-sensor principes onderzocht. Drie van deze principes zijn gebaseerd op een concentratieafhankelijk modaal veld: een speciaal type gesegmenteerde golfgeleider (iSWS), een modale dempingsensor (MAS) en een directionele koppelaar. Als laatste is onderzocht hoe de GAC toegepast kan worden voor immuno-sensing.

De MAS combineert een goede waarde voor de resolution ( $\approx 10^{-5}$  nm) met een simpel fabricageproces. De iSWS is veruit het simpelste te fabriceren, terwijl nog steeds een redelijke resolutie ( $\approx 7 \cdot 10^{-4}$  nm) mogelijk is. De iDC lijkt minder aantrekkelijk dan de voorgaande mogelijkheden, aangezien de fabricage moeilijker is dan de iSWS en de resolutie ( $\approx 4 \cdot 10^{-4}$  nm) slechts marginaal beter. De GAC kan een zelfde resolutie als de MAS bereiken, maar is erg gevoelig voor technologische onvolkomenheden, heeft een ingewikkeld fabricageproces nodig en is erg gevoelig voor veranderingen in de brekingsindex van het oplosmiddel.

## **De Cut Off Sensor (COS)**

De verklaring van de onverwacht sterke afname van het uitgangsvermogen, zoals waargenomen bij de karakterisatie van de GAC, leidde tot het idee voor de COS. Wanneer  $n_{\text{sens}}$  hoger dan een bepaalde waarde was, bleek het dat de golfgeleider geen geleide mode meer kon bevatten. Er is ontdekt dat de response van de sensor significant verbeterd kon worden door de dikte van een dunne top laag, net boven de kernlaag, te optimaliseren. Deze sensor heeft een resolutie van  $3 \cdot 10^{-6}$ . Een zeer interessante toepassing is als alarmsensor. De fabricage is uiterst simpel.

## **Conclusie**

Het doel van het promotieonderzoek is gehaald. Naast het grondig analyseren van zowel de SWS en de GAC zijn verscheidene nieuwe sensorprincipes ontdekt. Met name de iSWS en iMAS zijn zeer interessante opties die nader onderzoek verdienen.

## Appendix A: Analysis of the rest field

In a segmented waveguide at the transition between two segments a guided mode inside the first segment ( $E_1$ ) is decomposed into a guided mode inside the second segment ( $E_2$ ) and radiation modes ( $E_r$ ), which from now on we will refer to as the rest field. If  $E_r$  is known, using Fourier transformation it is also possible to determine in approximation the angular distribution of the light in the rest field.

There are three reasons why we are interested in the field and angular distribution of the rest field. Firstly it is necessary to know the angular distribution of the rest field to see if it is possible to reduce a 3D SWS structure to a 2D structure for calculation purposes. Secondly, although the calculation methods mentioned in chapter 2 give a lot of insight in what happens inside an SWS structure, none of these methods give insight into the relation between the rest field generated at the transition and the behavior of the SWS. Using the angular distribution of the rest field it is possible to give more qualitative explanations about the behavior of the SWS. Thirdly, using this extra insight, it is possible to design SW sensors by tailoring the rest field, an approach which yields very interesting results as is shown in section 2.7.

In this appendix firstly the calculation procedure will be explained. Secondly the approximations and their influence on the interpretation of the calculated results will be discussed.

The relation between the field distributions  $E_1$ ,  $E_2$  and  $E_r$  is given by:

$$E_r = E_1 - S_{12} \cdot E_2 \quad (A1)$$

where  $E_1$  and  $E_2$  are the mode profiles of the guide mode in respectively segment 1 and 2. The expression for the overlap integral  $S_{12}$  depends on the polarization state of the mode. In our sensors we are considering TE modes and for these modes  $S_{12}$  can be expressed as

$$S_{12} = \frac{\int_{-\infty}^{\infty} \int_{-\infty}^{\infty} E_1 \cdot E_2 dx dy}{\sqrt{\int_{-\infty}^{\infty} \int_{-\infty}^{\infty} E_1 \cdot E_1 dx dy \cdot \int_{-\infty}^{\infty} \int_{-\infty}^{\infty} E_2 \cdot E_2 dx dy}} \quad (A2)$$

Here the z-axis corresponds with the propagation direction of the guided mode, the x- and y-axis are oriented parallel and perpendicular to the substrate surface respectively. The distribution of the rest field over the  $k_x$  and  $k_y$  vectors can be obtained by Fourier transformation of the rest field.

For determining the angle distribution of the emitted radiation we have introduced an approximation. It will be assumed that this rest field will propagate through a uniform

medium with a refractive index equal to the average of the refractive indices of the buffer layer and cladding layer materials. This is a reasonable approximation since for the structures considered the values of the cladding and buffer index are close to each other, while most of the radiation is generated outside the core of the waveguide, which is small (typically 60 nm high) in comparison with the dimensions of the rest field (typically 5  $\mu\text{m}$  high). This approximation however does have some side effects. Part of the rest field will propagate as slab modes (for which  $k_y = 0$ ). In our approximate model this confinement cannot be obtained: according our model the Fourier transform of such a slab mode should result into radiation out of the  $xz$  plane. By calculating the complex overlap of the Fourier transform of the rest field at  $k_x = 0$  and the Fourier transform of a calculated field profile of a slab mode, it can be determined which fraction of the radiation is transferred to the slab mode. In the cases considered in this thesis the overlap is either almost 0, which implies very little radiation in  $xz$  plane, as with the SWS designed in section 2.4, or almost 1, in which case almost all the radiation is confined within the slab, as is the case for the SWS designed in section 2.7 and the iSWS in section 4.2.

Using this approximation, the  $k_x$  and  $k_y$  vectors can be calculated. In the range  $0 < k_x, k_y < k_0 n_{clad}$  the direction of each plane wave ( $k_x, k_y$ ) can also be expressed in terms of the angles  $\Theta_x$  and  $\Theta_y$  with the  $z$ -axis, being the propagation direction of the guided mode. Here  $\Theta_x$  is the angle in the  $xz$  plane and  $\Theta_y$  the angle in the  $yz$  plane.  $k_x$  and/or  $k_y > k_0 n_{clad}$  correspond to evanescent modes, which only attenuate but don't propagate in the  $z$  direction.

As an example a rest profile is shown in Figure A1 as has been calculated for the SWS sensor which was designed in section 2.4, Table 2.2. (7  $\mu\text{m}$  channel width, 60 nm channel height and ridge height 20 nm) for a cladding index difference 0.001. The centre position in the waveguide channel corresponds with  $x=y=0 \mu\text{m}$ .

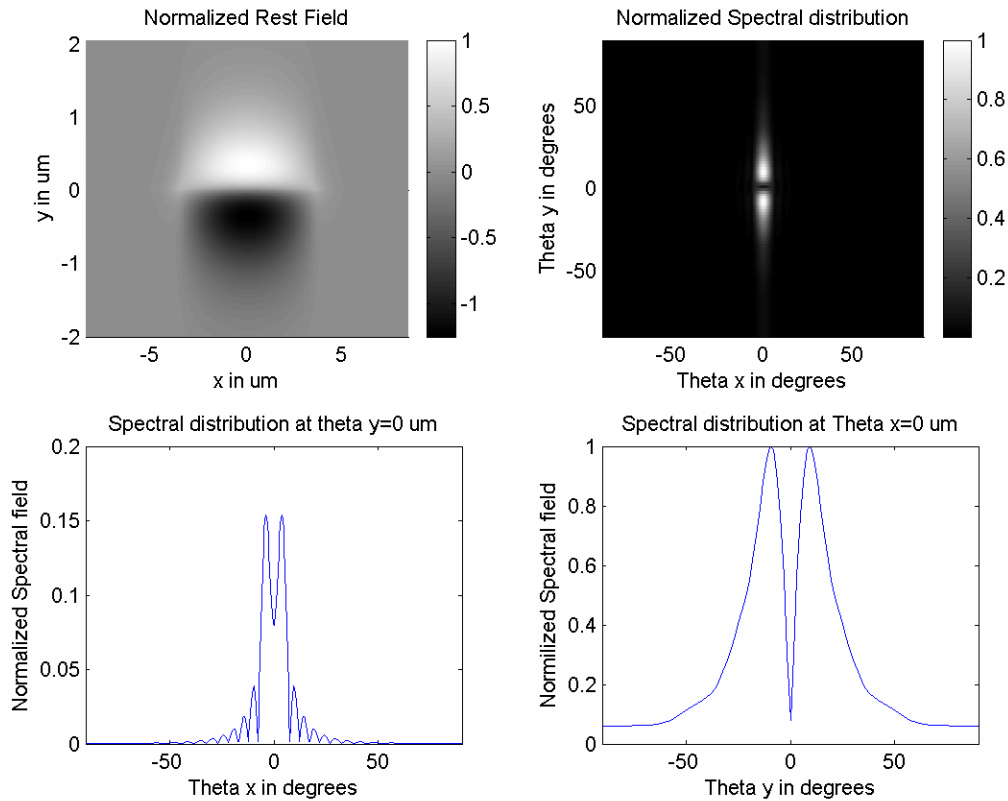


**Figure A1: Field and angular distribution of the ‘rest’ field.**

Both the rest field and its Fourier transform are normalized on their maximum values.

From Figure B1 we can conclude that the radiation modes are primarily directed to the  $y$ -direction, which supports our decision to approximate the 3D SWS structure by an equivalent 2D slab structure (section 2.2.2). From Figure B1 we can also conclude that the angular distribution is centered around  $\theta_y = \theta_x = 0^\circ$ , so part of the light will couple back into the guided mode of the next transition, even if large segment lengths are used. It has been observed that by decreasing the core height the lateral dimensions of the rest field increases, which decreases the average angle in the angular distribution. In order to obtain destructive interference between the radiation modes and the guided modes, now a larger segment length is necessary. Thus, just by just looking at the rest field we can qualitatively explain Figure 2.13.

## Appendix B: V-groove design

In Figure B1 an optical fiber inside a V-groove has been depicted. From overlap calculation of the field profile inside the fiber and waveguide structure an optimum value for  $h$  can be determined, which minimizes the FC coupling losses. The angle ( $\alpha$ ) of the V-groove inside a silicon wafer is always constant, provided that the V-groove is properly aligned with the crystal axis. Thus, using expression (B-1), the required V-groove width  $2W$  for a given  $h$  can be calculated. Depending on the layer in which the V-grooves will be defined, under-etch has to be taken into account. Usually the V-grooves are defined in the core layer, thus the value of  $2W$  needs to be corrected for under-etch in the optical buffer. For illustration in table B1 the design of the V-groove width for a type 1 SWS (parameters in Table 2.2) is shown.

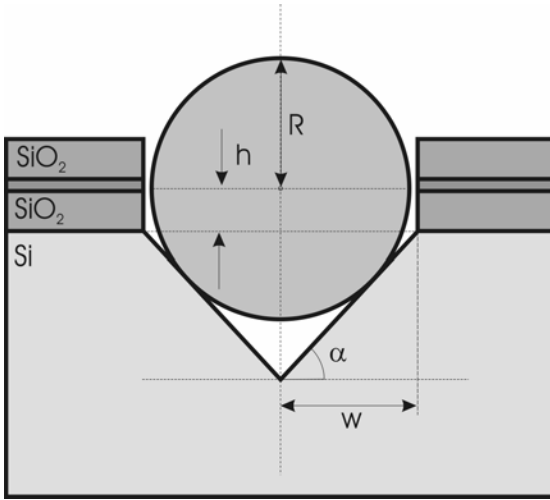


Figure B1. A fiber inside a V-groove.

$$2W = 2R \left[ \frac{1}{\sin(\alpha)} - \frac{r_{\langle 111 \rangle}}{r_{\langle 100 \rangle}} \tan(\alpha) \right] - 2h \left[ \frac{1}{\tan(\alpha)} - \frac{r_{\langle 111 \rangle}}{r_{\langle 100 \rangle}} \sin(\alpha) \right] \quad (\text{B-1})$$

Table B1. Properties V-groove SWS as designed in section 2.4, table 2.2, type 1.

Parameter / Property	Symbol	Value
V-groove angle	$\alpha$	54.74 °
Fiber radius	$R$	62.5 $\mu\text{m}$
Etch-rate ratio	$r_{\langle 111 \rangle}/r_{\langle 100 \rangle}$	1/100
Optimum position fiber	$h$	3.6 $\mu\text{m}$
Underetch buffer layer		6 $\mu\text{m}$
V-groove width	$2W$	146.5 $\mu\text{m}$

## Appendix C: Mixing of liquids with different refractive index

For testing the performance of SW sensors, liquids with varying refractive index can be used and they can be fed to the sensing section using a cuvette or a micro fluidic system applied on top of the sensing section.

For the control of the refractive index of the liquid a suitably binary solvent mixture is needed. Because we intend to use SW sensors designed for gelatin interfaces requiring  $n_{\text{SION}} = 1.52$ , also for testing with liquids, the refractive index of the mixture has to be variable around 1.52 with sufficient range ( $\pm 0.02$ ). The viscosity of the mixture should be low ( $< 0.01$  PaS), both to keep the pressure inside the MF channels low and to facilitate easy mixing. Additionally the mixture should not be explosive or toxic.

After extensive research it was found that benzyl alcohol and ethanol formed a very suitable couple. Both liquids have low viscosities, they mix well and the refractive index range is more than sufficient to characterize both the SW and the GAC sensor. Some relevant properties are given in C1.

**Table C1. Several relevant properties of ethanol and benzyl alcohol (at 25 °C and  $\lambda_0=546.1$  nm).**

Property	Ethanol	Benzyl Alcohol
Viscosity	0.0012 Pas	0.006 Pas
Refractive index	1.3612	1.5424
$\partial n/\partial T$	-0.004 K <sup>-1</sup>	-0.0042 K <sup>-1</sup>
Density ( $\rho$ )	0.7852 g/ml	1.0416 g/ml
$\partial \rho/\partial T$	-0.008 g/Kml	-0.008 g/Kml

There are a few requirements when using a benzyl alcohol - ethanol mixture. The mixture should always be in a closed environment, because the ethanol is more volatile than the benzyl alcohol and hence during evaporation composition and hence also the refractive index of the mixture will gradually change. Mixing liquids usually will be accompanied with volume contraction. This has to be taken into account when calculating refractive index changes induced by changes of the flow rate of one of the components. The refractive index has to be characterized as a function of volume ratios and using existing models, from that characterization, the volume contraction can be estimated.

The empirical Gladston-Dale equation describes the relationship between the densities, volume ratios and refractive indices.

$$\frac{1}{\rho_{12}}(n_{12} - 1) = \frac{1}{V_1\rho_1 + V_2\rho_2}(V_1(n_1 - 1) + V_2(n_2 - 1)) \quad (\text{C-1})$$

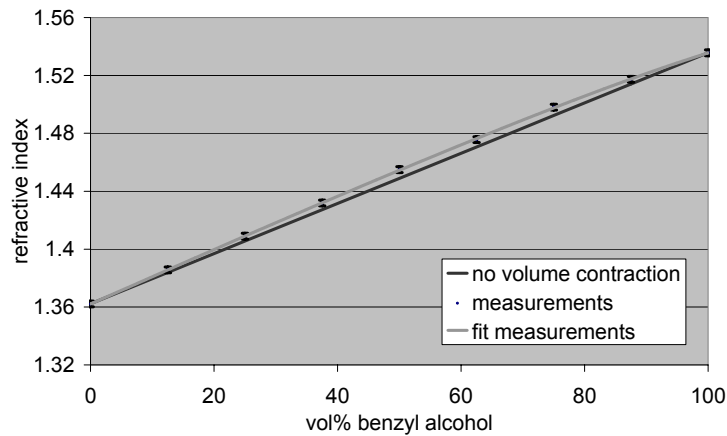
Here  $\rho$  represents a density,  $V$  a volume fraction and  $n$  a refractive index. The indices 1,2 and 12 refer to liquid 1, 2 and the mixture of the liquids 1 and 2. Assuming no volume contraction  $\rho_{12}$  can be written as:

$$\rho_{12} = V_1\rho_1 + V_2\rho_2 \quad (C-2)$$

and expression (C-2) now reduces to:

$$(n_{12} - 1) = V_1(n_1 - 1) + V_2(n_2 - 1) \quad (C-1)$$

Note that when the refractive index of the mixture is measured as a function of the volume ratio, then using expression (C-1) an estimate can be made of the volume contraction as a function of volume ratio. This relation between the refractive index and the volume fraction is depicted in Figure C1 for the benzyl alcohol - ethanol mixture.



**FigureC1. Refractive index characteristic ethanol – benzyl alcohol mixture.**

The black line depicts the refractive index calculated assuming no volume contraction takes place. The grey line depicts the measured refractive indices. As can be seen there is indeed volume contraction present, a little bit, but its effect on the refractive index cannot be neglected. It will appear later that it is necessary to have knowledge of the volume contraction of a mixture. We define the volume contraction factor  $q$ :

$$q(V_1) = \frac{\rho_{12without}(V_1)}{\rho_{12with}(V_1)} \quad (C-4)$$

The index ‘without’ refers to the case when no volume contraction is present and the  $\rho_{12without}$  is calculated using expression (C-3). The index ‘with’ refers to the case with volume contraction and  $\rho_{12with}(V_1)$  can be calculated from expression (C-1) and the data

given in Figure C1. In Figure C2 the volume contraction factor has been calculated. From direct volume measurements it could be derived that at  $V_I = 50 \%$ ,  $1 < q < 1.025$ , which confirms the data in Figure C2.

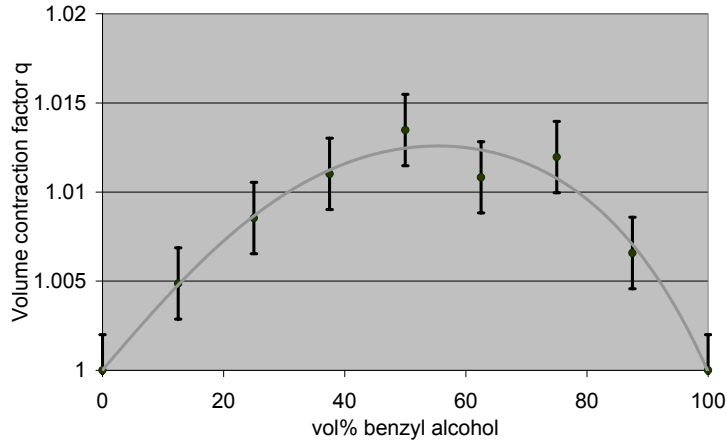


**Figure C2. Volume contraction factor as a function of volume fraction benzyl alcohol.**

For the mixing of the liquids and the supply of the mixture to the sensing section two different methods have been used.

In a crude method, a mixture was prepared and its refractive index was measured with an Abbe refractometer (accuracy  $\pm 5 \cdot 10^{-4}$ , white light). The temperature dependence of the index and the unknown dispersion introduce a systematic error in the refractive index, which is estimated to be about  $\pm 5 \cdot 10^{-4}$ . Such a mixture was inserted into the cuvette using a syringe. After that it took about 15 minutes for the output signal to stabilize, most probably due to the dead volumes in the cuvette, which contain liquid with a different refractive index from a previous measurement. After that a measurement was performed. Note that with a micro fluidic system there is an extremely small dead volume and no stabilization time will be required. This method of measuring is very time consuming and the sensor can only be characterized at a limited number of different refractive indices.

A more advanced method of varying the refractive index continuously in a well controlled way has been developed. This new method is schematically presented in Figure C3.

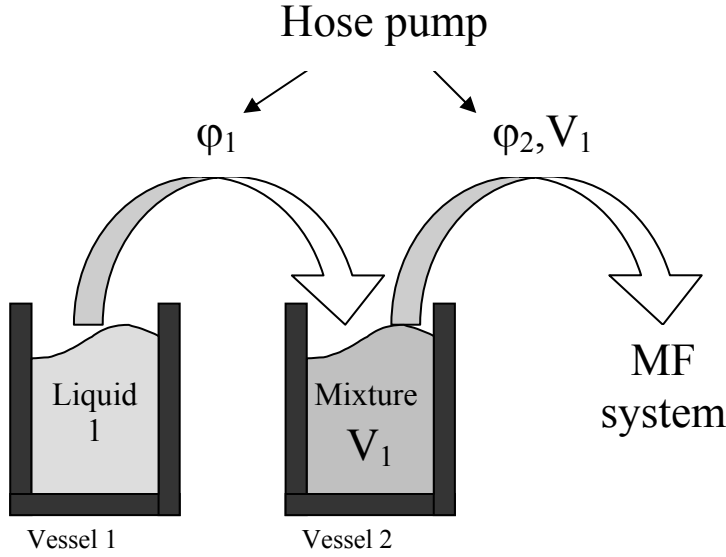


**Figure C3. Liquid mixing system.**

A single hose pump with two hoses attached ( $\phi_1 \approx \phi_2$ ) is used to pump liquid from vessel 1 into vessel 2 and then into the MF system. At the start vessel 1 is filled with liquid 1 and vessel 2 is filled with liquid 2. The volume ratio  $V_1$  in vessel 2 will change with time from 0 at  $t=0$  to 1 at  $t \rightarrow \infty$ . This way it is possible to create in vessel 2 a mixture with a continuously monotonously changing refractive index. The SWS is expected to have a very narrow peak in output power at a very specific refractive index. By scanning slowly over a continuous refractive index range it is not possible to miss this peak, while using discrete refractive index intervals it is almost impossible to find that peak. The rate at which the refractive index is changing (related to the accuracy with which the refractive index is known) can be controlled by the flow rates  $\phi$  and the initial volume of liquid 2 in vessel 2 ( $v_{20}$ ). When  $\phi_2$  and  $\phi_1$  are determined after the measurement, the refractive index as a function of time can be calculated. The following model can be used for that.

$v_1$  and  $v_2$  are the volumes of liquid 1 and liquid 2 in vessel 2. The volume fraction of liquid one is defined as  $V_1 = v_1 / (v_1 + v_2)$  and that of liquid 2 as  $V_2 = v_2 / (v_1 + v_2) = 1 - V_1$ . The time dependence of volumes  $v_1$  and  $v_2$  can be described by the following set of differential equations:

$$\frac{\partial v_1}{\partial t} = -\phi_2 \frac{v_1}{v_1 + v_2} + \phi_1 \tag{C-5}$$

$$\frac{\partial v_2}{\partial t} = -\phi_2 \frac{v_2}{v_1 + v_2} \tag{C-6}$$

And the initial conditions:

$$v_1(0) = v_{10} \quad \text{and} \quad v_2(0) = v_{20}$$

Adding expression (C-5) to (C-6) and solving the resulting equation gives the relation  $v_1 + v_2 = (v_{10} + v_{20}) + (\phi_1 - \phi_2)t$ . Inserting the  $(v_1 + v_2)$  value thus obtained into expression (C-5) and solving that equation yields the general solution:

$$V_2(t) = \frac{v_{20}}{v_{10} + v_{20}} \left( \frac{v_{10} + v_{20}}{(v_{10} + v_{20}) + (\phi_1 - \phi_2)t} \right)^{\left( \frac{\phi_2}{\phi_1 - \phi_2} + 1 \right)} \quad (\text{C-7})$$

Using the values found for  $\phi_1$  and  $\phi_2$  now expression (C-7) gives us  $V_2(t)$  and thus also using the data of Figure C1 the refractive index can be determined as a function of time. It has been verified whether this idea for mixing liquids really works. The calculated time dependence of a mixture and the experimentally measured values of the refractive index are depicted in Figure C4.

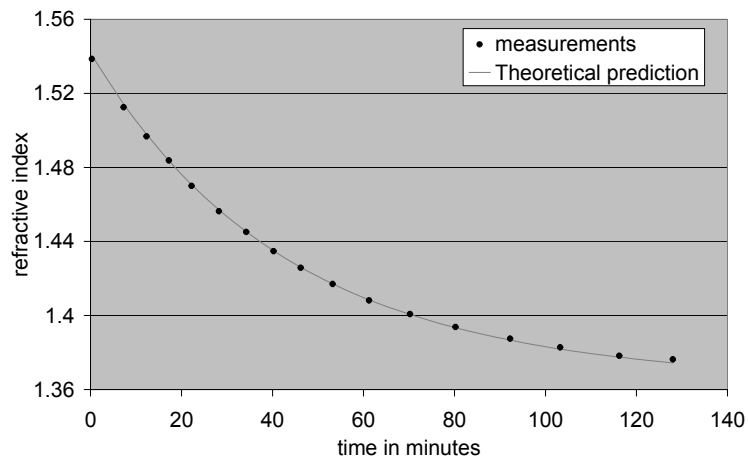


**Figure C4. Refractive index control using mixing system of Figure C3.**

Here the experimental values of the refractive indices have been determined using an Abbe Refractometer with 632.8 nm light, which yields the refractive index at 632.8 nm with a small unknown offset only. As can be seen the measurements fit the model within the measurement accuracy of the Abbe refractometer (depicted by the size of the dots) over the whole time range. This also means that all the other unquantifiable inaccuracies together have little influence on the accuracy of this method. Of course for extra security during the actual measurements at certain moments the refractive index of the mixture has to be measured using the Abbe refractometer.

## Appendix D: The microfluidic system

For transporting the available liquid to the sensing section, a micro fluidics (MF) system will be used. The system is not allowed to contain dead volumes and in the channel above the sensing section a laminar flow has to be obtained in order to suppress fluctuations due to turbulence. The MF channels will be defined in a thin glass plate, followed by gluing of this MF chip on top of the IO-chip. This MF chip has been deigned in cooperation with Lionix BV, where our task was to design the cross sectional dimensions of the channel itself. The system should be realized and mounted (glued) to the IO chip by Lionix BV.

For the connection of the flow in-and outlets Lionix BV proposed a Teflon plate to be attached (clamped) on top of the glass. It contains holes above the flow in-and outlets where Teflon hoses can be screwed inside for contact with the outside world. The inlets will be sealed with Teflon rings. This plate can be used to characterize multiple sensors. As for the design of the MF channel dimensions: the channels should be wide enough to facilitate easy alignment of the MF-chip on the IO-chip, while the pressure inside the MF channels should be smaller than 0.1 Bar. The width of the channel is chosen to be 0.5 mm and this leave the maximum pressure inside the MF channel as the criterion to determine the minimum height of the channel.

The Pressure difference over a rectangular channel for laminar flow is given by:

$$\Delta p := \left( \frac{4 \cdot \mu \cdot L \cdot \phi}{a \cdot b^3} \right) \cdot \left[ \frac{16}{3} - 3.36 \frac{b}{a} \cdot \left( 1 - \frac{b^4}{12 \cdot a^4} \right) \right]^{-1} \quad (\text{D-1})$$

with  $\mu$  the viscosity in Pas,  $L$  the length of the channel in m,  $\phi$  the flow in  $\text{m}^3/\text{s}$ ,  $a$  the width and  $b$  the height of the channel, also in m. A total channel length of 10 cm is taken and a maximum flow of  $5 \mu\text{l}/\text{s} = 5 \cdot 10^{-9} \text{m}^3/\text{s}$  is assumed. Using an MF channel height of  $100 \mu\text{m}$  and a width of  $500 \mu\text{m}$ , the pressure difference needed is about 1190 Pa for a liquid consisting of benzyl alcohol, which is acceptable.

## Appendix E: Characterization optical transduction materials

Two different optical transduction materials were available that could be applied on the SWS: gelatin and AEO/PTMS polysiloxane (recipe was provided by Dr. A. Brandenburg of Fraunhofer Gesellschaft).

Gelatin is extremely sensitive to relative humidity (RH), being most sensitive around 100 % RH. Since the sensing domain around 100% RH is relevant for various applications, while accurate measurements using common RH sensors are very difficult, gelatin could be an interesting material to use. Gelatin (Type B from bovine skin; 225 bloom) had been characterized in the past by various people, but because the results were conflicting, new measurements had to be performed. Gelatin was spun on a silicon wafer and characterized using an ellipsometer inside the same simple climate chamber in which the SWS has also been characterized. In Figure E1 the refractive index of Gelatin is depicted as function of RH. In Figure E2 the layer thickness is shown as a function of RH. Note that the change in refractive index is accompanied by a quite large expansion of the material. The measurements were performed twice and showed to be perfectly reproducible. No hysteresis was present.

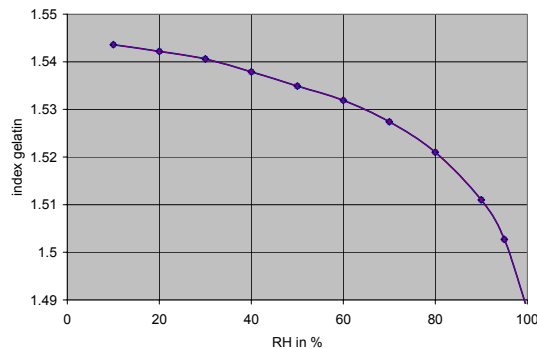


Figure E1. Characterization index gelatin.

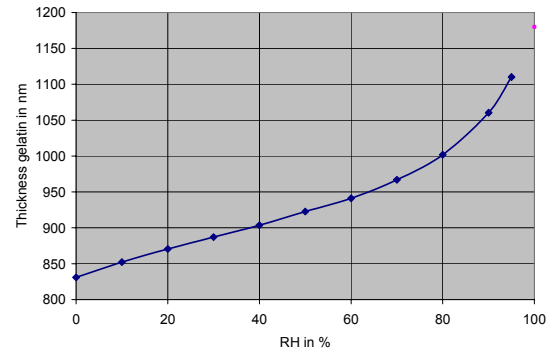
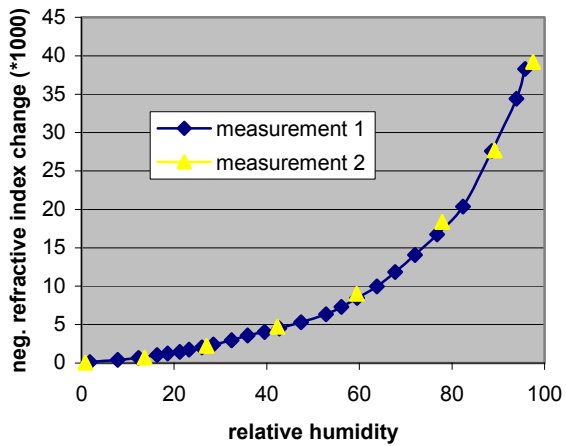


Figure E2. Characterization thickness gelatin.

The refractive index of AEO/PTMS polysiloxane is supposed to be sensitive to CO<sub>2</sub>. Since CO<sub>2</sub> detection has many safety related applications it is very interesting to apply this material in a SWS. The polysiloxane also has a cross sensitivity to relative humidity. Both dependencies were characterized using a Mach Zehnder interferometer on which 2.8 μm polysiloxane was spun. In Figure E3 the refractive index change as function of RH is shown. For some unknown reason the material was completely insensitive to CO<sub>2</sub> concentration. The material will still be used to characterize SWS sensors, only using the RH dependency. The material has been characterized extensively (spin curves, reproducibility tests, aging effects, thermo- optic effect, etching characteristics) [1] and it has been used later in the fabrication of the GAC sensor in chapter 3 of this thesis.



**FigureE3. Characterization RH dependence polysiloxane.**

For the characterization of sensing platforms we need interface layers with large and very reproducible effects. The development and characterization of such interface layers however is not within our expertise. Thus we are not able to solve problems directly related to the nature of the interfaces.

[1] P.Tabbers, MSc. Graduation report, *Design, Realisation and Characterization of a Mode-mismatch sensor with thermo-optical feedback and a AEO/PTMS polysiloxane cladding*, Lightwave Devices Group, University of Twente, June 2001.

## Appendix F: Investigated technological steps

### F1: Implementation of detectors in the Si wafer

The packaging of optical chips is a costly business, mostly determined by the cost of the fiber-chip coupling. If light source and photo detector can be integrated on the chip, possibly the cost of packaging can be reduced considerably. Therefore at the beginning of the project we considered the possibility to integrate optical detectors on the chip. Starting point of the design of the technological process for realizing the IO system was that all the steps should be compatible with the fabrication of the optical detectors.

The photodiodes should be created by implantation of a p-type dopant (Boron) into an n-type (Phosphorus) doped silicon wafer using an ion-implanter. Such an implantation is not possible if the common optical buffer layer (2-3  $\mu\text{m}$  thick thermal oxide) would be already applied, while thermal oxidization of the silicon after the implantation would destroy the photo diodes. Hence the use of thermal oxide as an optical buffer layer is excluded; considering the integration of photodiodes, now and in future devices, the only alternative seems to be to deposit at moderate temperature the optical buffer layer on top of the silicon wafer.

Several options to deposit such layers have been investigated. First experiments have been performed with LPCVD (Low Pressure Chemical Vapor Deposition) TEOS, requiring a low substrate temperature (700°C). However it appeared to be impossible to grow such layers with a thickness required for a buffer layer, without cracking as a result of too high stresses in the layer. In Figure F1 a picture of a wafer with a 1.7  $\mu\text{m}$  TEOS layer is given and in Figure F2 a close up of the cracks is shown.

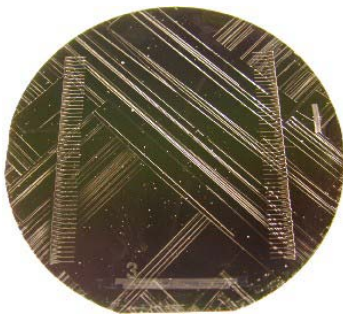


Figure F1. Cracks in TEOS layer.

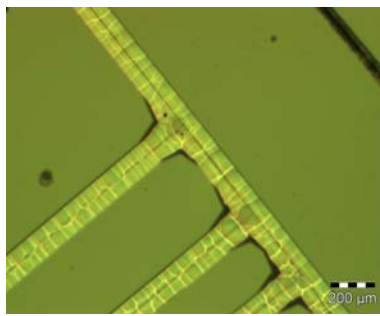


Figure F2. Close up of cracks in TEOS layer.

Another option is to use PECVD  $\text{SiO}_2$ . However it appeared that after having deposited the complete layer stack on the top of the wafer the wafer curled up strongly, severely reducing and sometimes even impeding the definition of the lithography. Apparently the stresses in the layers were very high. Although such a curvature can be eliminated by depositing a similar layer stack on the back side of the wafer and although using this

technology operational waveguide/detector systems have been produced [1], this option has been rejected because it would need many additional process steps and the realized waveguides would show increased scatter losses due to the rough SiO<sub>2</sub> surface.

Abolishing the production of thermal oxide gave rise to a new problem with applying the structures for determining the crystal orientation. First a thin gate oxide layer (~45 nm) was used as a mask layer when etching these structures. This layer turned out to be too thin, since the KOH etching solution also attacked the SiO<sub>2</sub>. Secondly a 100 nm thick sacrificial Si<sub>3</sub>N<sub>4</sub> layer was tried as a mask layer. However after the removal of this layer using BHF etching brown spots were visible on the surface and these spots could only be removed using chemical mechanical polishing. There is still no explanation for the appearance of these brown spots, but they also came up when the process was performed a second time. Thirdly a PECVD oxide has been deposited as a definition layer. This material however appeared to suffer from such a severe under-etch that it cannot be used for this purpose.

In the end we gave up on integration of the photo diodes into the optical chip and settled for a thermal oxide layer. Thermal oxide can be grown easily and reproducibly and is not porous. It can also be well used for the definition of the crystal alignment markers, making the fabrication process a lot easier.

## **F2: The etching process for a SiON-cladding layer**

For the SW sensing sections to show maximum sensitivity, the walls of the SiON pillars left in the cladding after etching should be perpendicular to the wafer surface. Slanting of the side walls reduces the amount of radiation generated at a transition (an angle of 50° approximately causes a reduction in  $A$  value of 10%).

Also the surfaces of the side walls and the bottom obtained after etching should be smooth to prevent scatter losses. Smoothness of the bottom plane implies that a very thin SiON layer has to be left because any etching of the core layer would cause unacceptably high scatter losses. These requirements demand an etching process that yields straight, smooth walls, gives good control of the etching rate and a large uniformity of the etching process as well on-chip as from run to run. This etching process appeared to be the most critical step in the fabrication of the SWS.

Two types of SiON layer etching processes are available: wet etching using a BHF solution and dry etching using RIE. Wet etching is an isotropic etching process and due to under-etch the etched regions are expected to show very rounded side walls (Figure F3, middle hole). Imperfect adhesion of the resist at the SiON enhances this under-etch and often very slanted side walls with angles ( $\alpha$ ) down to 20 degree are obtained (see Figure F3 right hole and Figure F4 for a SEM photo). Such sidewalls are unwanted. Also the large under-etch can be disastrous when etching a cladding layer with a thickness of 2  $\mu\text{m}$ ; all structures with a lateral dimension smaller than 4  $\mu\text{m}$  will be removed or heavily damaged. However etch rate is very well controlled and the homogeneity of the etch rate

over whole the wafer is pretty good. Reactive ion etching (RIE) is an anisotropic etch process giving more vertical side walls (see Figure left hole) but the angle they make with the substrate plane and their roughness depend strongly on the process parameters. These parameters have to be tuned carefully in order to get or approach the desired type of walls. However all experiments with a large variation of parameter sets resulted in (slightly) slanted walls ( $\alpha = 53^\circ$ ). In RIE the etch rate is expected to be not uniform and to be dependent on the local ratio of masked and unmasked areas.

A series of dry etching experiments have been performed. We started with a conventional (RIE) process and since it was known that the conventional photoresist shows a too high etch speed to serve as a mask, a lift-off process has been applied by depositing metal mask layers on top of the resist. However re-deposition of the metals resulted in “grassy” bottom faces causing unacceptably high losses. This re-deposition was stronger when using Cr (the standard mask in the clean room lab) than when using Ni (a process developed by G.Sengo). And indeed the etching rate appeared to be dependent on the dimensions and the (relative) positions of the mask openings.

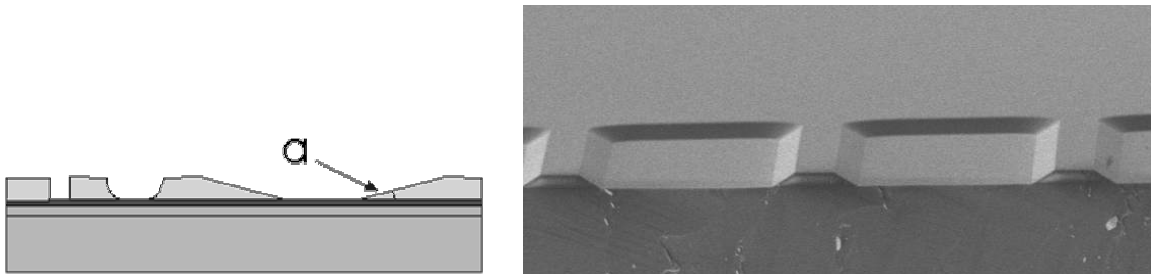


**Figure F3. (left) Several typical shapes of etched holes.**

**Figure F4. (right) BHF etched SiON segments.**

In the mean time at Lionix BV another RIE-process had been developed. This could do with a resist layer to define the structure; no metal layer was necessary. The process produces very smooth walls. On a flat wafer the etch rate uniformity was about 5%. The etch rate however still depends on the size of the holes that are etched. We have solved this problem by, instead of etching holes, etching off nearly the whole layer and leave SiON pillars standing only. For the operation of the SWS this wouldn't make any difference, but because there were no closed holes anymore in the structure the uniformity in etch rate was improved very much.

Still there is a non-uniformity in etch rate of at the very least 5%, or about 50 nm. Therefore we decided to use RIE to remove nearly all SiON, leaving a 70 nm thin SiON layer that will be etched off using BHF wet etching. In contrast to RIE, the BHF etching has a very high selectivity for SiON with respect to  $\text{Si}_3\text{N}_4$ ; hence the non-uniformity of the RIE process is in fact compensated by the BHF process resulting into smooth end faces. As an alternative a thin layer of SiON may be left standing, just to make sure that the core layer will not be etched. In Figure F5 the results of the last etching process are depicted. The angle of the sidewalls with the wafer was determined to be  $53 \pm 5^\circ$ .

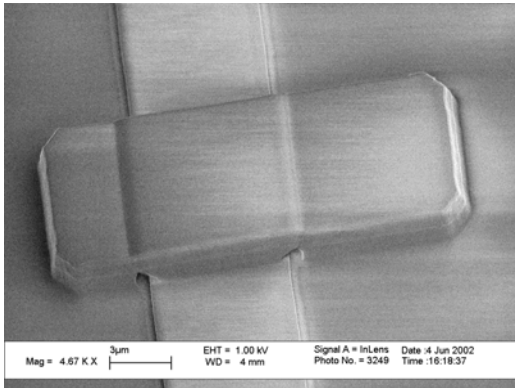


figure F5. Example of a cladding segment fabricated using the final etching process

### F3: References

- [1] T. Koster, doctoral thesis, *TE/TM based integrated optical sensing platforms*, Lightwave Devices Group, University of Twente, dec. 2000, p 47.

## Appendix G: Realization of a vertical taper

The usual way of making vertical tapers in LPCVD  $\text{Si}_3\text{N}_4$  is as follows: on top of the  $\text{Si}_3\text{N}_4$  layer a sacrificial  $\text{SiO}_2$  layer is deposited. Then resist is applied on top of this layer, patterned using photolithography and the wafer is submerged in a BHF solution. The sacrificial  $\text{SiO}_2$  layer is etched away from the side (etch front moves in lateral direction) relatively quickly and at the areas freed of  $\text{SiO}_2$  also the  $\text{Si}_3\text{N}_4$  starts to etch (etch front moves in transverse direction). Due to the very big difference in etch rate between  $\text{SiO}_2$  and LPCVD  $\text{Si}_3\text{N}_4$ , the horizontal under-etch rate is much larger than the vertical  $\text{Si}_3\text{N}_4$  etch rate, resulting in a vertical taper. The bigger the difference in etch rate, the smaller the taper angle that can be obtained. The practical etch rates result in taper angles  $> 3^\circ$ : too large for making an adiabatic taper, which should require a taper angle of  $0.1^\circ$  at maximum (section 3.3.4).

During the characterization of polysiloxane for sensing purposes it was also investigated if polysiloxane could be patterned. It appeared that the etch rate of polysiloxane in a BHF solution was very large, much larger than the  $\text{SiO}_2$  etch rate. Thus the idea was born to use polysiloxane as a sacrificial layer instead of  $\text{SiO}_2$ . The first try however showed that, due to both dust particles originating from the PECVD process and non-uniformities in the polysiloxane layer, holes had been created in the resist layer. Because of the very big under etch, a single hole defect destroys a relatively large wafer area as is shown in Figure G1. A solution to this problem can be found by removing the polysiloxane everywhere where it is not necessary. This way the defects which still are created only can destroy the small area in which the tapers will be applied, because elsewhere there is, due to the absence of polysiloxane, no under-etch present anymore. In Figure G1 a vertical taper (connecting a 500 nm thick  $\text{Si}_3\text{N}_4$  layer to a 100 nm thick layer) is depicted. The taper angle is typically  $0.015^\circ$ , which is extremely small!!

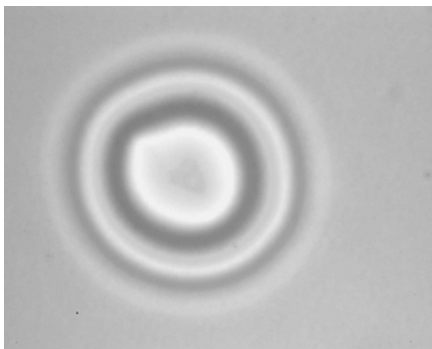
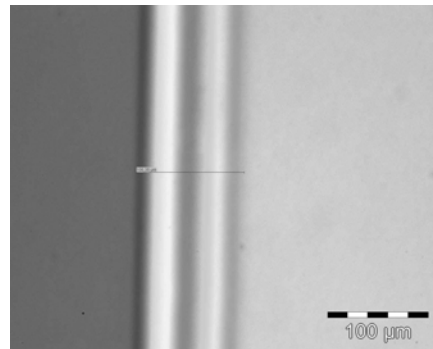


Figure G1. A single defect.



A Vertical taper.

## Appendix H: Analysis test structures GAC sensor

Characterization of a fabricated test sensor hinted at several problems with the fabrication process. In this section these problems will be discussed and the proposed solutions will be given. This appendix will also give some insight into how a fabrication process can develop.

The first problem that was encountered refers to the fiber to chip coupling: the coupling efficiency appeared to be very low (much lower than had to be expected theoretically) and the coupling was unstable in time. A photograph of the fiber to chip coupling area as in Figure H1 reveals the origin of this bad FC coupling.

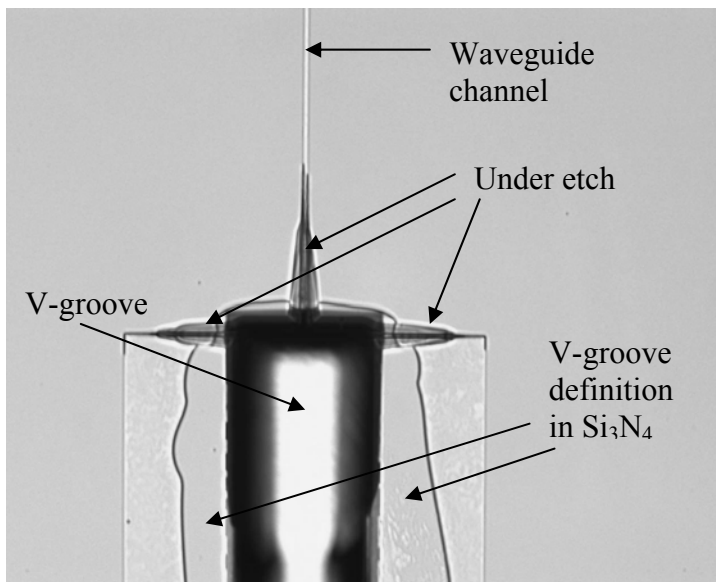


**Figure H1. Fiber to chip coupling.**

The photograph shows a substantial under-etch of the Si<sub>3</sub>N<sub>4</sub> at the beginning of the waveguide channel and at the sides of the Si<sub>3</sub>N<sub>4</sub> planes used to define the V-groove. This causes the end of the Si<sub>3</sub>N<sub>4</sub> waveguide core layer to be suspended freely in the air. Due to this under-etch the mode profile of the waveguide channel has been changed and this explains the bad coupling efficiency. The fragile nature of the waveguide explains the instability of the FC coupling. This problem can be solved by completely milling away the damaged part of the waveguide, at the cost of a somewhat reduced control during the FC coupling adjustment. An explanation for this severe under etch will be given later.

A second problem was encountered; the light was not guided in waveguide channels inside a sensing window. A SEM photograph (Figure H2) of this area reveals that there are no waveguides present anymore. No surprise that the light is not guided.

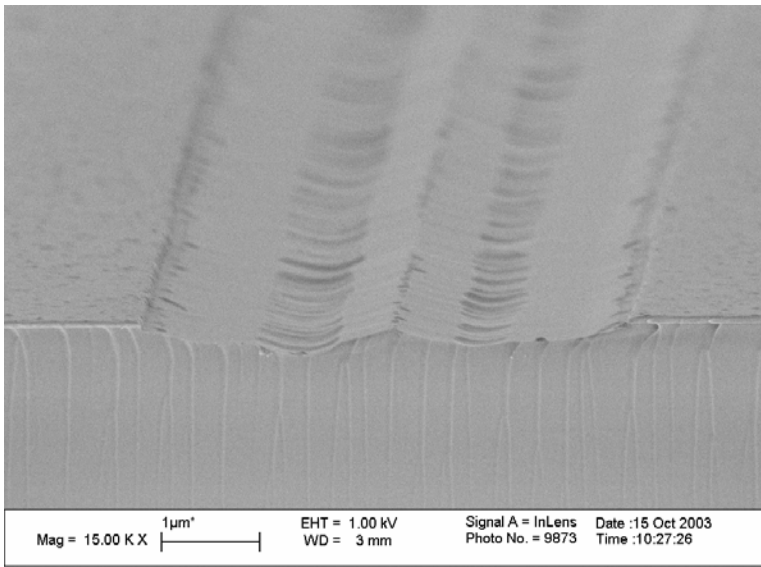


**Figure H2. Absent waveguide in thick core region without cladding.**

A SEM photo of a channel in a region outside a sensing window (Figure H3) reveals the origin of all these problems.

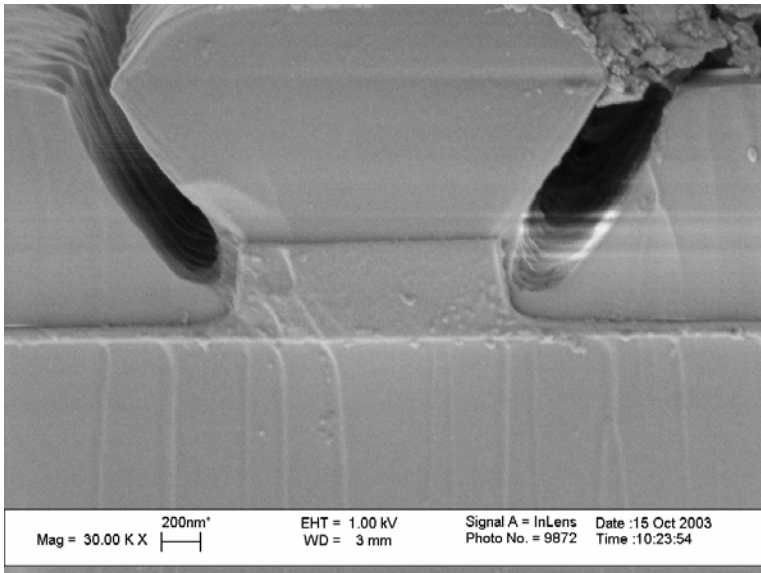


**Figure H3. Waveguide channel in thick core region.**

At both sides of the waveguide ridge a void can be discerned. A decoration BHF dip is used to enhance the contrast for the SEM picture, and as a result the voids also widen. Without a decoration dip the voids are almost completely closed, but their presence can also then clearly be observed. These voids usually develop when a thick PECVD SiO<sub>2</sub> or SiON layer is deposited over a structure with steps in the upper layer. The SiON starts growing on the bottom and on the sidewalls. There where both growing layers meet a small void remains; the larger the step, the larger the void. For this structure with a step

height of 400 nm only such voids had not been expected. These voids are responsible for the under-etch at the FC coupling region and the disappearance of the channel inside the sensing window. After fabrication of the V-grooves the sensing windows are etched using wet chemical BHF etching. From the openings at the V-grooves the BHF solution can enter the voids, similarly like what happened during the decoration dip. The BHF will now start etching away the  $\text{SiO}_2$  around the channel, leaving just a freestanding  $\text{Si}_3\text{N}_4$  channel.

When the sensing windows are wet-etched, the cladding will not etch uniformly. The BHF solution enters the voids and starts etching the cladding from the inside. It also starts etching the thin  $\text{Si}_3\text{N}_4$  slab adjacent to the voids. Once it's etched through the  $\text{Si}_3\text{N}_4$  slab it will start etching the buffer layer isotropically. In Figure H2 it can be seen very nicely where the  $\text{Si}_3\text{N}_4$  slab was broken and from where the isotropic etching process of the buffer layer started. Hence the buffer layer underneath the waveguide channel is removed, all that remains is a very fragile, free standing, narrow channel, which easily breaks and lifts off of the wafer.

The formation of voids can be prevented by using P- or B-doped SiON, thereby reducing its melting point, followed by annealing at a temperature close to this temperature. During this annealing the voids will contract gradually and finally they will disappear. Presently however this technology is not yet available thus we are limited to minimizing both the magnitude and the influence of these voids. Reducing the ridge height to 20 nm proved to prevent the formation of voids. Dry etching, instead of wet chemical etching, presents another solution.

The last problem encountered was the high propagation and bending loss of the channels. Figure H4 shows a SEM photo of a waveguide. Except for a little roughness to the side of the waveguide, there is nothing here that could explain the exceptionally high propagation losses. It is tempting but probably incorrect to attribute these losses to the presence of the voids, because in these structures the value of the modal field at the position of the voids is very small. The propagation losses of waveguides with a ridge height of 20 nm only, fabricated later, proved to be acceptable.

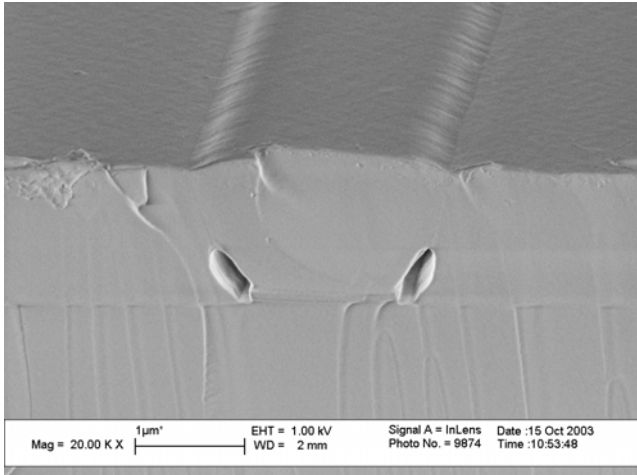


**Figure H4. Waveguide channel in thin core region.**

## Bibliography

- J. van Lith, S. Gaál, P.V. Lambeck, H.J.W.M. Hoekstra, Rene G. Heideman, The Segmented Waveguide sensor: Principle and Experiments, *proceedings ECIO 2003*, pp. 339-342.
- J. van Lith, S. Gaál, P.V. Lambeck, H.J.W.M. Hoekstra, R.G. Heideman, R. Wijn, The Segmented Waveguide sensor: Principle and Experiments, *J. of Lightwave technology*, Vol 23, No. 1 (2005).
- G. Klaasse, R. Stoffer, J. van Lith, H.J.W.M. Hoekstra, P.V. Lambeck, Optische Golflengte Multiplexer-demultiplexer, applied 22 May 2003, Patent number NL1023499.
- H.J.W.M. Hoekstra, J. van Lith, S. Gaál, P.V. Lambeck, The Spectral Decomposition Method: a Transparent Theory for Losses in Segmented Waveguides, *proceedings ECIO 2003*, pp. 339-342.
- P.V.Lambeck, H.J.W.M.Hoekstra, J. van Lith and G. van Elzaker, Two novel Integrated Optical sensor types for measuring chemical concentrations, based on chemically induced changes of modal field profiles, *J. of Nonlinear Optics*, Vol 13, No. 2 (2004) pp.209-217.
- W.Hopman, P. Pottier, D. Yudistira, J. van Lith, P. Lambeck, R. De La Rue, A. Driessen, H.J.W.M. Hoekstra, R.M. de Ridder, Quasi 1-dimensional photonic crystals as building block for compact integrated optical sensors, *proceedings ICTON 2004*, pp. 338-342.
- Wico Hopman, Pierre Pottier, Didit Yudistira, Joris van Lith, Paul V. Lambeck, Richard M. De La Rue, Alfred Driessen, Hugo J.W.M. Hoekstra, René M. de Ridder, Quasi One-Dimensional Photonic Crystal as a Compact Building-Block for Refractometric Optical Sensors, *IEEE Journal on selected topics in quantum electronics*, January 2005.
- J. van Lith, P.V. Lambeck, H.J.W.M. Hoekstra, R.G. Heideman, R.Wijn, A spiralized segmented waveguide structure for sensing; design and characterization, *Sensors and actuators*, submitted for publication January 2005.
- J. van Lith, P.V. Lambeck, H.J.W.M. Hoekstra, Theoretical feasibility study of several novel integrated optical immuno-sensing principles, *Sensors and actuators*, submitted for publication February 2005.
- J. van Lith, H.J.W.M. Hoekstra, P.V. Lambeck, R.G. Heideman, R.Wijn, The spiral segmented waveguide sensor: principles and experiments, *proceedings ECIO 2005*.
- A. Driessen, H. J.W.M. Hoekstra, W. Hopman, H. Kelderman, P.V. Lambeck, J. van Lith, D.J.W. Klunder, R.M. de Ridder, E.Krioukov, C. Otto and J. Greve, Ultracompact optical sensors based on high index-contrast photonic structures, *Proceedings ASKOS 2004*.

## Acknowledgements

I will grab the opportunity given by this most read part of the thesis, with both hands, to thank all the people, who in one way or another helped me to reach this stage in my life.

I would like to start by thanking Paul; I could not have wished for a supervisor who is more patient, understanding, supporting and motivating, as well in good as in bad times. I enjoyed the many scientific discussions we had and I would especially like to thank you for the hard work during the last months of the writing of this manuscript.

Thank you; Hugo for the very pleasant cooperation and for your invaluable input on the theoretical and mathematical aspects of the project. Robert for fabricating impossible devices and for pushing the boundaries of existing technologies. Rene for his practical ideas and Iwan for taking care of the technology at the beginning of the project. Anton for your good mood, willingness to help out where and whenever necessary and your eternal enthusiasm. Henk for being slightly jealous that I found a job in New Zealand. Rita for helping me with the countless organizational chores. And of course I would like to thank all the other clean room technicians who at one time or another contributed to the project: Gabriel, Lucie and Meindert.

Further I would like to mention all my (ex) colleagues. In particular the persons with which I had the opportunity of experiencing an unforgettable adventure in Puerto Rico: Sami (Don't let go of that palm tree!), Ton (bedankt voor de zwoele nachten) and Dion (You can tip me anytime). Thank you Geert for the many cups of coffee we shared and thank you Kazimir for being there whenever I felt like discriminating some Rumanians.

My friends (In no particular order!), for making the last four years as pleasant as it has been: Jacob, Diana, Andrei, Arup, Boris, Roman, Menno, Helmut, Iliane, Bobby, Erik, Jasper, Klaas, Andries, Paul, Chris, Herman, Erwin, Dessy, Eliane, Irena and Arko.

I would like to thank my parents for having given me the opportunity to develop in my way, for letting me study what I liked to study and for supporting me in whatever strange 'carrier choices' I will have in the future. Also for trying to understand again and again what exactly I have been doing and for believing that whatever I have been doing was in some mysterious way useful, somehow.....

Finally I would like to thank my girlfriend Niki for the amazing time we had in between the hard work and stress demanded from us by our PhD projects. You still have some unfinished business here, but I promise you that we'll be together again!

And because all of this is written in a thesis manuscript, it must be true.